Title

Nonresonant Nonlinear Optics of Semiconductors Studied Using Ultrashort Mid-Infrared Pulses

Author

Matteo, Daniel

Publication Date

2024

Peer reviewed|Thesis/dissertation

UNIVERSITY OF CALIFORNIA

Los Angeles

Nonresonant Nonlinear Optics of Semiconductors Studied Using Ultrashort Mid-Infrared Pulses

A dissertation submitted in partial satisfaction of the
requirements for the degree Doctor of Philosophy
in Electrical and Computer Engineering

by

Daniel Alexander Matteo

2024

ABSTRACT OF THE DISSERTATION

Nonresonant Nonlinear Optics of Semiconductors
Studied Using Ultrashort Mid-Infrared Pulses

by

Daniel Alexander Matteo
Doctor of Philosophy in Electrical and Computer Engineering
University of California, Los Angeles, 2024
Professor Chandra J. Joshi, Chair

With the rapid development of mid-infrared laser sources with high peak power and ultrashort pulse durations, it is essential to understand the nonlinear optical properties of materials used for optical elements and photonic devices in the intensity regimes that are now accessible. Further progress in the field demands a new database for nonresonant nonlinear characteristics of widely used transparent mid-infrared materials. In this dissertation, we experimentally characterize the mid-infrared nonlinear optical response of semiconductor materials far from band gap resonances using orders of magnitude higher intensity and shorter pulse durations compared to previous studies with nanosecond laser pulses.

This is first done using 200 ps, 10.6 μm CO_2 laser pulses at intensities between 1–10 GW/cm^2. The nonlinear refractive indices of mid-infrared transparent semiconductors GaAs, n-Ge, and ZnSe are determined, and observations of beat-wave nonlinearity enhancement in GaAs are attributed to a controllable free carrier nonlinearity. Unexpectedly high nonresonant nonlinear absorption is measured, which is a result of accumulated free carrier absorption effects over the course of the intense, picosecond pulses.

Measurements of the same materials' nonlinear optical response at similar intensities are made using 220 fs laser pulses around 10 μm produced via difference-frequency generation. Nonlinear refraction is shown to be nearly constant over this broad parameter range. However, nonlinear absorption of femtosecond pulses is found begin at much higher intensity and exhibit stronger intensity scaling than with picosecond pulses. Strong-field photoionization is discussed in the context of the Keldysh theory. Additionally, measurements of the third-order nonlinearity of the remarkable semiconductor Tellurium are made for the first time, demonstrating a giant nonlinear refractive index ranking among the largest known in a bulk material. Three-photon absorption is observed, and the interplay between strong nonlinear optical and propagation effects are investigated numerically by solving the two-dimensional generalized nonlinear Schrödinger equation.

Finally, mid-infrared photonic applications are demonstrated. The first measurements of second harmonic generation using 3 ps CO_2 laser pulses are made, showing promise for a future platform delivering high-power, high-energy laser pulses around 5 μm or a two-color mid-infrared source suitable for THz generation in air-plasma filaments. All-optical semiconductor switching is studied on femtosecond timescales, employing different materials and wavelengths, for future ultrafast pulse switching and modulation applications.

The dissertation of Daniel Alexander Matteo is approved.

Warren B. Mori

Benjamin S. Williams

Chee Wei Wong

Chandra J. Joshi, Committee Chair

To my parents and sister, for their complete support and love throughout this lifelong journey.

To Sophie, for her daily motivation and strength without which this would not have been possible.

To the unending mysteries of science, thank you for keeping me curious.

Table of Contents

List of Figures

List of Tables

Acknowledgements

I would like to extend my sincerest thanks to my advisor, Professor Chan Joshi, who generously gave me the opportunity to pursue research and guided me through every step of the journey. Through his research group, I have learned deeply about diverse topics reaching far beyond just those contained in this dissertation. Without his mentorship, encouragement, and belief in me, this work would not have been possible.

I am also indebted to Dr. Sergei Tochitsky, whose day-to-day support, guidance, and motivation in the Neptune lab have allowed me to achieve my goal of becoming an experimentalist. He gave me the tools to succeed both with my hands and brain. Special thanks to Dr. Tochitsky for always being able to lighten the mood with great anecdotes about former students or experimental campaigns.

I would like to thank Dr. Jeremy Pigeon for taking me under his wing at the start of my research journey, and being a friend and mentor to this day. He is a constant source of inspiration both in science and life in general.

I have much gratitude for Eric Welch for our morning discussions about a huge array of topics, and for being a great friend and partner in making liquid resistors and spark gaps. I would also like to thank Dana Tovey for many great discussions and fun times at Neptune, and Gerhard Louwrens for educating me on so many hands-on engineering topics.

Countless discussions and pieces of advice from Ken Marsh and Dr. Chris Clayton have proven very useful over the years, and I am thankful to them for this. I would also like to acknowledge Dr. Chaojie Zhang, Dr. Zan Nie, Dr. Chen-Kang Huang, and Dr. Yipeng Wu for their thought-provoking conversations and camaraderie. I am grateful to Mitchell Sinclair for his great friendship throughout the years, and his perspective, as well as Hiroki Fujii, Jen Quintana, Audrey Farrell, and Noa Nambu for their camaraderie and guidance in learning many new research topics in Friday meetings. I am also thankful for a continuing friendship with Ravi Varma, who helped me hone my own mentorship skills.

I thank Professor Warren Mori, Professor Benjamin Williams, and Professor Chee Wei Wong

for serving on my Dissertation committee.

Michelle Phan, Ivy Barrera, and (briefly) Maria Guerrero provided much needed support for which I am thankful.

Finally, an extremely important thank you goes to my family, partner, friends, and pets who have been beyond understanding and supportive during my entire graduate school adventure.

In this dissertation, there are several figures and textual passages that are adapted from or reproduced from previously published work. This includes D. Matteo, J. Pigeon, S. Tochitsky, I. Ben-Zvi, and C. Joshi, "Measurements of nonlinear absorption of intense 10 μm laser pulses in n-Ge, GaAs, and ZnSe," Appl. Opt. 59, 7912 (2020) doi.org/10.1364/AO.399513, on which Section 4.2 is based. Section 4.5 is adapted from D. Matteo, J. J. Pigeon, S. Ya. Tochitsky, U. Huttner, M. Kira, S. W. Koch, J. V. Moloney, and C. Joshi, "Control of the nonlinear response of bulk GaAs induced by long-wavelength infrared pulses," Opt. Express 27, 30462 (2019) doi.org/10.1364/OE.27.030462. Much of Chapter 5 is reproduced or adapted from D. Matteo, S. Ya. Tochitsky, and C. Joshi, "Tellurium crystal pumped with ultrafast 10 μm pulses demonstrates a giant nonlinear optical response," Opt. Express 31, 27239 (2023) doi.org/10.1364/OE.497186. Section 6.1 is a version of D. Matteo, E. Welch, S. Tochitsky, P. G. Schunemann, S. Guha, and C. Joshi, "Efficient second harmonic generation of a high-power picosecond CO_2 laser," Opt. Lett. 47, 1259 (2022) doi.org/10.1364/OL.445099. Section 6.2 is a version of D. Matteo, S. Ya. Tochitsky, and C. Joshi, "Study of photoexcited semiconductor plasmas for ultrafast mid-infrared switching," (in preparation). The previously published articles are adapted or reproduced under the copyright agreements of ©Optica Publishing Group.

I was the original creator of all of the figures and text adapted or reproduced from these articles – of course with assistance from co-authors – with the exception of Figs. 4.11, 4.12, and 4.13. These were the result of simulation work performed by Dr. Uli Huttner and the late Dr. Stephan W. Koch from the University of Marburg, with contributions from Professor Jerry Moloney from the University of Arizona and Professor Mackillo Kira from the University of Michigan.

This work was supported by grants from the Office of Naval Research MURI (N00014-17-1-2705) and Air Force Office of Scientific Research (FA9550-16-1-0139).

Vita

2013 – 2017 B.S. in Astrophysics, University of California, Los Angeles

2017 – 2019 M.S. in Electrical and Computer Engineering, University of California, Los Angeles

Publications

D. Matteo, S. Ya. Tochitsky, and C. Joshi, "Tellurium crystal pumped with ultrafast 10 μm pulses demonstrates a giant nonlinear optical response," Opt. Express 31, 27239 (2023).

D. Matteo, E. Welch, S. Tochitsky, P. G. Schunemann, S. Guha, and C. Joshi, "Efficient second harmonic generation of a high-power picosecond CO_2 laser," Opt. Lett. 47, 1259 (2022).

D. Matteo, J. Pigeon, S. Tochitsky, I. Ben-Zvi, and C. Joshi, "Measurements of nonlinear absorption of intense 10 μm laser pulses in n-Ge, GaAs, and ZnSe," Appl. Opt. 59, 7912 (2020).

D. Matteo, J. J. Pigeon, S. Ya. Tochitsky, U. Huttner, M. Kira, S. W. Koch, J. V. Moloney, and C. Joshi, "Control of the nonlinear response of bulk GaAs induced by long-wavelength infrared pulses," Opt. Express 27, 30462 (2019).

S. Ya. Tochitsky, E. C. Welch, **D. Matteo**, P. Panagiotopoulos, M. Kolesik, J. V. Moloney, and C. Joshi, "Self-channeling of a multi-Joule 10 μm picosecond pulse train through long distances in air," Opt. Express 32, 2067 (2024).

E. Welch, **D. Matteo**, S. Tochitksy, G. Louwrens, and C. Joshi, "Observation of breakdown wave mechanism in avalanche ionization produced atmospheric plasma generated by a picosecond CO_2 laser," Phys. Plasmas 29, 053504 (2022).

J. J. Pigeon, **D. Matteo**, S. Ya. Tochitsky, I. Ben-Zvi, and C. Joshi, "Measurements of the nonlinear refractive index of $AgGaSe_2$, GaSe, and ZnSe at 10 μm," J. Opt. Soc. Am. B 37, 2076 (2020).

Z. Nie, N. Nambu, K. A. Marsh, E. Welch, **D. Matteo**, C. Zhang, Y. Wu, S. Patchkovskii, F. Morales, O. Smirnova, and C. Joshi, "Cross-polarized common-path temporal interferometry for high-sensitivity strong-field ionization measurements," Opt. Express 30, 25696 (2022).

Z. Nie, F. Li, F. Morales, S. Patchkovskii, O. Smirnova, W. An, C. Zhang, Y. Wu, N. Nambu, **D. Matteo**, K. A. Marsh, F. Tsung, W. B. Mori, and C. Joshi, "Highly spin-polarized multi-GeV electron beams generated by single-species plasma photocathodes," Phys. Rev. Research 4, 033015 (2022).

Z. Nie, F. Li, F. Morales, S. Patchkovskii, O. Smirnova, W. An, N. Nambu, **D. Matteo**, K. A. Marsh, F. Tsung, W. B. Mori, and C. Joshi, "*In Situ* Generation of High-Energy Spin-Polarized Electrons in a Beam-Driven Plasma Wakefield Accelerator," Phys. Rev. Lett. 126, 054801 (2021).

Chapter 1
Introduction

Nonlinear optics, or the study of how properties of matter change in response to increasing laser light intensity, is a critical tool in countless disciplines of scientific research and engineering. In nonlinear optical processes, the frequency spectrum of a laser can be significantly modified, allowing access to wavelengths where laser gain media do not exist or cannot support desired pulse formats. For example, ultrafast near-infrared (NIR, wavelength $\lambda = 0.75 - 3$ μm) laser pulses have been down-converted via various nonlinear processes to generate frequencies as low as THz radiation, enabling many applications in medical and industrial imaging [1] as well as probing of fundamental properties of matter [2]. On the other end of the spectrum, NIR lasers can be up-converted via high-harmonic generation (HHG) to the extreme ultraviolet for applications such as attosecond spectroscopy [3], and even as high as X-rays [4] including the use of relativistic harmonic emission [5]. In addition, the growth of integrated nonlinear photonics [6] has allowed for implementation of nonlinear optical effects in chip-scale devices with immense technological potential [7].

The use of NIR lasers for the applications mentioned above is mainly driven by the enormous amount of research, development, and successful commercialization of such laser sources and optical materials in this spectral range in the decades since the ruby laser was first demonstrated [8]. On the other hand, the mid-infrared (MIR) spectral range, broadly defined here as $\lambda = 3 - 20$ μm, has not experienced nearly as much source development. This is currently a frontier of photonics, attracting significant recent attention. The MIR wavelength region is often called the molecular fingerprint region because numerous commonly encountered molecules have rotational and vibrational transitions with resonant frequencies in this range. Thus MIR sources are crucial for applications in industrial, environmental, and medical sensing, fundamental spectroscopy, and standoff detection. Of particular interest are two atmospheric transparency windows with little water vapor absorption – the mid-wave IR (MWIR, 3–5 μm) and the long-wave IR (LWIR, 8–14 μm), in which sources find broad application in remote sensing, optical communications, and infrared countermeasures. The measurements presented in this dissertation are taken primarily in the LWIR but include the

MWIR as well.

MIR laser pulses are also of immense fundamental interest. Since the ponderomotive energy of electrons scales with $U_p \propto I\lambda^2$, where I is the laser intensity, many strong-field physics phenomena have favorable scaling with the laser wavelength. This includes, but is not limited to, the harmonic cut-off of HHG [9, 10], conversion efficiency into THz frequencies [11], or laser-driven particle acceleration [12].

Despite the usefulness of high-power MIR laser sources, there has unfortunately not been nearly as much development compared to the NIR. This is largely due to the relative lack of solid-state laser gain media; molecular gases such as CO_2, CO, and NH_3 are used, but in most cases cannot support ultrafast MIR pulses due to natural bandwidth limitations. In recent years, however, there has been an explosion in short-pulse MIR laser source development. This includes substantial progress in generating 2-3 picosecond laser pulses using discharge pumped high-pressure CO_2 [13, 14], which provides an avenue for amplifying to high peak power in the 9-11 μm region – especially when high pulse energy is desired. Driven by advances in nonlinear crystals and ultrafast NIR pump lasers, parametric nonlinear down-conversion sources have also seen significant development. Among them are difference frequency generation (DFG) sources which can provide widely tunable ultrafast laser pulses, as well as more complex optical parametric chirped pulse amplifiers (OPCPA), demonstrated to produce gigawatt-scale (or higher) ultrafast pulses at wavelengths between 3.9–8 μm [15, 16].

Wider use of high power MIR laser systems requires knowledge of materials' nonlinear optical properties to build photonic devices operating at GW/cm^2 level and higher intensities, up to the fundamental dielectric breakdown limit. The most widely used materials in the MIR are semiconductors such as GaAs, n-Ge, and ZnSe, which have low optical losses and superior mechanical characteristics. Progress in MIR source development has not necessarily translated to progress in understanding the nonlinear response of important MIR materials, however. In many cases, parameters such as the nonlinear refractive index quoted in the literature are taken from measurements made with low peak intensity lasers (on the order of 1-10 MW/cm^2) or extrapolated from NIR measurements. With this in mind, the nonlinear optical response warrants reinvestigation with modern laser systems, where ultrashort pulses allow for higher intensity interactions (> 1 GW/cm^2) while staying below material damage thresholds. Other nonlinear effects can also become significant in

this regime, including nonlinear absorption and self-focusing. Furthermore, the MIR photon energy ($\sim 0.1 - 0.4$ eV) is ideal to pump solids with a wide range of band gap energies for study of fundamental light-matter interactions. This is particularly true of narrow-gap semiconductors, which have remained relatively unexplored as they are not transparent to NIR wavelengths. For instance, narrow-gap semiconductors such as tellurium (Te) and $CdGeAs_2$ are predicted to have extremely high nonlinear refractive indices [17], which makes them ideal candidates for future MIR photonic applications or even integration into chip-scale devices. However, some of the most relevant aspects of these materials' MIR nonlinear optical responses are unknown.

In this dissertation, we use state-of-the-art mid-infrared laser sources to experimentally investigate various aspects of the nonlinear optical response in semiconductors, as well as implement the lasers and materials in specific photonics applications. Many fundamental concepts and equations from nonlinear optics and semiconductor physics will be used throughout the dissertation; these are introduced in Chapter 2 along with the main numerical method used to model experimental results, the generalized nonlinear Schrödinger equation. The laser systems we use and their working principles are detailed in Chapter 3. These include both megawatt- and gigawatt-class picosecond CO_2 lasers, as well as a high repetition rate sub-picosecond DFG source. Experimental results in Chapter 4 address one of the problems introduced above – the nonlinear response of semiconductors has not been characterized using high intensity MIR laser pulses. To help fill the gap, nonlinear refraction and nonlinear absorption are quantified in GaAs, n-Ge, and ZnSe at intensities between 1-10 GW/cm^2. In addition, a method to optically control the nonlinear response in GaAs is described. We extend these measurements to the sub-picosecond pulse regime in Chapter 5. Here, we also measure nonlinear refraction of Te for the first time, uncovering a giant nonlinear optical response. The interplay of bound electron and free carrier responses are studied in tellurium. Finally, photonics applications are explored in Chapter 6; first, efficient second harmonic generation with picosecond CO_2 lasers is systematically characterized for the first time using nonlinear crystals with a range of effective nonlinearities (with varying degrees of success); then, we study the dynamics of semiconductor switching and modulation of mid-infrared pulses on femtosecond timescales.

Chapter 2
Theory of Nonresonant Nonlinear Optics in Semiconductors

In this chapter, we give the theoretical framework that is used to interpret various aspects of the nonresonant nonlinear optical response of semiconductors in the mid-infrared spectral range. Of particular interest is the nonlinear optical response of multiple semiconductor materials with a range of physical parameters such as electronic band gap energy and refractive index. While some of the discussion in this chapter is common to both dielectrics and semiconductors across the entire optical as well as infrared frequency range, it is given here for completeness as it will provide an introduction to the equations and theoretical concepts that govern the topics in the following chapters.

2.1 Nonresonant Nonlinear Optics in Semiconductors

Semiconductors are ideal materials for studying nonresonant nonlinear optical effects with MIR lasers as they have fundamental energy gaps typically ranging from 0.3 to 3 eV. Here, nonresonant refers to the photon energy far less than the band gap energy of the semiconductor. For instance, photons with energy 0.09 - 0.15 eV ($\lambda = 8 - 14$ μm) have energy 2-3 times smaller than the band gap, giving access to 2 or 3 photon resonant regimes. On the higher end, the energy gap requires the simultaneous absorption of >10 photons to excite an electron from the valence to conduction band. In this case light-semiconductor interaction is extremely far from resonance.

It goes without saying that much of our modern technology relies on semiconductors and their carefully controllable electrical properties. Although linear optical properties such as the wavelength dependence of the real and imaginary part of the dielectric constant (refractive index) has been well documented using incoherent light, it was the invention of the laser that prompted the study of nonlinear properties of semiconductor materials. In the MIR, the principal materials used are GaAs, n-Ge, and ZnSe due to their high transparency in this region. Many linear optical and physical properties of these materials are well documented. While their nonlinear optical response

is known to be large based on some studies and extrapolation from the NIR, the high intensity ($\gtrsim$GW/cm^2) response has not been documented.

2.1.1 Nonlinear Optics Introduction

The macroscopic nonlinear response of matter to electric fields is typically described using a perturbative expansion of the electric polarization $\vec{P}$ in the electric field $\vec{E}$,

$$\vec{P}(\vec{r},\omega) = \epsilon_0 \left[\chi^{(1)} + \chi^{(2)} \cdot \vec{E} + \chi^{(3)} \cdot \vec{E}\vec{E} + ...\right] \vec{E}, \tag{2.1}$$

where ω is the angular frequency associated with the electric field, ϵ_0 is the permittivity of free space, and $\chi^{(n)}$ is the nth order electrical susceptibility (rank $n+1$ tensor). Note that in general both the electric field and the susceptibilities have space ($\vec{r}$) and frequency (ω) as well, but they have been left out for compactness.

$\vec{P}$ can be split into a linear (in $\vec{E}$) part $\vec{P_L} = \epsilon_0 \chi^{(1)} \vec{E}$ and nonlinear ($\vec{E}^n$) part

$$\vec{P}_{NL} = \epsilon_0 \sum_{n=2}^{\infty} \chi^{(n)} \vec{E}^n, \tag{2.2}$$

The linear susceptibility encodes all linear optical properties of the material, such as linear absorption and refractive index. In most situations, the first two nonlinear susceptibilities $\chi^{(2)}$ and $\chi^{(3)}$ are sufficient to describe the nonlinear interaction because the product of $\chi^{(n)}\vec{E}^n$ rapidly vanishes as n increases due to our assumed perturbative process. Since each higher order susceptibility tends to be much smaller than the previous order, nonlinear optical effects are only observed with the strong electric fields attainable in laser beams. Due to symmetry considerations [18], only noncentrosymmetric materials (including many common semiconductors) possess a nonzero $\chi^{(2)}$, whereas all materials have a nonzero $\chi^{(3)}$.

The electric polarization and susceptibility physically arise from the a collection of microscopic electric dipole moments, which are classically represented as $\vec{d} = e\vec{r}$. Here $\vec{r}$ is the displacement of two charges with the fundamental unit of charge e and opposite signs. In a quantum system with

wavefunctions ψ_j for each state j, the dipole moment between states k and l is the overlap integral

$$\vec{d_{kl}} = e \int \psi_k^* \, \vec{r} \, \psi_l \, d\vec{r}. \tag{2.3}$$

Dipole moments and thus material polarization can be straightforward to calculate in atomic systems. However in more complicated solid-state systems, density matrix formalism should be employed (Section 2.2.2).

The nonlinear wave equation is written in the slowly varying amplitude approximation (valid when a laser is not extremely tightly focused) as

$$\nabla^2 \vec{E} - \frac{\epsilon_r}{c^2} \frac{\partial^2 \vec{E}}{\partial t^2} = \frac{1}{\epsilon_0 c^2} \frac{\partial^2 \vec{P}_{NL}}{\partial t^2}. \tag{2.4}$$

From this, countless nonlinear optical phenomena arise naturally, including various wave-mixing processes (e.g. second harmonic generation, difference frequency generation).

In the simplest example of second harmonic generation, photon energy conservation, $\hbar\omega_2 = \hbar(\omega_1 + \omega_1)$, and photon momentum conservation, $\hbar\vec{k}_2 = \hbar(\vec{k}_1 + \vec{k}_1)$, must be satisfied to have significant growth of the second harmonic wave $\mathcal{E}_2$ without rapid oscillation in space/time. The phase mismatch ($\Delta k = \vec{k}_2 - 2\vec{k}_1$) defines the coherence length, $l_{coh} = \frac{\pi}{|\Delta k|}$, the length over which mismatched waves generate maximum signal. It can be shown [19] that when the propagation length L is much longer than l_{coh}, the associated nonlinear wave-mixing process is negligible in the description of wave propagation. So while any combination of frequencies contained in the pump electric field is energetically allowed, only those that are phase matched or nearly phase matched will grow substantially. A notable exception to this is the cascaded quadratic nonlinearity [20]. In practice, phase matching for differing frequencies can be achieved with the use of birefringent crystals [21].

2.1.2 The Nonlinear Refractive Index

One of the most remarkable nonlinear optical phenomena, and one of major importance in this dissertation, is the intensity dependence of the refractive index. This is a third order nonlinear

optical effect related to the nonlinear optical susceptibility $\chi^{(3)}(\omega = \omega + \omega - \omega)$. To understand this effect, also called the optical Kerr effect, we assume all electric fields are plane waves with the same polarization and wavevector. In other words, photons from a single collimated laser beam interact with each other.

Starting from Eq. 2.4 and introducing the paraxial approximation ($\partial^2\mathcal{E}/\partial z^2 \gg \nabla_\perp^2$) and slowly varying envelope approximation ($d^2\mathcal{E}/dz^2 \ll k\, d\mathcal{E}/dz$), the following first order differential equation in the electric field envelope $\mathcal{E}$ is attained [22]:

$$\frac{d\mathcal{E}}{dz} = -\frac{i}{2k}\frac{\omega^2}{\epsilon_0 c^2}\frac{3}{4}\epsilon_0\chi^{(3)}\mathcal{E}\mathcal{E}\mathcal{E}^* \tag{2.5}$$

As this interaction does not explicitly generate new frequencies it possesses automatic energy conservation and phase matching. Using the definition of the light intensity, $I = \frac{1}{2}n_0\epsilon_0 c|\mathcal{E}|^2$, this expression can be simplified to

$$\frac{d\mathcal{E}}{dz} = -i\frac{\omega}{c}\left(\frac{3\chi^{(3)}}{4c\epsilon_0 n_0^2}I\right)\mathcal{E}. \tag{2.6}$$

It can be seen that this phase-matched self-effect only modifies the phase (imaginary part) of the electric field. For this reason, the expression inside the parentheses acts the same as an effective refractive index. The total refractive index can then be rewritten as

$$n = n_0 + n_2 I \tag{2.7}$$

where n_2 is the nonlinear refractive index. Comparison to Eq. 2.6 shows the relationship $n_2 = \frac{3\chi^{(3)}}{4c\epsilon_0 n_0^2}$.

The impacts of the nonlinear refractive index are far-reaching and of critical importance to the design of any laser system or photonic device, especially when considering ultrafast laser pulses. In most practical cases, n_2 can effectively be used as a proxy for describing the third-order nonlinearity of a material. In this dissertation, we encounter the nonlinear refractive index in multiple different contexts, including four-wave mixing, self-phase modulation (SPM), and self-focusing. There are different physical origins of the nonlinear refractive index which will be discussed in this dissertation; some of these mechanisms will be presented throughout the chapter.

A useful quantity for tracking the nonlinear phase shift of a laser beam during propagation is

the B integral. The B integral is defined as

$$B_{NL} = \frac{2\pi}{\lambda_0} \int_0^L n_2 I(z) dz \tag{2.8}$$

where λ_0 is the vacuum central wavelength and L is the total propagation length. The B integral is simply the total accumulated nonlinear phase shift accounting for dynamic changes in intensity due to beam focusing, dispersion, or other causes. In general the B integral varies across a laser beam, but the peak value at the most intense point of the beam is typically stated. A useful quantity related to the B-integral is the nonlinear length [23],

$$L_{NL} = \lambda_0 / 2\pi n_2 I \tag{2.9}$$

or the length over which 1 radian of nonlinear phase is accumulated with a constant light intensity.

Similar to linear optics, where the refractive (real) and absorptive (imaginary) parts of the susceptibility can be related to each other via the Kramers-Kronig relationship, often whenever strong nonlinear refraction exists nonlinear absorption (NLA) will also be present. This will be discussed below in the context of semiconductor band structures.

2.1.3 Self-Phase Modulation

While the optical Kerr effect does not explicitly generate new frequencies in the same way other nonlinear optical interactions do (e.g., second harmonic generation), phase modulating a laser pulse does indeed broaden its spectrum. This can be seen by introducing the definition of the instantaneous frequency as $\omega_{inst} = d\phi/dt$, where ϕ is the phase of the electric field. Consider a Gaussian laser pulse in time with electric field

$$E(t) = \mathcal{E}_0 e^{-2\ln 2(t/\tau)^2 - i(\omega_0 t - kz)}. \tag{2.10}$$

When including the nonlinear refractive index,

$$\omega_{inst} = \frac{d}{dt} \left[i\omega_0 t - ik_0 (n_0 + n_2 I(t,z)) z \right] \tag{2.11}$$

where ω_0 and k_0 are the central frequency and central vacuum wavenumber, respectively. Clearly, there is a time dependent instantaneous frequency proportional to $n_2\, dI/dt$. Based on the sign of dI/dt, the local frequency is either downshifted (change is toward the red during the rising intensity edge of the laser pulse) or upshifted (change is toward the blue during the falling intensity edge) - assuming n_2 is positive. Along with spectral broadening, this process introduces positive chirp in the central region of a Gaussian laser pulse.

Depending on the context, the spectral broadening and chirp from SPM can be detrimental or beneficial. For example, SPM can be used in conjunction with a negatively dispersive structure (e.g. grating compressor) to introduce additional bandwidth and compress the pulse in time to a shorter duration. However, due to the intensity dependence of SPM, a Gaussian laser beam will experience varying levels of spectral broadening and nonlinear phase across the beam. Inhomogeneity of this sort can often be detrimental in laser systems.

2.1.4 Self-Focusing

Perhaps the simplest to understand multi-dimensional nonlinear optical effect is self-focusing, a spatial analogue of time-domain SPM. A high intensity laser beam in any medium - including air - will produce an intensity dependent phase delay across the beam. If n_2 is positive, this phase delay acts the same as a convex lens - the laser beam focuses itself, after which the intensity grows and the focusing strength increases.

This runaway focusing is an extremely important nonlinear optical effect. On one hand, self-focusing can be beneficial; a widely used laser mode-locking technology, Kerr-lens mode-locking, is only possible through self-focusing. In addition, self-guiding and filamentation regimes are of immense scientific and practical interest, enabling low-loss propagation over long distances in the atmosphere, or generating low resistance channels to guide electrical discharges [24]. On the other hand, It has been empirically shown that when the peak B integral exceeds 3-5 radians, small scale self-focusing, beam breakup, and other potentially detrimental nonlinear effects may begin to occur [25].

In order for nonlinear self-focusing of a laser beam to just overcome spreading due to diffraction,

the peak power must be above the critical power for self-focusing [18]

$$P_{crit} = \frac{3.77\lambda^2}{8\pi n_0 n_2}. \tag{2.12}$$

The λ^2 scaling of P_{crit} hugely increases the required power to self-focus in the MIR compared to the NIR. In air, which has $n_2 \approx 10^{-19}$ cm^2/W across the NIR and MIR [26], the critical power for self-focusing for a 1 μm and 10 μm laser are 5 GW and 500 GW, respectively. While $P > P_{crit}$ is attainable for both regimes, it is much more readily reached at 1 μm where ultrafast and high-power laser technology is far more developed.

In this dissertation we consider materials that possess extremely large n_2, so that our MIR laser peak powers are almost always much above P_{crit}. A semiconductor with Kerr nonlinearity on the order of $n_2 \approx 10^{-14}$ cm^2/W reduces P_{crit} at 10 μm to the order of 1 MW.

In experiments where we routinely use laser peak powers much higher than this, a self-focusing length z_{SF} can be introduced, which represents the distance at which an unfocused Gaussian pulse with spot size w_0 will self-focus to an intensity singularity [27, 28]:

$$z_{SF} = \frac{2.306 n_0 w_0^2}{\lambda_0} \left[\left(\sqrt{\frac{P}{P_{cr}}} - 0.852 \right)^2 - 0.0219 \right]^{-1/2} \tag{2.13}$$

While the self-focusing length changes dramatically with beam divergence [29], and a singularity is never actually reached due to various arresting mechanisms, it still serves as a qualitative guide as to when self-focusing needs to be heeded.

Consider a 10 μm beam loosely focused to $w_0 = 1$ mm in a material with $n_0 = 3.27$. With $P/P_{crit} = 10$, $z_{sf} = 31$ cm, on the same order of the Rayleigh length and much longer than the $L \leq 1$ cm samples we use in experiments. In this regime, while the nonlinear phase accumulated during propagation will cause a nonlinear focus downstream, the beam size will change by an insignificant amount over the length of the sample. When $P/P_{crit} = 1000$, $z_{sf} = 2.3$ cm. Here, self-focusing may modify propagation in a meaningful way over the length of the sample. Numerical modeling of nonlinear propagation is an important tool to determine the impact of self-focusing on experimental results.

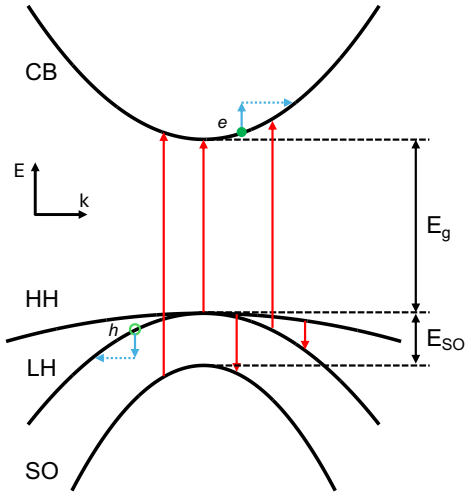

Figure 2.1: Schematic band structure in the parabolic approximation showing one lowermost conduction and three uppermost valence bands with a direct band gap. Possible direct optical transitions are shown with red arrows, whereas intraband indirect transitions (e.g. phonon assisted) are shown with blue arrows.

2.1.5 Semiconductor Band Structures

The energy band theory of solids provides a model of how electronic wavefunctions of atoms at solid density ($N \approx 10^{23}$ cm^{-3}) blend to form allowed and forbidden energy bands. Without delving into the intricacies of the theory, which has been described in a large number of textbooks, we will summarize the main features of relevance in this dissertation.

An example of a band structure for a typical III-V semiconductor is drawn in Fig. 2.1, which simply represents the dispersion relation of electronic energy states. Consideration of the 4 bands nearest the band gap is usually sufficient to describe most nonresonant nonlinear optical interactions (in many cases, only two bands are required). The near parabolic shaped conduction band (CB) contains any quasi-free electrons, which from here on will be called free electrons. With negative energy inverted parabolic curves are the 3 valence bands heavy-hole (HH), light-hole (LH), and split-off (SO), for which spin-orbit splitting has broken degeneracy due to their nonzero angular momentum quantum number. Each of these four bands is two-fold spin degenerate. In an unexcited semiconductor, the valence bands are fully filled with electrons. After excitation, the free hole quasiparticle will be generated, acting like an electron with opposite charge.

While full-scale quantum mechanical description of the band structure can be made, e.g. using the density functional theorem (DFT) formalism, the parabolic approximation helps in many cases. The parabolic approximation maps the energy band dispersion onto the kinetic energy of an unbound electron; for the example of a conduction band,

$$E = E_g + \frac{\hbar^2 k^2}{2m^*} \tag{2.14}$$

where the influence of the periodic ion potential is captured in the effective mass $m^* = \hbar^2(d^2E/dk^2)^{-1}$, with $\hbar k$ as the electron crystal momentum. Similarly, the group velocity of an electron or hole wavepacket is related to the band dispersion via $v_g = (1/\hbar)dE/dk$. In general the electron crystal momentum/wavevector exists in a 3 dimensional reciprocal space, but for our purposes we can reduce it to a 1 dimensional quantity. While semiconductor crystal structure naturally results in the orientation dependence of the band structure as well as many linear and nonlinear optical properties, in this dissertation we will primarily use pump lasers linearly polarized along orientations of high symmetry. Polarizations and carriers are only excited/driven in along the polarization of the laser, also justifying the simplification of the tensor structure of $\chi^{(3)}_{ijkl}$ to the scalar n_2, where the nonlinear refractive index is defined along the orientation being pumped. Relevant band gap energies and effective masses for semiconductors we study in this dissertation are tabulated in Appendix B.

A more accurate description of the semiconductor band structure includes nonparabolic deviations from the parabolic approximation. The consequences of nonparabolicity in the nonlinear optical response will be discussed in Section 2.1.10.

2.1.6 Bound Electron Nonlinear Response

The effective Kerr nonlinearity of a semiconductor can be represented as a sum of all contributions to the nonlinearity, which may have different spectral dependencies and time dynamics. In our work, the bound electron and free carrier nonlinear response are the most important, so that $n_{2,eff} = n_{2,bound} + n_{2,free}$.

The bound electron response in semiconductors can be understood through a simple picture of an electron in a periodic potential (Fig. 2.2). The anharmonic oscillator model gives a nonlinear

restoring force and thus polarization density when under the influence of a periodic electric field. Using an asymmetric periodic potential (as in a noncentrosymmetric crystal), recovers the even-order nonlinear response as well. The bound electron nonlinear response is a baseline nonlinearity present in all materials and experimental configurations.

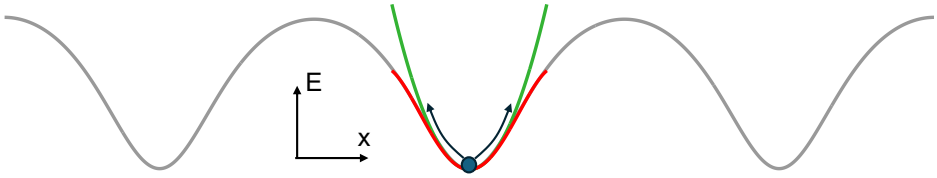

Figure 2.2: Breakdown of the simple harmonic oscillator model for an electron in a periodic potential.

2.1.7 Nonlinear Absorption and the Free Carrier Nonlinear Response

Nonlinear absorption (NLA), or any light energy loss mechanism that scales with the light intensity, is of equal importance to the refractive nonlinear response. In semiconductors, nonresonant nonlinear absorption is associated with photoionization and the subsequent interaction of the laser with generated quasi-free photocarriers. The presence of free carriers in a semiconductor, via photoionization or any other source (e.g. intentional doping, impurities, thermal generation, or injection), makes the nonlinear optical response much more dynamic. This is especially true for irradiation with MIR lasers, as the laser field interacts with free carriers with a strength related to the ponderomotive energy $U_p \propto I\lambda^2$.

A general expression for nonlinear absorption is

$$\frac{dI}{dt} = \alpha\left(I, N, T, \cdots\right) I \tag{2.15}$$

where the absorption coefficient depends on any number of variables including intensity, carrier density, and temperature. Similarly, the carrier density grows with a photoionization rate w_{PI}:

$$\frac{dN}{dt} = w_{PI}\left(I, N, T, \cdots\right). \tag{2.16}$$

The nontrivial coupling of I and N often requires numerical calculations to fully elucidate the

behavior of the light-matter interaction (Section 2.2).

2.1.8 Multiphoton Absorption

Multiphoton absorption (MPA) is a well-documented nonlinear absorption mechanism that can conveniently be described in a perturbative nonlinear optics framework. For example, starting from Eq. 2.5 if we take $\chi^{(3)}$ to be imaginary, it is clear that there will be nonlinear loss. Multiplying both sides by $\mathcal{E}^*$ and substituting the light intensity gives

$$\frac{dI}{dz} = -\alpha_2 I^2 \tag{2.17}$$

where α_2 is the two-photon absorption coefficient proportional to $\mathrm{Im}\chi^{(3)}$. This is another self-effect where phase-matching is automatically satisfied, and energy conservation is satisfied provided an available energy state exists at $E = 2\hbar\omega$ above the initial state.

Any order M of multiphoton absorption is theoretically possible in a semiconductor with $M \leq \lceil E_g/\hbar\omega \rceil$, with higher orders being less likely and requiring higher intensity. The total absorption can then be represented as

$$\frac{dI}{dz} = -\sum_{M=1} \alpha_M I^M \tag{2.18}$$

where α_1 is linear absorption. Two-photon absorption (2PA) has been the most widely studied multiphoton absorption process in semiconductor nonlinear optics, largely due to the prevalence of NIR lasers near 1 μm ($\hbar\omega \approx 1$ eV) and common semiconductor band gap energies of 1-2 eV. In the MIR, MPA orders are typically large due to the large ratio $E_g/\hbar\omega$, and have not been studied. However, lower MPA orders (and thus stronger absorption) are possible in narrow-band gap materials like InAs and Te.

While the multiphoton absorption coefficient is calculable in certain situations [30], it is almost always empirically determined for specific laser parameters and materials. In addition, large band-width laser pulses (or multiple pulses with different frequencies) can lead to in non-degenerate MPA, further complicating the physics.

Multiphoton absorption tends to be a limiting factor in operation of nonlinear photonic devices

including all-optical switches. A figure of merit (FOM) can be defined as

$$FOM = \frac{n_2 I_{peak}}{\lambda} \frac{1}{\sum_{M=1} \alpha_M I_{peak}^{M-1}} \tag{2.19}$$

which represents the usefulness of a material to provide nonlinear phase shift with low loss. Different thresholds of the FOM have been established, but FOM between 1-10 have been quoted for all-optical switching and nonlinear directional couplers [17], both extremely useful devices for any future MIR photonics devices.

2.1.9 Keldysh Theory of Photoionization

A unified model of photoionization was proposed in 1964 by L. V. Keldysh [31], providing a theoretical framework linking the seemingly opposed regimes of multiphoton and tunneling ionization. It captures much of the physics present in photoionization in a wide range of materials, and gives a convenient analytical formula to calculate the ionization rate. While a full band structure is not included, key insights are still possible.

A defining quantity in the Keldysh theory is the so-called Keldysh parameter

$$\gamma = \sqrt{\frac{I_p}{2U_p}} \tag{2.20}$$

where I_p is the ionization potential (band gap energy in semiconductors) and

$$U_p = \frac{e^2 E^2}{4 m_r^* \omega_0^2} \propto I \lambda_0^2 \tag{2.21}$$

is the ponderomotive energy, with m_r^* taken to be the appropriate reduced effective mass of the electron-hole pair. The Keldysh parameter helps delineate major photoionization regimes. When $\gamma \ll 1$, the interaction is in the tunneling limit, where the laser field is strong enough to significantly modify the ionization potential (Fig. 2.3(a)) and allow for electron tunneling to a free state. Here, the ionization rate is approximated by an exponential. The opposite limit, $\gamma \gg 1$, denotes the multiphoton regime, where energy of multiple individual photons are summed to span the ionization potential, giving perturbative power scaling of the ionization rate.

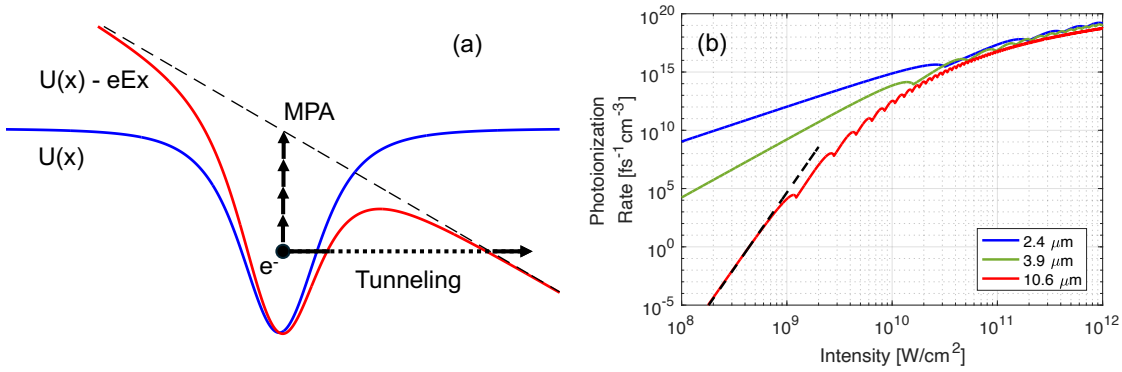

Figure 2.3: (a) Schematic of strong field photoionization. (b) Keldysh photoionization rate calculated in GaAs. Channel closing and non-perturbative effects are clearly observed in all cases, but most apparently for $\lambda = 10.6$ μm. The black dashed line shows an MPA fit, $\propto I^{13}$.

Between these two limits, where $\gamma \approx 1$, is the so-called diabatic (or non-adiabatic) tunneling regime [32]. Photoionization of this kind is a dynamic mixture of both MPA and tunneling processes. If MPA is "vertical" ionization and tunneling is "horizontal" ionization (Fig. 2.3(a)), then diabatic tunneling is diagonal, including contributions of both. This regime has been less explored than the high-frequency and low-frequency limits, and is of great fundamental interest [32]. Remarkably, most of our experimental measurements exist within the diabatic tunneling range.

Examples of the Keldysh ionization rate calculated for GaAs ($I_p = 1.42$ eV) with different laser wavelengths are presented in Fig. 2.3(b). A notable result of the Keldysh model is the dynamic modification of the effective ionization potential on a transient time-scale based on the local laser intensity. This can be seen in Fig. 2.3(c) as the kinks, where the ionization rate is locally reduced due to an M-photon absorption process becoming an M+1 photon process - for this reason, this mechanism is sometimes called multiphoton channel closing. A physical interpretation of this is that the electron and hole states are modified by the strong field, and gain total energy equal to the ponderomotive energy. Thus, when the laser intensity is high enough where $\gamma_{NP} = U_p/\hbar\omega_0 > 1$, the interaction can change the effective band gap and be considered in the nonperturbative intensity regime. Description of the light-semiconductor interaction when $\gamma_{NP} > 1$ can be quite complicated, with different parts of the laser in space and time experiencing different ionization dynamics.

The Keldysh theory will be applied throughout this dissertation to provide insight into nonlinear absorption processes of different forms.

2.1.10 Free Carrier Nonlinear Response

When electrons and holes are photogenerated at a time t_0, they will continue to interact with the laser field for all time $t > t_0$. This is a cumulative effect which, given a constant peak intensity, will have a bigger impact on longer pulses than shorter pulses.

An important aspect of the free carrier nonlinear response is nonparabolicity of the energy bands. Observation of the nonparabolic free carrier nonlinearity was first observed by Patel et al. [33] in doped semiconductors and described analytically by Wolff and Pearson [34]. It also applies to dynamically generated photocarriers, and can be understood using the semiclassical Bloch acceleration theorem [32].

In this model, a spatially localized electron wavepacket traverses the conduction band with a trajectory

$$\vec{k}(t) - \vec{k}(t=0) = -\int_0^t \frac{e}{\hbar}\vec{\mathcal{E}}(t)dt \tag{2.22}$$

where $\vec{k}$ is the central wavevector of the wavepacket and $\vec{\mathcal{E}}(t)$ is the laser electric field. Acceleration of the electron results in a current $J \propto v_g$, which also acts as a source term in the nonlinear wave equation Eq. 2.4, as $J = \partial P/\partial t$.

An example of this is given in Fig. 2.4. Fig. 2.4(a) shows the conduction band of GaAs along the [111] axis calculated with 3 different models - the parabolic approximation (black curve), the first order nonparabolic correction (dotted blue), and a full scale DFT calculation (dashed red). Clearly, the parabolic approximation ($m_e^* = 0.067m_0$) is only valid near the band edge, whereas the nonparabolic approximation extends the validity region slightly further.

For demonstration purposes, an electron wavepacket centered at $k = 0$ is irradiated with an 80 fs duration laser pulse with peak intensity 15 GW/cm^2 and central wavelength 10 μm. The group velocity trajectory is calculated via Eq. 2.22 for the parabolic approximation and the DFT band structure (Fig. 2.4(b)). In the parabolic approximation, the group velocity, and thus current, follows the driving field exactly. Clearly, with a more accurate nonparabolic band structure (DFT), there are strong deviations of the group velocity from the driving field. Fourier transforming the velocity (Fig. 2.4(c)) gives the spectral distribution of the current, and thus source frequencies

in the nonlinear wave equation. The nonparabolic band structure generates a broadened current frequency spectrum with significant odd harmonics as well. Also shown is the current spectrum under irradiation of an identical laser pulse, but with central wavelength 2 μm. Clearly, MIR light can drive free carrier nonlinearities very efficiently.

While true electron dynamics are more complicated than this simple model, e.g. scattering and dephasing dynamics, this model gives good qualitative understanding of an important MIR free carrier nonlinearity. It should be noted that at several times higher intensity, electrons can be driven to the edge of the band and Bragg reflect during a single laser cycle, resulting in huge accelerations and broad frequency generation. Dynamical Bloch oscillation, as this is called, is one mechanism responsible for solid high-harmonic generation at long wavelengths [32].

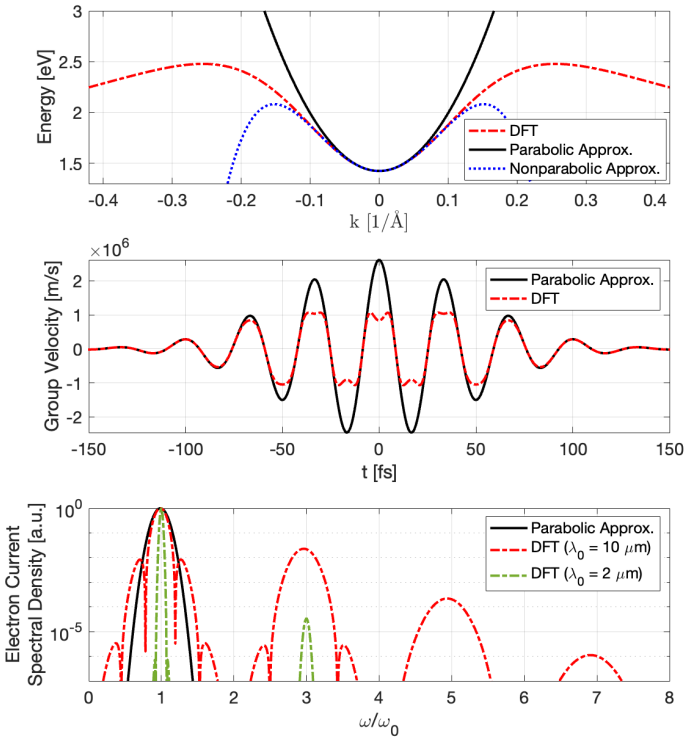

Figure 2.4: (a) Conduction band of GaAs calculated via different methods. (b) Group velocity dynamics of an electron accelerated by a 10 μm, 15 GW/cm^2 laser pulse under the Bloch acceleration theorem. (c) Spectral content of the current via Fourier Transform. The same calculation is done changing only the central wavelength to 2 μm, shown in green, clearly demonstrating the wavelength scaling of the free carrier nonlinearity.

An excited semiconductor can also be viewed through the lens of a classical plasma, with some modifications. Under the Drude model, a photoexcited electron-hole plasma will have a characteristic plasma frequency of

$$\omega_{ehp}^2 = \frac{e^2 N}{m_r^* \epsilon_r \epsilon_0} \tag{2.23}$$

where N is the plasma density (assuming charge neutrality), ϵ_r is the background dielectric constant, and m_r^* is the reduced effective mass of the electrons and holes.

An M-photon ionized semiconductor plasma, assuming no band-filling and a Boltzmann distribution, will have average excess carrier energy $E_{ex} < M\hbar\omega - E_g$. With MIR photon energies near 0.1 eV, this is easily considered a "cold" plasma (with respect to most gas plasmas), and far from a regime associated with ablation and permanent damage of the material. The semiconductor plasma cools to the lattice temperature on picosecond time scales [35].

An electron-hole plasma provides a negative change to the linear refractive index

$$\Delta n_{plas} = n_0 \sqrt{1 - \frac{N}{N_{crit}}} - n_0 \tag{2.24}$$

where N_{crit} is the critical plasma density, when $\omega_0 = \omega_{ehp}$. When $N \ll N_{crit}$, this is often approximated as

$$\Delta n_{plas} \approx -\frac{N}{2N_{crit}} \tag{2.25}$$

Note that collisional damping (Ohmic loss) is ignored above. For typical Drude damping rates in semiconductors (e.g. $\tau \approx$100 fs in GaAs), the damping will only significantly affect the mid-infrared plasma dispersion once carrier density is within approximately 10% of the critical density.

When a high power laser beam self-focuses, plasma generation will introduce a defocusing mechanism which, in addition to diffraction, can arrest the self-focusing process and lead to a filamentation regime. Assuming an intensity dependent carrier generation mechanism, this plasma modification of the refractive index acts as another effective nonlinearity. The B integral offers a convenient way to assess the impact of plasma generation during propagation and compare to phase shift from other

sources of nonlinear phase. The plasma B-integral is

$$B_{ehp} = -\frac{\pi}{\lambda_0}\int_0^L \frac{N(z)}{N_{crit}}dz. \tag{2.26}$$

2.1.11 Free Carrier Absorption (FCA)

The Drude model predicts an imaginary susceptibility causing absorption. However, in the confines of the band structure, intraband transitions require a 3rd body (e.g. a phonon) to provide momentum matching, besides just energy matching. A full quantum calculation gives so-called free carrier absorption (FCA) cross sections σ_{FCA} for various scattering mechanisms, all of which scale strongly with laser wavelength, between $\lambda^{1.5} - \lambda^{3.5}$ [36].

In most semiconductors, including GaAs, n-Ge, and ZnSe, the lifted degeneracy between the heavy-hole and light-hole valence bands allows for direct intervalence band hole transitions which have large and broadband absorption cross section in the MIR and FIR. This is the primary reason many p-type semiconductors have poor optical quality in the MIR. Because of these various mechanisms contributing to FCA, σ_{FCA} is usually experimentally determined on a material-by-material basis.

It should be noted that pumping a material in the vicinity of an interband resonance (including the HH-LH transitions) can introduce resonant enhancement of the nonlinearity. This is an analog to linear refractive index enhancement near a resonance.

2.1.12 Excitonic Effects

Excited semiconductors have attracted a lot of experimental and theoretical attention due to the existence of many-body interactions. A well-known example of this is a correlated electron-hole pair binding into a hydrogenic energy substructure called an exciton. The nonlinear response of excitons can be very strong, and is usually studied by pumping and probing a semiconductor at or near the band gap resonance. In bulk semiconductors, exciton binding energies are on the order of $<$10 meV [37]. For our studies, the semiconductor samples are kept at room temperature, where thermal energy is $k_BT = 25$ meV. In this regime, excitons are not stable, meaning we can assume

that photoexcited electrons and holes will not bind to each other on timescales long enough to impact our experimental results.

2.2 Numerical Modeling of Light-Semiconductor Interactions

Two main strategies for modeling light-semiconductor interactions are employed in this dissertation – first, the generalized nonlinear Schrodinger equation (gNLSE), which approaches the problem from the optics and nonlinear propagation point of view. Second, the semiconductor Bloch equations (SBEs), which instead use a microscopic point of view to study light-semiconductor interactions. These formalisms and their pros and cons will be reviewed in this section.

2.2.1 Generalized Nonlinear Schrödinger Equation (gNLSE)

The gNLSE is a pulse propagation equation that accounts for several linear and nonlinear optical effects [23]. The form that we use in this dissertation is the result of several approximations to the nonlinear wave equation, Eq. 2.4. In particular, we assume both $\vec{E}$ and $\vec{P}$ are linearly polarized in the same direction, and that the light pulse propagates unidirectionally in the forward direction. In addition to the slowly varying amplitude approximation that was made to derive Eq. 2.4, we decompose the electric field into a slowly varying complex envelope A and a rapidly oscillating phase

$$E = \frac{1}{2}\left(A(r,z,t)e^{i\omega_0 t - ik_0 z} + c.c.\right). \tag{2.27}$$

where cylindrical symmetry has been assumed ($\vec{r} \to r$).

In doing this, we assume that an initially Gaussian pulse has frequency content consisting of a Gaussian spectrum centered at the carrier frequency ω_0. To simplify the calculation further, a reference frame moving with the frame of the pulse is defined with time $T = t - z/v_g(\omega_0)$, where $v_g(\omega_0)$ is the group velocity of the pulse central frequency, calculated $v_g(\omega_0) = (dk/d\omega|_{\omega_0})^{-1}$.

Under these approximations, the nonlinear wave equation is simplified to the generalized non-

linear Schrodinger equation (gNLSE):

$$\begin{aligned}\frac{\partial A}{\partial z} = &\left[\frac{i}{2k_0}\nabla_\perp^2 + i\left(k(\omega) - k(\omega_0) - \frac{\omega-\omega_0}{v_g(\omega_0)}\right) - \frac{\alpha_1}{2}\right]A \\ &+ \left[ik_0 n_2\left(1 + \frac{i}{\omega_0}\frac{\partial}{\partial T}\right)|A|^2 - \frac{\alpha_M}{2}|A|^{2M-2}\right]A\end{aligned} \tag{2.28}$$

Terms in the upper brackets represent the linear optical effects taken into account: diffraction, dispersion, and linear absorption, in order from left to right. The terms in the lower brackets contain relevant nonlinear optical effects, here the Kerr nonlinearity and MPA. Implicitly included in the Kerr term is self-phase modulation, phase-matched four-wave mixing, and self-focusing. Details on our implementation of the 2D gNLSE of this form can be found in Appendix A along with numerical benchmarks of the code. Further information on the derivation of this equation and other related pulse propagation equations can be found in several excellent references [38].

This highlights one of the major benefits of the gNLSE - terms containing different physical processes can be easily added or removed based on their relevance to the interaction being modeled. As an example, in the presence of free carrier generation due to MPA, a free carrier absorption and dispersion term can be included under the approximation of Eq. 2.25 with the form:

$$\frac{\partial A}{\partial z} = \left(-\frac{\sigma_{FCA}}{2} - ik_0\frac{1}{2N_{crit}}\right)A\int_{-\infty}^{T}\frac{\alpha_M|A(T')|^{2M}}{M\hbar\omega_0}dT'. \tag{2.29}$$

Here, the integral represents dynamic accumulation of carrier density over the duration of the pulse, and the imaginary term gives the phase shift from the plasma (Eq. 2.25). For higher accuracy, the full form of plasma refraction (Eq. 2.24) should be used when plasma density is $\geq 0.01N_{crit}$. As discussed in Section 2.1.10, the phase term becomes important to the overall propagation when $|B_{ehp}| \approx B_{NL}$.

An analytic estimate of the intensity at which this occurs is found by equating $B_{ehp} = k_0 N/2N_{crit} = B_{NL} = k_0 n_2 I_0$ [39]. To do this, we use the plasma density at the center of the pulse ($T = 0$) as the upper limit of the integral in Eq. 2.29 and a Gaussian pulse profile of the form $I(t) = I_0 \exp(-4\ln 2\, t^2/\tau^2)$ such that τ is the FWHM pulse duration. With this estimate, the threshold

intensity for free-carrier dispersion effects to play a significant role is

$$I_{FC} = \left(\frac{8 n_2 N_{crit} M^{3/2} \hbar \omega_0}{\alpha_M \tau} \sqrt{\frac{\ln 2}{\pi}} \right)^{\frac{1}{M-1}} \tag{2.30}$$

Due to the intensity dependence of NLA, the trailing half of the pulse is much more strongly affected by free-carrier effects than the leading half. Similar to SPM, this time dependent phase change can manifest itself as a frequency up-shift [40].

The derivative in front of the Kerr term in Eq. 2.28 introduces a real component taking into account the self-steepening effect, or the intensity dependence of group velocity caused by nonlinear phase accumulation. This reshapes the temporal pulse in an asymmetric way, causing asymmetry in effects like self-phase modulation and self-focusing. After sufficient nonlinear lengths, an optical shock forms at the back of the pulse (assuming $n_2 > 0$), causing extreme spectral broadening due to the huge amplitude of its derivative. However, in reality, dispersion tends to smear in time broadband features such as this.

It should be noted that the interplay between dispersion and nonlinearity and their relative strengths tends to dominate the qualitative aspects of nonlinear pulse propagation. In analog to the nonlinear length (Eq. 2.9), a dispersion length is defined as $L_D = \tau^2 / 4 \ln 2 |k_2|$, or the characteristic length at which a Fourier transform limited pulse is broadened by $\sqrt{2}$ [41]. Materials with negative GVD (anomalous dispersion, which many MIR transmissive materials tend to have) have the special property where higher frequencies travel faster than lower frequencies. This results in natural pulse compression of a pulse undergoing SPM, and is often used as a post-compression method to compress high power laser pulses to durations shorter than available from the active medium's gain bandwidth. A unique case is $L_D = L_{NL}$, and a pulse can propagate as a fundamental soliton without evolving throughout propagation (in the absence of perturbations). In this dissertation, we are mostly interested in materials with large nonlinearity pumped at high enough intensities such that $L_{NL} \ll L_D$.

To this point, the optical nonlinearity was assumed to be electronic in nature and instantaneous. In the near-IR, a delay between the electric field and the response of electrons has been seen [42], but it is negligible for MIR laser periods (∼30 fs). A more robust delayed nonlinear response is

possible with stimulated Raman scattering (SRS), which consists of inelastic scattering of photons off optical phonons in matter.

The gNLSE in the form we use is an ideal choice of model when propagation effects are important and the approximations are valid - pulse duration is at least several cycles ($\gtrsim$3, or $>$100 fs pulse duration for 10 μm central wavelength) [43] and focusing is weak. The latter point is usually satisfied even with strong self-focusing due to arrest of the process due to photoionization, nonlinear loss, and/or dispersion.

However, no microscopic structure of the material is included in the gNLSE, which requires that the complicated physics of band structures, electron and hole currents, scattering mechanisms, etc. be distilled into simple relations like Eq. 2.7. This is certainly a severe approximation, but one that works well for many materials and pump schemes.

When a semiconductor is driven with very strong fields and/or becomes highly excited, the full quantum structure should be taken into account. To do this, the semiconductor Bloch equations (SBEs) are a preferred choice.

2.2.2 Semiconductor Bloch Equations

The two level system (2LS) is our starting point to understanding light-semiconductor interaction in a microscopic picture. A generic 2LS with relative energy separation ΔE (Fig. 2.5(a)) will have a dipole moment between the states $d_{10} = e \langle 1 | r | 0 \rangle$ (Eq. 2.3), where scalar quantities are assumed by projecting onto the linear polarization direction of the electric field. Under 2nd quantization and in the Heisenberg picture, the light-matter interaction Hamiltonian has the form $\hat{H}_{LM}(t) = -E(t)(d_{10}a_1^\dagger a_0 + d_{10}^* a_0^\dagger a_1)$, where $a_j^\dagger$ and a_j are the creation and annihilation operators for state j. Quantities of interest for describing the 2LS are the state occupation, $N^j = \langle a_j^\dagger a_j \rangle$, and the microscopic polarization, $p = \langle a_1^\dagger a_0 \rangle$. The dynamics of these observables follow the Heisenberg equation of motion, for example

$$i\hbar \frac{dN^0}{dt} = -i\hbar \frac{dN^1}{dt} = \left[N^0, \hat{H} \right] \tag{2.31}$$

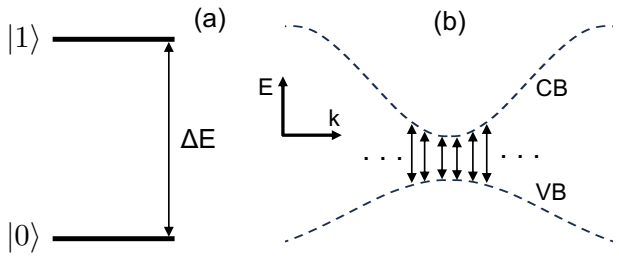

Figure 2.5: (a) Two level system (b) Collection of two level systems to model a semiconductor. Discretization of k space is represented by the broken lines.

where $\hat{H}$ is the total Hamiltonian and the bracket is the commutator of N^0 and $\hat{H}$. Expanding commutators for state occupations and polarizations will result in the well-known optical Bloch equations (OBEs) [37], which contain all the physics of Rabi flopping and other coherent optical effects. The OBEs have an equivalent derivation using density matrix formalism.

To make the jump to a semiconductor, we must expand from a single isolated 2LS to many coupled 2LS. We consider one dimensional reciprocal space (i.e. linear polarized laser along a direction of high symmetry) of a two-band semiconductor with one valence band (h) and one conduction band (e). Discretizing k space will allow us to treat the band structure as a collection of 2LS at each k (Fig. 2.5(b)), each with their own dipole moments d_k, and interband polarizations p_k. Carrier occupations in the bands are represented with $f_k^{e,h}$, invoking the Fermi-Dirac distribution function f.

These 2LS are coupled together in multiple ways. First, the occupations are modified by intraband currents, where k follows the Bloch acceleration theorem, Eq. 2.22. Next, there is a Coulombic interaction that introduces attraction and repulsion amongst carriers, as well as screening. Introducing the Coulombic Hamiltonian to Eq. 2.31 causes an infinite hierarchy of many-body correlations, which is often truncated as a background mean-field, called the Hartree-Fock approximation [37].

Coulombic interactions have energy scales on the order of the excitonic binding energy, which for bulk semiconductors is ≤ 10 meV. For strong offresonant nonlinear optical interactions, where the characteristic light-matter interaction energy $\sim d_{eh}E$ is much larger than the exciton energy, the many-body Coulomb interaction does not significantly influence the system response. Instead, it is treated as a perturbation and included in phenomenological damping terms [44]. This approximation

is valid in our experimental measurements for intensities >0.8 GW/cm^2.

The two-band SBEs that we use in this dissertation read as follows [44]:

$$i\hbar\frac{\partial}{\partial t}p_k = \varepsilon_k p_k - (1 - f_k^e - f_k^h)d_k E(t) + ieE(t)\nabla_k p_k - i\frac{\hbar}{T_2}p_k \tag{2.32}$$

$$\hbar\frac{\partial}{\partial t}f_k^{e(h)} = -2\mathrm{Im}\left(d_k E(t) p_k\right) + eE(t)\nabla_k f_k^{e(h)} - \Gamma_k \tag{2.33}$$

where $\varepsilon_k = \varepsilon_k^e - \varepsilon_k^h$ is the momentum dependent band separation, ∇_k is the differential operator driving intraband currents, and T_2 is the phenomenological polarization (transverse) dephasing time. T_2, which controls how long microscopic coherence lasts, is not a known parameter and may depend on many material or experimental quantities. It is often used as a fitting parameter in numerical studies, and is a topic of much debate [45, 46]. $\Gamma_k = \hbar(f_k^{e(h)} - f_{-k}^{e(h)})/T_2$ is a phenomenological relaxation term which tends to damp currents and relax the carriers to symmetric distributions. The nonlinear response is obtained by finding the total polarization $P(t) = \sum_k d_k p_k$ and current $J(t) = \sum_{k,\lambda} f_k^\lambda \frac{e}{\hbar}\nabla_k \varepsilon_k^\lambda$. Then, as discussed in Section 2.1.10, the total emission will be proportional to $\frac{\partial P(t)}{\partial t} + J(t)$. It is clear that accurate wavefunctions and band structure are required throughout momentum space for correct calculation of dipole moments and polarizations - typically DFT is utilized.

In the SBEs, the nonlinear optical response is generated *ab initio* with the exception of the dephasing time T_2. In this form, they have been used to successfully model strong field processes like high harmonic generation (HHG) and high-order sideband generation (HSG), as well as uncover fascinating physical effects behind them. These are the situations where the SBEs usefulness is fully on display - where there are dynamic light matter interactions, including strong coupling between conduction and valence bands as well as significant free carrier dynamics.

However, propagation effects such as diffraction, dispersion, phase-matching, and self-focusing are not taken into account as the calculation is performed locally and simply averaged over the length of the crystal. Coupling together microscopic dynamics and propagation would be a more accurate modeling method. This is an active area of research [46], but has not been applied to multiple spatial dimensions or propagation lengths larger than 100 μm due to computational complexity.

We will see in Chapter 5 that full description of our experimental results may require more advanced modeling techniques such as this.

2.3 Estimating Semiconductor Nonlinearities

In many ways, the nature of the effective third order optical nonlinearity does not lend itself to predictions - it is highly dependent on many laser and material parameters. With that in mind, we look at a few different predictive models to estimate the Kerr nonlinearity in MIR optical materials. First is the two band model of Sheik-Bahae et al. [17]. Using a higher order Kramers-Kronig relationship, they derive dispersion of $n_{2,bound}$ ($\mathrm{Re}(\chi^{(3)})$) from dispersion of 2PA and other contributions to $\mathrm{Im}(\chi^{(3)})$, shown in Fig. 2.6(a). They find that this dispersion can be scaled for any material with proportionality $C/n_0E_g^4$, where C is approximately material independent. In the MIR most materials will have $\hbar\omega/E_g \ll 1$, where the two-band model predicts low dispersion. Because of this, the strong E_g^{-4} scaling dominates. This is plotted in Fig. 2.6(b) normalized to the nonlinearity of GaAs, which will be used as a standard candle for MIR optical materials. This model has shown good predictive capabilities for a variety of materials and pump wavelengths.

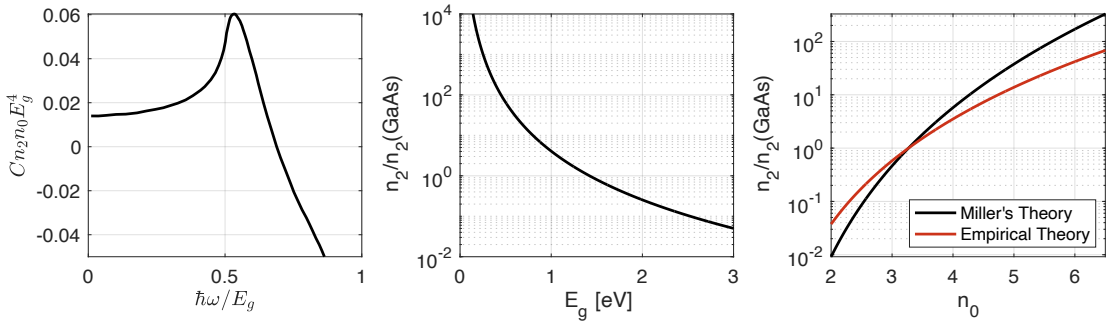

Figure 2.6: (a) Dispersion of $n_{2,bound}$ predicted by the two-band model. (b) E_g^{-4} scaling of $n_{2,bound}$ at $\lambda = 10$ μm in the two-band model, assuming $n_0 = 3.27$ (scales weakly with n_0). (c) n_0 scaling of $n_{2,bound}$ at $\lambda = 10$ μm in the generalized Miller's theory.

Two other predictive – though heuristic – models have been established. First is the generalized Miller's theory, which relates nonlinear susceptibilities to linear susceptibilities. The original form

is based off an empirical observation that the quantity

$$\delta = \frac{\chi^{(2)}(2\omega = \omega + \omega)}{\chi^{(1)}(2\omega)\chi^{(1)}(\omega)\chi^{(1)}(\omega)} \tag{2.34}$$

is constant within a factor of ~ 2 for a wide range of materials [47]. Extrapolating this to the third order nonlinearity, and converting susceptibilities to refractive indices, gives the following ratio of n_2 between materials A and B [48]:

$$\frac{n_{2,A}(\omega)}{n_{2,B}(\omega)} = \left(\frac{n_{0,A}^2 - 1}{n_{0,B}^2 - 1}\right)^4. \tag{2.35}$$

Lastly, an empirical model similar to those used for fluoride crystals and chalcogenide glasses [49] was used by Polyanskiy et al. to give reasonable agreement for a very recent survey of different classes of materials [50]. It produces the following relationship:

$$\frac{n_{2,A}(\omega)}{n_{2,B}(\omega)} = \frac{n_{0,B}^2}{n_{0,A}^2}\frac{(n_{0,A}^2 - 1)^3(n_{0,A}^2 + 2)}{(n_{0,B}^2 - 1)^3(n_{0,B}^2 + 2)}. \tag{2.36}$$

These relationships are plotted in Fig. 2.6(c), again normalized to GaAs ($n_0 = 3.27$ at $\lambda = 10\mu$m). The validity of Eq. 2.35 has not been experimentally validated in the way that it has for the second-order nonlinearity - and both Eq. 2.35 and 2.36 should be taken as order of magnitude estimations.

	n_0	E_g [eV]	n_2 Two-Band Model	n_2 Miller's Theory	n_2 Empirical Model
GaAs	3.27	1.42	1.00	1.00	1.00
n-Ge	4.00	0.795	8.11	5.74	3.51
ZnSe	2.40	2.71	0.103	0.0583	0.135
Te (o-axis)	4.80	0.33	234	26.7	10.8
Te (e-axis)	6.24	0.342	155	235	53.1

Table 2.1: Predictions of $n_{2,bound}$ in semiconductors using the two-band model [17], a generalized Miller's theory [48], and the empirical relation of Ref. [50].

Numerical predictions of $n_{2,bound}$ for these models in the materials used in this dissertation are given in Table 2.1, again relative to GaAs. The models give similar predictions for n-Ge and ZnSe, but diverge by more than a factor of 10 for the narrow band gap, high index Tellurium.

Chapter 3
Mid-Infrared Laser Sources

Advancements in optics and material science have enabled high-power ultrafast laser sources such as Ti:Sapphire, Yb doped, and Cr:ZnS lasers typically operating with central wavelengths near 800 nm, 2.35 μm, and 1030 nm respectively. While near-infrared sources such as these have received the bulk of the research and development, the mid-infrared and in particular the long-wavelength infrared spectral range have become a frontier of laser science.

There are two main methods for generating high power laser pulses in the MIR - direct amplification using a picosecond CO_2 laser and nonlinear frequency downconversion of ultrafast near-infrared lasers. Both methods carry their own advantages and disadvantages, and both will be utilized for different experiments in this dissertation. This chapter will briefly overview the basic physics behind the lasers and detail the specific laser systems that we use for experiments.

3.1 The Picosecond CO_2 Laser

3.1.1 Picosecond Pulse Amplification in the CO_2 Gain Medium

The CO_2 laser generated first light in the 1960s [51], and in the decades since has been utilized extensively for many applications. Continuous wave and long-pulse ($\tau > 1$ ns) CO_2 lasers can generate high average power or high energy pulses that are a workhorse for industrial manufacturing, including cutting, welding, and engraving.

While there are many research problems that benefit from long-pulse lasers, the majority of contemporary topics in nonlinear optics and strong field science call for picosecond and femtosecond laser pulses. These ultrafast laser pulses are critical to optically probe timescales on which electrons move and other microscopic dynamics occur, as well reach high peak intensities while staying below permanent material damage thresholds in solids.

Because of this, there has been a concerted (and successful) effort to develop picosecond CO_2 lasers, primarily led by the National Research Council (Canada) [52], Accelerator Test Facility at

Brookhaven National Lab (ATF-BNL) [14] and the UCLA Neptune Lab [13, 53].

The key to the picosecond CO_2 laser is pressure broadening of the gain spectrum, which is several combs of lines originating from rovibrational transitions. The 10P branch of the gain spectrum of a 1 atm transversely excited atmospheric (TEA) CO_2 laser is shown in Fig. 3.1 [54]. Homogeneous pressure broadening for a chosen gas mix (1:1:12 CO_2:N_2:He) will broaden each individual line at a rate of ∼3.9 GHz/atm. In the atmospheric case, the laser is line-tunable (line separation 54 GHz), but can only support the bandwidth to amplify pulses as short as a few nanoseconds in practice due to gain-narrowing.

In contrast, when pressure is increased to 10 atm the individual rovibrational lines broaden to nearly 40 GHz each, making the spectrum quasi-continuous. Here, a single rovibrational line supports pulses around 200 ps in practice. The quasi-continuous spectrum will also allow for amplification of a laser pulse with spectral content spanning several rovibrational lines. While the full branch has a 750 GHz FWHM bandwidth that can in theory support sub-picosecond pulse lengths, in practice the shortest pulse is around 3 ps. In addition, the spectral modulation results in the natural formation of a pulse train, with ∼3 ps pulses separated by 18.5 ps (inverse of 54 GHz line separation).

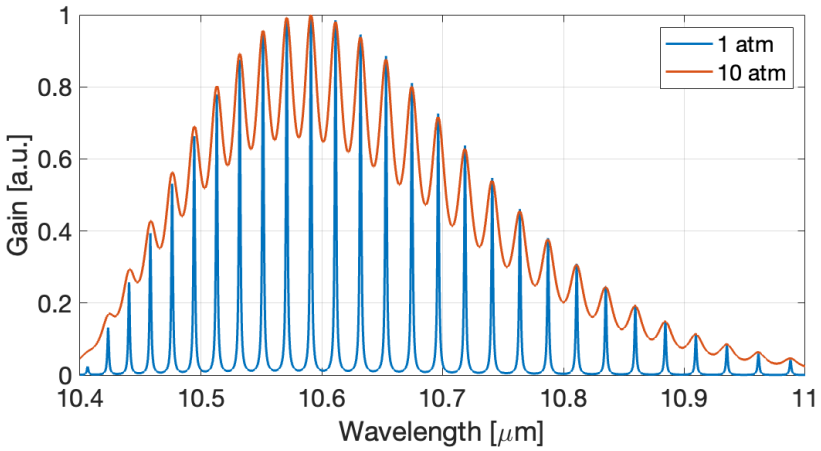

Figure 3.1: Gain spectrum of the 10(P) branch of a CO_2 laser at 1 atm and 10 atm pressure with a 1:1:12 CO_2:N_2:He gas mix.

Increasing total pressure to 25 atm will completely eliminate gain modulation and thus pulse splitting. However, this brings up a critically important practical consideration that limits the

maximum pressure of a CO_2 laser. In order to efficiently extract energy from the gas a large (cm scale) aperture should be used - this implies a large separation between electrodes used to drive a glow discharge that excites the gas. Above a few atmospheres of pressure, high voltage pulses from 50-100 kV or more are required, even with the assistance of preionization. This makes traditional discharge pumped CO_2 lasers impractical at pressures above 10 atm.

It should be noted that there are some methods that skirt around this engineering limitation. First, different isotopes of CO_2 can be used, e.g. $^{13}C^{16}O_2$ or $^{12}C^{18}O_2$, which each have slightly shifted gain spectra. When used at pressures near 10 atm, isotopic CO_2 will help fill in the gaps in the spectrum, and has been demonstrated to amplify 2 ps quasi-single laser pulses [14]. Unfortunately, this solution is prohibitively expensive, especially when using large high-pressure gas chambers which necessitate recirculation and separation of the isotopic mix for reuse. Secondly, optically pumping CO_2 gives the ability to eliminate the high voltage circuitry entirely. While this was investigated decades ago [55], our group has recently revisited the problem in the context of picosecond pulse amplification [56, 57] using state of the art Fe:ZnSe [58] and Cr:Er:YSGG [59] laser technology. This is an exciting avenue of research that may open new capabilities of the CO_2 laser in the near future.

Overall, the picosecond CO_2 laser is a high wall-plug efficiency laser and the only MIR laser source that can generate short pulses with pulse energies of $\sim$10 mJ and above, with records in the vicinity of 100 J. Peak powers of > 1 GW up to the TW regime are attainable [13], and are of great interest for strong field science, including laser-plasma interactions.

3.1.2 Picosecond CO_2 Laser at the UCLA Neptune Lab

A schematic overview of the gigawatt peak power picosecond CO_2 laser master oscillator power amplifier (MOPA) system at UCLA is presented in Fig. 3.2. The master oscillator is in a hybrid scheme [54], using a TEA CO_2 laser and a low-pressure CO_2 laser (LPL, $\sim$30 Torr) in the same cavity. This generates a gain-switched $\sim$300 ns pulse with a single longitudinal mode. The oscillator wavelength(s) can be tuned using an intracavity diffraction grating. In this dissertation, we use either single wavelength 10.59 μm (10P(20) transition) pulse or dual wavelength 10.59 μm and 10.27 μm (10R(16) transition) beat-wave. Pulse energy is around 50 mJ.

This long energetic MIR pulse is combined with a focused picosecond 1.06 μm pulse in a CS_2

Kerr cell acting like a transient waveplate; the portion of the 10 μm pulse overlapped with the 1.06 μm pulse in time will be polarization rotated due to induced birefringence. This nonlinearity is an orientational nonlinearity with response time 2 ps [60], which ultimately limits the shortest pulses attainable with this method. When put between crossed polarizers, this gates a picosecond 10 μm pulse which emerges with very low energy, on the nJ scale. Two different NIR lasers were used to drive the Kerr switch: a 25 mJ 100 ps pulse from an Nd:YAG laser, or a $\sim$ 3 mJ pulse 2 ps pulse from an Nd:Glass laser utilizing chirped pulse amplification (CPA). Use of the Nd:YAG laser results in 200 ps 10 μm pulses after final amplification, whereas the Nd:Glass laser allows for 3.5 ps pulse trains. After the Kerr switch, another split off NIR pulse activates a reflective semiconductor switch based on a Brewster's angle n-Ge (Section 6.2) which further cleans the contrast of the pulse.

From here, the picosecond 10 μm pulse seeds a 7 atm regenerative CO_2 amplifier. The output pulse train is decoupled from the seed vector using the now-deactivated semiconductor switch, and a single pulse containing up to 5 mJ is selected with a CdTe Pockels cell. Further amplification is performed with another high-pressure (7-10 atm) CO_2 laser, and the final pulse energy can be between 20-80 mJ depending on the specific setup. The entire MOPA system described thus far runs at a repetition rate of 1 Hz.

This is the furthest amplification we use for experiments described in this dissertation. However, a large-aperture (10 cm) electron-beam sustained CO_2 final amplifier (MARS laser) uses a power-broadened gain spectrum to amplify these MIR pulses to pulse energies from 30-100 J and TW-scale peak powers [13] on a single-shot basis. This unique capability has enabled experiments in

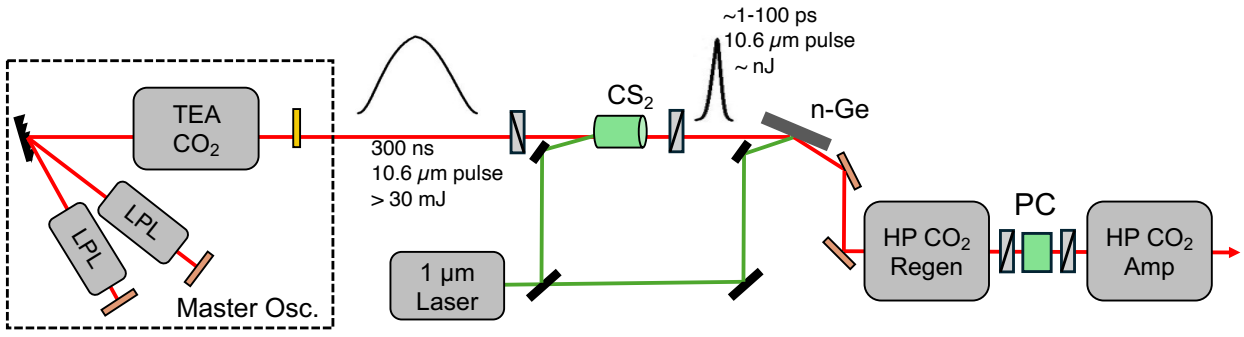

Figure 3.2: Block diagram of UCLA Neptune Lab picosecond CO_2 laser system. HP is high-pressure and PC is Pockels cell.

atmospheric nonlinear propagation [61] and particle acceleration [62].

To measure temporal features longer than ∼1 ns, we use HgCdTe (HCT) photodiodes with 1 GHz bandwidth to fully resolve the pulse structure. For picosecond pulses, the measurement is not as straightforward a task. As is a theme for MIR optics and photonics, we implement a frequency up-conversion technique to imprint information of the MIR pulse onto a visible laser in order utilize more well-developed detection technologies in the visible and NIR spectral regions. For picosecond-scale pulse measurement, we use a CS_2 Kerr cell similar to that described above; in this case though, the intense 10 μm laser pulse modulates a weak visible diode laser. The polarization modulated visible light, which has the MIR temporal information encoded on it, is then detected with a streak camera (Fig. 3.3). Temporal pulse profiles measured in this way are shown for both 200 ps pulses and 3.5 ps pulse trains that we use in experiments.

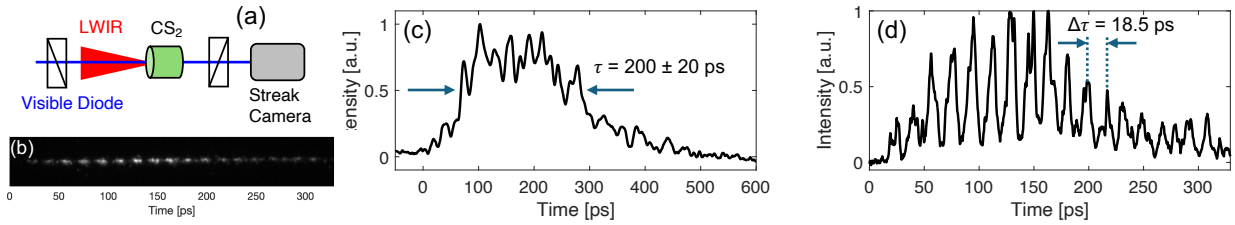

Figure 3.3: (a) Block diagram of the up-conversion method used to measure picosecond MIR temporal profiles. (b) Raw image of electrons swept across the streak camera's fluorescent screen. This data is vertically summed and corresponds to the pulse train of part (d). (c) 200 ps CO_2 laser pulse (d) 3.5 ps CO_2 laser pulse train.

Experimental uncertainty of the 200 ps pulse duration is found to be ±10% due to shot-to-shot fluctuations. The instrumental resolution of the pulse train measurement given in Fig. 3.3(d) is approximately 10 ps, but the 3.5 ps individual pulse width has been established in previous measurements. The streak perfectly reproduces 18.5 ps pulse periodicity and the overall envelope width of ∼200 ps, both defined by the Fourier transform of the gain spectrum.

Sub-picosecond MIR pulses that are required for ultrafast science on the femtosecond time scale are not yet possible with the CO_2 laser - this is the domain of the parametric nonlinear optical source.

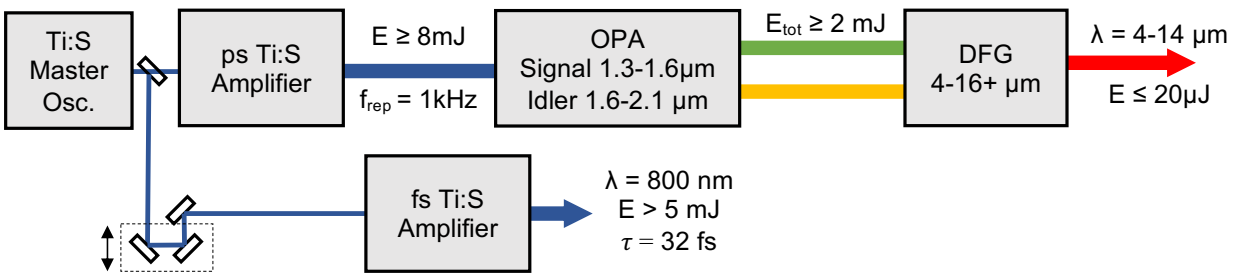

Figure 3.4: Block diagram of two-color, widely tunable MIR and NIR ultrafast laser system at 1 kHz.

3.2 Nonlinear Frequency Down-Conversion

Recent years have seen a surge of interest and development of MIR laser sources based on nonlinear frequency conversion of femtosecond NIR lasers [63]. These sources have demonstrated broad capabilities (e.g. wavelength tunability, bandwidth, and repetition rate) by taking advantage of second order nonlinear optical effects optical parametric amplification (OPA, $\omega_p = \omega_s + \omega_i$) and difference frequency generation (DFG, $\omega_{DFG} = \omega_s - \omega_i$). In particular, pulse lengths <100 fs for wavelengths throughout the MIR have been achieved, enabling studies of strong field physics with microJoule-level energies and high pulse repetition rates ($f_{rep} \geq 1$ kHz). A major disadvantage of parametric MIR sources compared to the picosecond CO_2 laser is the relatively low pulse energies (current cutting edge is 60 μJ in 185 fs pulses at 11.4 μm [64]), ultimately limited by inherently low efficiency imposed by Manley-Rowe photon conservation considerations. Advanced OPCPA techniques have reached milliJoule energies at 3.9 μm [15] and 7 μm [16], but for higher energy pulses direct amplification in CO_2 is still the best option.

3.2.1 Two-Color Tunable MIR and NIR Ultrafast Laser Source at the UCLA Neptune Lab

We have recently commissioned a widely tunable MIR laser system. A block diagram is shown in Fig. 3.4.

The master oscillator (Element 2, Spectra-Physics) operates at a repetition rate of 79 MHz and produces ≥1 W average power in broadband pulses centered at 798 nm ($\Delta\lambda$ = 76 nm, FWHM).

This output is split, with half of the energy seeding a picosecond Ti:Sapphire CPA system (Spitfire, Spectra-Physics) consisting of a regenerative amplifier and double-pass booster amplifier. To obtain picosecond pulses, the stretcher is modified to mask a significant amount of energy, passing only a small bandwidth centered at 800 nm required for a 1 picosecond pulse. After compression, the amplifier outputs >8 mJ pulses at a repetition rate of 1 kHz. A measured multi-shot autocorrelation trace is presented in Fig. 3.5(a), showing 1 ps pulse length. The corresponding spectrum given in Fig. 3.5(b) is measured with a fiber-coupled spectrometer (Ocean Optics HR2) with resolution 0.165 nm.

This pulse pumps a multi-stage tunable OPA system (commercially known as TOPAS-800/TOPAS-HE, Light Conversion), which generates broadband signal and idler and amplifies them to combined total energy up to 2 mJ. For our purposes, signal is tuned between 1.3–1.6 μm, and idler is tuned between 1.6–2.1 μm. Pulse shortening occurs during the several nonlinear stages, resulting in approximately 500 fs signal pulses as measured via multi-shot autocorrelation (Fig. 3.5(c)). Signal pulse duration is consistent as wavelength is tuned, and a measured signal spectrum measured with a spectrometer (Ocean Optics NIRQUEST) is shown in Fig. 3.5(d) for $\lambda_{sig} = 1485$ nm, corresponding to $\lambda_{DFG} = 10.3$ μm.

Finally, signal and idler are combined non-collinearly in a 10 mm aperture GaSe crystal. Here, a phase matched DFG process occurs. We have confirmed DFG tunability throughout the MIR in the range 4-16+ μm. DFG efficiency and thus pulse energy varies significantly across this range, but a maximum of 70 μJ is observed at 4 μm and $\leq$ 5 μJ is measured above 14 μm. In the vicinity of 10 μm, most used in this dissertation, the DFG process produces up to 20 μJ. Temporal characterization of the DFG source is discussed in Section 3.2.2. The MIR light is linearly polarized and has a near-Gaussian transverse beam profile throughout it's tuning range.

In addition to the picosecond amplifier, the other half of the master oscillator output is sent to a femtosecond Ti:Sapphire CPA system (Spitfire, Spectra-Physics), which amplifies bandwidth supporting >30 fs 800 nm pulses above 5 mJ at 1 kHz repetition rate. This NIR pulse is fully characterized with a SPIDER (Compact LX-Spider, APE Electronics), showing pulses as short as 32 fs with a time bandwidth product (TBP) < 0.5 (Fig. 3.5(a-f)). The MIR and NIR arms of this laser system are synchronized via an external delay stage and seed pulse selector that supports

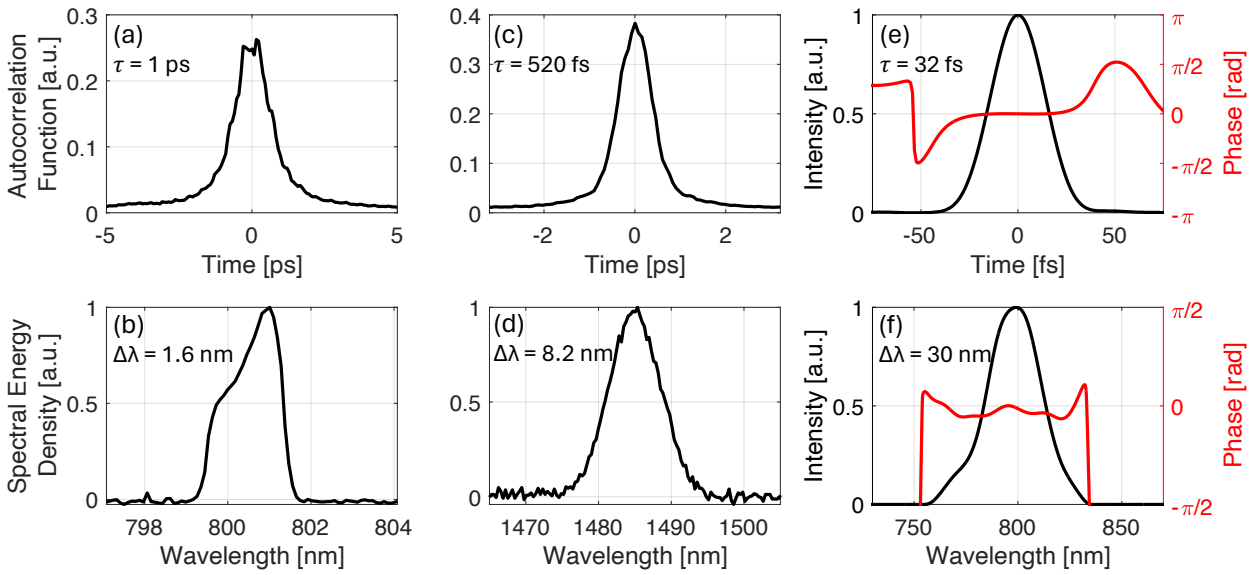

Figure 3.5: (a) Autocorrelation trace and (b) spectrum of 800 nm Ti:Sapphire pump pulse giving a time-bandwidth product of 0.74. (c) Autocorrelation trace and (d) spectrum of 1485 nm signal from the OPA giving a TBP of 0.58. (e) Temporal and (f) spectral characterization of the 32 fs Ti:Sapphire pulse giving a TBP of < 0.5.

arbitrary temporal delays between the NIR pulse and DFG pulse with jitter on the order of 2 fs. This setup is ideal for pump-probe and cross-correlation experiments.

3.2.2 Ultrafast MIR Pulse Characterization with XFROG

Full pulse characterization - measurement of spectrum and spectral phase, or equivalently temporal profile and temporal phase - is essential for the optimization and utilization of ultrafast laser pulses. We use cross-frequency resolved optical gating (XFROG) to do this with our DFG pulses using a custom sum frequency generation (SFG) XFROG device (Mesa Photonics). The SPIDER-characterized ultrafast 32 fs 800 nm pulse is a gating pulse noncollinearly frequency mixed with the DFG pulse in a 100 μm thick $\chi^{(2)}$ crystal (Fig 3.6(a)). $LiNbO_3$ or $AgGaS_2$ of different cut angles are angle tuned to achieve phase matching for a wide range of MIR wavelengths. The time resolved SFG spectrum is measured and a full reconstruction of the pulse can be performed.

Illustrative results of XFROG measurements are given in Fig. 3.6(i-iv) for a MIR pulse with central wavelength 9 μm. A short, 220 fs pulse duration is reconstructed, with a slightly asymmetric spectrum favoring the blue. Using an expansion of the spectral phase similar to that we use in

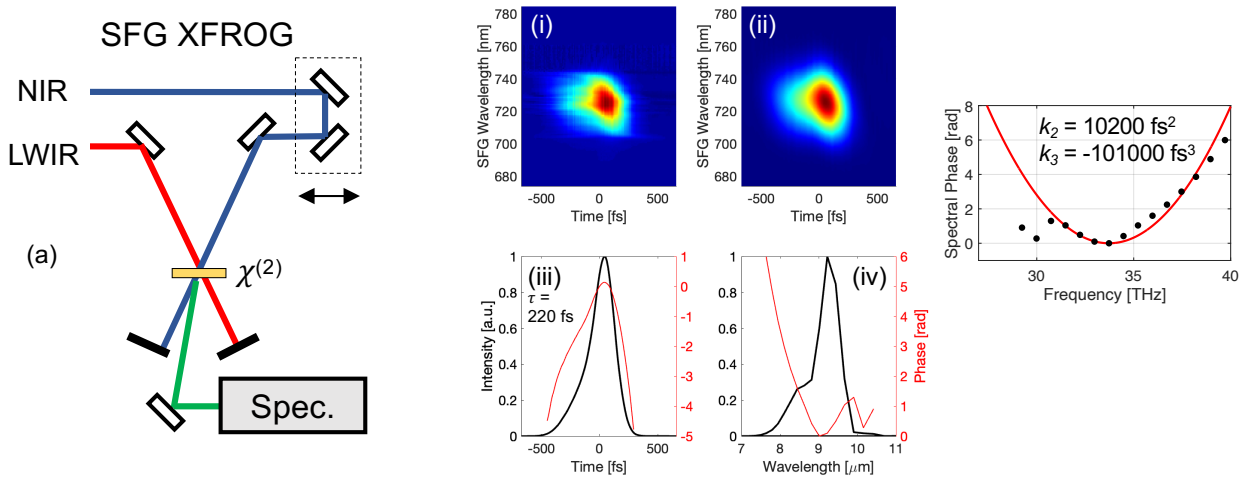

Figure 3.6: (a) Schematic of the SFG XFROG. (i) Measured XFROG trace. (ii) Reconstructed XFROG trace. (iii) Reconstructed pulse and phase. (iv) Reconstructed spectrum and spectral phase (b) Fit to spectral phase to obtain GDD and TOD on the pulse.

modeling nonlinear propagation (Section 2.2.1),

$$\Delta\phi(\omega) = \frac{k_2}{2!}(\omega - \omega_0)^2 + \frac{k_3}{3!}(\omega - \omega_0)^3 + \cdots \tag{3.1}$$

where k_2 is the group delay dispersion (GDD) and k_3 is the third-order dispersion (TOD), we can fit the measured phase. This fit is given in Fig. 3.6, with reasonable GDD = 10200 fs^2 and TOD = -101000 fs^3.

In the case of a 9 μm laser pulse, the cycle period of the electric field is 30 fs. Therefore, a 220 fs pulse is $<$ 10 cycles in duration. These pulses are not quite in the few-cycle regime, where different effects such as carrier envelope phase and breakdown of the slowly-varying envelope approximation occur, but they approach this regime.

By adjusting the intensities and spatio-temporal overlap of pump and signal seed pulses in one of the stages of the TOPAS OPA, the DFG output characterstics can be modified. In particular, this was used to increase the MIR pulse length. The XFROG measurements in Fig. 3.7 are examples of both wide-tunability and the near-Gaussian pulse profiles found between 5.5 μm and 10.6 μm central wavelength with durations between 500-600 fs. For reference, these pulses have GDD = 45,000 fs^2 and 28,000 fs^2, and TOD = -1.4 x 10^6 fs^3 and -320,000 fs^3, respectively.

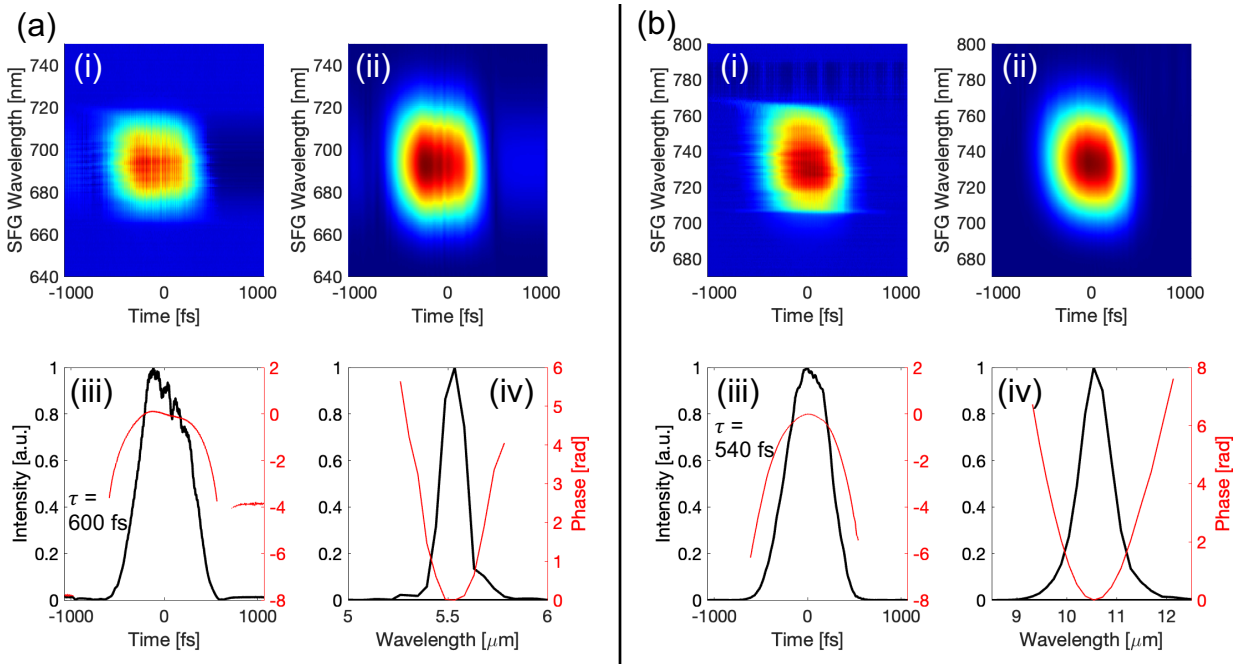

Figure 3.7: XFROG measurements of (a) 5.5 μm and (b) 10.6 μm DFG pulses. (i) Measured XFROG trace. (ii) Reconstructed XFROG trace. (iii) Reconstructed pulse and phase. (iv) Reconstructed spectrum and spectral phase.

Chapter 4

Experimental Characterization of the Nonresonant Nonlinear Optical Response of Semiconductors using Picosecond Pulses

Understanding the nonlinear response of optical components is of critical importance in designing high power laser systems or photonic devices. Some of the most common MIR materials that are transparent in the wavelength range are GaAs, n-Ge, and ZnSe. Despite well known linear optical characteristics, there is a lack of data on the mid-infrared nonlinear optical properties of these materials at high intensities, >1 GW/cm^2. Nonlinear absorption and refraction are measured in this chapter to help fill the gap. A short description of each of these materials follows, including details of specific samples we use in experiments.

4.1 Semiconductor Materials Studied

GaAs

We begin with GaAs, which is an archetypical semiconductor used to study nonlinear light-semiconductor interactions. This is partly due to the extensive investment from the semiconductor industry for its favorable electrical and optical properties. This investment has in turn led to extremely high quality crystal samples of various physical dimensions and orientations. A III-V semiconductor, GaAs has also attracted much theoretical attention and can be modeled very accurately. As an infrared material, GaAs has high transmission starting near its band gap (E_g = 1.42 eV, direct) at 1 μm and the onset of phonon absorption around 18 μm. Chromium compensated semi-insulating (SI) samples have high resistivity, and are as close to intrinsic ($\gtrsim 10^6$ cm^{-3} at room temperature) as can be achieved in standard semiconductor crystal growth. The GaAs sample we study is a 7 mm long semi-insulating slab ($\rho > 3 \times 10^8\,\Omega$·cm) anti-reflection coated around 10.6 μm wavelength. Measurements are performed with the electric field parallel to the [111] orientation, known to possess the largest $\chi^{(2)}$ [65].

n-Ge

n-type germanium is of high optical quality not in spite of the doping but because of the doping. Optical quality Ge samples typically have resistivity 10-40 Ω·cm [66], corresponding to equilibrium carrier concentrations on the order of 10^{14} cm^{-3}. The indirect band gap is 0.66 eV, whereas the direct band gap is 0.795 eV. 2 mm thick samples are used in experiments. The transparency range of n-Ge is between 2-12 μm before linear absorption kicks in at longer wavelengths.

ZnSe

ZnSe is a wide gap (2.71 eV) II-VI semiconductor with a broad transparency range between 0.6 μm to nearly 20 μm. Difficulties in the crystal growth process make most optical samples polycrystalline, but these are still of high optical quality. ZnSe has attracted attention recently as a material that supports random quasi-phase matched nonlinear wave mixing [67–69]. In our experiments, we use uncoated samples of different lengths between 3-12 mm thick with grain size measured to be approximately 40 μm.

4.2 Nonlinear Absorption of Picosecond CO_2 Laser Pulses

Nonlinear absorption (NLA) is often detrimental to practical applications due to the introduction of unwanted laser energy loss, and can ultimately lead to single-shot or multi-shot optical damage with enough deposited energy. Nonlinear absorption in semiconductors has mainly been studied close to band gap resonances in the 1-3 μm range, in particular for two-photon and three-photon resonances. The MIR spectral range is far from resonance, requiring several-photon transitions with low cross sections to span the band gap. As described in Ch. 2, strong interaction with free carriers and nonperturbative effects tend to be more important in the MIR and may dominate the absorption.

Although NLA data are relatively scarce in the MIR, it has been shown to play a role in diverse nonlinear optical effects such as supercontinuum generation [70] and high-harmonic generation [71]. Furthermore, the recent success in delivering of a multi-Joule CO_2 laser beam in air over tens of meters [61] has created interest in high power laser-semiconductor interaction for infrared counter-

measures application.

NLA has been studied in p-type [72–75], intrinsic [76, 77], and optical grade n-type [78–82] germanium samples. Measurements with nanosecond duration TEA CO_2 laser pulses at intensities up to ∼50 MW/cm^2 have demonstrated varying levels of absorption. Results have been explained theoretically with several different models, such as 7PA and subsequent free carrier absorption (FCA) [79], or FCA and impact ionization [83, 84]. While nanosecond laser experiments have revealed nonlinear absorption in semiconductors at low field strengths, higher intensity regimes could not be reached without irreversible damage to the samples. Picosecond CO_2 lasers have enabled these higher intensity experiments.

4.2.1 Experiments

We perform NLA measurements in semiconductors using 200 ps CO_2 laser pulses generated in the CO_2 laser MOPA system described in Chapter 3. Pulses were centered at 10.59 μm, the 10(P)20 line of the CO_2 gain spectrum. Linearly polarized pulses contained up to 6 mJ per pulse at a 1 Hz repetition rate. The beam was focused with a 2.5 m focal length curved mirror to a $1/e^2$ spot size of 0.7 mm on the semiconductor samples. Samples were placed close to normal incidence and slightly after the beam's focus to minimize the effect of Kerr self-focusing in the bulk. Peak powers of $\leq$ 30 MW are between $4P_{crit}$ for ZnSe and $170P_{crit}$ for n-Ge, taking literature values of n_2 from Refs. [70, 85]. Despite the high power, the calculated self-focusing length is at minimum several times longer than the sample in all cases.

The semiconductor samples we study are 2 mm n-Ge, 7 mm SI-GaAs, and 12 mm poly-ZnSe. All samples are optically polished and of optical quality, with linear absorption ≤ 0.01 cm^{-1}. Due to the 1 Hz repetition rate and thus negligible average laser power, air cooling was sufficient to keep the samples at room temperature throughout the measurements. Care was taken to stay below the surface damage thresholds so that surface effects played a minimal role in the study - fluence on the front surface was below 1 J/cm^2 even for the highest energy pulses, and no surface damage was observed on any sample after several hundred shots of irradiation each. In a different experimental setup with a tighter focus, damage was observed on the GaAs surface on a multi-shot basis at I $\geq$ 20 GW/cm^2.

Nonlinear transmission measurements are made by measuring pulse energy transmitted through the semiconductor sample, normalized to a pulse energy reference from a NaCl beam sampler before focusing. This data is shown in Fig. 4.1(i) for all three materials. The transmission is normalized to low intensity transmission, removing the influence of Fresnel reflection in this particular geometry. CaF_2 windows of different thicknesses were also used as calibrated attenuators, affording some level of peak intensity control in the range 0.1-5 GW/cm^2. Each data point represents approximately five binned raw data points while error bars represent their standard deviation. It should be noted that the error bars when plotted as E_{in} versus E_{out} are approximately the same across all intensities – large errors near $T = 1$ essentially result from division by a small number.

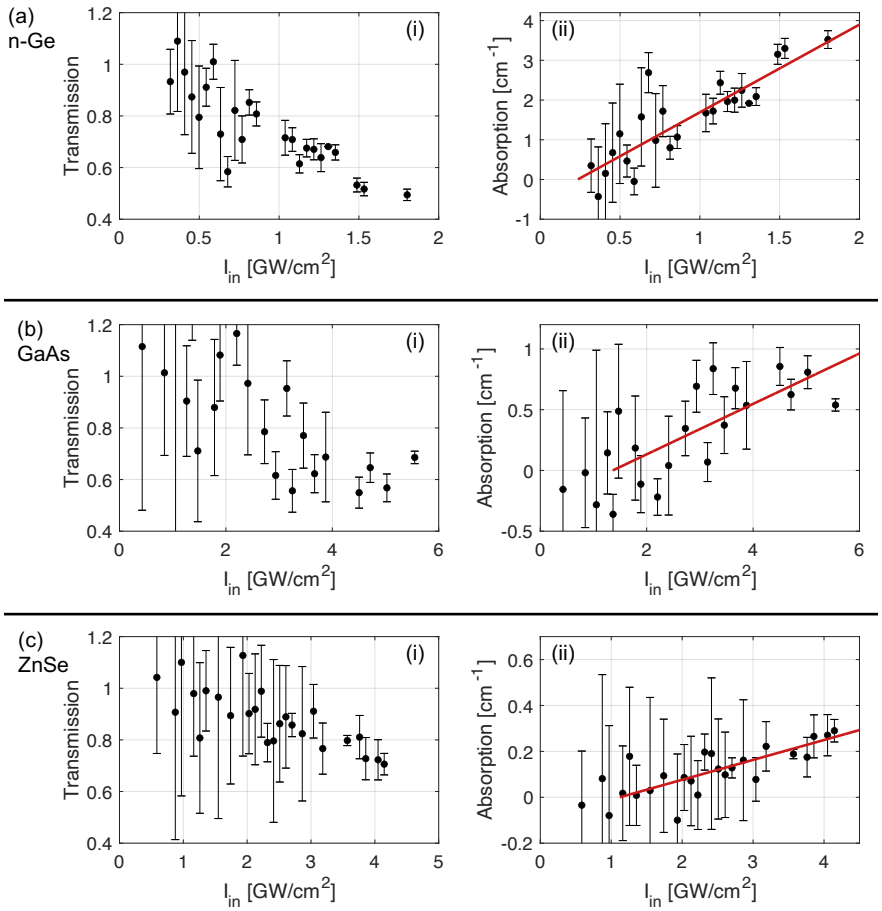

Figure 4.1: NLA measurements in 2 mm n-Ge, 7 mm GaAs, and 12 mm ZnSe at 10.6 μm. Panel (i) gives simple measured transmission corrected for Fresnel reflection, and panel (ii) gives a length averaged absorption coefficient with a linear fit overlaid.

An effective absorption coefficient averaged over the length of the sample is calculated on a point-by-point basis using the formula $\alpha = (1/L)\ln(T)$, where L is the crystal length. Error values are calculated using standard propagation of uncertainty. In all materials, the transmission appears to be lossless within uncertainty at low intensities, but deviates into a nonlinear absorption regime with intensity scaling that appears linear.

We can make an estimate of the NLA intensity scaling by assuming the following form of Eq 2.15:

$$\frac{dI}{dz} = -\alpha_{NL} I^M. \tag{4.1}$$

If we make the (very) strong assumption that the intensity is constant through the sample, $dI/dz \approx \Delta I/\Delta z$, integrating over z and taking the logarithm gives $\log \Delta T \approx (M-1)\log(-\alpha_{NL} L I)$. Thus when we plot the differential transmission logarithmically, the slope can be related to the intensity scaling of the nonlinear process. For example, in a pure MPA process the theoretical slope would be $M-1$. While this relation is derived assuming constant intensity, it has been shown to fit data well for high-order MPA even with rather large changes in transmission up to $-\Delta T = 30\%$ [86]. Slope fitting of data points with $5\% < -\Delta T < 30\%$ is shown in Fig. 4.2. Error bars on the slope-fitting (95% confidence interval of the fit) are large, caused by a combination of data scatter and the lesser number of data points in the range of ΔT considered. Regardless, this fitting gives a qualitative guide to the NLA intensity scaling.

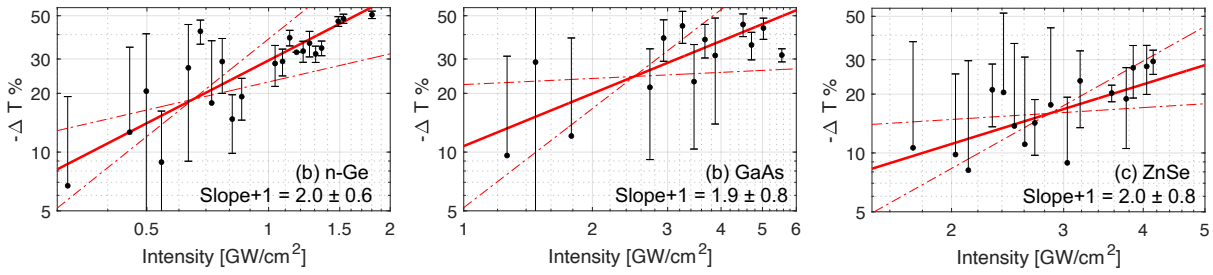

Figure 4.2: Slope fitting of the NLA data as described in the text. Dash-dot curves represent the 95% confidence intervals of the fit.

The slope fitting gives nearly identical NLA intensity scaling of $M = 2$ for all three materials, implying a process that scales like 2PA. On one hand, this is unsurprising given the observations in Fig. 4.1. However in these materials with such a diversity of $E_g/\hbar\omega_0$ ratios (between 6.8–23),

the same intensity scaling of NLA is surprising. It may also suggest that the physical mechanism is similar for all the materials.

Calculation of the Keldysh photoionization rate in these semiconductors at 10.6 μm, as described in Chapter 2, is presented in Fig. 4.3(a) for the peak intensity range of interest. Due to the varying levels of nonresonance, photoionization rate is many orders of magnitude different between the materials. Peak local photoexcited carrier density from this rate, integrating over a 200 ps gaussian pulse, is plotted in Fig. 4.3(b). While the Keldysh theory is not expected to be a one-to-one model in these semiconductors, it gives good qualitative and order of magnitude quantitative results. Just by comparing the local carrier densities, say at 2 GW/cm^2, it becomes clear that this model projects approximately 6 orders of magnitude more photons lost due to photoionization in n-Ge than in GaAs. In ZnSe, with a band gap double the size of GaAs, the pulse generates negligible carriers and thus negligible photoionization loss. The highly nonlinear photoionization rate and local electron-hole plasma density make it difficult to explain the observed NLA behavior in all materials this way. Carrier multiplication through impact ionization [84] also cannot explain our results, as the intensity dependence is far too strong. Instead, we can turn to an optical process that by definition shares the same intensity dependence between the samples: linear absorption.

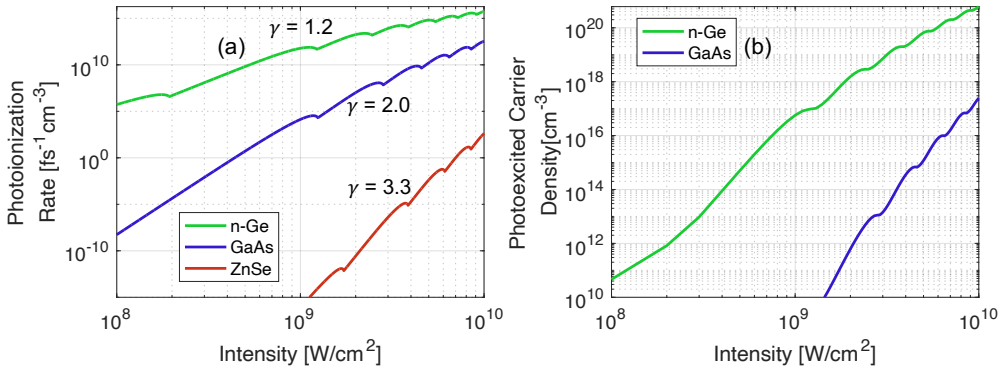

Figure 4.3: (a) Calculated Keldysh photoionization rates (LH band to CB) in semiconductors at 10.59 μm. (b) Peak local photoexcited carrier density calculated for a 200 ps gaussian pulse. Keldysh parameters are given at 1 GW/cm^2.

Linear absorption in our specific samples is not detectable with the present signal to noise ratios and data scattering, but is known to be $\alpha_1 \leq 0.01$ cm^{-1} for the optical quality materials. Taking

$\alpha_1 = 0.01$ cm^{-1} gives 1% loss over 1 cm propagation, totally negligible compared to the NLA. Primary sources of linear absorption are free carrier absorption (FCA) from residual equilibrium carrier densities, (multi)phonon absorption, and absorption on crystal defects/impurities [87]. In a polycrystalline material such as ZnSe, grain boundaries are two-dimensional defects introducing absorption via mid-gap energy levels [88]. Regardless of the physical origin, if a small fraction of the linear absorption leads to nonequilibrium carrier production, the high photon density and long pulses (relative to electronic timescales and cycle period) can lead to significant carrier densities. As is described in Chapter 2.1, any generated carrier density will subsequently interact with and absorb the light more and more as it accumulates over the duration of the pulse. We hypothesize this two-step process is a primary nonlinear loss mechanism in experiments.

We realize the presumed two-step NLA mathematically as

$$\frac{dI}{dz} = -\alpha_1 I - \sigma_{FCA}\left[\frac{\eta\alpha_1}{\hbar\omega_0}\int_{-\infty}^{t} I(t')dt'\right] I \approx -\alpha(I,t)I \tag{4.2}$$

where the expression in the bracket is the accumulated carrier density over time during the pulse and η is introduced as the fraction of linear absorption causing carrier generation. There may be other physical effects that accumulate over the duration of the pulse and contribute to the nonlinear effects, such as carrier heating, which can be lumped in to the NLA term. Carrier trapping or recombination is not considered. Assuming the first term is negligible, the FCA contribution reproduces I^2 intensity dependence observed in slope fitting. It is important to note that NLA of the kind hypothesized here is largely a long wavelength phenomenon due to strong wavelength scaling of σ_{FCA}. Taking into account the extra factor from Eq. 4.2, the NLA coefficient may scale as strongly as $\alpha_{NL} \propto \lambda^{2.5} - \lambda^{4.5}$.

Time and intensity dependent absorption of this form is modeled with the 2D gNLSE as described in Chapter 2. NLA measurements are numerically reproduced by scanning peak pulse intensity of 200 ps gaussian pulses with a gaussian beam profile matching experiment and propagating them through the materials used in experiment. Material dispersion are taken from Sellmeier equations in Refs. [65, 89, 90], and $n_{2,eff}$ values are taken from the measurements presented later in this chapter. Since the predicted nonequilibrium carrier density is expected to be small, plasma dispersion has been neglected. The total pulse energy is integrated after propagation to find a

numerical transmission value for each input pulse energy with $x = \sigma_{FCA}\eta\alpha_1/\hbar\omega_0$ taken as a fitting parameter. Finally, for each x, the root mean square error (RMSE) is calculated between binned data points and numerical transmission curves, weighted by intensity to decrease contribution of the low intensity points with high relative uncertainty. Best-fit results are shown in Fig. 4.4. For all samples, but especially GaAs, the model over-estimates absorption at lower intensities in the range. It is possible that certain loss channels only activate above a certain threshold intensity – an example being phonon emission – and may explain the low intensity dynamics observed in Fig. 4.1.

A notable effect which is not included in this description of NLA is saturation of FCA cross sections. This has been observed and attributed to bleached intervalence band hole absorption in p-Ge and p-GaAs, and follows the trend $\sigma_{FCA,h} = \sigma_{FCA,h,0}/\sqrt{1 + I/I_s}$ where I_s is the saturation intensity [83]. At 10.6 μm, saturation intensities were measured to be $I_{s,\mathrm{Ge}} = 3.2$ MW/cm^2 [74] and $I_{s,\mathrm{GaAs}} = 22$ MW/cm^2 [83]. FCA saturation has not been measured in ZnSe to the best of our knowledge, but given the similar band structure should also be expected to exist.

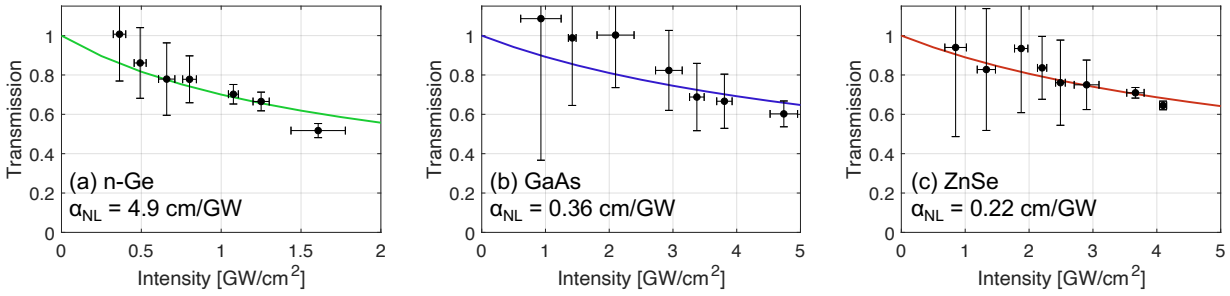

Figure 4.4: Best fit transmission curves for the 2-step NLA described in the text, calculated using the gNLSE.

To contextualize this NLA, the integral in Eq. 4.2 is solved analytically assuming a Gaussian pulse with FWHM duration τ. Choosing integral limits of $t = -\infty$ to 0 to find the accumulated FCA at the peak of the pulse, we obtain

$$\frac{dI}{dz} \approx -x\left[\int_{-\infty}^{0} I(t')dt'\right] I = -\frac{\tau}{4}\sqrt{\frac{\pi}{\ln 2}}xI^2 = -\alpha_{NL}I^2. \tag{4.3}$$

Applying this formula to the modeling results gives best fit α_{NL} of 4.9, 0.36, and 0.22 cm/GW for n-

Ge, GaAs, and ZnSe respectively. Error bars can be considered ±15% based on the parameter scan discretization. Note that the simple linear fits in Fig. 4.1(i) give $\alpha_{NL,emp} = 2.3 \pm 0.5,\ 0.18 \pm 0.06$, and 0.09 ± 0.03 , respectively. While these empirical values are systematically lower due to averaging over the sample, they give reasonable results compared to the much more complex 2D model.

While the underlying effects are different, direct comparison between the two-step model and NIR 2PA coefficients (α_2) is possible given they share the same intensity dependence and thus units. In GaAs, α_2 has been measured to be 2.5 cm/GW at $\lambda = 1.68$ μm [91] and 26 cm/GW at $\lambda = 1.064$ μm [92]. Similarly in ZnSe, 2PA coefficients have been measured to be $\alpha_2 = 3.5$ cm/GW at $\lambda = 780$ nm [93] and 5.8 cm/GW at $\lambda = 532$ nm [92]. The values we measure at 10.59 μm are an order of magnitude smaller than the NIR values, but NIR measurements are performed at wavelengths near the 2PA resonance, whereas MIR measurements are not in the vicinity of any absorption resonances. With this in mind, the NLA we observe in n-Ge, GaAs, and ZnSe is much stronger than might be expected so far from the band gap resonance and must be considered in future design of MIR laser systems and photonic devices.

While not all of the relevant physics is taken into account, this model still gives a good explanation of the experimental results and scaling to apply to different pulse formats. With ultrafast MIR laser pulses at similar intensity with duration shorter than ∼10 ps, NLA would become negligible for the semiconductors we study. For example, if we take a pulse format that is used in experiments described later (Fig. 6.1), a pulse train of four 3.5 ps duration micropulses, the peak intensity must be 6x higher than a single 200 ps pulse at 10.6 μm to achieve the same peak absorption due to pulse length scaling. Similarly, for 220 fs pulses generated from the DFG laser system, peak intensity must be 30x larger than the 200 ps pulse to achieve the same local absorption. In GaAs, the onset of macroscopic NLA wouldn't occur until 60+ GW/cm^2 for these sub-picosecond pulses. At these much higher intensities, other nonlinear absorption mechanisms can come to life and dominate the interaction – measurements will be presented in the following chapter.

4.3 Nonlinear Refraction in GaAs, n-Ge, and ZnSe

Besides understanding nonlinear absorption, characterization and control of nonlinear refraction in semiconductors is essential to enable their use as nonlinear optical materials. To study nonresonant nonlinear refraction in GaAs, n-Ge, and Znse, we use a nondegenerate collinear four-wave mixing (FWM) technique. Over the decades since the laser first allowed for systematic study of nonlinear optics, FWM has become a "gold standard" method for determining the effective nonlinear refractive index ($n_{2,eff}$), of materials. It is also the basis of powerful material diagnostics such as multidimensional coherent spectroscopy [94].

Nondegenerate collinear FWM is a third order nonlinear optical effect in which two frequencies contained in a single laser pulse ($\omega_1 < \omega_2$, by convention) mix to create a Stokes (low frequency) sideband at $\omega_3 = \omega_{S1} = 2\omega_1 - \omega_2$ and an anti-Stokes (high frequency) sideband at $\omega_4 = \omega_{AS1} = 2\omega_2 - \omega_1$. Sidebands are by definition separated at the beat frequency $\Delta\omega = \omega_2 - \omega_1$. A schematic of this process is given in Fig. 4.5(a). In principle, FWM of this kind cascades to higher-order sidebands; for example, the 2nd Stokes sideband can be generated with several different frequency combinations, including $\chi^{(3)}(\omega_{S2} = \omega_1 + \omega_{S1} - \omega_2)$ or $\chi^{(3)}(\omega_{S2} = 2\omega_{S1} - \omega_1)$.

The nonlinear refractive index is calculated from FWM sideband efficiency as follows. With narrowband pump pulses ($\Delta\omega \gg 2\pi/\tau$) with negligible SPM, sidebands are generated discretely without significant energy between them. In this limit, which is valid for our experimental parameters ($\Delta\nu = 872$ GHz, $1/\tau = 5$ GHz, B < 1 rad), each pump and sideband frequency can be treated individually. Beginning with the nonlinear wave equation (Eq. 2.4) for the 1st Stokes sideband under the paraxial and slowly varying envelope approximation, we find

$$\frac{\partial \vec{\mathcal{E}}}{\partial z} = \frac{i\omega_3^2}{2\epsilon_0 c^2 k_3} \vec{P}_{NL}(\omega_3) e^{i(\omega_3 t - k_3 z)}. \tag{4.4}$$

To simplify the derivation, absorption at ω_3 ($\alpha(\omega_3)$) is assumed to be 0. The nonlinear polarization driving the Stokes sideband is

$$\vec{P}^{(3)}(\omega_3) = \frac{3}{4}\chi^{(3)}(\omega_3 = 2\omega_1 - \omega_2)\vec{\mathcal{E}}_1^2 \vec{\mathcal{E}}_2^* e^{i(\omega_3 t - (2k_1 - k_2)z) - (\alpha_1 + \alpha_2/2)z}. \tag{4.5}$$

If we assume low efficiency, substituting the polarization into Eq. 4.4 and integrating over the length of the crystal L gives

$$I_3 = \frac{\omega_3^2}{c^2} n_{2,eff}^2 I_1^2 I_2 \left(\frac{e^{-2\Delta\alpha L} - 2\cos(\Delta k L) e^{-\Delta\alpha L} + 1}{\Delta k^2 + \Delta\alpha^2} \right) \tag{4.6}$$

where $\Delta k = 2k_1 - k_2 - k_3$, $\Delta\alpha = \alpha(\omega_1) + \alpha(\omega_2)/2$, and $\chi^{(3)}$ was converted into $n_{2,eff}$ following the discussion in Section 2.1.2. In the simple case where loss is negligible ($\alpha(\omega_1) = \alpha(\omega_2) = \alpha(\omega_3) = 0$), this reduces to

$$I_3 = \frac{\omega_3^2}{c^2} n_{2,eff}^2 I_1^2 I_2 L^2 \mathrm{sinc}^2 \left(\frac{\Delta k L}{2} \right), \tag{4.7}$$

with the familiar sinc^2 function associated with phase matching [19]. In terms of experimental observables, pulse energy W_j at frequency ω_j, the Stokes sideband yield for a phase matched process ($\Delta k L \to 0$) is

$$W_3 = n_{2,eff}^2 \frac{\omega_3^2 L^2}{\sqrt{3} c^2 \tau^2 A^2} W_1^2 W_2 \tag{4.8}$$

where τ is the pulse length, A is the beam area and the $\sqrt{3}$ factor arises due to shortening of the sideband pulse length in the low conversion efficiency regime [21].

In the experiment, we use 200 ps CO_2 laser beat-waves generated with the two-wavelength picosecond CO_2 MOPA described in Chapter 3. Measurements are performed using the 10P(20) ($\lambda_1 = 10.59$ μm) and 10R(16) ($\lambda_2 = 10.27$ μm) lines of the CO_2 gain spectrum. With these pump wavelengths the 1st Stokes (anti-Stokes) sideband is at 10.93 μm (9.97 μm). Due to small pump wavelength separation, the FWM coherence length is $l_{coh} = \pi/\Delta k > 5$ cm in all materials. This is much longer than the crystal lengths, so back conversion or saturation of the frequency mixing does not play a significant role.

A simplified experimental setup is displayed in Fig. 4.5(b). The beam emerging from the final high-pressure CO_2 amplifier was sampled by a NaCl window and dispersed by a diffraction grating. Two calibrated calorimeters were used to measure the total energy in each pump wavelength every shot for normalization. The pump beams contained up to 0.5-5 mJ each. Due to slightly higher gain on the P branch than the R branch, the pump energy ratio was $W_1/W_2 \lesssim 2$.

A 2.5 m focal length curved mirror focused to a $1/e^2$ spot size of $w = 0.70 \pm 0.02$ mm on the

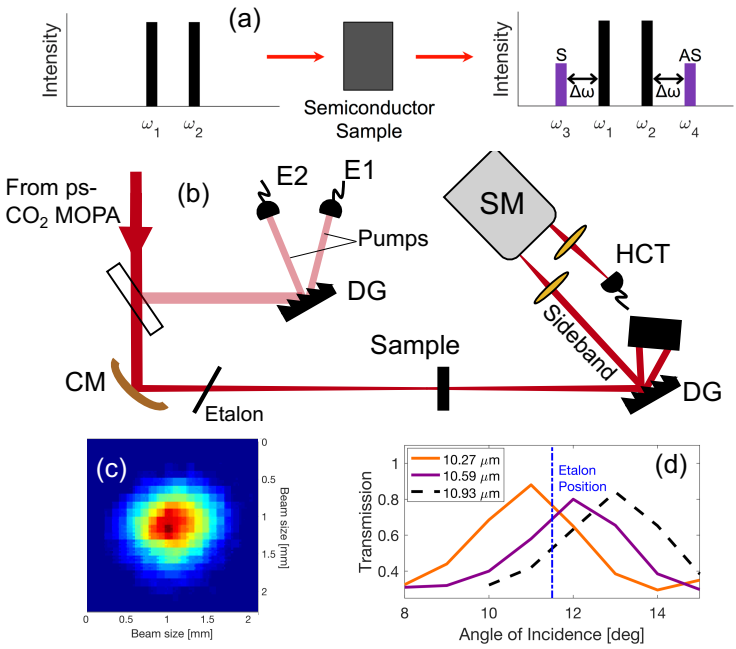

Figure 4.5: (a) Simplified schematic of the FWM process. (b) Experimental setup to measure FWM sidebands produced in semiconductor samples. SM is scanning monochromator, DG is diffraction grating, and E1/E2 are reference calorimeters. (c) Typical beam profile on the semiconductor surface. (d) Transmission character of the GaAs etalon at the pump wavelengths (measured [95]) and 1st Stokes sideband wavelength (extrapolated).

surface of the GaAs and n-Ge samples. An image of this beam measured with a pyroelectric array is shown in Fig. 4.5(c). Due to the sample mount and space restrictions, the position of the ZnSe crystal was slightly closer to the focus and had a slightly smaller spot size of $w = 0.67 \pm 0.05$ mm. As before, samples were placed slightly after the focus to mitigate self-focusing. However, since the Rayleigh length was $z_R = 15$ cm, the electric field in the samples were approximately plane waves.

After passing through the semiconductor sample, the resultant beam was dispersed by a 135 groove/mm diffraction grating. Pump frequencies were dumped on a razor-blade stack and the sideband was focused with a short focal length ZnSe lens onto the input slit of a scanning monochromator (Horiba iHR-550). After the output slit, a short focal length ZnSe lens focused the beam onto a cryogenically cooled 1x1 mm HCT detector. With the 50 grooves/mm grating (blazed at 12 μm) in the spectrometer and a 0.5 mm output slit, the ultimate resolution was approximately 7 nm. This was insufficient to resolve the transform limited laser bandwidth of $\sim$ 1 nm, so the full spectral energy density is integrated for sideband conversion efficiency measurements. The double grating

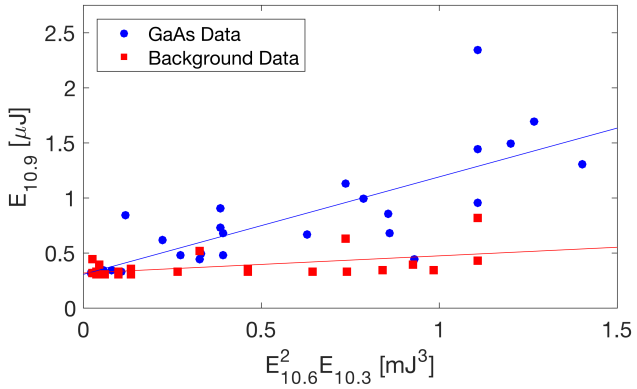

Figure 4.6: Example of raw FWM data measured in [111] GaAs with peak intensity up to 2 GW/cm^2.

setup was necessary to increase signal to noise ratio. These measurements could be tuned across the entire range of sideband wavelengths used in experiments by rotating the external diffraction grating and tuning the spectrometer.

Low efficiency FWM occurs in air as well as various optical elements throughout the laser system, including ZnSe and NaCl windows, n-Ge polarizers, and a CdTe Pockels cell. In order to filter out this background FWM signal generated before the crystal being studied, we place a 700 μm thick (100) GaAs wafer acting as an etalon. The etalon selectively reflects certain frequencies depending on the beam's angle of incidence. Fig. 4.5(d) shows transmission curves measured for $\lambda = 10.59$ and 10.27 μm and extrapolated to $\lambda = 10.93$ μm. This etalon was tuned to 11.5° increasing the ultimate signal to noise ratio to $\geq$5.

A typical data set measured in GaAs with peak intensities near 2 GW/cm^2 is given in Fig. 4.6. Data sets consisted of up to 100 shots, half with the sample in the beam path and half with the sample removed from the beam path (background). Low energy or failed shots are removed from the data set. The measured 1st Stokes sideband energy (W_3) is plotted against $W_1^2 W_2$. Absolute sideband energy measurements are done with careful HCT calibration and throughput measurement of the double grating apparatus. Since we are well within the low-conversion efficiency regime, according to Eq. 4.6 the sideband energy should scale linearly against $W_1^2 W_2$. This scaling is reproduced in the experiment, as shown by the linear fit in the figure.

To extract $n_{2,eff}$ from measured data, the background fit was subtracted from the signal on a

point-by-point basis to get the ratio $W_3/W_1^2W_2$. At the present intensities, up to 10 GW/cm^2 with most shots $\lesssim$ 6 GW/cm^2, nonlinear absorption cannot be ignored. We take $\Delta\alpha = 3\alpha_{NL}I/4$, where α_{NL} is taken from modeling results in Fig. 4.4. An additional factor of 1/2 is included due to the beat-wave doubling the peak intensity while keeping the integrated intensity the same. Inserting this in Eq. 4.6 and solving for $n_{2,eff}$ finally results in

$$n_{2,eff} = \frac{\tau c A}{L\omega_3}\sqrt{\frac{\sqrt{3}W_3}{W_1^2W_2}}\left[L^2\frac{\Delta k^2 + \frac{9}{16}\alpha_{NL}^2I^2}{e^{-\frac{3}{2}\alpha_{NL}IL} - 2\cos(\Delta kL)e^{-\frac{3}{4}\alpha_{NL}IL} + 1}\right]^{1/2}. \tag{4.9}$$

The term in brackets, which equals unity in the case of lossless phase-matched interaction, causes calculated $n_{2,eff}$ to increase due to dynamic nonlinear pump absorption over the course of the interaction. This factor is shown for each material in Fig. 4.7, where it is evident that absorption plays a role even at intensities toward the bottom of the range. The sideband yield and nonlinear refractive index in n-Ge in particular is dramatically affected by nonlinear absorption.

Each individual point is plugged into Eq. 4.9 to find a distribution of $n_{2,eff}$ over many shots, plotted in Fig. 4.8. The mean values are denoted with dashed lines, and are recorded in Table 4.1. Uncertainty in these measurements is dominated by scattering of the data. Plotting $n_{2,eff}$ as a function of intensity yields zero meaningful slope, indicating that up to $\sim$ 10 GW/cm^2 the effective nonlinear refractive index is constant for the experimental parameters.

Our measurements of the nonlinearity in GaAs, n-Ge at 10.6 μm agree with literature values, despite being measured at approximately 1000x higher peak intensities using and 1000x shorter pulses. The consequences of this are potentially far reaching – it implies that high intensity light-

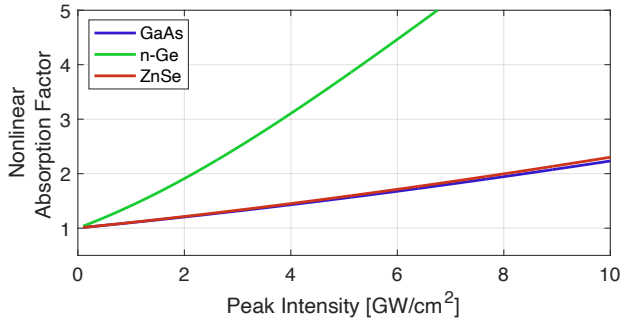

Figure 4.7: Calculated multiplication factor for $n_{2,eff}$ extraction due to measured NLA.

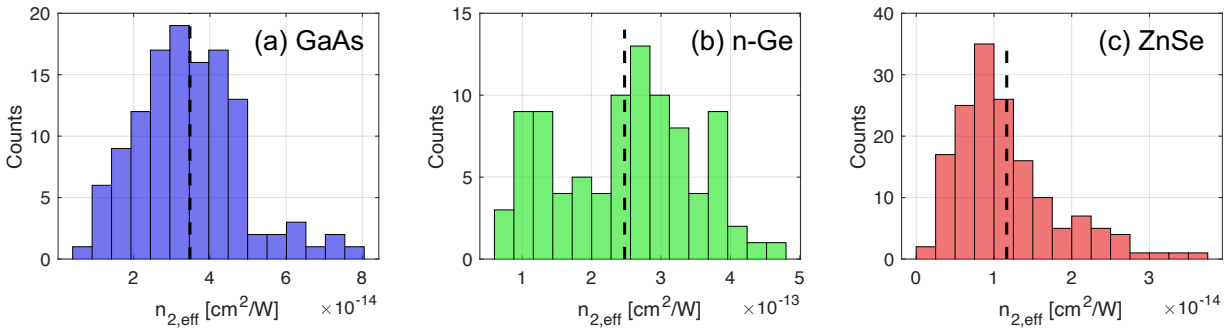

Figure 4.8: Distribution of $n_{2,eff}$ measured for GaAs, n-Ge, and ZnSe between 1-10 GW/cm^2. Means are indicated by vertical dashed lines. There is no significant trend in the data as a function of intensity.

semiconductor interactions provide the same nonlinear refractive response as low intensity interactions, provided the pulse length scales proportionally. This correspondence should hold to higher intensities and shorter pulses as well, up to the limit where significant photoionization occurs and $n_{2,\text{free}}$ dominates. We compare our measurements with 200 ps and 220 fs pulse duration in the following chapter. In addition, $n_{2,\text{free}}$ can be manipulated in other ways besides simply scaling intensity, as we demonstrate in Section 4.5.

In all, the agreement with previous experiments performed over different wavelength regions and intensity scales gives confidence in these measurements and adds important data points to the sparse but growing database of nonlinear optical material properties in the mid-infrared.

	$n_{2,eff}$ [10^{-14} cm^2/W]		
	GaAs	n-Ge	ZnSe
This Work	3.4 ± 1.4	25 ± 10	1.2 ± 0.6
Literature	4 ± 2 [85]	30 ± 15 [85]	1.2 ± 0.3 [70]

Table 4.1: Measured $n_{2,eff}$ at 10.6 μm. Literature measurements in GaAs and n-Ge are made at 1 MW/cm^2 ($\tau = 200$ ns) and for ZnSe at 5 GW/cm^2 and $\lambda = 3.9$ μm ($\tau = 200$ fs).

4.4 Figures of Merit

For use in photonics applications, figures of merit (FOM) are useful to compare materials. Applying the FOM introduced in Eq. 2.19, which gives the ratio of nonlinear phase to absorption, to include

the NLA we observe in experiment results in the following expression:

$$FOM = \frac{n_{2,eff} I}{\lambda} \frac{1}{\alpha_1 + \alpha_{NL} I}. \tag{4.10}$$

Including the linear scaling of α_{NL} with pulse length (Eq. 4.3), the FOM of GaAs, n-Ge, and ZnSe for nonlinear photonics applications are given in Fig. 4.9 using experimentally measured $n_{2,eff}$ and α_{NL}. $\alpha_1 = 0.01$ cm^{-1} is assumed, which is a reasonable value for all of the optical quality samples. Vertical dashed lines indicate the highest intensity at which NLA was measured in experiment, so higher intensities are simple extrapolations. Linear absorption is the limiting factor at low intensities, whereas NLA intensity scaling causes FOM saturation at high intensities. For specific samples with higher (or lower) linear absorption, the low intensity FOM scales proportionally to what is plotted by the factor 0.01 cm$^{-1}/\alpha_1$, but the asymptotic behavior at high intensity is identical.

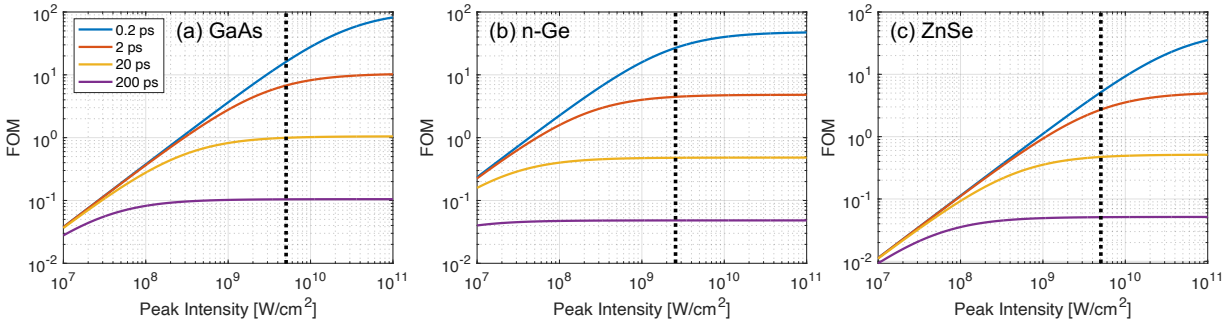

Figure 4.9: Figure of merit at 10.6 μm for nonlinear photonic devices using different pulse lengths. $\alpha_1 = 0.01$ cm^{-1} is assumed.

Despite the large nonlinear refractive indices in these semiconductors, the FOM for pulse lengths longer than 20 ps never reaches useful values > 1. Picosecond or sub-picosecond scale pulses are required to take full advantage of the nonlinear phase shifts. As mentioned above, this integrated NLA scales strongly with wavelength. Although we only measure nonlinear parameters at 10.6 μm, if we assume $\alpha_{NL} \propto \lambda^3$, then the saturated high intensity FOM scales extremely strongly with wavelength, λ^{-4}. This further emphasizes the critical importance of cumulative, pulse length dependent nonlinear optical effects in the mid-infrared.

Strong field photoionization will eventually dominate the NLA at higher intensities than used in this chapter. Shorter pulse lengths are required to probe materials in this regime while staying

below the damage thresholds. Photoionization and NLA of this kind is studied in Chapter 5. As photoionization so far from resonance is highly nonlinear (e.g. I^4 or stronger), once it causes significant energy loss the FOM will drop rapidly, assuming no change in $n_{2,eff}$. Under this scenario, the intensity range between $\sim$ 1-5 GW/cm^2 and pulse lengths $\lesssim$2 ps is a "sweet spot" for nonlinear photonics applications using semiconductors around 10 μm.

4.5 Control of the Nonlinear Optical Response of Bulk GaAs

For any photonics applications the ability to enhance or modify the nonlinear optical response of a material in a controllable way is key to its broad applicability. Here we use GaAs, a standard material of MIR photonics and semiconductor physics, to investigate the ability to optically control the nonlinear response. Significant enhancement has been reported in bulk intrinsic semiconductors for resonant or near-resonant pump configurations [96, 97] or doped p- and n- GaAs [98]. This enhancement comes at the cost of unavoidable optical losses - for example in p-GaAs linear absorption reached 5000 cm^{-1} [98]. Another approach to manipulating the optical response of semiconductors is by engineering materials with reduced dimensionality. Systems based on GaAs or other materials such as quantum wells [99–101], quantum dots [102], and thin films [103] have demonstrated controllable nonlinearity over a wide range. These have become more prevalent for miniaturization of photonic processes into chip-scale devices. High nonlinearities of these systems stem from various electron confinement or excitonic effects, but are rooted in resonant processes which also introduce inherent loss for light beams. While near-resonant interactions in bulk or structured materials are widely studied and useful in many applications, similar control over the nonlinearity in a bulk semiconductor far away from resonance (and therefore with low optical losses) would prove valuable for infrared photonics and nonlinear optics.

Here, we experimentally demonstrate that the nonlinear optical response of bulk GaAs, excited using MIR photons with energies far below the band gap energy ($\hbar\omega \approx E_g/12$) can be controlled at laser intensities in the range 1-10 GW/cm^2. This control is achieved by changing the beat frequency of a CO_2 laser beat-wave.

Nonlinearity is evaluated using FWM in the same 7 mm long [111] SI-GaAs sample as above.

FWM spectra are measured using two different laser beat-waves with duration 200 ps; a high frequency beat-wave (HFBW) with the same CO_2 laser lines as above, $\lambda_1 = 10.59$ μm and $\lambda_2 = 10.27$ μm; and a low frequency beat-wave (LFBW) with $\lambda_1 = 10.59$ μm and $\lambda_2 = 10.55$ μm (10P(16)). The beat frequencies are $\Delta\nu = 872$ GHz and 106 GHz, respectively. Electric fields of the two spectrally close pump wavelengths interfere and create beat-waves with almost double the peak intensity while maintaining the same energy fluence. Beating occurs on 1.1 ps and 9.4 ps timescales for the HFBW and LFBW respectively; each beat contains many individual cycles of the electric field ($\sim$ 30 fs). There is only one meaningful modification to the experimental layout presented in the previous section; due to the close separation of pump wavelengths in the LFWB, the etalon proved ineffective and was removed. As a result, these measurements had higher incident intensities (no Fresnel reflection from the etalon) and suffered from a worse signal to noise ratio ($\geq$2 for all LFWBW sidebands measured) as any background FWM was not filtered out.

Figure 4.10 shows measurements of 1st Stokes sideband energy generated in the GaAs sample for the HFBW (a) and LFBW (b) plotted in the same way as in the previous section. Effective intensity is the intensity corresponding to $(W_1^2 W_2)^{1/3}$ assuming $W_1/W_2 = 2$. Considering the HFBW data is multiplied by a factor of 10 on this scale, the absolute FWM yield is $\sim$40x larger in the LFBW case. This corresponds to a 10x increase in sideband generation efficiency for comparable intensities and thus >3x increase in effective nonlinearity. In Figs. 4.10(c-d) the full experimental FWM sideband spectra for the HFBW and LFBW, respectively, including every sideband measurable above the noise. Spectral energy is integrated over the spectral region with width defined by the 7 nm instrumental resolution. The LFBW interaction produced more sidebands above the noise on both Stokes and anti-Stokes sides than the HFWB, and also had higher efficiency across all sidebands, confirming the increase of FWM yield demonstrated by Fig 4.10(a-b).

Referring to the NLA measurements in GaAs, peak intensities of 5 GW/cm^2 result in 40% energy loss over 7 mm. While this is non-negligible, the peak absorption coefficient $\alpha_{NL} I$ is $\sim$2 cm^{-1}, still extremely small compared to resonant interactions. As discussed above, the presence of nonlinear absorption is associated with free carriers. An aspect of the nonlinear optical response that has not yet been discussed is free carrier nonlinearities, additively contributing to the overall nonlinearity like $n_{2,eff} = n_{2,\text{bound}} + n_{2,\text{free}}$. With the semiclassical Bloch acceleration theory (Eq. 2),

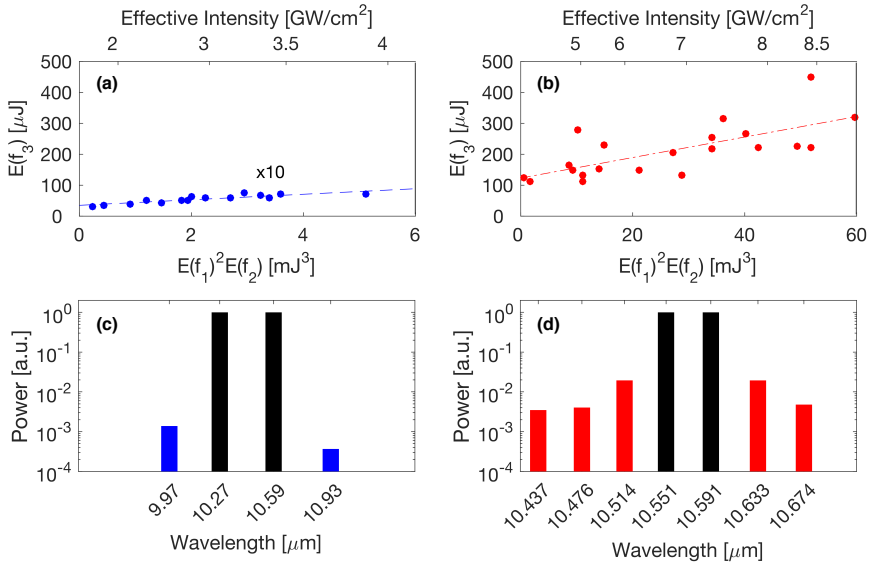

Figure 4.10: 1st Stokes sideband data measured in GaAs and its linear fit for the (a) HFBW (energy multiplied by 10x to enable comparison) and (b) LFBW. The background level is essentially flat, represented by the value of the fit at zero laser intensity. (c-d) FWM sideband spectra for the HFBW and LFBW.

it is found that peak beat-wave intensities used in experiments can drive nonequilibrium electrons born at the band edge to states with wavevectors that begin to break the parabolic approximation. In these high fields, nonlinear currents will be driven and scattering and dephasing processes will dynamically modify carrier distributions. To model these complicated dynamics and the combined effects of the bound electron and free carrier nonlinearities in a realistic band structure, we turn to the fully microscopic semiconductor Bloch equations (SBEs, Section 2.2.2) to self-consistently describe the laser-semiconductor interaction.

The band structure of [111] GaAs was calculated with DFT, giving the band structure presented in Fig. 4.11. The calculations reproduce the 4 major bands near the band gap, and also give the transition dipole moments d_k between all bands and for all k. By far the strongest dipole in the $\vec{E}$ // [111] orientation is the LH-CB dipole, causing the heavy-hole and split-off band dynamics to be rather inconsequential to the nonlinear response of GaAs at 10.6 μm. To simplify the simulations, they are performed only using the CB and LH bands. The dynamical evolution of interband polarization and intraband currents, as well as their mutual interplay, is described with the SBEs in the form presented in Eqs. 2.32–2.33. Coulomb interaction between charge carriers in the nonresonant

interaction manifests as an effective dephasing of the polarization as discussed in 2.2.2 and gives rise to higher order scattering processes, which we include as a phenomenological carrier relaxation and effective polarization damping. The phenomenological damping timescale of the polarization due to coulomb interactions was chosen to be $T_2 = 300$ fs as a representative value for this nonresonant interaction.

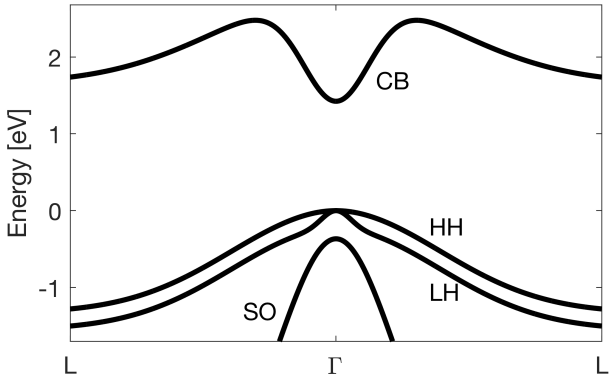

Figure 4.11: GaAs [111] band structure calculated with DFT used in SBE simulations.

To model experiments, the SBEs are solved in the time domain for an initially unexcited GaAs sample interacting with a 200 ps long beat-wave electric field with a gaussian intensity profile and pump energy ratio matching that in experiment. Since carriers and polarizations are excited primarily along the direction of the linearly polarized pump pulses, the simulations in reciprocal space are effectively one dimensional. This method has been successfully applied to describe strong field excitations [44]. Again, we characterize the nonlinear response by calculating 1st Stokes sideband yield as a function of input intensity. It should be noted that propagation effects are not considered in this model, and for this reason should not be considered as one-to-one modeling of the experiment. The calculations presented here were performed by Dr. Ulrich Huttner (University of Marburg) as part of a collaborative effort.

The results of these calculation are shown by the curves in Fig. 4.12. Both beat-waves exhibit a similar trend, except that the sideband generation efficiency is significantly increased for the LFBW. Specifically, with increasing laser intensity the sideband efficiency grows rapidly by several orders of magnitude up until 1 GW/cm^2, at which point it stagnates and exhibits a slowly increasing oscil-

latory behavior, signature of a highly nonlinear regime. Calculations indicate that transient carrier populations are created, and carrier populations and interband polarizations modulate each other causing Rabi-flopping like oscillations. In experiment, since the sideband intensity is integrated over many laser shots and the laser propagates through a thick sample, any potential signs of oscillation is likely washed out. Therefore, similar averaging is applied in the computations. Experimental data were separated into different intensity bins with their mean values and standard deviations represented by the points and error bars. There is reasonable agreement between experiment and simulations - importantly, the LFBW yields are consistently higher by a similar magnitude than HFBW yields in both experiment and theory.

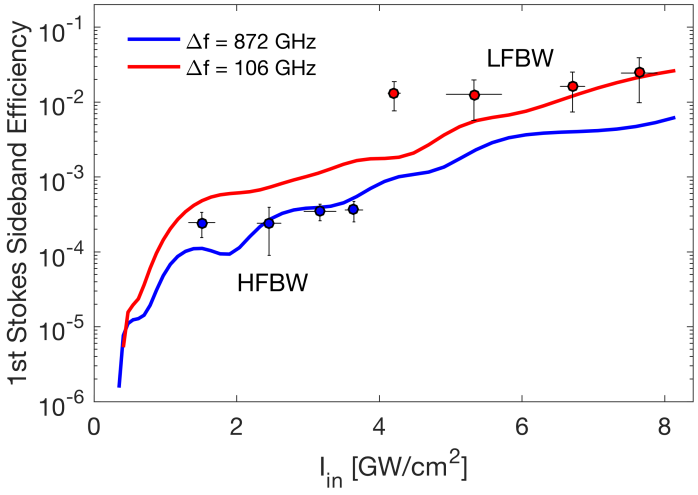

Figure 4.12: Simulation results modeling the efficiency of the 1st Stokes FWM sideband. Experimental data are shown for each beat-wave as well.

The microscopic calculations attribute the observed increase of FWM yield to efficient driving of intraband currents by the laser beat-wave. Although photon energies are highly nonresonant, strong electric fields produce a finite transition probability between an occupied valence and empty conduction state. Once carriers are generated, the beat-wave acts as a bias to accelerate electrons and holes through the Brillouin zone, causing intraband currents. Especially when $\Delta\nu \ll 1$ THz, the beat-wave modulation envelope provides a very low frequency component to the bias field that accelerates electrons and holes to high-k states and non-parabolic regions of the Brillouin zone, modulating the charge carriers' contributions to the optical nonlinearity as described in Section

2.1.10. The introduction of nonlinear currents represents a deviation from perturbative scaling of the nonlinear response.

When intraband currents are disabled in simulation, leaving only interband polarization (bound electron response), the calculated sideband efficiency lies below the curve for $\Delta\nu = 872$ GHz. With respect to the $n_{2,eff}$ measurements we made with the HFBW, this indicates that there may be a small free-carrier contribution to the effective nonlinearity even for the higher frequency beat-wave, but not nearly as strong as the LFBW. The detailed partitioning of $n_{2,bound}$ and $n_{2,free}$ in experiment requires further study, but measurements with sub-picosecond 10 μm pulses suggests that for GaAs, the majority of the nonlinear response to the HFBW is still the bound electron contribution (Section 5.3).

This analysis suggests that nonlinear intraband currents are responsible for the increased strength of the nonlinear response of GaAs pumped with low frequency beat-waves. In general, driving currents in solids is more efficient the longer the wavelength of the driving field because the duration of a half cycle of the beat pattern (the time before its sign flips) increases, leading to a larger excursion in k-space, the same argument behind ponderomotive energy scaling with $U_p \propto I\lambda^2$. With this physical picture, the effective nonlinearity enhancement should continue to scale as $\Delta\nu$ is further reduced. We test this prediction by extrapolating the simulations to $\Delta\nu = 4$ GHz, which has a half cycle bias time of 125 ps. Results are plotted in Fig. 4.13. The sideband efficiency and thus nonlinearity is even further enhanced at all intensities for $\Delta\nu = 4$ GHz.

The dramatic enhancement of the nonlinear response in bulk GaAs seen both in experiment and theory has temporal limitations imposed on it by the period of the beat frequency chosen – the duration of the pulse must be longer than the beat period for the effect to manifest. The relatively long pulses used in this experiment are useful for reaching the smallest beat frequencies provided by the CO_2 laser [54] – regular band laser lines provide a convenient method to tune $\Delta\nu$ smoothly to values as low as ~ 50 GHz, whereas simultaneous oscillation on the regular and sequence bands [104] could allow for 10 μm laser beat-waves as small as 4 GHz.

To summarize, we have shown that at GW/cm^2 level intensities, much below the dielectric breakdown threshold, the nonresonant nonlinear optical response of GaAs can be enhanced due to a free carrier contribution. Nonlinear currents are efficiently driven by CO_2 laser beat-waves, and

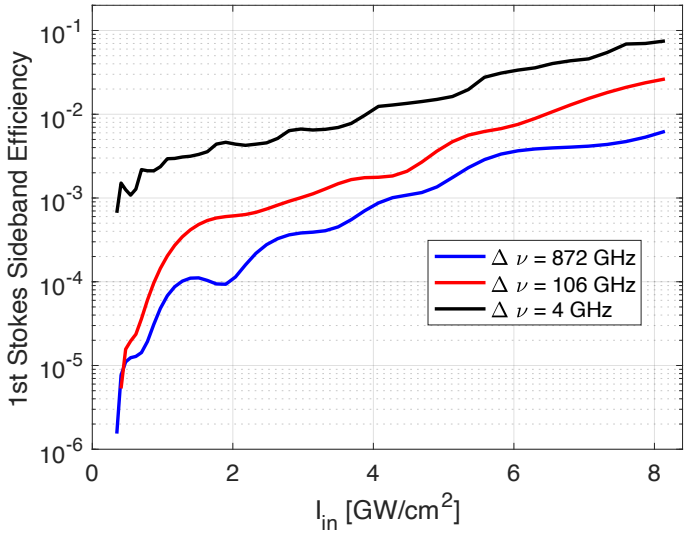

Figure 4.13: Extrapolation of the beat-wave enhancement of the Kerr nonlinearity in simulations.

decreasing the beat frequency gives the ability to control the nonlinearity with a high dynamic range. The robust control may prove useful for a variety of applications. For example, efficient sideband production can act as a proxy for self-phase modulation to effectively broaden the spectrum and allow for post-compression to reduce pulse length and increase peak power. Since the efficient production of a family of MIR sidebands with small (and constant) frequency separations has a spectral structure similar to that found in Kerr optical frequency combs, one can also envision the nonlinearity enhancement we observe assisting in future MIR frequency comb generation [105].

Finally, the nonperturbative physics presented is general - besides GaAs being of high optical quality and having well developed models of its electronic structure, nothing should stop beat-wave control of the nonresonant optical nonlinearity to exist in other semiconductor materials. Materials with higher nonparabolicity should in theory generate stronger nonlinear currents at lower intensities, and thus experience more beat-wave enhancement. Conduction band nonparabolicity has been shown to be universal, with the degree of nonparabolicity scaling with ε/m_e^* [106]. Since the effective mass and dielectric constant scale inversely and directly with band gap energy respectively [107], the nonparabolicity scales roughly with E_g^2. With this in mind, there is a balancing act in the band gap energy to increase nonparabolicity, while maintaining relatively low optical loss - lower band gap materials will experience stronger NLA eventually reaching multiphoton resonances.

Reducing the pulse duration and sample length may help increase transmission while maintaining high efficiency sideband generation in a narrower band gap material.

Chapter 5

Experimental Characterization of the Nonresonant Nonlinear Optical Response of Semiconductors using Femtosecond Pulses

Recent years have seen major development of ultrafast mid-infrared lasers, particularly with pulse durations less than 1 ps. Pulses of this kind at high repetition rates enable the study of novel nonlinear optical processes in both well-known and less-well-known materials with high precision. In many instances, this requires a new set of diagnostics, such as the MIR XFROG we use to fully characterize our laser pulses.

In this chapter, we report on the characterization of the MIR nonlinear optical response of bulk semiconductors at intensities between 0.1-20 GW/cm^2 using ultrafast sub-picosecond laser pulses generated by the Ti:Sapphire pumped OPA/DFG (Section 3.2). We pay particular attention to the unique semiconductor tellurium, which possesses remarkable linear and nonlinear material properties. The third order optical nonlinearity of bulk Te in its transparency region has not been reported before our work. In addition to this we combine experiment, theory, and numerical modeling to demonstrate an extreme dynamic nonlinear optical response in Te. We will discuss its merits as a material for MIR nonlinear photonic devices as well as a potential test bed for future studies of fundamental physics.

5.1 Tellurium

Tellurium, one of the main materials we study in this chapter, warrants an introduction. It is an elemental narrow-gap (E_g = 0.33 eV) semiconductor owning unusual optical, electrical, and magnetic properties due to its asymmetric chiral crystal structure. It is trigonal, with helical chains rotating along the crystal growth axis c. These 1-dimensional chains are arranged in a hexagonal

array, where each chain is bonded to neighboring chains via van der Waals interactions. The bond asymmetry, strong covalent bonds parallel to c and weaker bonds perpendicular to c, leads to large birefringence: the ordinary orientation (electric field of light E $\perp$ c) has refractive index $n_o = 4.8$ at 10 μm, whereas the extraordinary orientation (E // c) has refractive index $n_e = 6.2$ [108]. Te and its chalcogen neighbor Se are the simplest examples of chiral crystals, which has motivated intense study into their unique responses to external fields.

Several magneto-electric and magneto-optic effects in bulk Te have been discovered, including the photogalvanic effect [109], current induced magnetization [110], and kinetic Faraday effect (current induced optical activity) [111]. Recent work has focused on the potential of crystalline Te as a topological material exhibiting more exotic electrical and spin properties [112–117]. In addition, one- and two-dimensional Te structures have been isolated over a relatively large scale [116, 118, 119], showing photoelectric responses that could have an impact on engineering nano-scale electron transport devices.

Despite the intense recent study into material properties, the nonlinear optical response of bulk Te has been largely unexplored. Te possesses a number of remarkable optical characteristics, including an ultrawide transparency region that extends from mid-to-far-infrared (4-30+ μm). The large birefringence allows for straightforward phase-matching of second harmonic generation (SHG) – performing SHG of 10.6 μm CO_2 laser pulses uncovered the highest second order optical nonlinearity among natural crystals, $d = \chi^{(2)}/2 = 600$ pm/V [21]. Refractive index and band gap scalings of n_2 (Table 2.1) predict the nonresonant $n_{2,eff}$ of Te should be extremely large.

The electronic band structure of bulk Te has been studied both theoretically and experimentally [120–122], with a recent DFT calculation [123] reproducing experimental observables such as band gap energies, structural parameters, and band-edge absorption coefficients. Experiments and calculations both show that the band gap between the upper valence band (VB1) and the conduction band is $E_g = 0.33$ eV, but the effective absorption edge is blue shifted by approximately 10-20 meV for $E//c$ [124]. This has been associated with symmetry selection rules and vanishing transition dipole moments at the exact band edge in the $E//c$ orientation. A schematic of this band structure is shown in Fig. 5.1(a), with two primary conduction bands degenerate at the band edge (H point in momentum space) and two valence bands separated by 0.11 eV. In p-doped samples, a strong

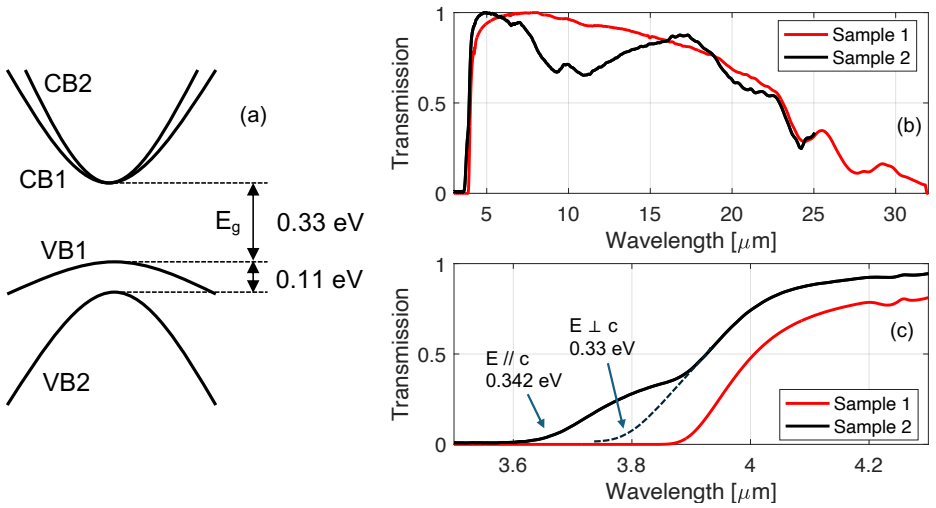

Figure 5.1: (a) Simplified band structure at the band gap of tellurium, showing two uppermost valence bands and two lowermost conduction bands. (b) Normalized transmission spectrum (unpolarized) measured for the crystal used in experiments (Sample 2) and a reference sample with different cut axis (Sample 1, not used in experiments). (c) Detail of the band edge. Sample 2 shows a blue-shifted band gap for the $E//c$ orientation [124]. Dashed continuation of the E $\perp$ c band edge is approximate, drawn to guide the eye. The origin of the band edge red-shift for sample 1 is unknown.

intervalence band absorption feature has been observed at 11 μm [108]. This absorption only exists in the $E//c$ orientation, as the transition is forbidden for the perpendicular polarization. In reality, the uppermost valence band has a characteristic "camelback" shape with a depth on the order of 1 meV due to spin-orbit interaction [120].

The Te sample we use in our experiments is 5 mm long, with transverse dimensions 10 x 10 mm (Princeton Scientific Corp.). It is cut at 90° from the crystal growth axis with input surface orientation $(10\bar{1}0)$. In this orientation, the electric field of a linearly polarized laser beam can be easily oriented either perpendicular ($E \perp c$) or parallel ($E//c$) to the growth axis c simply by rotating the crystal 90° about the cut face.

In both orientations we study, linearly polarized light propagates perpendicular to the helical atomic chains. While certain physical effects depend on the chirality handedness, these are present only when the propagation vector is parallel to the atomic chains. Because of this the handedness of our sample, which is unknown, should not play a significant role in our measurements.

Linear transmission of this crystal was measured with an FTIR spectrometer at UCLA, shown

as Sample 2 in Fig. 5.1(b). This measurement is a combination of transmission for $E \perp c$ and $E//c$. Data is corrected to account for the effect of Fresnel reflection. While Te is not transparent in the near infrared, it has a nearly fully transparent MIR window, followed by extended transparency beyond 25 μm. The spectrometer only extended to 25 μm, but a different 5 mm long sample (Sample 1 in Fig. 5.1) from the same manufacturer was previously measured to have transmission on the $\sim$15% level up to 30 μm.

Two features are of particular note here. First, we observe dips in linear transmission in the band between 8-12 μm, at 9.3 μm and 10.9 μm (Fig. 5.1(a)). This is manifestation of intervalence band hole absorption due to equilibrium hole populations with $E//c$. Dynamics of these transitions in tellurium have been well-studied in the linear regime [125–127]. Based on our transmission data, we estimate a peak absorption coefficient $\alpha_1 = 1.9$ cm^{-1} at 10.9 μm. Comparing to previous studies [108], this correlates with an equilibrium hole concentration of $< 1 \times 10^{15}$ cm^{-3}.

Sample 1 is cut for SHG of 10.6 μm light, ($\theta = 14°$), so the vast majority of light is projected onto the ordinary crystal axes ($E \perp c$). The MIR and FIR absorption features (e.g. phonon absorption at 24 μm) correspond between the two samples besides the hole transition bands, giving confidence in our assessment of sample orientations. The absorption coefficient at 10.3 μm is estimated to be ≈ 0.1 cm^{-1} from the Sample 1 transmission data.

5.2 Experimental Setup

We perform experimental measurements using the ultrafast MIR DFG source that was presented in detail in Chapter 3. The MIR pump pulses used for most of these experiments were centered at 10.3 μm and measured to have a pulse width (FWHM) of $\tau = 220$ fs. XFROG characterization of these pulses is given in Fig. 5.2. The pulse is slightly asymmetric in time, but a Gaussian pulse with FWHM 220 fs is a close approximation to the measured pulse shape. Careful spectral measurements using a scanning monochromator show a pulse bandwidth of 850 nm, giving a close to transform limited time-bandwidth product of 0.53. Pulse energy is ≤ 20 μJ.

Measurements of bulk semiconductor nonlinear optical properties are performed using the closed and open aperture z-scan method [128] and measurements of self-phase modulation. A simple

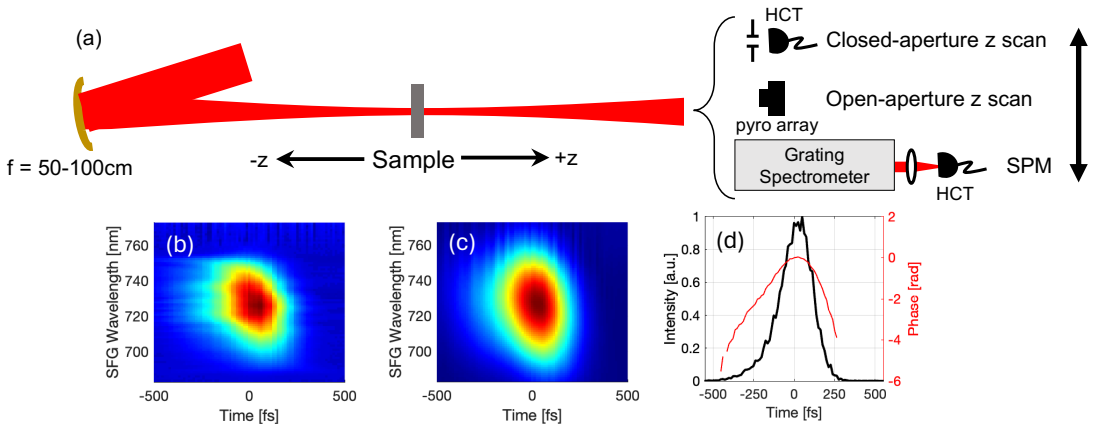

Figure 5.2: (a) Simple experimental schematic. Interchangeable diagnostics are shown on the right. (b) Measured XFROG trace of 10.3 μm pump pulse. (c) Retrieved XFROG trace of 10.3 μm pump pulse. (d) Reconstructed pump pulse profile (FWHM τ = 220 fs) and phase.

optical setup is used (Fig. 5.2). The MIR beam is allowed to propagate for approximately 2 meters, expanding to a centimeter-scale size. We then focus it with either a 50 cm or 100 cm focal length Cu mirror. Interchangeable diagnostics are used after the laser interacts with the focus to measure different effects.

The focal region of the MIR beam is carefully mapped, as this is the setup used for z-scan measurements. Here, the 10.3 μm beam profile is nearly Gaussian as measured using a pyroelectric array with pixel pitch 80 μm. Where the beam waist is <500 μm, it is magnified by a factor of 5 to provide sufficient resolution. As shown in Fig. 5.3(a), the $1/e^2$ beam radius in the focus (w_0) for both the horizontal and vertical planes is between 250-380 μm, with an ellipticity of $w_{0x}/w_{0y} = 0.7$.

Despite the ellipticity, the overall intensity profile (Fig. 5.3(b)) can be fit well using Gaussian optics. That is, we use the expression

$$I(z) = I(0)\left(1 + \frac{(z - z_0)^2}{z_R^2}\right)^{-1} \tag{5.1}$$

where z_0 is the focal point and $z_R = \pi w_0^2/\lambda_0$ is the usual Rayleigh length. This fit, shown in Fig. 5.3(b), gives an effective spot size of 260 μm and corresponding z_R = 2 cm. The peak intensity in focus is 56 GW/cm^2. Example images of the beam in the focus (Fig. 5.3(c)) and $4z_R$ from the focus (Fig. 5.3(d)) are given. Beam quality factors M_x^2 = 1.49 and M_y^2 = 1.76 are calculated, indicating

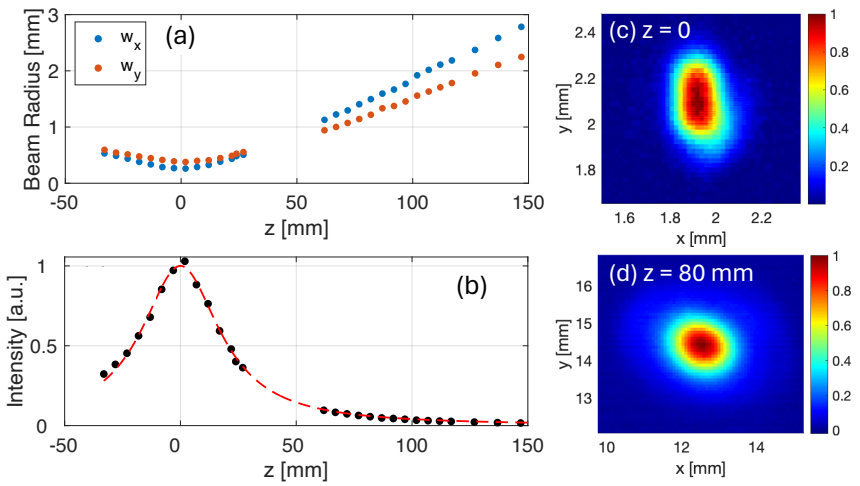

Figure 5.3: (a) Pump beam radius in the horizontal and vertical planes after focusing with a 50 cm focal length curved mirror. (b) Calculated intensity profile fit with standard gaussian optics to find $w_0 = 260$ μm. (c-d) pump beam profile in air at different locations near focal region.

good quality focusing.

The samples we use are the same 7 mm [111] slab of semi-insulating GaAs and 2 mm slab of n-Ge described in Chapter 4. Along with the tellurium crystal we discuss above, we also study a 3 mm thick polycrystalline ZnSe. As mentioned previously, the exact grain structure is not known, but it is a commercially grown optical quality crystal that typically has 30-40 μm grain size. In all the following high-field measurements, no optical damage is observed on the polished semiconductor surfaces after extended exposure to laser radiation at a 1 kHz pulse repetition rate. Experiments are performed at room temperature.

5.3 Closed Aperture Z-Scan

The closed aperture z-scan is a widely used technique to measure nonlinear refraction in dielectrics [128]. It is based on the change in relative transmission through an aperture in the far field caused by self-focusing as the sample is translated through the focal region. For our z-scan measurements, the sample is mounted on a translational stage such that it can interact with converging and diverging parts of the beam, as well as a scan of intensity (Fig. 5.2). The aperture is placed 40 cm from focus (z = +20 z_R), and has a radius $r_{ap} = 0.35$ mm. Directly after the aperture, an HgCdTe

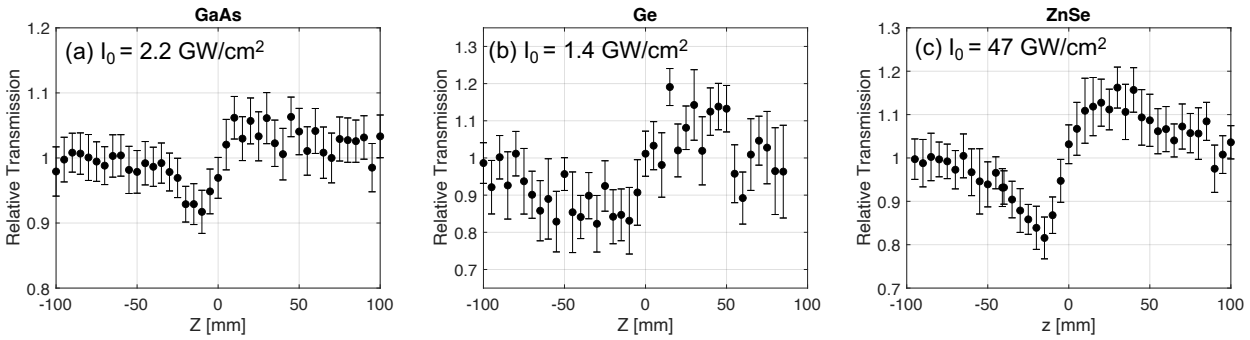

Figure 5.4: Closed aperture z-scan results in (a) 7 mm GaAs, (b) 2 mm n-Ge, (c) 3 mm ZnSe.

(HCT) photodetector with a 1x1 mm active area measures the transmission through the aperture as a function of sample position. In this geometry, linear transmission through the aperture with no sample in the beam path is low, approximately 0.5%.

Results of the closed aperture z-scan measurements in GaAs, n-Ge, and ZnSe at $\lambda_0 = 10.3$ μm are given in Fig. 5.4. To reduce the effect of shot-to-shot energy fluctuations, the signal measured by the HCT detector after the aperture is averaged over 16 individual shots to comprise one data point. The total data set at each z position consists of 150 data points; shown are the mean value with error bars representing the standard deviation of this set.

In all cases, relative transmission through the aperture is reduced when the sample is placed in an intense converging beam (z $<$ 0) and increased when the sample is placed in an intense diverging beam (z $>$ 0). This dependence gives the characteristic z-scan shape corresponding to positive $n_{2,eff}$. The intensities given in the figure are the calculated peak intensity inside the crystal at z = 0, I_0, taking into account external attenuation and Fresnel reflection from the surface.

The closed aperture z-scan technique sensitively measures the nonlinear phase shift/B integral accumulated over the length of the sample. The peak nonlinear phase shift at the center of the beam is $\Delta\Phi_0 = k_0 n_{2,eff} I_0 L$, where k_0 is the vacuum central wavenumber of the laser and L is the sample length. In extracting this quantity, and thus $n_{2,eff}$, the thin sample approximation (TSA) is often used [128]. This states that the length of the sample is much shorter than the characteristic length over which the beam size changes, or $L \ll z_R/\Delta\Phi_0$. When this is satisfied, the beam size and intensity can be considered constant throughout the length of the sample, simplifying the analysis

tremendously.

In the special case where linear transmission through the aperture is small, as it is in our experiments, and $\Delta\Phi_0 \leq \pi$, there is a definite linear relationship between the nonlinear phase shift and ΔT_{p-v}, the transmission difference between the peak and valley of the z-scan trace. This relationship is [128]

$$\Delta T_{p-v} = 0.406\Delta\Phi_0 = 0.406 k_0 n_{2,eff} I_0 L \tag{5.2}$$

Calculations of the nonlinear phase shift and $n_{2,eff}$ using this formula are summarized in Table 5.1.

	I_0 [GW/cm^2]	ΔT_{p-v}	$\Delta\Phi_0$ [rad]	$L\Delta\Phi_0/z_R$	$n_{2,eff}$ [10^{-14} cm^2/W]	$n_{2,eff}$ (200 ps) [10^{-14} cm^2/W]
GaAs	2.2	0.14	0.36	0.12	4 ± 1	3.4 ± 1.4
n-Ge	1.4	0.29	0.69	0.068	40 ± 13	25 ± 10
ZnSe	47	0.35	0.86	0.12	1 ± 0.1	1.2 ± 0.6
Te (E ⊥ c)	0.60	1.1	2.8	0.68	150 ± 20	-
Te (E // c)	0.50	1.3	3.3	0.80	310 ± 30	-

Table 5.1: Measured and calculated parameters of the closed aperture z-scan experiment under the TSA. The final column are $n_{2,eff}$ measured using FWM of 200 ps CO_2 laser beat-waves (Chapter 4).

As can be seen in the table, all three of these materials fully satisfy the TSA, as $\Delta\Phi_0 \leq \pi$ and $L\Delta\Phi_0/z_R \ll 1$. This justifies using Eq. 5.2 to calculate the nonlinear refractive index. Error bars are calculated through propagation of different sources of experimental error (pulse energy, beam size, pulse length) contributing to intensity uncertainty, along with the measured standard deviations from data scattering.

The values extracted from the z-scan match, within error bars, literature values as well as our own measurements presented in Chapter 4. The consistency of the MIR nonlinear refractive index in these three materials across different experimental methods and, critically, pump pulse durations highlights their usefulness as broadband materials for nonlinear photonics in a wide range of applications using different pulse parameters.

We also perform the closed aperture z-scan measurements in both orientations of tellurium, the results of which are presented in Fig. 5.5. As is obvious by comparing to the "control" sample data in Fig. 5.4, the peak to valley transmission change in both Te orientations is huge, despite having

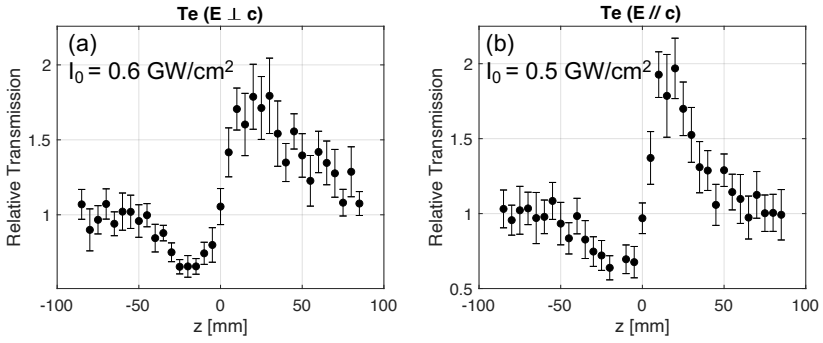

Figure 5.5: Closed aperture z-scan results in (a) 5 mm Te, E $\perp$ c orientation, (b) 5 mm Te, E // c orientation.

much lower intensity. Referring to Table 5.1, the calculated nonlinear phase shift is very large, on the order of π even at intensities < 1 GW/cm^2. Qualitative observations of the beam size after the tellurium crystal support this, with strong self-focusing causing the beam to evolve into a tight spot only a few centimeters after the sample at the highest intensities. Note that the z-scan shape confirms a self-focusing nonlinearity (positive $n_{2,eff}$), such that the contribution of a self-defocusing nonlinearity (e.g. free carrier generation) plays a small role. There is a possibility that thermal focusing caused by local heating from nonlinear absorption may contribute to the apparent self focusing effect in tellurium, but this is proven to be a small contribution (Appendix C).

For this experimental setup, the TSA is not satisfied for either orientation of Te. A thick sample z-scan theory exists [129], but it requires $\Delta\Phi_0 \ll \pi$, so it is not applicable here. In breaking the TSA, we should expect a departure form linearity in Eq. 5.2 such that $n_{2,eff}$ calculated in this way gives only a lower limit of the real value in Te.

We calculate an extremely large $n_{2,eff}$ for both orientations, approaching 100x larger than that in GaAs and 10x larger than in n-Ge. An effective length $L_{eff} = (1 - \exp(-\alpha_1 L))/\alpha_1 = 3.5$ mm is used for the E // c orientation to account for linear absorption. The effective length for E $\perp$ c is within 2.5% of the physical length, which as an uncertainty source gets drowned out by other experimental uncertainties. $n_{2,eff}$ in the E // c orientation is $\sim$2x larger than in the E $\perp$ c orientation, indicating a significant anisotropy. This anisotropy correlates with the crystal symmetry and birefringence. Furthermore, being in the spectral vicinity of the resonant intervalence band transitions may introduce a resonant contribution to the nonlinear refractive response.

Despite the calculated values being lower limits of the real $n_{2,eff}$ in bulk Te, they are among the largest known nonlinear refractive indices. It is on the order or approaching extremely large third order nonlinearities measured in organic solutions or semiconductors in the near infrared, where nonlinear effects are naturally stronger.

5.4 Self-Phase Modulation

It is clear from the z-scan analysis that we need an alternative method to establish a more reliable value of $n_{2,eff}$ in tellurium. To do that, we fix the position of the sample and measure spectral broadening incurred by self-phase modulation (SPM).

The 100 cm focal length curved mirror is used giving $z_R = 4.5$ cm, such that the beam size stays essentially constant over the 5 mm sample length. Taking into account Fresnel reflection, peak intensity inside the crystal for SPM measurements is 1.5 GW/cm^2 for E $\perp$ c and 1.2 GW/cm^2 for E // c. A 76.2 mm focal length off-axis parabolic mirror (OAP) directly after the crystal collects all transmitted light and focus it onto the entrance slit of a scanning monochromator (Horiba iHR550). The light is dispersed by a 100 grooves/mm diffraction grating blazed at 9 μm with known spectral efficiency. The 550 mm base length combined with a narrow, 0.1 mm exit slit gives a spectral resolution of 5 nm at the central wavelength of 10.3 μm. After the exit slit, the light is focused with an OAP onto the 1x1 mm chip of a liquid nitrogen cooled HCT detector to measure spectral energy density. The pump spectrum is measured using the same setup but without the sample.

Spectral broadening measured in both orientations of Te are shown in Fig. 5.6. The spectral region shown was scanned in 50 nm steps where each displayed data point is averaged in the same way as described for the closed aperture z scan measurements. Error bars again are the standard deviations of these data sets. 50 nm steps are made to improve acquisition speed.

Spectral modulations are observed in both input and broadened spectra near the central wavelength, particularly on the longer wavelength side. However, when step sizes as small as 10 nm are made, it is clear from the Fourier transform that the modulation is simply random noise and does not have any systematic components. Because of this noise, a moving average over a 200 nm window is displayed in the solid line to guide the eye. for the sake of comparison, to avoid differences

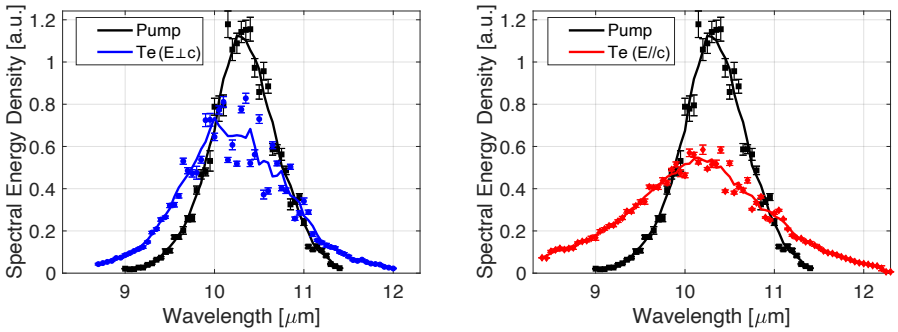

Figure 5.6: Measurements of spectral broadening in (a) Te, E $\perp$ c and (b) Te, E // c caused by self-phase modulation.

in ordinary and extraordinary linear refraction and nonlinear absorption each curve is normalized such that the total integrated energy is the same. In addition, corrections are made according to the spectral dependence of relative grating efficiency, detector sensitivity, and spectral resolution.

The input spectrum is close to Gaussian, and has a FWHM bandwidth of 0.85 μm. After propagating through 5 mm of Te (E $\perp$ c) it has been broadened to 1.38 μm, a bandwidth increase of 1.6x. Similarly, for E // c, the spectrum is broadened to 1.82 μm, a 2.1x increase. The anisotropy of the spectral broadening follows that seen in the z-scan measurements, where E // c has a stronger nonlinear interaction despite slightly lower intensity; this further supports the conclusion that $n_{2,eff}(//) > n_{2,eff}(\perp)$. To emphasize the giant nonlinearity of Te, the same SPM measurement was carried out in the 7 mm GaAs at 2 GW/cm^2 - no detectable spectral broadening was observed.

A blue-shift of the central wavelength is observed in both broadened spectra. The most likely explanation is the asymmetry of the pump pulse in time with a faster falling edge than rising edge (Fig. 5.2(d)) causing asymmetric SPM favoring higher frequencies (Section 2.1.3). Ionization blue shift associated with plasma generation [40] may be contributing as well, but is shown in the following section to be minor at 1.5 GW/cm^2. As a final sanity check, nearly symmetric spectral broadening further confirms the assertion that this nonlinearity is primarily a bound-electron phenomenon. Besides the lack of strong blue shift associated with plasma generation, a thermal nonlinearity would have negligible effect on the pulse spectrum as the refractive index does not change during the sub-picosecond pulse length, especially after thermal steady state is reached at 1 kHz repetition

rate. It is interesting to note that the SPM measurements in Te (E // c) do not show significant loss near the 11 μm absorption band. This may be evidence of the intervalence band hole transitions being bleached to some extent by the high intensity pulse, similar to that discussed in Chapter 4 for GaAs and Ge.

In principle, the amount of spectral broadening should depend on $n_{2,eff}$. Analytical theories take advantage of a model like Eq. 2.11 to estimate spectral broadening in a fiber (in which the most research on SPM-based spectral broadening has been done). For example, in Ref. [130], the bandwidth increase is calculated to be

$$\frac{\Delta\omega}{(\Delta\omega)_0} = \frac{\Delta\lambda}{(\Delta\lambda)_0} = \sqrt{1 + \frac{4}{3\sqrt{3}}B^2}. \tag{5.3}$$

Using the nonlinear indices determined in the z scan experiment, the theoretical bandwidth increase is 6.1x and 7.0x for the perpendicular and parallel orientations, respectively. These are significantly larger than what we measure in the experiment. Besides ignoring nonlinear absorption and dispersion, analytic models fail largely because they do not consider the two-dimensional beam structure that is always present in non-guiding structures like bulk semiconductors. While the spectral broadening at the center of the beam may indeed be 6-7x, most of the beam energy is contained in lower intensity regions which do not experience as much nonlinear phase shift.

Clearly, one needs more sophisticated multidimensional modeling for experimental situations with large nonlinear phase shifts, nonlinear absorption, high dispersion, etc. Before that can be done, nonlinear absorption must be characterized.

5.5 Open Aperture Z-Scan

Throughout measurements described in the previous sections, we observed signs of nonlinear absorption in Te and other semiconductors as we remove attenuation or scan the sample through the focal region at high intensity. To assess the nonlinear absorption, we will use the open aperture z-scan technique.

We use the same experimental setup and focusing geometry as the closed aperture z-scan (Fig.

5.3). Instead of an iris and HCT photodetector, we collect the full beam with a 75 mm focal length OAP. This focuses the pump light transmitted through the sample onto a 2D pyroelectric array (Pyrocam IV). The array has a linear response throughout the MIR spectral region, acting as a total energy detector with dynamic range corresponding to 15 bits. Beam collection is necessary as strong self-focusing is observed, which dramatically affects the beam size and spatial distribution in the far field.

Ten individual shots were summed, and the total counts were integrated over the entire beam (with careful background subtraction) as a measure of total energy while scanning the sample through the focus. Fifteen of these measurements are averaged at each sample z position, and normalized to the total integrated counts when the sample was far from the focus ($|z| > 100$ mm).

Results of these experiments and analysis for GaAs and n-Ge are given in Fig. 5.7 and for Tellurium in Fig. 5.8. Panel (i) gives the open aperture z-scan trace, with the intensity profile overlaid. Note the much higher intensities used compared to closed aperture z-scan and SPM experiments. Unfortunately, our signal to noise ratio and laser stability was not sufficient to reliably measure transmission changes less than $\sim 5\%$. However, with this data (Panel (ii)) we can still observe the onset of macroscopic nonlinear absorption, which begins at approximately 10 GW/cm^2 and 6 GW/cm^2 in GaAs and n-Ge, respectively. It should be noted that these onset intensities are a factor of 10 higher than observed for 1000x longer 200 ps pulses. A comparison between these results is made in the discussion of Section 5.7. NLA was also measured in ZnSe, but no absorption was found up to 40 GW/cm^2. In Te there is a much earlier onset of NLA, occurring at approximately 0.75 GW/cm^2 with E $\perp$ c and 1.3 GW/cm^2 for E // c. The NLA at maximum intensities results in as low as 20% transmission for both orientations of Te. While the magnitude of the peak absorption is the same for both Te orientations, the intensity dependence appears to be different.

Measurements of NLA in Tellurium at a pump wavelength of 7.5 μm, the boundary between 2PA and 3PA regimes, are presented in Fig. 5.9. The results are qualitatively similar to those at 10.3 μm. In processing these shorter wavelength data, we assume that the laser spot size in focus is smaller than the 10.3 μm spot by ratio of the wavelengths.

As shown during the analysis of NLA with 200 ps laser pulses (Section 4.2), slope fitting of $-\Delta T$ versus intensity gives intensity scaling of the NLA. This fit is shown in Panel (iii) of Figs. 5.7

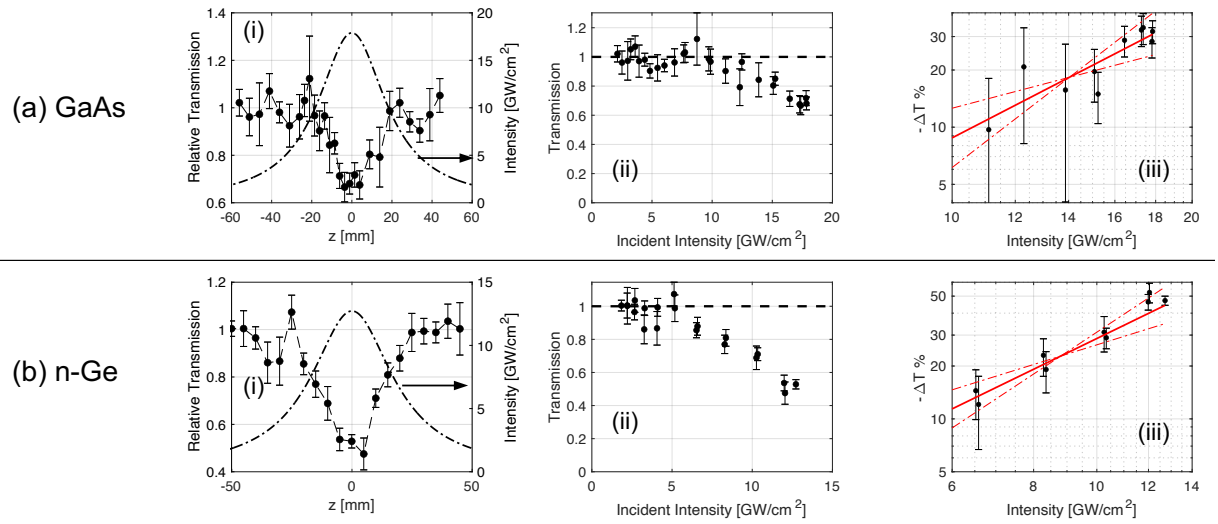

Figure 5.7: NLA measurements in (a) 7 mm GaAs and (b) 2 mm n-Ge using the open-aperture z-scan. Panels (i) and (ii) are the same data represented in different ways. Panel (iii) gives slope fitting of the NLA data, with dash-dot lines as 95% confidence inteveral of the fit.

and 5.8 for data points with $5\% < -\Delta T < 30\%$. It is clear that the linear dependence is no longer satisfied at the highest intensities, which can be attributed to the failure of the approximation due to pump depletion. Results of the fitting for all materials are given in Table 5.2. Slopes obtained in Tellurium at both wavelengths are reasonable, giving intensity dependence close to the nominal I^3 associated with 3 photon absorption.

	GaAs	n-Ge (4-6 GW/cm^2)	n-Ge (6-10 GW/cm^2)	Te (E $\perp$ c) $\lambda = 10.3\mu$m	Te (E // c) $\lambda = 10.3\mu$m	Te (E $\perp$ c) $\lambda = 7.5\mu$m	Te (E // c) $\lambda = 7.5\mu$m
Slope + 1	3.2 ± 1.1	3.9 ± 0.5	2.8 ± 0.6	2.3 ± 0.4	3.4 ± 0.8	3.2 ± 0.8	2.3 ± 0.8

Table 5.2: Slope fitting results for open-aperture z-scan measurements.

The results in GaAs and n-Ge are somewhat surprising, giving much lower values than would be predicted by $M = \lceil E_g/\hbar\omega_0 \rceil = 12$ for GaAs and $M = 7$ for n-Ge. This indicates that the intensity scaling we observe in experiments is weaker than predicted by the perturbative I^M scaling.

To make sense of this, we look more closely at the Keldysh theory of photoionization (Section 2.1.9). At low intensities ($\gamma \gg 1$) the photoionization rate scales perturbatively ($w_{PI} \propto I^M$) until channel closing occurs. At this point, the photoionization slope increases step-wise to $w_{PI} \propto I^{M+1}$. This continues until $\gamma \ll 1$ and the tunneling limit is reached. In our NLA measurements above the ultrafast MIR laser pulses are firmly within the diabatic tunneling regime, with $\gamma_{\text{GaAs}} = 0.54$ and

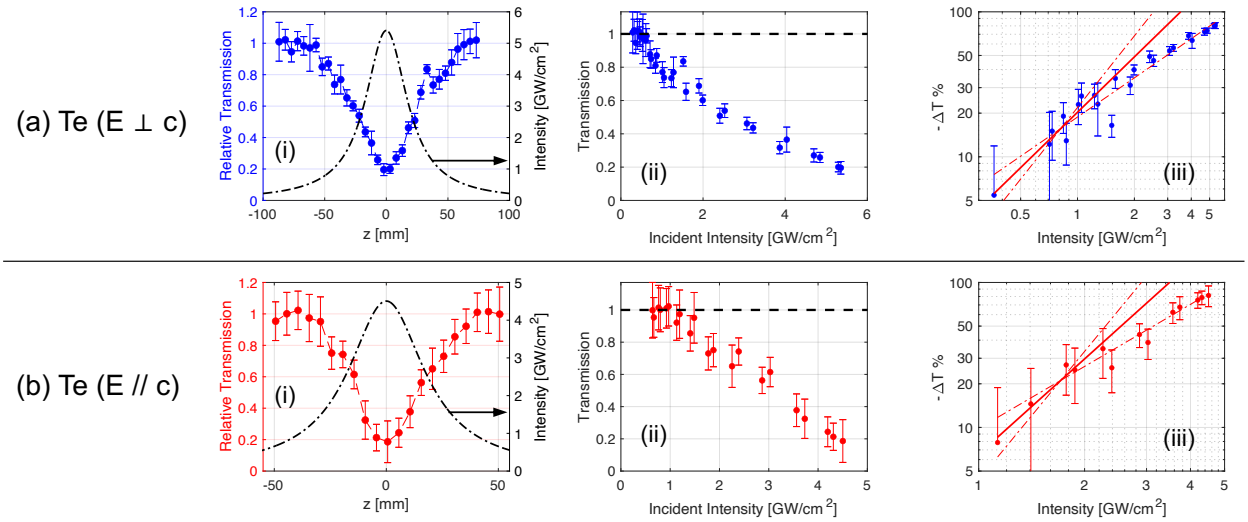

Figure 5.8: The same as Fig. 5.7 for (a) Te E ⊥ c and (b) Te E // c.

$\gamma_{\mathrm{Ge}} = 0.52$. Thus, we should expect a combination of MPA and tunneling causing photoionization in these semiconductors. Furthermore, the nonperturbative intensity parameter defined in Chapter 2 is $\gamma_{NP,\mathrm{GaAs}} = 10$ and $\gamma_{NP,\mathrm{Ge}} = 6.1$, both indicating that nonperturbative physics is complicating the physical picture.

Keldysh photoionization rates have been plotted for GaAs (Fig. 5.10(a)) and n-Ge (Fig. 5.10(b,c)) combining LH→CB and HH→CB interband transitions. The two n-Ge data sets are taken with different peak intensities. Intensity ranges of interest are delineated by the vertical dashed lines. Clearly, channel closing is strongly modulating the overall photoionization rates in these intensity ranges ($\gamma_{NP} > 1$). Moreover, the gradual transition to pure tunneling causes the averaged photoionization rate slope to decrease at higher intensities. Fitting a slope to the intensity range of interest supports this - these fits are given in the figures.

Remarkably, the nonperturbative intensity scaling of photoionization predicted by the Keldysh theory matches rather closely the experimentally measured intensity scaling of NLA, especially for n-Ge (compare to Table 5.2). In GaAs, the B integral for this intensity range is between 2-3, indicating that SPM is broadening the spectrum. Given the negative GVD, self-compression of the pulse during propagation, combined with self-focusing, results in positive feedback and a significant increase in peak intensity. gNLSE simulations support this, with peak intensity at the center of

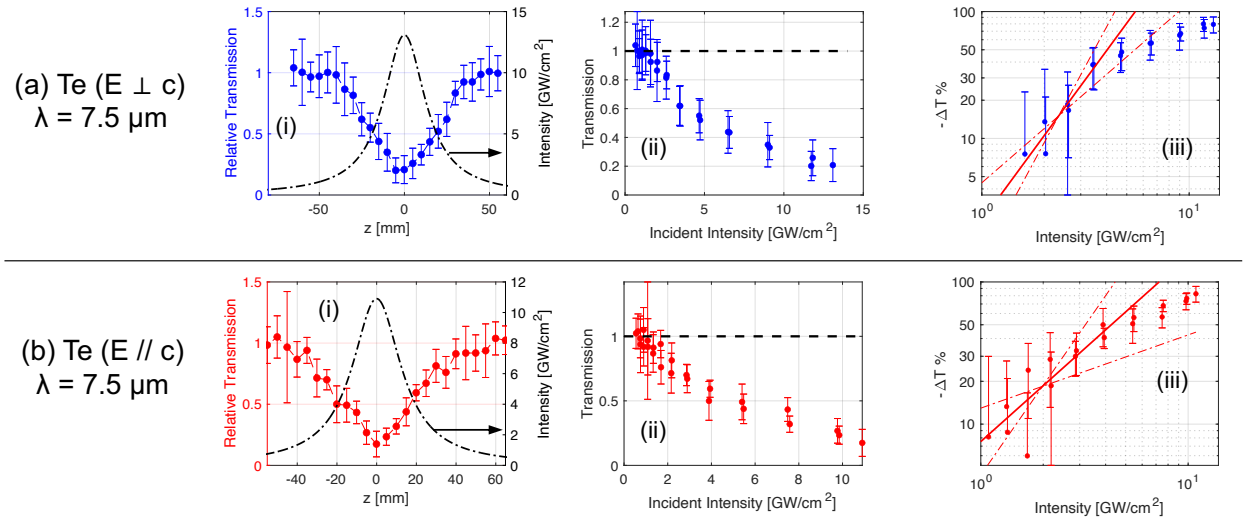

Figure 5.9: The same as Fig. 5.7 for (a) Te E ⊥ c and (b) Te E // c at a central pump wavelength of 7.5 μm.

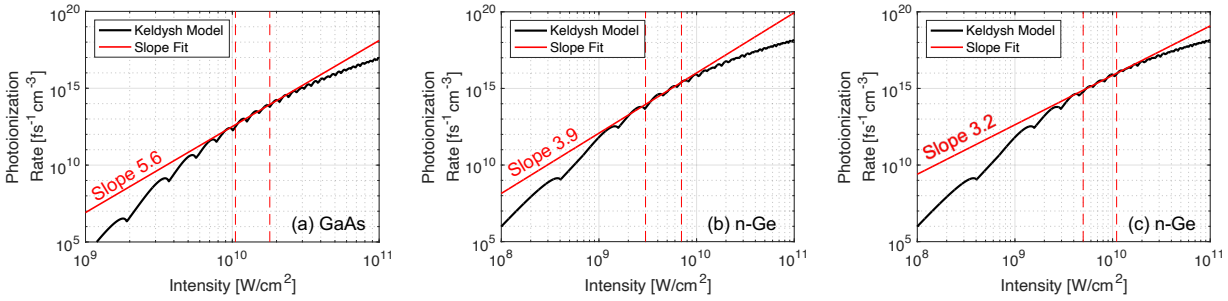

Figure 5.10: Slope fitting the Keldysh photonionization rate in (a) GaAs and (b-c) n-Ge. The vertical dashed lines indicate the intensity range over which fitting is performed.

the beam >2x higher than the initial intensity. Dynamic intensity increase not only brings the Keldysh rate to a shallower slope, matching more closely with experiment, but also makes the absolute photoionization rate very similar in both GaAs and n-Ge. This supports the experimental observation of similar absolute energy loss in the two materials. Without self-compression, the integrated excited carrier density over a 220 fs pulse is more than 10x smaller in GaAs than in n-Ge. Note that at intensities > 20 GW/cm^2 in GaAs, the Bloch acceleration theorem (Eq. 2.22 shows that electron k excursion can reach > 0.2 1/Å, a significant portion of the Brillouin zone. With large k and thus carrier energy, impact ionization becomes plausible. However comparing to the DFT band structure in the [111] orientation (Fig. 4.11), band dispersion does not allow

the electronic energy to surpass the energy threshold for impact ionization [131], 1.57 eV, greatly suppressing this additional ionization and loss channel.

Averaging the photoionization rate over a range of intensities like we do here can be justified in a bulk semiconductor. While the peak intensity of a Gaussian pulse is quoted for all intensities in this dissertation, the reality is that a majority of the photons contained in that pulse interact with the medium at significantly lower intensities. That is, different radial portions of the beam have less intensity but more total photons, naturally blurring the overall interaction. In this way, multi-dimensional effects (including propagation, a main theme of the following section) complicate and may obscure specific physical effects, but in other ways this averaging has helped reveal strong-field physics.

Observations of nonperturbative or extreme nonlinear optics are quite common - most modern high-harmonic generation experiments are highly nonperturbative by definition and intense few-cycle near-infrared laser pulses have been driving strong-field physics for many years [132]. Unique in our case, though, is the long wavelength laser pulses that enable breakdown of the perturbative nonlinear optics and thus fundamental transient modifications of the semiconductor properties at relatively low intensities. Besides the exciting physics phenomena, this allows laser pulses to be kept much below the damage thresholds of the material; for future application in transient control of semiconductor properties, this is a major advantage.

Returning to Tellurium, where the NLA scaling appears to be closer to pure multiphoton ionization, an analytical theory is used which has been developed for open-aperture z-scan for MPA orders 3-5 [133]. Assuming Gaussian beams and pulses in time, analytical expressions for $T(z)$ are derived and can be used to fit MPA coefficients to our experimental data. The fitting of this theory for both E $\perp$ c and E // c are shown in Fig. 5.11. The best fit is found by minimizing the root mean square error (RMSE) of the analytic curve and the experimental data, with α_M as the only free parameter. For E $\perp$ c, there is a good fit for pure 3PA using $\alpha_3 = 5.6$ cm^3/GW^2. Compared to other common semiconductors, this is a rather large 3PA coefficient. At wavelengths between 2.3-2.7 μm, α_3 has been measured in GaAs and Si to be 0.35 and 0.035 cm^3/GW^2, respectively [91, 134]. However, compared to other narrow band gap semiconductors such as InSb or InAs, where 3PA coefficients have been found to be as large as α_3 = 1-100 $\times 10^3$ cm^3/GW^2 [135–137], the NLA in Te is quite

low.

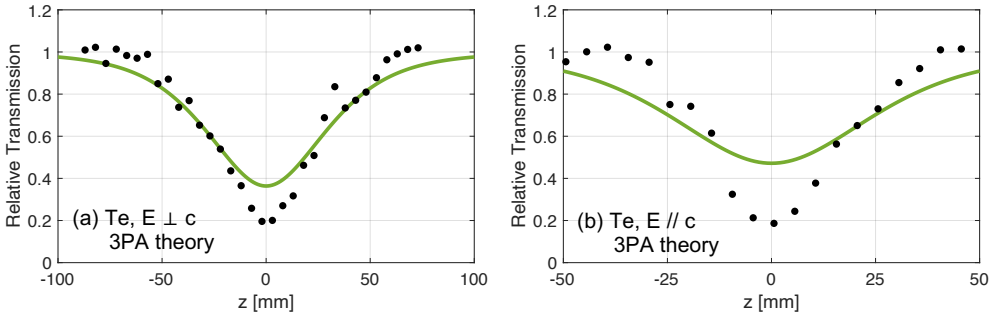

Figure 5.11: Fitting to analytical theory of z-scan with 3PA from Ref. [133]. The curves shown are calculated with $\alpha_{3,\perp} = 5.6$ cm^3/GW^2 and $\alpha_{3,//} = 4.4$ cm^3/GW^2. In E // c, 3PA, 4PA, and 5PA theory all produce equally poor fits to the experimental data.

In this orientation, the 3PA theory slightly overestimates absorption in the region $|z| > 2.5z_R$, and underestimates within 1 Rayleigh length of the focus. This behavior suggests stronger intensity dependence; when 4PA theory is applied, however, the best-fit ($\alpha_4 = 15$ cm^5/GW^3) does not improve the data matching a significant amount. In fact, the 3PA and 4PA theory curves are so similar that it is difficult to unambiguously assign a single MPA order to this data. In the E // c orientation, Fig. 5.11(b), fitting any MPA order is unsuccessful, again suggesting a difference in physics between the two orientations, possibly related to hole dynamics in the valence bands.

Applying the analytical theory to the 7.5 μm data results in good fits for both crystal orientations. Best fit 3PA coefficients are $\alpha_{3,\perp} = 1.14$ cm^3/GW^2 and $\alpha_{3,//} = 1.68$ cm^3/GW^2. Dispersion of measured $\alpha_{3,\perp}$ between 7.5-10.3 μm, a ratio of 0.21, is close to a theoretically predicted ratio of 0.14 [30].

In order to get an independent measurement of NLA for both orientations at 10.3 μm, we used measured energy throughput at a fixed z position ($w = 0.95$ mm) and use a series of calibrated attenuators to vary intensity. For these measurements, the pulse length is ~500 fs due to slight modifications to the laser system but the peak laser intensity was similar, on the order of 2 GW/cm^2. Total energy throughput for each orientation is found using a calibrated power meter and normalized for Fresnel reflection (Fig. 5.12). Using gNLSE modeling, this experimental data matches well with $\alpha_3 = 10$ cm^3/GW^2 in the E $\perp$ c orientation, a value consistent with the analytic 3PA theory. In the E // c orientation, this method gives $\alpha_3 \approx 15$ cm^3/GW^2, a slightly larger NLA coefficient than for

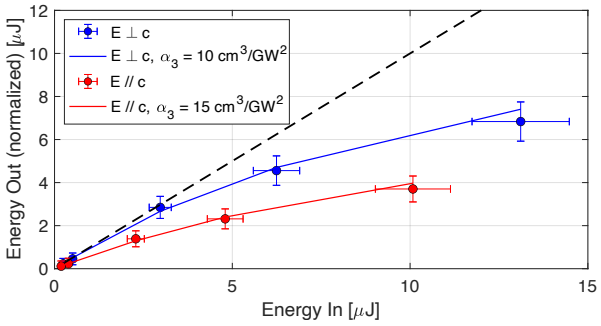

Figure 5.12: Nonlinear absorption measurements in Te with a fixed sample position. Solid lines represent modeling results for the 3PA coefficients listed in the legend. Dashed line is the case of no nonlinear absorption.

E $\perp$ c. It should be emphasized that interaction with longer pulse lengths will increase contribution of free-carrier effects, perhaps explaining the effective increase in measured α_3, as FCA was not included. In addition, these measurements show that at low intensities where NLA is negligible, transmission in the E // c orientation is lower than in the E $\perp$ c orientation. This supports the attribution of linear absorption features near 10 μm to the E // c orientation (Fig. 5.1), and is also in line with literature measurements [108].

5.6 Modeling and Discussion

To assign numerical values of $n_{2,eff}$ and α_M to the nonlinear refraction and absorption processes we observe in tellurium, we turn to numerical modeling. Both self-phase modulation and the open-aperture z-scan measurements are modeled using the gNLSE (Section 2.2.1).

Gaussian pulses and transverse beam profiles are assumed to simplify the analysis, taking into account measured experimental parameters of pulse length, beam profile, and intensity. In all cases, the beam is taken to have no initial divergence entering the sample; this is a reasonable approximation given the Rayleigh length inside a dielectric is $n_0 z_R$, which even in the tightest experimental focusing is $\sim$10 cm, much longer than the 5 mm crystal.

We solve the gNLSE in the form of Eq. 2.28. That is, we assume a pure multiphoton absorption process as the only source of nonlinear loss, and free-carrier absorption and free-carrier dispersion are not included at first to simplify the analysis. As will be presented, these are reasonable assumptions

for the intensity range of most interest, up to 1.5 GW/cm^2. The validity of these assumptions at higher intensities will be discussed. Linear absorption in the E // c orientation is taken to be $\alpha_1 = 1.5$ cm^{-1}, whereas it assumed to be zero in for E $\perp$ c – a reasonable assumption given the estimation of $\alpha_1 \leq 0.1$ cm^{-1} has a negligible overall effect on the interaction over 5 mm crytsal length (Fig. 5.1(b)). Nonlinearities are assumed to be instantaneous. Ignoring a delayed Raman response is justified due to low frequency Raman modes in Te (3.7 THz) [118, 138] combined with a short pump pulse. Experimentally, we do not observe Stimulated Raman Scattering (SRS) sidebands with these short pulses. Since no seeded nonlinear processes are modeled, such as SRS, numerical noise is not included in the simulations.

Material dispersion is calculated with the Sellmeier equation found in Ref. [139]. Besides the large refractive indices, the group velocity dispersion (GVD) is rather large as well. At 10.3 μm, the GVD in tellurium is $k_{2,\perp} = 2100$ fs^2/mm and $k_{2,//} = 3200$ fs^2/mm. Tellurium stands out with germanium as some of the only transparent materials with positive group velocity dispersion (GVD) beyond 10 μm. In nonlinear propagation, the positive dispersion results in pulse spreading and intensity reduction in the presence of SPM, as opposed to compression and intensity increase that gives positive feedback to nonlinear effects in materials with negative GVD. Dispersion length for the two orientations for the nominal 220 fs pulse is $L_{D,\perp} = 8.3$ mm and $L_{D,//} = 5.5$ mm.

To model SPM experiments, the numerical pulse is propagated 5 mm and the resulting spectrum is integrated over the spatial profile of the beam to give total spectra energy density. In comparing these calculations and experiment, the experimental data has been frequency-shifted to compensate for the observed blue-shift; the blue-shift does not appear in simulations as we have considered a symmetric Gaussian pulse and no plasma dispersion at this point. We also perform a series of calculations varying the initial beam size to simulate the open aperture z-scan. Total energy throughput is found by integrating the resulting pulse over both time and radius for every initial spot size.

To find best-fit values of nonlinear coefficients, we scan a two-dimensional parameter space of $n_{2,eff}$ and α_M, with values from analytic z-scan analysis as starting points. Fitting is done by comparing the calculations to the experimental results, and finding the RMSE between the observables: spectral energy density and relative transmission. Total RMSE is added for both SPM

and NLA experiments (weighted equally) to realize a simultaneous best-fit for both $n_{2,eff}$ and α_M. This procedure is shown in Fig. 5.13 for E $\perp$ c, with points on the 2D grid representing normalized RMSE calculated for each pair of $n_{2,eff}$ and α_M. As is seen for SPM fitting (Fig. 5.13(a)), the best fitting $n_{2,eff}$ for a wide range of α_M is between 2-4 $\times 10^{-12}$ cm^2/W. Similarly, modeling the open aperture z-scan, Fig. 5.13(b) gives α_3 between 5-8 cm^3/GW^2 for the entire range of $n_{2,eff}$. When these sets of simulations are combined a unique global RMSE minimum is established (Fig. 5.13(c)). In this case, the error is minimized when $n_{2,eff} = 3 \pm 0.5 \times 10^{-12}$ cm^2/W and $\alpha_3 = 6 \pm 1$ cm^3/GW^2. Uncertainty is assigned based on the discretization of the scanned parameter space. The same fitting procedure is used for E // c, but there is relatively poor reproduction of the open aperture z-scan experiments. For completeness, best-fit parameters in this orientation are $n_{2,eff} = 5.5 \pm 0.5 \times 10^{-12}$ cm^2/W and $\alpha_3 = 6 \pm 1$ cm^3/GW^2.

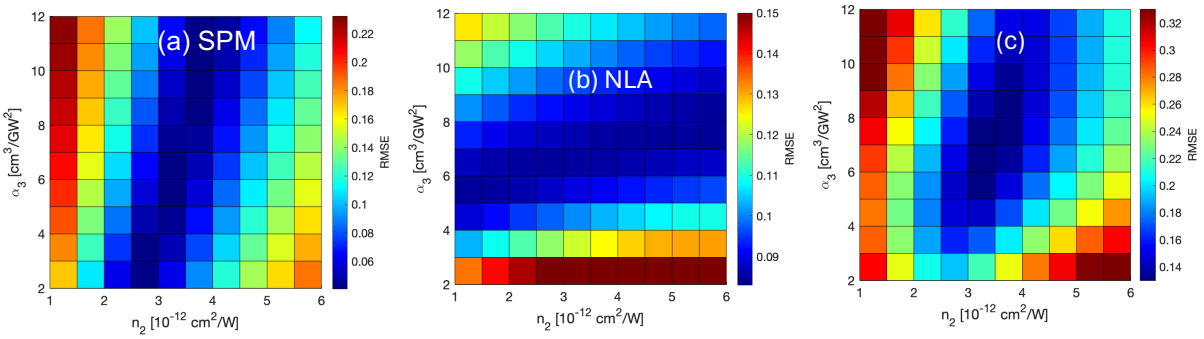

Figure 5.13: Fitting procedure for Te in the E $\perp$ c orientation. Plots show error between experimental measurements and numerical calculations for a 2D parameter space of $n_{2,eff}$ and α_3. (a) SPM measurement (b) open-aperture z-scan experiment (C) summed error of (a) and (b), resulting in a global minimum error. This is considered the best fit.

The best fit spectrum and z-scan for both orientations are overlaid on the experimental results in Fig. 5.14. The fit $n_{2,eff}$ values for both orientations are close to, but larger than those measured in the closed aperture z-scan experiment. This follows the prediction that the z-scan method provided only a lower limit of the nonlinearity. Good agreement is achieved for the SPM experiments, giving confidence in the $n_{2,eff}$ measurements. The open aperture z-scan measurements are also reproduced rather well for E $\perp$ c, especially at lower incident intensities. Numerical calculations nearly exactly overlap the MPA theory presented in Fig. 5.11, suggesting that propagation effects such as self-focusing and dispersion do not play a dominant role in our measurements. Similar to the MPA

theory, NLA measurements at high intensities in the perpendicular orientation and throughout the parallel orientation do not fit this model well, indicating onset of nonperturbative effects or more complex interactions with the band structure. For instance, the existence of the VB1 ↔ VB2 dipole moment in this orientation may enable near-resonant contributions or even effects such as quantum interference of interband transition pathways [140].

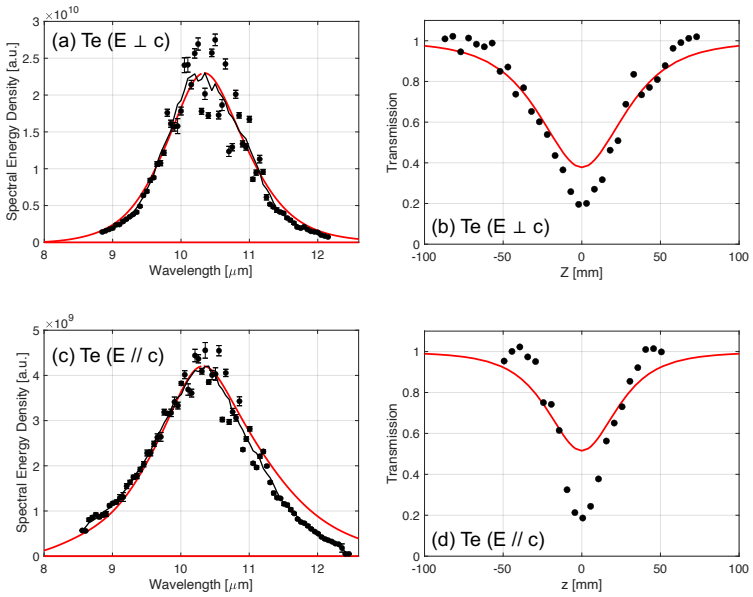

Figure 5.14: Results of best-fit modeling for tellurium (a) SPM (E ⊥ c) (b) NLA (E ⊥ c) (c) SPM (E // c) (d) NLA (E // c)

Besides the extraction of important nonlinear optical parameters in tellurium, we can also make some physics insights with the gNLSE modeling. In Fig. 5.15, certain pulse parameters are plotted as a function of propagation length of a 220 fs pulse at initial intensities (inside the crystal) of 1 and 2.5 GW/cm^2 in Te (E ⊥ c). The spot size $w_0 = 500$ μm is chosen for consistency. For both intensities, the peak B integral increases most rapidly at the front of the crystal, correlated with the initial nonlinear length of $L_{NL} = 550\mu$m for $I_0 = 1$ GW/cm^2, and 2.5x shorter for the higher intensity. The growth slows as propagation continues; comparing the B integral slopes for the two intensities shows that nonlinear phase shift is increasing at approximately the same rate. As this is a function of local intensity only, it is clear that the NLA and dispersion have caused a "clamping" of the peak intensity after about 2 mm of propagation. In addition, diminishing returns with respect to the nonlinear phase shift are obvious, where 2.5x higher initial intensity only gives 1.3x larger

B integral. This ratio is 1.8 at z = 0.5 mm and 1.6 at 1 mm. Bandwidth increase (integrated over the full beam) shows interesting dynamics in both cases, staying nearly constant over the first millimeter then rapidly increasing between 1 and 3 mm. The growth then slows, as the broadened frequency spectrum disperses, further lowering the intensity. These dynamics highlight the strong coupling between nonlinear and linear optical effects during nonlinear propagation of ultrafast MIR lasers in semiconductors.

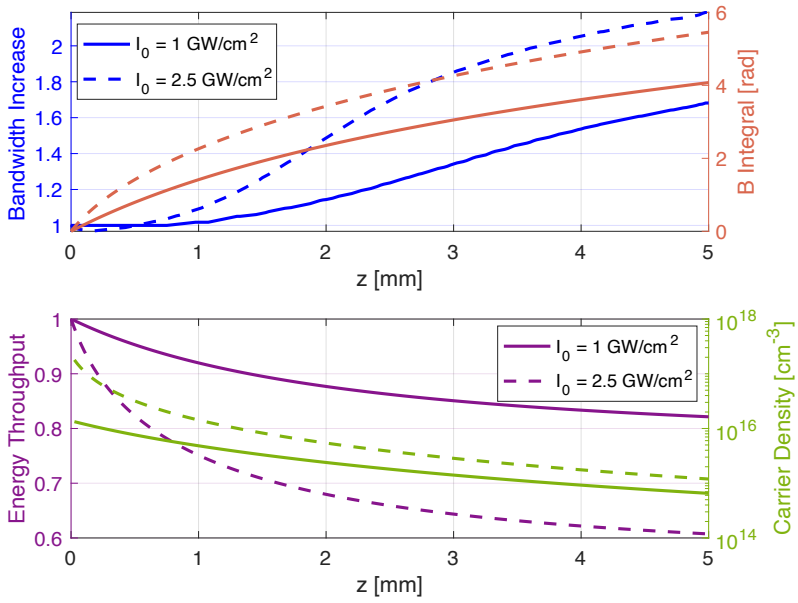

Figure 5.15: Diagnostic of various parameters as a function of propagation length modeling Te (E $\perp$ c).

Also shown are the total energy throughput and local peak electron-hole plasma density generated by 3PA. Especially for the higher intensity a significant portion of the total loss occurs within the first millimeter of propagation, naturally correlating with the highest plasma density. At 2.5 GW/cm^2 the peak plasma density is still more than 100x smaller than N_{cr} = 2.7 $\times 10^{19}$ cm^{-3} in Te. At higher intensities, plasma dispersion and FCA will become more important as photoexcited carrier densities get closer to N_{cr}.

Calculating length scaling of various observables helps assess the material as a candidate for nonlinear photonics applications. It is clear from this analysis that tellurium can be a very useful material at this intensity range if the sample were to be shortened, say to 0.5 mm or less. At this

distance, there is $\gtrsim 1$ rad nonlinear phase shift, but significant modification of spectral width, pulse energy, or beam shape have not yet occurred. sub-millimeter scale or even thin-film tellurium layers can achieve these goals in the MIR.

These enormously large values of $n_{2,eff}$ introduce a very small critical power for self-focusing, $P_{crit,\perp} = 11$ kW. Our laser pulses with 1 GW/cm^2 initial peak intensity have peak power 8 MW, for $P_0/P_{crit} = 710$. At this power level and spot size, the self-focusing length is 10 mm, close to the length of the sample. Increasing intensity to 2.5 GW/cm^2 brings the predicted self-focusing singularity essentially to the edge of the sample, $z_{SF} = 6.5$ mm. Tight focusing or collapse of the beam is not observed in the lab within a few millimeters of the sample - in fact there is little change in the beam size measured within 20 mm of the sample from the beam entering the crystal. Instead we see a more gradual nonlinear focus: a 1 mm radius beam at similar peak powers come to a tight focus at 200+ mm after the sample, 6x longer than predicted by Eq. 2.13.

A main reason for this contradiction is demonstrated in Fig. 5.16. Panel (a) shows the radial energy distribution during numerical propagation with the best fit nonlinear parameter. Initial peak intensity is 2.5 GW/cm^2. The intensity "clamping" discussed above is apparent here, with the strong NLA at the front of the sample reducing the peak intensity and causing the beam to become quasi-

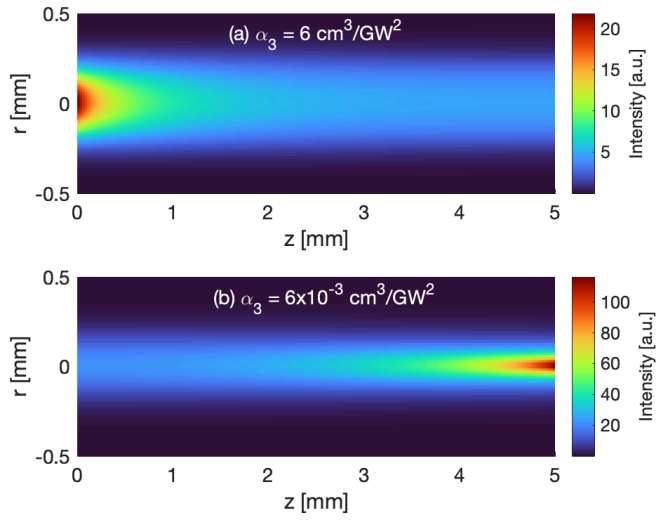

Figure 5.16: Self focusing in tellurium arrested by MPA. Slices at each z are the radial energy distribution, as if a camera integrating over time was detecting the beam. $w_0 = 180$ μm in both cases.

flat-top as opposed to Gaussian. This inhibits self-focusing in two ways. First, the significantly reduced peak intensity has a much weaker nonlinear interaction and phase shift. Second, the quasi-flat-top beam structure accumulates a flatter radial nonlinear phase distribution than a Gaussian beam. That is, the nonlinear phase appears less like a focusing lens and more like a constant phase delay across the flat-top portion of the beam. Plasma dispersion at high intensities will only further defocus the beam and extend the self-focusing length.

Contrast this to panel (b), which is the beam profile of an identical initial pulse interacting with Te which has had its 3PA coefficient decreased by a factor 10^{-3}. Here, self-focusing is the dominant nonlinear process affecting propagation, and the beam collapses at a distance much closer to the theoretical self-focusing length. Peak intensity at the exit face of the crystal is more than 5x higher than at the entrance face. From this analysis, we can see that NLA is the primary limiting factor in arresting ultrafast MIR self-focusing in narrow-gap semiconductors.

5.6.1 Keldysh Theory in Tellurium

The Keldysh parameter in Tellurium is plotted in Fig. 5.17(a). γ in both orientations is essentially identical, between 1.8 at 1 GW/cm^2 and 0.82 at 5 GW/cm^2, crossing 1 at 3.35 GW/cm^2. The nonperturbative intensity parameter, on the other hand, is $\gamma_{NP} = 0.2 - 1.0$ over this same range. Perturbative scaling of photoionization should hold for the lowest intensities, but may fail for higher intensities near 5 GW/cm^2. This may be one explanation of the poor fitting at $I_0 \approx 5$ GW/cm^2 in the E $\perp$ c orientation. This represents a fundamentally different intensity regime than in GaAs and n-Ge.

In Fig. 5.17(b), we plot the Keldysh photoionization rate for both orientations as well as the MPA ionization rates in the E $\perp$ c orientation from gNLSE modeling: $w_{MPA}(I) = \alpha_M I^M / M\hbar\omega_0$. While the Keldysh and numerical ionization rates do not match exactly, they are rather close in the intensity range where the experimental values fit best, I = 1-3 GW/cm^2. Uncertainty in carrier effective mass (theory assumes parabolic bands) adds uncertainty to the theoretical ionization rate. Comparing the two orientations' theoretical ionization rates, E // c has a significantly lower rate for all intensities below 1.35 GW/cm^2, after which the ionization rates nearly match. This is due to channel closing of 3PA near 0.8 GW/cm^2, when the effective band gap has increased such that

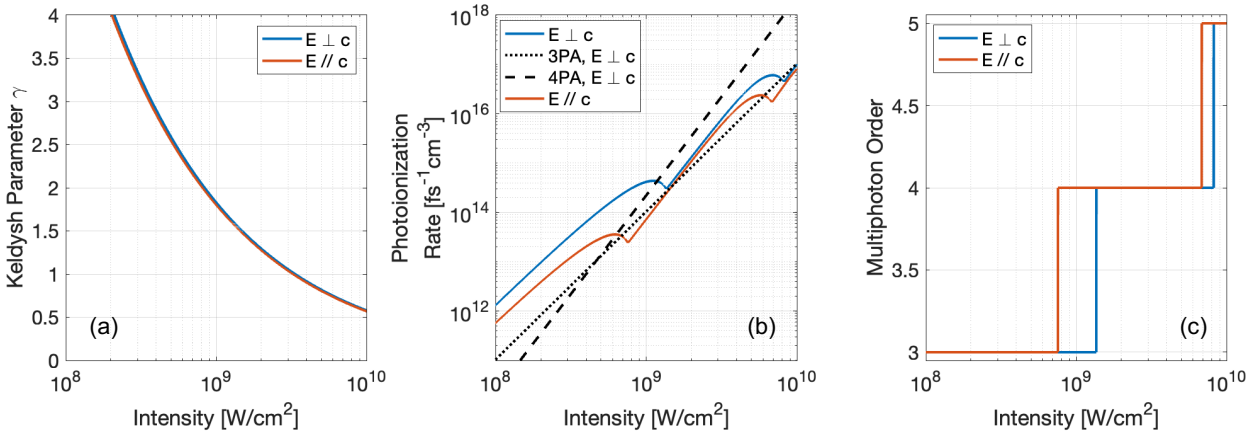

Figure 5.17: (a) Keldysh parameter in Te (b) Theoretical photoionization rate in Te. Best-fit multiphoton rates in E ⊥ c are overimposed for 3PA and 4PA. (c) Effective band gap increases causes channel closing and dynamic increase of the multiphoton order.

4 photons are required to span the gap (Fig. 5.17(c)). This behavior of relative ionization rates may partially explain the experimentally reduced NLA in E // c below 1 GW/cm^2, but strong absorption at higher intensities.

5.6.2 Free-carrier Effects in Tellurium

With the extended discussion of photoionization and electron-hole plasma generation in tellurium, the free-carrier effects must be addressed. As has been discussed, high intensity mid-infrared laser fields couple very strongly to free carriers in a semiconductor. This highly dynamic linear and nonlinear free carrier response (FCR) can have a strong impact on pulse propagation.

The FCR can be difficult to treat properly with only the gNLSE in the form we have implemented it. Additionally, details of the band structure/Brillouin zone in which the electrons and holes exist are distilled to a simplified effective mass/parabolic approximation and the free carrier distributions are treated like classical plasmas without any quantum mechanical effects included, such as electron-hole correlations or Pauli-blocking from filled density of states. Despite these limitations, we can still make some insights into the impact of free carrier interactions in our experiments.

FCA cross sections are not known in Te, however a stark difference between the two orientations should be expected. In the semiconductors we study, the strongest FCA is caused by intervalence band hole transitions, which have a large cross section in the MIR (though this can saturate at

relatively low intensities). These are a resonant in Te (E // c) but forbidden in Te (E $\perp$ c), leaving only weaker FCA from intraband scattering processes. In the E $\perp$ c orientation, σ_{fca} was estimated to be 5×10^{-17} cm^2 in the context of nondegenerate 2PA during second harmonic generation [141].

When we repeat the numerical modeling of SPM and NLA experiments in Te including FCA in the gNLSE, spectral broadening changes negligibly at 1.5 GW/cm^2 and the transmission change in the open aperture z-scan change only by a small fraction. Even with local peak carrier densities reaching close to 10^{18} cm^{-3}, these densities are only generated over very short lengths. It is possible that a much larger σ_{fca} would give reasonable agreement, but this requires mutual fitting of the MPA and FCA coefficients which is beyond the scope of the work. It is possible that Ohmic loss in electron-hole plasmas contributes an extra loss channel at the highest intensities/generated plasma densities, effectively increasing the FCA coefficient. Scattering rates are not well characterized in tellurium, especially under such nonequilibrium conditions, so it is not considered in this analysis.

To compare the relative importance of MPA and FCA, we can generalize the expression used in Chapter 4 to compute NLA coefficients to the case where both are relevant. Equating the effective absorption coefficients for the two processes gives:

$$\alpha_M I^{M-1} = \sigma_{fca} N = \sigma_{fca} \int_{-\infty}^{t_0} \frac{\alpha_M I^M}{M\hbar\omega_0} dt'. \tag{5.4}$$

Assuming a Gaussian pulse $I(t)$ with the peak of the pulse at $t = t_0$, this can be solved analytically to give the ratio

$$\frac{\alpha_{FCA}}{\alpha_{MPA}} = \frac{\sigma_{fca} I_0 \tau}{4M^{3/2}\hbar\omega_0} \sqrt{\frac{\pi}{\ln 2}}. \tag{5.5}$$

This expression is used to determine whether MPA or FCA dominates NLA for given pulse length and intensity. Since it does not depend on the MPA coefficient α_M, this becomes a kind of figure of merit that is broadly applicable to a range of materials and pulse parameters. The ratio is plotted in Fig. 5.18(a) for M = 3 and τ = 220 fs at 10.3 μm wavelength. Curves are overlaid tracing the contours for GaAs and Ge using their saturable FCA cross sections and Te (E $\perp$ c) using the predicted value from Ref. [141].

In Tellurium between 1 and 5 GW/cm^2 peak intensity, the ratio of effective NLA coefficients

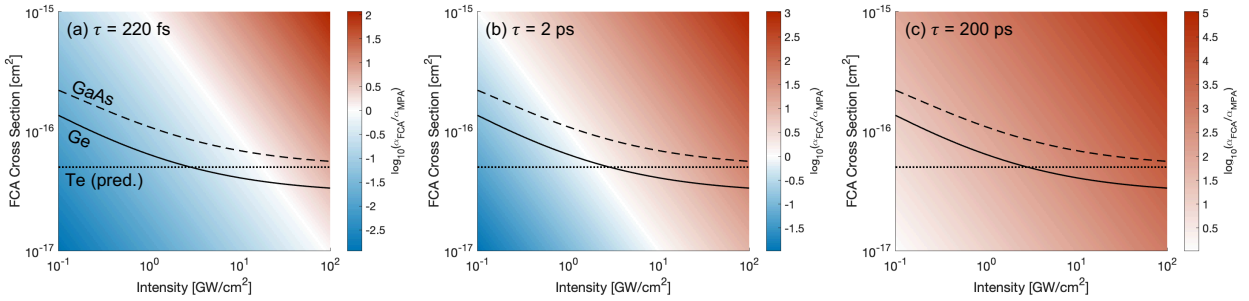

Figure 5.18: Ratio of α_{FCA} to α_{MPA} for different material and laser pulse parameters. Note the logarithmic scale of the colormap.

scales from $\frac{\alpha_{FCA}}{\alpha_{MPA}} = 0.06$ to 0.29 for sub-picosecond pulses, indicating that MPA is the dominant source of pulse energy loss. Even though 3PA is not the strictly correct intensity scaling for GaAs or n-Ge, the empirical scaling is similar (Table 5.2) such that this calculation gives a qualitatively correct answer. n-Ge has $\frac{\alpha_{FCA}}{\alpha_{MPA}}$ between 0.22 and 0.31 for 4-6 GW/cm^2. In contrast, for the range we observe NLA in GaAs, 10-18 GW/cm^2, the ratio is between 0.81 and 1.3 indicating that both MPA and FCA may contribute to the nonlinear loss. It is important to note that this ratio is calculated using peak pulse intensity at the center of the beam – Outer beam regions will experience a smaller ratio. Furthermore, as NLA and other propagation effects modify the temporal pulse profile and spatial beam profile, this ratio dynamically changes.

Fig. 5.18(b) plots $\frac{\alpha_{FCA}}{\alpha_{MPA}}$ for 2 ps pulses in the 3PA regime (results are qualitatively the same for different MPA orders). These plots reinforce how critical the free carrier nonlinear response is to the NLA and overall nonlinear response of semiconductors in the mid-infrared. Once MIR pulse lengths are longer than a few picoseconds, FCA becomes the dominant source of nonlinear energy loss in all semiconductors above intensities of ~ 1 GW/cm^2. This only becomes more apparent for longer pulses such as the 200 ps pulse length result shown in Fig. 5.18(c), where even down to a few 100s MW/cm^2 intensity the FCA is orders of magnitude stronger than MPA. This supports the interpretation of NLA using 200 ps pulses we arrived to in the previous chapter.

The free carrier response includes refraction in addition to absorption. We revisit the critical intensity derived in Eq. 2.30 and apply it to the case of tellurium, where perturbative MPA nominally holds. Free carrier dispersion must be considered when intensities of 4.2 GW/cm^2 and 4.8 GW/cm^2 are reached in the perpendicular and parallel orientations, respectively, at 10.3 μm. This

justifies the simplifying assumption to not include free carrier dispersion in previous modeling, particularly at intensities used in SPM measurements ($\leq$ 1.5 GW/cm^2). The highest intensities used for NLA measurements may not be immune of free carrier dispersion, however, another possible reason behind poor fitting of modeling and analytics at the highest intensities.

To demonstrate the specific effects free carrier dispersion and absorption have on nonlinear propagation in tellurium, we compare numerical simulations with the FCR (Eq. 2.24) turned off and on. These comparisons are presented in Fig. 5.19 for 220 fs 10.3 μm laser pulses at initial intensities of I_0 = (a) 1.5, (b) 3.0, and (c) 4.5 GW/cm^2. Initial beam radius is 500 μm for consistency, and propagation length is 5 mm to match experiment. $n_{2,eff}$ and α_3 are taken from the best fit in Te with E $\perp$ c. In panels (i) and (ii), which show $I(t, r)$ and spectral energy density after 5 mm of propagation respectively, the upper half of the plot is the result with no free carrier response, whereas the bottom half of the plot is the result with free carrier dispersion and absorption included. Note that for these figures, the pulse propagates from negative time to the right toward positive time.

In both time and spectrum, the free carrier response has a small overall effect for I_0 = 1.5 GW/cm^2 (the intensity at which SPM measurements were made). The pulse in time looks similar across the beam, and a very slight blue shift at the center of the beam is observed. This correlates with the integrated spectrum (iii), which has a wavelength centroid shifted only $\sim$ 0.5% with FCR, supporting the assertion that the experimental blue shifts we find in the broadened spectra are mainly associated with the asymmetric temporal pump pulse shape.

When intensity is doubled to 3 GW/cm^2, the plasma effects become more apparent. The onset of free carrier effects around this input intensity correlates with the critical intensities estimated above. The total blue shift of the spectrum in the presence of free carrier interactions is stronger. In addition, the ionization blue shift at the center of the beam is strong enough such that the central portion of the beam is delayed in time due to high positive dispersion. This introduces complex spatio-temporal [142] and spectral coupling.

Finally, with 4.5 GW/cm^2 peak intensity all of the same effects of the FCR have become even more pronounced, and the spatio-temporal and spectral couplings even more severe. It should be noted that the central region of the beam where plasma refraction is highest also experiences

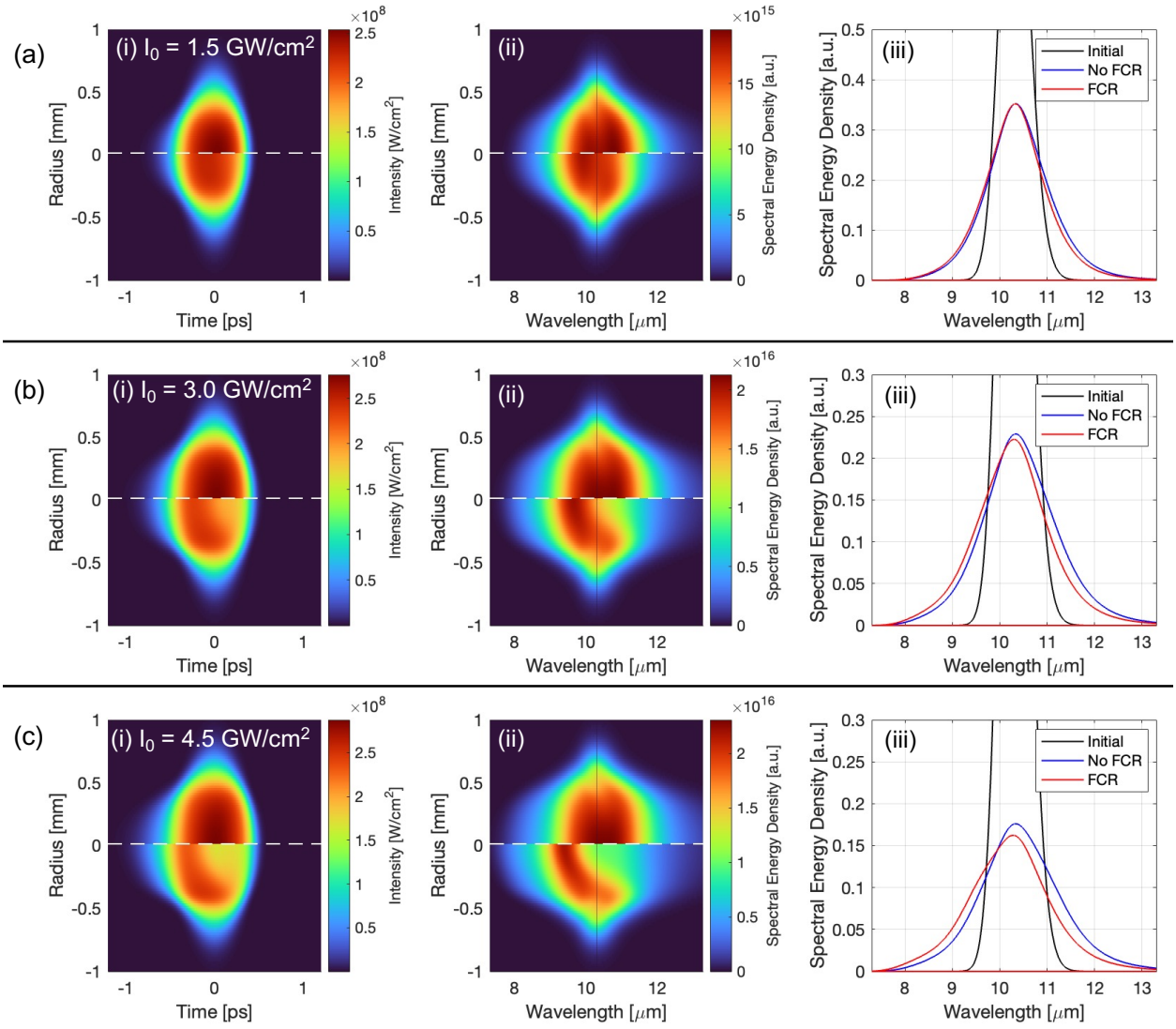

Figure 5.19: Comparison of nonlinear propagation of 220 fs 10.3 μm pulse in 5 mm of Te (E $\perp$ c) with and without the free carrier response (FCR). (i) Temporal profile along the beam $I(t,r)$ (ii) Spectral energy density along the beam E_λ(λ,r) (iii) Integrated spectral energy density.

defocusing after leaving the sample, only causing further distortions as beam the propagates.

The free carrier response also scales strongly with initial pulse length. The same simulations are presented in Fig. 5.20 for a 1 ps incident pulse length at $I_0 = 3$ GW/cm^2. All of the observables associated with the FCR are greatly enhanced, including spatio-temporal coupling, blue shift at the center of the beam, and a large blue shoulder in the integrated spectral energy density.

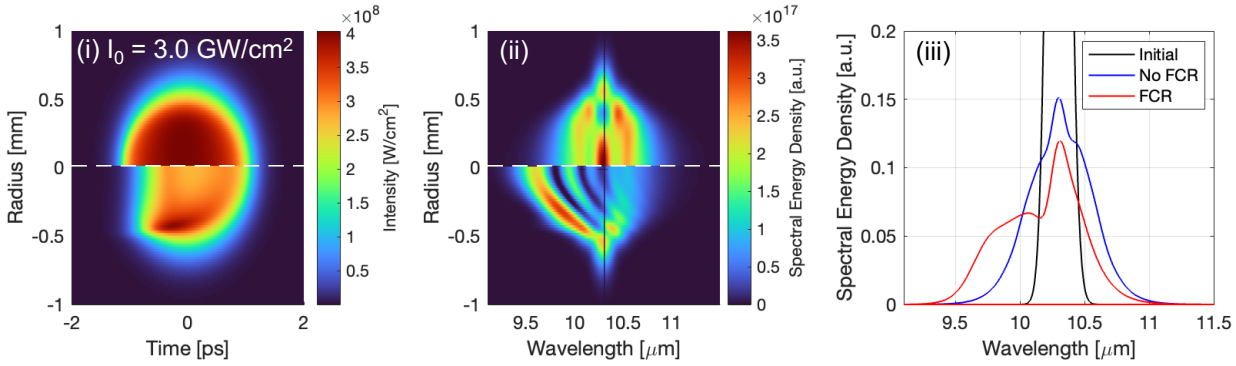

Figure 5.20: Same as Fig 5.19(b), but with a 1 ps pump pulse duration.

5.7 Summary of Results

We present a summary of our study of nonlinear properties in tellurium in Table 5.3. The figure of merit (FOM) for all optical switching devices (Eq. 2.19) is presented as well. Due to the multiphoton nature of the absorption, the FOM will depend on intensity, and will drop at low intensity due to linear absorption ($\alpha_1 = 0.1$ cm^{-1} taken for E $\perp$ c). The value given in the table represents the intensity range at which FOM > 1. The high intensity (10s of GW/cm^2) FOM is deceptive though, as the free carrier response and nonperturbative effects can take hold far before this. A more practical upper edge of usefulness is critical intensity discussed above ($\gtrsim$4 GW/cm^2).

	$n_{2,eff}$ [10^{-12} cm^2/W]	α_3 (z-scan) [cm^3/GW^2]	α_3 (fixed z) [cm^3/GW^2]	FOM Intensity [GW/cm^2]	FOM at 1 GW/cm^2
Te (E $\perp$ c)	3.0 $\pm$ 0.5	6 $\pm$ 1	10	0.034 $<$ I $<$ 49	18
Te, (E // c)	5.5 $\pm$ 0.5	6 $\pm$ 1	15	0.29 $<$ I $<$ 51	3.2

Table 5.3: Summary of nonlinear optical measurements and modeling in tellurium. For calculation of FOM, α_3 is taken from the z-scan for E $\perp$ c and the average of the z-scan and fixed-z measurements for E // c.

The $n_{2,eff}$ predictions presented in (Table 2.1) turn out to be accurate in tellurium, at least to the order of magnitude. The two band model [17] predicts $n_2 = 9 \times 10^{-12}$ cm^2/W in both orientations, a factor of 2-3 higher than what we measure. Meanwhile, the heuristic Miller's theory predicts $n_{2,\perp} = 1.1 \times 10^{-12}$ cm^2/W and $n_{2,//} = 9 \times 10^{-12}$ cm^2/W, both within 3x of the measurements. These models show reasonably good predictiveness, even for the extremely nonlinear Te.

The giant nonlinearity observed in tellurium, one of the largest known in a bulk material,

raises the question of how large the nonresonant Kerr nonlinearity can be in solids. Engineered structures, such as quantum wells [143], 2D materials [144, 145] or metamaterials [146], boast giant optical nonlinearities on the order of $|n_2| \sim 10^{-10}$ cm^2/W or higher due to electron confinement and/or field enhancement. However, because of the resonant or near-resonant character of these nonlinearities, they are associated with high linear absorption, saturate at extremely low intensities ($I_s < 1$ MW/cm^2), may be accessible only over in a narrow spectral region, and may have slow ($>$ ns) recovery times. For instance, a GaAs/AlGaAs multiple quantum well structure (MQW) has been measured to have a remarkably large $n_2 = 2 \times 10^{-4}$ cm^2/W but saturate at a paltry $I_s = 600$ W/cm^2 [147]. While this parameter space is highly useful for laser pulses with very low peak power or cw lasers, they are not practical for high-power ultrafast laser pulses of interest in this dissertation.

Another set of materials with near zero refractive index (epsilon-near-zero, ENZ) have been shown to exhibit enhancement of the nonlinearity [148] as well as nonperturbative scaling of the total refractive index as a function of intensity [149] (reminiscent of the controversial higher-order Kerr effect [150]). These properties arise largely due to plasmonic effects and the assumption of $n_2 I \ll n_0$ being broken.

Keeping the focus on nonresonant bulk materials and bound electron nonlinearities, we can make a more direct comparison to the measurements in tellurium. According to the two-band model, bound electron nonlinearities can theoretically take any value if the band gap is small enough. As E_g shrinks, NLA strength correspondingly increases - this trade-off is fundamental. While the nonlinearity might be extremely large, strong NLA even at low intensities (and the plasma it produces) can totally dominate the overall material response [151].

In order to maintain the same band gap scaling, the ratio $\hbar\omega_0/E_g$ should be maintained. Increasing laser wavelength in a constant ratio to the reduction of E_g only further increases photoionization rate, as the Keldysh parameter is reduced into the tunneling regime. In addition, longer wavelengths are absorbed and interact much more strongly with plasmas. As an ultimate limit, when very high carrier densities are achieved, the semiconductor becomes degenerate and acts like a metal, breaking many of our previous assumptions. Under this line of thinking the nonresonant bound electron nonlinearity is unlimited. However, the practical effects of extreme nonlinearities are limited by non-

linear absorption and plasma generation before giant nonlinear phase shifts can be accumulated, even for few cycle pulses.

A comparison between Te and the even narrower-gap semiconductor InSb ($E_g = 0.17$ eV) is apt to demonstrate this. Around 10 μm, the bound electron nonlinearity of InSb is predicted to be 1×10^{-10} cm^2/W [152], about 30x larger than what we measure in Te. However, it suffers from massive multiphoton absorption loss: $\alpha_2 = 3 \times 10^3$ cm/GW and $\alpha_3 = 2.5 \times 10^4$ cm^3/GW^2 (measured in an n-type sample with shifted band gap [151]), orders of magnitude larger than Te. Comparing the FOM with 2PA in InSb, Te provides better operation at 10.3 μm in the range 0.1–15 GW/cm^2 despite the smaller n_2. In fact, for InSb to match the tellurium FOM at 1 GW/cm^2, $n_{2,\mathrm{InSb}}$ must be 6x larger still. When 3PA is considered in InSb, Te has a larger FOM for *all* intensities above 40 MW/cm^2, and $n_{2,\mathrm{InSb}}$ would have to be a remarkable 450x larger to match at 1 GW/cm^2. Much of these are moot points when the intensity for free carrier dispersion to become significant (Eq. 2.30) is considered; with these parameters $I_{FC,2PA} < 300$ MW/cm^2 and $I_{FC,3PA} < 100$ MW/cm^2, (40x smaller than in Te). Detrimental free carrier effects can essentially never be decoupled from the nonlinear response of InSb at long wavelength. Comparison of Te and InAs (E$_g$ = 0.35 eV, $n_{2,eff}$ = 6.2×10^{-13} cm^2/W [33], α_3 = 1000 cm^3/GW^2 [135]) yields very similar results for both FOM and I_{FC} relative to Te. Based on these comparisons, it is clear that Te has a unique combination of giant nonlinearity, but also low enough NLA to be viable in applications with high power MIR lasers. With this in mind, we postulate that the maximum usable nonresonant MIR nonlinearity in semiconductors at high power is near what we measure in Tellurium.

Besides the first known measurement of nonlinear refraction in tellurium, we have also shown that free carrier linear and nonlinear effects have a significant impact on the propagation of intense ultrafast mid-infrared laser pulses. This is true in GaAs and n-Ge as well, but to a lesser extent. While effects are largely detrimental to photonics applications, giant nonlinearity of tellurium allows for thin samples ($\ll$ 1 mm) or much lower intensities ($<$ 100 MW/cm^2 in E $\perp$ c) that can still provide significant phase shift without the same detrimental processes. This reduces power requirements for future MIR photonics devices, and opens opportunities for thin-film nonlinear optical switches and devices based on Te. Furthermore, we have demonstrated that multi-dimensional modeling is a necessity to accurately describe ultrafast mid-infrared laser propagation and interac-

tions in semiconductors, as there is complex coupling between spatial beam distributions, nonlinear refraction, nonlinear absorption, dispersion, and free carrier dynamics.

Chapter 6
Mid-Infrared Photonics Applications

An important aspect of studying mid-infrared nonlinear optics is not only the characterization of materials, but also the development of real photonic devices to generate and manipulate MIR light at high peak intensity and peak power. In this chapter, we will present two different MIR photonics studies using the laser pulses and materials introduced thus far in the dissertation: second harmonic generation (SHG) of picosecond CO_2 laser pulses and all-optical semiconductor switching.

6.1 Efficient Second Harmonic Generation of a High-Power Picosecond CO_2 Laser

As previously discussed, wavelength scaling of nonlinear processes in gases and solids drives an interest in development of high-power short-pulse lasers in the mid-IR range [63]. At present, in the 4-5 μm range the most successful sources are optical parametric chirped pulse amplifiers (OPCPAs) pumped by 1 or 2 μm solid state lasers [15, 153]. Their development has enabled experimental demonstrations of mid-IR pumped high-harmonic generation [10], Kα X-ray production [154] and filamentation in air [155, 156]. However, mid-IR OPCPAs are rather complicated multistage systems that require a nontrivial energetic picosecond pump source.

An alternative to frequency down-conversion could be more straightforward (SHG) of a short 9-11 μm CO_2 laser pulse in a nonlinear crystal. With the goal of developing an energetic source operating in the 4.5–5.5 μm region, upconversion of a nanosecond TEA CO_2 laser in different materials has been studied extensively for decades. SHG was successfully accomplished in several quadratic nonlinear crystals, including $AgGaSe_2$ (AGSe), GaSe, $ZnGeP_2$, $CdGeAs_2$ (CGA), and Te with external energy conversion efficiency of $\geq$10% demonstrated [157–162]. For relatively long pulses on the order of 100 ns, the surface damage threshold limited pump intensities to $\leq$100 MW/cm^2. With the more recent emergence of picosecond duration, TW- [13, 163] and GW-class [164, 165] CO_2 lasers, much higher peak intensities are became available for nonlinear frequency conversion applications.

With this in mind, it is important to investigate if such picosecond CO_2 lasers are suitable for efficient SHG using nonlinear crystals. Taking into account the expected increase in the damage threshold by more than an order of magnitude due to a much shorter pulse length, SHG may ultimately become an attractive method to generate 4-5 μm GW power radiation pulses. However, no systematic study on frequency up-conversion of picosecond 10 μm pulses has been reported, and it remains to be seen how detrimental effects such as nonlinear absorption and self-focusing may impact the nonlinear conversion.

A schematic of the experimental setup is given in Fig. 6.1(a). SHG is performed using the 3.5 picosecond CO_2 laser system at 10.6 μm described in Chapter 3. The high-pressure CO_2 amplifiers generate picosecond pulse trains (pulse separation 18.5 ps) as shown in Fig. 6.1(b). A 152 mm focal length OAP focuses the beam after final amplification to a spot size of $w_0 = 72$ μm in the air. In this $f/6$ geometry, the laser reaches high enough intensity to optically breakdown the air, generating a plasma which screens the later parts of the pulse via a combination of refraction, reflection, and absorption. The goal of using such a plasma shutter was to reduce the duration of the incident pulse and therefore increase the 10 μm pump intensity and conversion efficiency. Indeed, the avalanche-ionized air plasma with electron density of 10^{18} – 10^{19} cm^{-3} effectively screened a significant portion of the pulse train. These ionization dynamics have been spatially and temporally characterized in another work [166].

The temporal pulse profile after the plasma shutter is shown in Fig. 6.1(c) as measured with a streak camera. The temporal resolution used here was sufficient to resolve 18.5 ps pulse separation, but not the exact duration of the individual 3.5 ps pulses. The pulse train transmitted through the plasma is recollimated by a short focal length ZnSe lens, which also largely compensates for plasma defocusing. On a typical shot, it contained the first 4-6 pulses, of which the most energetic pulse contained approximately 25% of the remaining energy.

A half-waveplate (if necessary) followed by an uncoated n-Ge plate at Brewster angle was used to provide clean S- or P-polarization to the nonlinear crystal, as required by phase matching conditions. The main focusing element is a 50 cm focal length ZnSe lens, giving a spot size of approximately w_0 = 0.45 mm on the crystal surface. In addition, an iris blocked light refracted from the plasma that could not be fully collimated and focused by the lenses. The pump energy at the interaction point,

up to ∼7 mJ, was measured by sampling the beam after recollimation with a NaCl beam splitter and a calibrated calorimeter.

The nonlinear crystals were again placed slightly after the focus to mitigate Kerr self-focusing. Two filters, 5 mm each of uncoated LiF and MgF_2 were placed after the crystal to absorb 10.6 μm pump light and pass 5.3 μm SH light. Absorption coefficients of both these materials at 10.6 μm are about 30 cm^{-1} [167], giving a theoretical attenuation of $> 10^{10}$, whereas the 5.3 μm attenuation is chiefly from Fresnel reflection, amounting to only 7.5% loss. The SH pulse energy was then measured by a calibrated calorimeter. A pyroelectric camera and streak camera (with requisite up-conversion as described in Section 3.1.2) are also used.

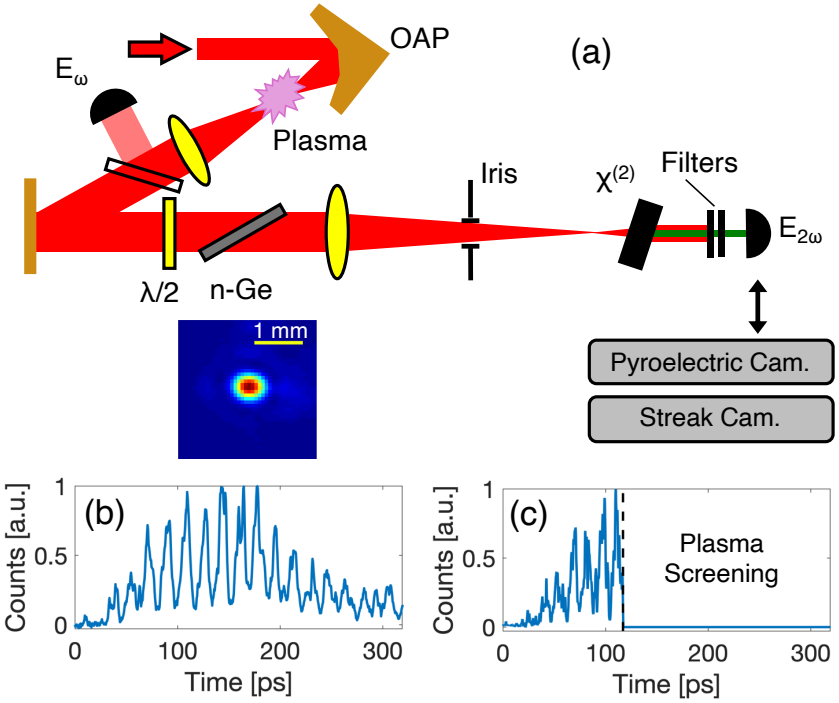

Figure 6.1: Schematic of the experimental setup. E_ω and $E_{2\omega}$ are energy detectors for pump and SH light, respectively. The SH energy detector could be swapped out with a pyroelectric camera to measure beam profiles or a streak camera setup to measure temporal profiles. (b) and (c) plot the measured temporal pulse structure before and after the plasma, respectively.

The crystals we study in this experiment and their relevant parameters are given in Table 6.1. We decided to revisit two materials with the highest $\chi^{(2)}$ nonlinearity – $CdGeAs_2$ and Te – as well as two other widely used MIR crystals $AgGaSe_2$. Despite being one of the most prominently known materials for CO_2 laser light upconversion, $ZnGeP_2$ was not used, as it has significant linear

absorption past 10 μm [168]. All of the crystals were used for type I phase matching, and only CGA was AR coated. The quasi-static length, aperture length, and Rayleigh length ($z_R = 4.5$ cm) were longer than the crystal for all samples [21]. Two-photon absorption is small at the 10.6 μm pump wavelength in all of these materials, however 3PA will arise in Te.

AGSe, CGA, and Te were cut at the phase-matching angle, and required only fine tuning of the external angle to achieve the highest conversion efficiency. GaSe, a layered crystal, cannot be cut and thus was phase matched via an external angle of 41°. During SHG measurements, the crystals were translated transversely to find the best pump throughput and SHG efficiency. All crystals were kept at room temperature throughout the experiment. No effort was made to optimize the crystal lengths, using just what we had available.

	Dimensions [mm]	Phase-matching	$\theta_{\rm pm}$ [Deg]	$d_{\rm max}$ [pm/V]	$d_{\rm eff}$ [pm/V]	FOM $d_{\rm eff}^2/n_\omega^2 n_{2\omega}$	Transparency [μm]
Te	10x10x5	*eeo* (Pos.)	14	$d_{11} = 600$	560	2800	4.0–32
CGA	6x6x7	*eeo* (Pos.)	33	$d_{36} = 282$	260	1300	2.5–18
GaSe	⌀10x7	*ooe* (Neg.)	14	$d_{22} = 54$	52	140	0.62–20
AGSe	10x10x14.4	*ooe* (Neg.)	55	$d_{36} = 33$	27	43	0.71–19

Table 6.1: Parameters of crystals used in the experiments. Values of the nonlinear optical coefficient d and transparency windows are taken from Ref. [21] Transparency ranges of CGA and Te are those of the samples used in this experiment, measured by FTIR interferometry. The Te sample used here is Sample 1 from Fig. 5.1.

In Fig. 6.2, we show the measured SH pulse energy in AGSe, GaSe, and CGA with the tuning angle set for maximum conversion efficiency plotted against total pump energy contained in the truncated pulse train incident on the crystal. Peak intensity (upper axis) is calculated inside the entrance face of the crystal (including Fresnel reflection) and assumes 25% of the total energy is contained in a single 3.5 ps pulse.

The most efficient SHG is found in AGSe, where at the highest pump intensities, up to 25 GW/cm^2, as much as 0.8 mJ of 5.3 μm light is generated. This corresponds to an average of ∼15% external energy conversion efficiency. On a single shot basis, the highest measured external conversion efficiency is over 20%. GaSe in contrast delivered a maximum of 0.3 mJ at 5.3 μm, with significantly lower conversion efficiency (∼5%). In both these crystals, it is apparent that the output

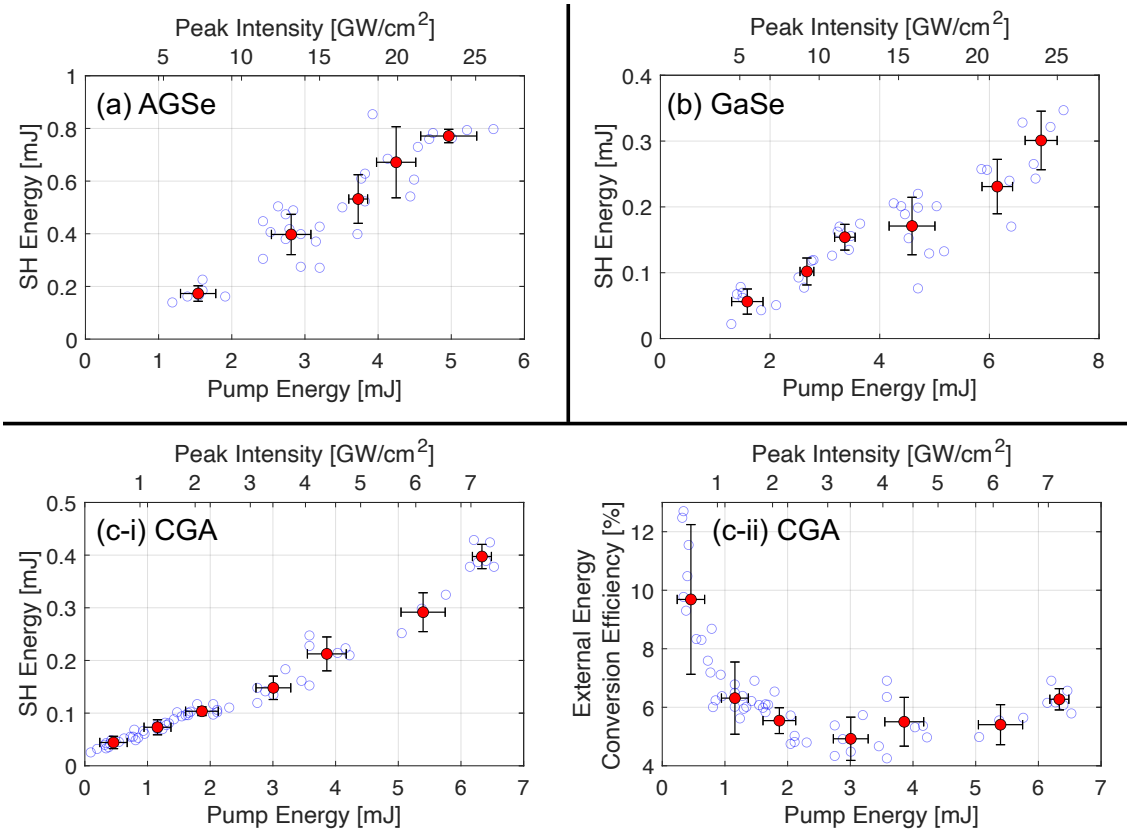

Figure 6.2: Data for second harmonic generation pumped with a picosecond 10.6 μm CO_2 laser. Peak intensity is calculated taking into account Fresnel reflection on the front surface of the crystal and the pulse train energy partitioning discussed in the text.

energies scale slower than the theoretical square dependence on the pump predicted for negligible pump depletion. Phase-matched conversion efficiency with pump depletion instead theoretically scales as

$$\eta_{SHG} = \frac{E_{2\omega}}{E_{\omega}} = \tanh^2\left(\frac{L}{L_{SHG}}\right) \tag{6.1}$$

where L_{SHG} is a normalized length scaling like $L_{SHG} \propto 1/d_{\text{eff}}\sqrt{I_1}$ [29]. 90% conversion efficiency is theoretically achieved at $L = 1.8L_{SHG}$. For both AGSe and GaSe, L_{SHG} is on the order of 1 mm even when averaged over the beam profile and temporal structure, such that the crystal length is several times longer than the nonlinear length. Despite this, conversion efficiency is much less than expected theoretically and there is no sign of back-conversion. Other high intensity nonlinear effects such as nonlinear absorption or self-focusing may be impacting the conversion efficiency. Note that

the efficiencies here can be increased in practice, as the measured pump fluence (<0.6 J/cm^2) is at least a factor of 2 below the surface damage threshold and proper AR coatings can be applied.

In CGA, the conversion efficiency tells a different story. Efficiency is near 10 % (external) at intensities below 1 GW/cm^2 (Fig. 6.2(c-ii)). This correlates with efficient 10 μm SHG observed previously in CGA at intensities up to ~500 MW/cm^2 [169]. However as intensity increases, the conversion efficiency is dramatically reduced, but increases again at the highest intensities used in experiment. Clearly there are some nonlinear dynamics in CGA which cannot be fully explained by simple conversion efficiency measurements.

Finally, negligibly small conversion efficiency, $< 1\%$, was found in tellurium. This completes the observed trend of higher d_{eff} and FOM resulting in lower efficiency SHG. This will be discussed further below.

Before this, we look closer at the most efficient measured SHG in AGSe. First, Fig. 6.3 shows the phase-matching tuning dependence. Dispersion is taken from [170]. The data are normalized to the maximum and fit with the regular phase mismatch dependence, $I_{2\omega} \propto a\,\text{sinc}^2(\Delta kL/2) + b$, with the amplitude a and vertical offset b allowed to vary. L is the crystal length, 14.4 mm. Based on the data and fit, two important features stand out. First, the 5.3 μm signal appears to be enhanced near perfect phase matching angle of $\sim 55°$ – given this, the fit shown in Fig. 6.3 excludes the three points with the highest energy. This apparent enhancement of the SH signal near perfect phase matching may be caused by a variety of effects, including increased contribution of phase matched sum frequency generation of different frequencies in the pulse [171] or multidimensional propagation effects related to self-focusing of the beam.

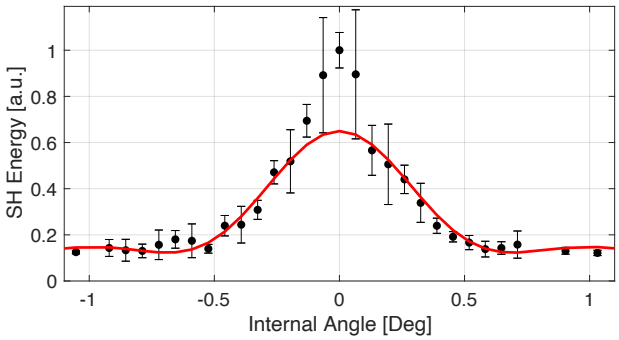

Figure 6.3: Phase matching curve measured in AGSe.

Next, there was a constant background around 10% of the peak at all angles we studied. Note that the background level dropped into the noise when the pump polarization was rotated 90°, indicating it was likely generated in the AGSe crystal itself. Spectral broadening due to SPM is likely the source of phase-matching in a wider range.

The SHG is also characterized in the space and time domains. Beam profiles (Fig. 6.4) were acquired 5 cm after the exit face of the crystal, for pulse energies near the maximum. The pump beam stayed round through the AGSe crystal (Fig. 6.4(a)), while the SH beam was generated with some elongated parts (Fig. 6.4(b)). In GaSe, the pump beam (Fig. 6.4(c)) was distorted during propagation, with the SH beam (Fig. 6.4(d)) nearly perfectly following the pump. In all cases, the lower intensity portions of the beam (including halo) did not efficiently generate SHG, as expected. The overall SH beam envelope and shape were relatively stable on a shot-to-shot basis in both crystals, indicating no long-term contribution of thermal lensing effects for short pulses, opposite to what was reported in a previous study in AGSe [168].

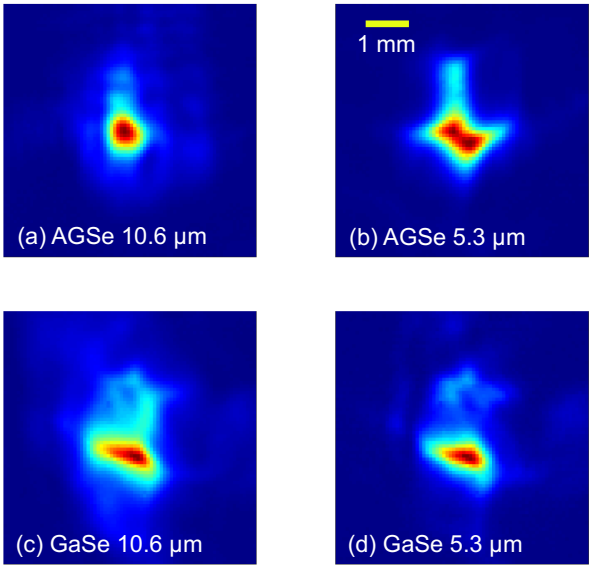

Figure 6.4: Beam profile of the (a,c) Pump beams and (b,d) SH beams after AGSe and GaSe crystals. Measurements are made near the peak pump energy, and color scales are normalized.

Beams of both wavelengths were transported to a picosecond streaking arrangement (Section 3.1.2) to perform temporal measurements after interacting with AGSe. As with beam profile measurements, temporal measurements for the two wavelengths were taken on different laser shots. To

isolate the pump wavelength, the polarization was rotated to destroy phase matching, but the 10.6 μm laser pulse still passed through the crystal.

Typical pulse trains are presented in Fig. 6.5. On a shot-to-shot basis, the SH pulse train showed variation in relative amplitude of the pulses, as well as pulse width. They also confirmed that a majority of the 5.3 μm energy is generated by the strongest pulse of the pulse train. As is apparent comparing Figs. 6.5(a) and (b). the SH pulses were shorter than the pump, implying the peak power conversion efficiency was much higher than the measured energy conversion efficiency. If we assume pulse shortening by a factor of $\sqrt{2}$ and the energy partition shown in Fig. 6.5(b), the strongest 5 μm pulse has a calculated peak power of 167 MW good for nearly 50% peak power conversion efficiency.

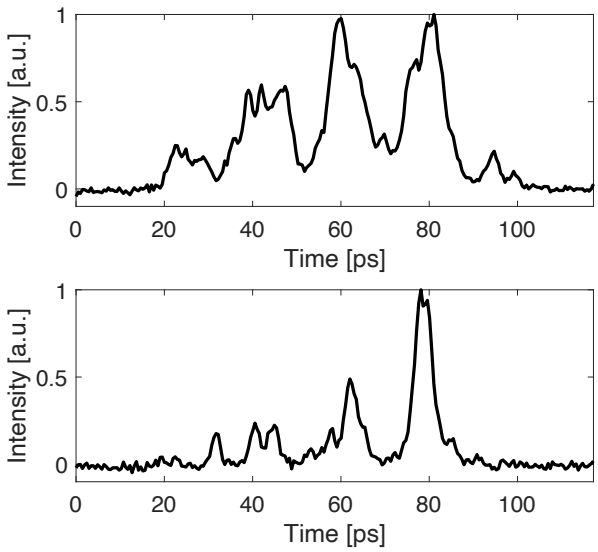

Figure 6.5: Temporal profile of (a) pump and (b) SH pulses after AGSe.

Finally, we return to CGA and Te samples with parameters specified in Table 6.1. Despite being champions of nonlinearity among all crystals, the SHG efficiency shows diminishing returns with intensity in CGA and is negligible in Te, with $< 1\%$ conversion efficiency detected. Linear absorption at the 11 μm intervalence band transition in Te is minimal in the phase matched orientation, confirmed by FTIR interferometry (Figure 5.1). A major factor in Te may be nonlinear absorption; we measured strong 3PA (Chapter 5) and any generated 5.3 μm light is above the photon energy threshold for both degenerate (5.3μm + 5.3 μm) and non-degenerate (5.3 μm + 10.6 μm) 2PA.

This has been observed to inhibit SHG efficiency even with nanosecond duration CO_2 lasers [141]. These results clearly indicated that the extremely large d_{eff}, and therefore FOM, of these materials (Table 6.1) cannot be fully taken advantage of at these high fields.

In fact, surprisingly, we see an exactly inverse relationship between $\chi^{(2)}$ (or FOM) and the effectiveness of the SH frequency conversion processes with short, intense CO_2 laser pulses. This is the second time in this dissertation we have found a deceptive FOM, with free carrier effects inhibiting nonlinear phase accumulation in tellurium (Section 5.7). The reason behind this in SHG is inextricable link between $\chi^{(2)}$, n_2, and the overall nonlinear optical response of semiconductors [48].

In Fig. 6.6, the pump beam is shown transmitted through Te at approximately 3 GW/cm^2 (a) and through CGA between 0.4-10 GW/cm^2 (b-d). Especially apparent in CGA, the pump beam shows a clear peak intensity (or peak power) dependence. At lower intensities (Fig. 6.6(b)) the beam is mostly unaffected. As the intensity is increased to 1.1 and 10 GW/cm^2, as shown in Figs 6.6(c) and 6.6(d) respectively, nonlinear propagation has clearly set in. This is likely a consequence of strong Kerr self-focusing combined with any resulting defocusing caused by plasma production. The temporal pulse structure also allows for cumulative effects (e.g. plasma formation) to grow, as we discussed in the context of NLA with 200 ps laser pulses (Chapter 4).

The square pattern that forms in CGA suggests that that the beam is trapped and guided by multiple total internal reflections ($\theta_c = 16^\circ$) off the transverse surfaces of the crystal. These patterns are relatively reproducible on laser shots with similar energy, and may even show onset of multifilamentation. As expected the SH beam from CGA (Fig. 6.6(e)) closely follows the pump beam pattern, as the beamlets have a significantly higher intensity than the beam as a whole. All together, these effects are detrimental for a continuous three-wave interaction over the entire length of the CGA crystal. The behavior of SHG conversion efficiency in Fig. 6.2(c) can also be explained with self-focusing in mind; as intensity/peak power increases, the beam begins to break up, limiting SHG conversion. However, at the highest intensities, intense beamlets form and can slowly increase the efficiency albeit with extremely complex spatial beam modes and complicated phase relationships.

Clearly strong higher order nonlinear effects like Kerr self-focusing limit the usefulness of CGA

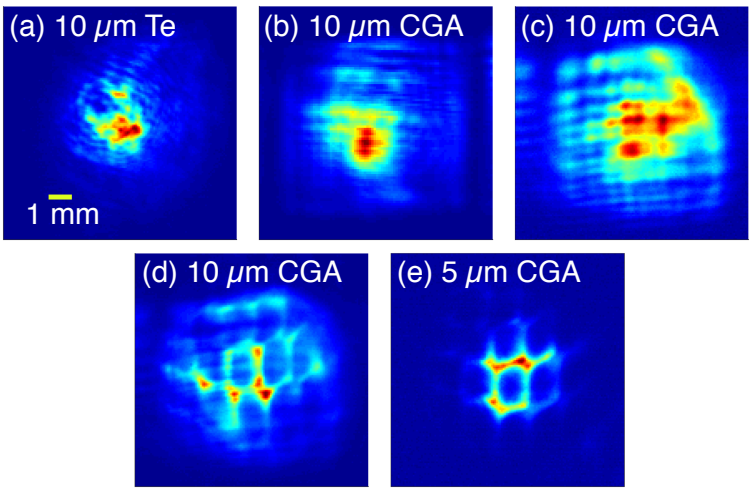

Figure 6.6: Pump beam profile measured 5 cm after the crystal after propagating through (a) 5 mm of Te at an approximate intensity of 3 GW/cm^2 (b)–(d) 7 mm of CGA at approximate intensities of (b) 0.4 GW/cm^2, (c) 1.1 GW/cm^2, (d) 10 GW/cm^2. (e) SH beam generated in CGA measured at the same position. The physical scale is the same for all of the images.

and Te as efficient SH generators for high-power picosecond CO_2 lasers. These effects over the sub-cm crystal lengths indicates (and confirms for the case of Te) that their third order nonlinearity are extremely large. We have measured $n_2 = 3 \times 10^{-12}$ cm^2/W in Te, whereas only one measurement of n_2 in CGA has been reported in the literature, to the best of our knowledge. Using third harmonic generation, n_2 values of 2×10^{-14} cm^2/W for the bound electron response and 4×10^{-13} cm^2/W for free carriers were measured [172]. As an aside, note that this bound electron nonlinearity measured in CGA is ∼100x smaller than that predicted by the two-band model [17], but only about 4x smaller than that predicted by the generalized Miller's rule [48]. Other ternary semiconductors such as AGSe (E_g = 1.1 eV) [173] and KD_2PO_4 (E_g = 7.1 eV) [17] have also been experimentally measured to have significantly lower n_2 than predicted by the two-band model.

Considering these extremely high n_2, the interactions in our experiment are carried out at peak powers that are between 100-20,000 times higher than the critical power for self-focusing in CGA and Te. At these power levels, the self-focusing length under the above experimental conditions can be anywhere between 2 cm and 1 mm, on the order of or shorter than the crystal lengths. The strong nonlinear optical response in both CGA and Te, coupled with their broad transparency ranges beyond 20 μm makes them good candidates for another very important nonlinear frequency conversion

process, supercontinuum generation throughout the MIR and beyond. Preliminary measurements of supercontinuum generation in Tellurium are presented in Appendix D.

To conclude this section, we have measured efficient SHG of a picosecond CO_2 laser in AGSe, GaSe, CGA, and Te. For high intensity pumps, however, it is clear that very large nonlinearities limit the SHG efficiency in both CGA and Te. Among the materials studied, AGSe in particular shows an ability to provide high peak power ($\geq$ 150 MW) and energetic ($>$ 0.8 mJ) laser source in the 4.5 - 5.5 μm spectral range in a technological way – and avoiding complicated OPCPA setups.

These high-power pulses could be used for a variety of strong-field experiments. For instance, the SH and pump light can be used together as a high-power two-color long-wavelength infrared laser source. A source such as this, which can still be improved by optimizing e.g. crystal lengths and AR coatings, may find applications in coherent control experiments, including extremely efficient generation of THz radiation in air plasmas excited by MIR light [174, 175].

6.2 All-Optical Mid-Infrared Semiconductor Switching

Semiconductor switching has been shown to be an important optical modulation technique for MIR laser systems. This operates by controlling the reflection and transmission properties of a normally MIR transparent semiconductor with an above-band gap laser pulse. If the fluence of this control pulse (typically in the near-infrared or visible) is high enough, it generates an electron-hole plasma above the critical plasma density ($\sim 10^{19}$ cm^{-3}) in a thin layer near the surface. This strongly modulates the dielectric constant, resulting in transient high reflectivity and absorption in the MIR. Reflectivity and transmission lifetimes are determined by various diffusion and carrier recombination processes.

Since the technique was first developed [176], semiconductor switching has been applied mostly to slice and modulate cw CO_2 lasers [177] or TEA CO_2 laser pulses ($\sim$100 ns duration) [178, 179] with maximum intensities below 100 MW/cm^2. Combining multiple switches together [180] or using semiconductors with fast carrier lifetimes [181] has resulted in sub-picosecond sliced 10.6 μm pulses.

Another major application is as a pulse selector in high-power CO_2 lasers. For example, the picosecond CO_2 laser systems at UCLA (Section 3.1.2) and Brookhaven National Lab use intracavity

or external reflective semiconductor switching to decouple from or dump a regenerative amplifier [13, 14]. In this way, semiconductor switching can fill a similar role as an electrically controlled Pockels cell. Pockels cell technology in the MIR, besides being limited to no faster than nanosecond response times and narrowband operation not suitable for sub-picosecond pulses, is difficult to scale and prohibitively expensive. This makes semiconductor switching a viable alternative with the potential for wide tunability. It should be noted that this technique has also been used in modulation applications for far-infrared and millimeter waves [182].

As briefly mentioned in Chapter 3, there is interest in developing an optically pumped high-pressure (>10 atm) CO_2 laser to amplify picosecond or sub-picosecond MIR seed pulses to the gigawatt level [57]. This is proposed as an alternative to OPCPA technologies, and also has the prospect of further amplification to reach terawatt-scale peak powers for use in high-field physics studies. An intracavity semiconductor switch can be used in this case to dump the short cavity of a regenerative amplifier, but with GW-scale pulses circulating it must have high damage threshold ($\geq$ 1 J/cm^2) and negligible optical losses in the LWIR. This limits the possible materials, with the standard n-Ge, GaAs, and ZnSe being ideal choices.

Optical quality n-Ge has been the semiconductor of choice in the past, but our observations of severe nonlinear absorption for short 10 μm laser pulses above 1 GW/cm^2 limit its usefulness as an intracavity element. Furthermore, as this is an accumulated effect, it becomes only more detrimental on successive round-trips in a short laser cavity. This is especially unfavorable for n-Ge, which is an indirect band gap semiconductor with long ($\geq$100 ns) carrier lifetime. Nonlinear absorption in GaAs and ZnSe is weaker.

Limited studies of semiconductor switching in the femtosecond regime have also revealed applications in ultrafast pulse reconstruction [183] and few-cycle pulse shaping [184], but there have been no systematic studies of different materials for MIR switching where both the control pulse and modulated pulse are ultrafast and high power.

Here we study semiconductor switching of sub-picosecond MIR pulses in n-Ge, GaAs, and ZnSe controlled by $\sim$30 fs pulses of a commercial ultrafast Ti:Sapphire laser. We measure switch efficiency as well as reflectivity time dynamics. We consider the specific application of an intracavity semiconductor switch, but the results are broadly applicable to mid-infrared modulators with different

functions.

6.2.1 Experimental Setup

We perform semiconductor switching using the Ti:Sapphire based laser system described in detail in Chapter 3. The MIR central wavelengths we use are between 10.5 and 14 μm, which have pulse energies between 10 μJ and 2 μJ in this setup, respectively. The control pulse is the deterministically synchronized ultrafast 800 nm laser pulse amplified to 5 mJ pulse energy. SPIDER measurements show 30 fs duration and a time-bandwidth product of 0.66 due to spectral broadening caused by self-phase modulation and dispersion passing through a beam splitter required for MIR pulse characterization. We characterize the 10.5 μm pulses with the MIR XFROG and retrieve $\sim$540 fs duration pulses and time bandwidth product of 1.0 (Fig. 3.7).

The materials we study are optical grade n-Ge, semi-insulating GaAs, and polycrystalline ZnSe with direct band gaps 0.80, 1.42, and 2.71 eV, respectively. They are all commercially procured. These three materials have extremely low linear absorption throughout the MIR ($\leq$0.01 cm^{-1} at 10.6 μm) and broad transmission ranges, making them ideal materials for MIR photonic devices. Two different control pulse wavelengths are used - the 800 nm pulse described above for controlling GaAs and n-Ge, and 400 nm to excite ZnSe due to its large band gap.

The semiconductor switching setup is shown in Fig. 6.7. The semiconductor is placed at Brewster's angle for the linearly polarized MIR pulse, which is focused to a $1/e^2$ radius of 0.9 mm on the surface using a 50 cm focal length copper mirror. Peak MIR intensity (in air) in the focus is 1.5 GW/cm^2 for a 10 μJ pulse. Reflected MIR light is analyzed by an HCT photodetector. The reflected signal is normalized to a reference HCT photodetector. In order to minimized depolarization of the MIR beam, we implement a thin film polarizer (n-Ge substrate). However, a perfect Brewster's angle is not achievable due to the rather broad laser bandwidth.

The 800 nm beam is unfocused and irised to a radius of 3.5 mm on the sample, giving beam shape that is close to flat-top. Peak absorbed 800 nm energy is no more than 2.3 mJ. Since the control laser is directed to the semiconductor at a small angle ($\sim$4.5°) from the MIR laser, fluence on the sample is reduced to a maximum absorbed 3.5 mJ/cm^2.

The 400 nm control pulse is generated using phase matched second harmonic generation in

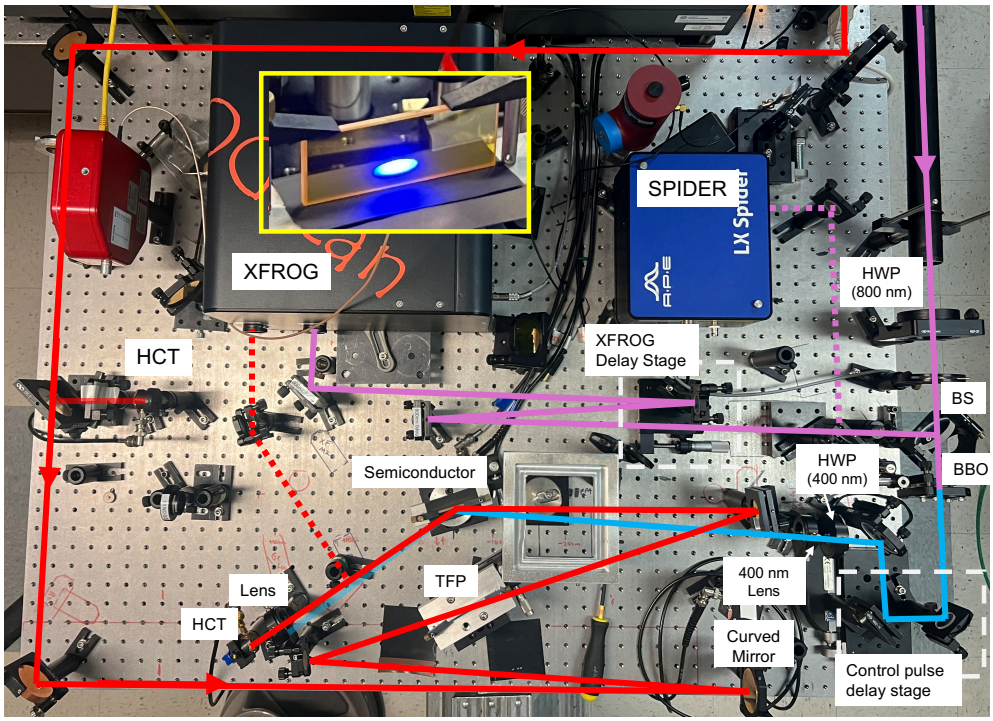

Figure 6.7: Experimental setup for MIR semiconductor switching measurements. Beams enter from upper right, Red = MIR, Pink = 800 nm, Blue = 400 nm. Thin-film polarizer (TFP) is used to clean MIR polarization before the semiconductor at Brewster's angle. SHG is used only for pumping ZnSe. Dashed beam lines indicate where drop-in mirrors are used. Inset: band-edge emission from photoexcited ZnSe at $\lambda \geq 457$ nm.

a 1 mm thick BBO crystal. 700 μJ of 400 nm light is used, which is focused to a spot size of approximately 2.4 mm on the sample for peak absorbed fluence of 2.9 mJ/cm^2. For both excitation wavelengths, a half-waveplate controls the laser polarization and thus the total balance between the absorbed and reflected fluence.

The large aspect ratio between the spatially overlapped control and MIR beams results in close to constant fluence across the entirety of the MIR beam. This allows for approximately constant reflection and robustness against pointing instability. A motorized translational stage is used to change the relative delay between control and MIR pulses with resolution better than 50 fs to study time dynamics of the semiconductor switch in a NIR pump-MIR probe measurement. Care is taken to block as much reflected and scattered control pulse light as possible to improve the signal to noise ratio for the MIR signal. The ultimate signal to noise ratio achieved is approximately 100:1.

The semiconductor samples are plates with similar dimensions and optically polished surfaces.

With up to 2 W absorbed laser power at 1 kHz and no additional cooling beyond convective cooling of the air and conductive cooling with the aluminum mount, the n-Ge and GaAs samples heat several 10s of degrees Celsius above room temperature. We did not carefully monitor the sample temperature, however we do not believe it plays a significant role in our observations.

6.2.2 Results and Discussion

A summary of our semiconductor switching measurements with MIR wavelength of 10.5 μm is given in Fig. 6.8. Figure 6.8(a) shows the peak reflectivity of the sub-picosecond 10.5 μm pulses from the three photoexcited semiconductors as a function of absorbed control pulse fluence. Measurements are performed with a calibrated power meter placed before and after the switch. Error bars are assigned based on the rms variation of the incident and reflected 10.5 μm power over a duration of 1 minute.

Over this range of fluences the reflectivity scales close to linearly, however some saturation is observed in n-Ge and ZnSe. Assuming linear absorption of the control pulse in a thin surface layer, the initial surface plasma density scales linearly with fluence, $N_s = \alpha_c F/\hbar\omega_c$, where α_c and $\hbar\omega_c$ are the absorption coefficient and photon energy of the control pulse. The critical plasma density, above which an ideal semi-infinite plasma will become fully reflective, is $N_{crit} = \varepsilon_0 m_r^* \omega_0^2 n_0^2/e^2$ (Section 2.1.10).

There is a clear hierarchy among the materials, with n-Ge demonstrating the highest reflectivity, followed by ZnSe and then GaAs. Broadly speaking, photon energy higher above the band gap will result in larger absorption coefficient, and thus a larger ratio of N_s/N_{crit}.

By changing the relative delay between the MIR and control pulses, we measure the lifetime of the switch reflectivity, presented in Fig. 6.8(b,c). In the time scans, each data point represents the average of approximately 150 individual laser shots. These scans were taken at the peak fluences in Fig. 6.8(a). Delay scans with time steps of 50 fs show a steady rise in reflection representing the cross-correlation of the sub-picosecond MIR pulse with the 30 fs control pulse.

For all samples, the empirical reflectivity lifetime can be approximated by an exponential curve of the form $R(t) = R(0)\exp(-t/\tau_r)$. The much longer time scale for n-Ge (τ_r = 310 ps) than in GaAs and ZnSe (17 ps and 55 ps) may derive from the long carrier lifetime associate with the

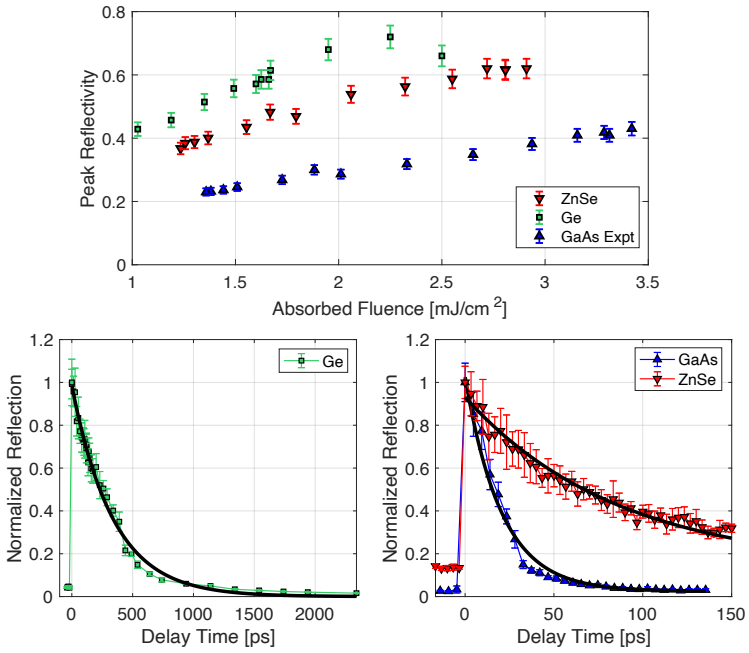

Figure 6.8: (a) Fluence dependence of peak 10.5 μm reflectivity for the three materials. (b-c) Pump-probe measurements of 10.5 μm reflectivity time dynamics, taken at the peak fluence in (a). Note the different time axes in (b) and (c).

indirect band gap.

To demonstrate the tunability of the semiconductor switching in novel regions of the MIR, we also investigate the reflectivity of different wavelengths from photoexcited GaAs. These measurements are presented in Fig. 6.9, where 12 μm is found to experience significantly more reflectivity than 10.5 μm, but the sample becomes less reflective for 14 μm. These results may be influenced by the strong wavelength scaling of both the critical plasma density ($N_{crit} \propto \lambda_0^{-2}$) and free carrier absorption (cross section $\sigma_{FCA} \propto \lambda_0^{1.5-3.5}$ depending on physical process [36]). The interplay between these effects, as well as the density, temperature, and MIR intensity dependence of the free carrier absorption require more detailed study and are beyond the scope of this work. To summarize, our measurements of peak reflectivity and reflectivity lifetime across all three semiconductors are given in Table 6.2. Note that the highest reflectivity $\sim 70\%$ for germanium correlates well with reflectivity measured earlier while using longer 3-200 ps glass laser pulses [185].

We also demonstrate the ability to perform ultrafast pulse shaping in Figure 6.10. With an n-Ge switch, we use the ultrafast cross-correlation capability of our XFROG diagnostic to control

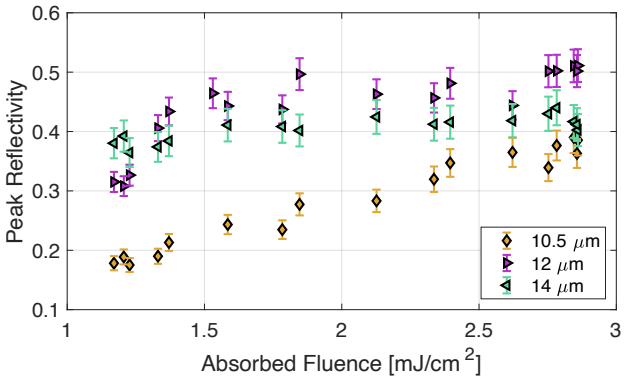

Figure 6.9: Fluence dependence of peak reflectivity at different MIR wavelengths in GaAs.

	$\hbar\omega_c/E_g$		**10.5 μm**	**12 μm**	**14 μm**
n-Ge	1.95	Peak Refl.	72%	80%	–
		Lifetime [ps]	310	480	–
GaAs	1.09	Peak Refl.	43%	52%	45%
		Lifetime [ps]	17	30	37
ZnSe	1.14	Peak Refl.	62%	–	41%
		Lifetime [ps]	55	–	52

Table 6.2: Summary of semiconductor switching results.

the pulse width of the reflected MIR light. The sliced pulse is obtained by overlapping the control and MIR pulses in time, with the 30 fs control pulse centered approximately at $t = 100$ fs. The rise time here is resolved, and found to be approximately 90 fs. This is close to the rise time of the cumulative integral of the control pulse fluence in time. Better compression (or a shorter switching pulse altogether) should improve the rise time and allow for sharper slicing.

The buildup time of the Drude plasma response, which allows us to treat the electron and hole

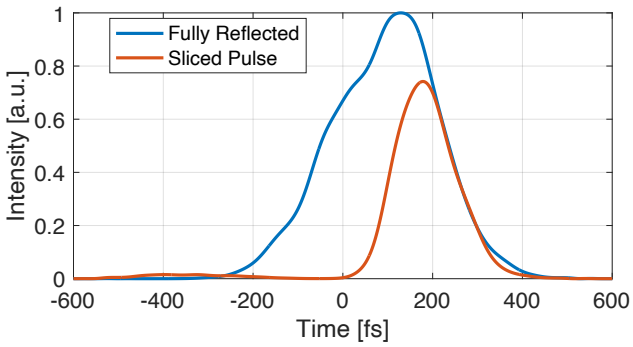

Figure 6.10: Cross correlation measurements demonstrating ultrafast MIR pulse slicing.

populations like a classical plasma with a collective response, is the ultimate limit of the slicing. This occurs on the timescale of the inverse plasma frequency, $2\pi/\omega_p$ [186]. For over-critical semiconductor plasmas required for high reflectivity, this is on the order of 10 fs or faster. This fast response gives potential for sub-cycle switching of MIR waveforms [184].

Modeling the peak reflectivity and lifetime of semiconductor switching can be done after making some simplifying assumptions. If we assume the above-band gap control pulse undergoes linear absorption, immediately after the energy is absorbed the plasma density is described by an inhomogeneous exponential decay from the peak at the surface: $N(z) = N_s \exp(-\alpha_c z)$. In a broadband control pulse, different frequency components will have varying degrees of absorption, complicating the plasma profile. Here, the absorption coefficient of the central wavelength (800 nm and 400 nm in our case) will be used as a simplifying approximation.

Because the above-band gap radiation can easily have absorption coefficients between $1 - 100 \times 10^3$ cm^{-1}, the absorption length $1/\alpha_c$ is between 100 nm and 10 μm. This short absorption length has two main effects. First, it causes extremely high plasma density, where $N_s \geq 10 N_{crit}$ for fluences measured in experiment. Also, the length of the plasma is on the order of or much shorter than the MIR wavelength in the crystal. In this thin plasma regime, high reflectivity is only found when surface density is much greater than the critical density, counter to the dielectric properties of a semi-infinite plasma.

Mid-infrared light reflection from such thin, exponentially decaying electron-hole plasma is modeled using the theory of Ref. [187]. There is a wide range of α_c present in the literature for our three materials, which may indicate differences in material properties from sample to sample, or overall uncertainty in the measurements. For our purposes, we will take absorption coefficients at the median of several experimental measurements. These are given in Table 6.3, with the corresponding surface plasma density at experimental fluences. Despite the higher absorption coefficient, the peak plasma density in ZnSe is lower as 400 nm excitation excites half the number of electron hole pairs per unit fluence compared to 800 nm excitation.

A problem arises under the assumptions made so far – limited density of states accessible in the conduction band. Since the control pulse is faster than the carrier thermalization time ($\sim$ 100 fs [191]), the population cannot redistribute and the linear interband absorption will saturate. As

an example, in the effective mass approximation (DOS $\propto (m_e^*)^{3/2}$) in GaAs or Ge for our 800 nm control pulse, the calculated saturated density from single photon absorption is approximately 6×10^{18} cm^{-3}. Clearly, this is below the critical plasma density and in a thin layer should not produce high reflectivity that we observe.

Since ultrafast control pulses are required for this to play a role, it has not been widely discussed in the semiconductor switching literature. A previous study with 18 fs control pulses [184] suggests that different excitation channels – e.g. two photon absorption (2PA) in a different region of the band structure – will help achieve the high densities required for efficient semiconductor switching. While a plasma profile excited by 2PA will not exactly match a decaying exponential from linear absorption, it can still be approximated as such to use the analytical theory of Ref. [187].

Applying this model treating α_c as a free parameter, a good fit to experimental data is achieved (Fig. 6.11). The best-fit empirical values of α_c are given in Table 2. Notably, the empirical absorption coefficients are systematically smaller than literature linear absorption. In GaAs, the 2PA coefficient α_2 has been measured to be 200 cm/GW at 800 nm [192]. Defining an effective absorption coefficient for 2PA as $\alpha_{eff} = \alpha_2 I_c$, the α_{eff} in GaAs is $23{\times}10^3$ cm^{-1} for the peak fluence ($I_c = 115$ GW/cm^2). However due to the nonlinear nature of 2PA, its penetration depth is longer than a linear absorption process with $\alpha_c = \alpha_{eff}$. This, in addition to averaging over the temporal structure of the pulse, may explain the relatively lower best-fit α_c observed in the model.

Interestingly enough, GaAs has the most room to increase its efficiency. By doubling the peak fluence, our model suggests that GaAs reflectivity would increase by 1.42x. In contrast Ge and ZnSe would only have reflectivity increase by 1.20x and 1.25x, respectively, due to the onset of saturation

	GaAs	n-Ge	ZnSe
Fluence [mJ/cm^2]	3.4	2.5	2.9
N_{crit} [10^{19} cm^{-3}]	0.65	1.4	0.69
Literature α_c [10^3 cm^{-1}]	13 [188]	43 [189]	62 [190]
N_s [10^{19} cm^{-3}]	17	43	36
Empirical α_c [10^3 cm^{-1}]	3.0	30	31

Table 6.3: Absorption coefficients at control pulse wavelengths. Empirical values are found by fitting experimental data as described in the text. Corresponding peak surface plasma densities are given below the absorption coefficients assuming purely linear absorption.

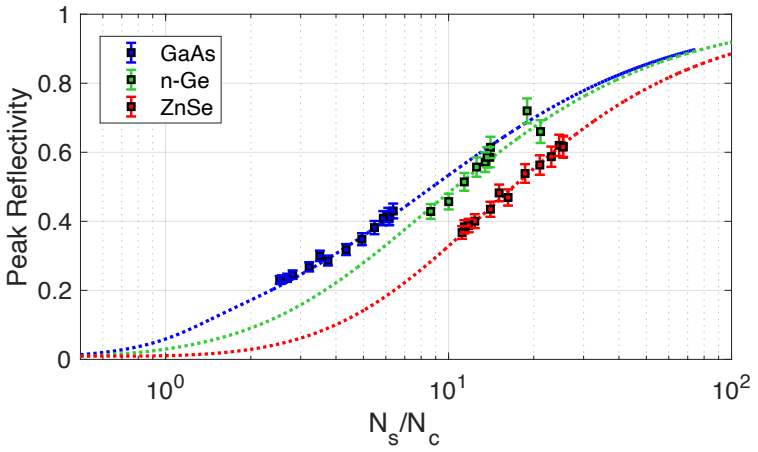

Figure 6.11: Peak reflectivity modeled following Ref. [187], using empirical α_c given in Table 6.3.

at high plasma densities.

We now turn our attention to describing the reflectivity time dynamics. The first stage of the electron-hole plasma time evolution is thermalization, where photoexcited carriers relax to the band edges. In the case of saturated linear absorption and 2PA excitation, the bottom of the lowest conduction band will be completely filled (especially in GaAs and ZnSe) and satellite valleys may have significant occupation. The satellite valleys have higher effective masses, and thus can support much greater populations. We assume instantaneous thermalization of carrier distributions, which is a good approximation as all diffusion and recombination processes occur on much longer picosecond and nanosecond time scales.

After thermalization, time dynamics of the photoexcited electron hole plasma can be described by solving a 1D diffusion-recombination equation of the form

$$\frac{\partial N}{\partial t} = -D\frac{\partial^2 N}{\partial z^2} - AN - BN^2 - CN^3 \tag{6.2}$$

where D is the diffusion coefficient, A is the trapping rate, B is the bimolecular recombination coefficient, and C is the Auger recombination coefficient. Plasma diffusion is ambipolar, owing to the density scale length being much longer than the Debye screening length [193]. This eliminates the need to consider space-charge fields and resulting drifts of individual electron and hole distributions. Transverse diffusion is presumed to be inconsequential due to much smaller density gradients and

	GaAs	n-Ge	ZnSe
D [cm^2/s]	22	65	4.5 [198]
A [$1/s$]	4.8×10^{10}	1.0×10^{7}	8.0×10^{7}
B [cm^3/s]	3.4×10^{-11} [199]	4.4×10^{-14} [200]	3.4×10^{-11} †
C [cm^6/s]	7.0×10^{-30} [199]	1.1×10^{-31} [200]	8.5×10^{-31}

Table 6.4: Material parameters used in the diffusion-recombination model. D in GaAs and n-Ge are calculated from carrier mobilities found in Ref. [107]. Values marked with a † are copied from those of GaAs as measurements were not found in the literature. A in ZnSe is measured in our sample using a time resolved transmission measurement, matching measurements in Ref. [201].

large control beam to probe beam aspect ratio, and surface recombination is ignored.

Since the initial electron and hole distributions are not excited at the band edge, the carriers will have excess energy and thus temperature above the lattice temperature, T_L. Since the carrier cooling time in these materials is $\sim$3 ps in GaAs and n-Ge but $\leq$1 ps in ZnSe [35, 194, 195], the majority of plasma evolution occurs with carrier temperatures equal to the lattice temperature. Therefore, excess energies do not contribute in a major way to the plasma evolution outside of heating the lattice. It should be noted that the diffusion dynamics of nonequilibrium carrier distributions are predicted to be quite complicated, with ambipolar diffusion coefficients changing rapidly with carrier temperature and density [196]. This is especially the case with degenerate distributions, where Fermi pressure further increases the carrier diffusion rate [197].

Parameters used in time domain modeling are presented in Table 6.4. Because temperature dynamics are not fully understood, ambipolar diffusion coefficients are taken to be constant. Due to their technological importance, much more is known about Ge and GaAs than ZnSe. Measurements of several ZnSe parameters are not present in the literature, so they were taken to be the same as GaAs due to their similarity as direct gap zincblende semiconductors.

To obtain time evolution of the reflectivity, the surface plasma density is taken at each step and interpolated onto the empirical curves found in Fig. 6.11. Clearly, the shape of the plasma distribution will no longer be exponential after diffusion and recombination, but this acts as a qualitative guide to the processes that impact reflectivity lifetime. Results of the modeling are shown in Fig. 6.12 for the peak fluences in experiments.

For the cases of GaAs and ZnSe, there is only one free parameter for each material – trapping rate and Auger recombination coefficient, respectively. The ZnSe reflection dynamics are dominated

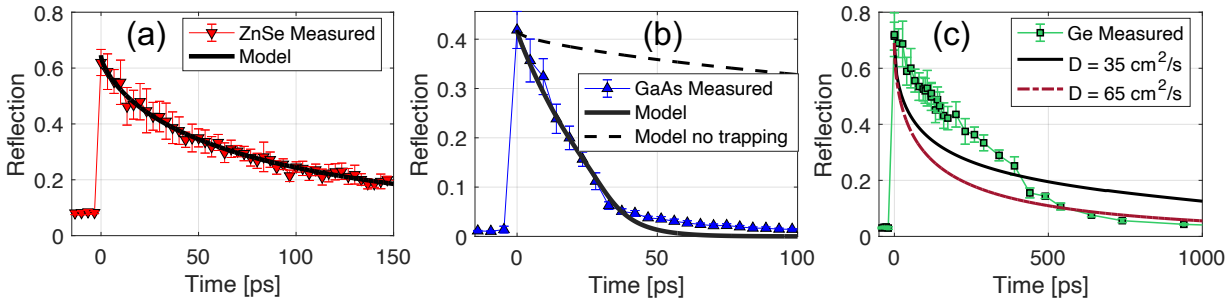

Figure 6.12: Results of time-dynamic modeling with the diffusion-recombination model.

by Auger recombination and diffusion due to the short absorption length. This simplified model fits the experimental data remarkably well with C_{ZnSe} = 8.5 x 10^{-31} cm^6/s, about 9 times smaller than that of GaAs.

In GaAs, which has a significantly longer absorption length and lower peak plasma density, the only process in this model that can explain the observed short reflectivity lifetime is carrier trapping. The result with $A = 1/\tau_{trap}$ = 21 ps is shown in Fig. 6.12(b). There is precedent for carrier lifetimes this fast or faster in GaAs, but they usually occur in samples grown or prepared in certain ways (e.g. low temperature [181] or ion bombarded GaAs [202]).

Another possible explanation of the rapid observed decay in GaAs is radiative carrier transfer, where electron-hole pairs radiatively recombine emitting band edge photons which are reabsorbed in a different transverse and longitudinal position, effectively smoothing and expanding the plasma distribution [203]. This process has been shown to be most efficient when population inversion and stimulated emission threshold is achieved, which in GaAs has been shown at fluences as low as 0.7 mJ/cm^2 [204]. While this mechanism is not included in the diffusion model, it was shown to cause exponential density decay in time [203] – thus, the trapping rate $\partial N/\partial t = -AN$ acts as a proxy for this mechanism.

In germanium, this simple model cannot reproduce time dynamics measured experimentally. Reducing the diffusion coefficient gives a slightly better fit, but the overall behavior is still not well-described. Diffusion is the dominant process in the given parameter space, but the poor fit suggests that a physical process not considered is impacting the dynamics. A prime candidate is temperature and density dependent diffusion. In particular, a high local temperature can strongly

reduce diffusion and carrier cooling dynamics can also be modified at high density [196].

The varying reflectivity lifetimes among these materials suggest different mechanisms limiting the process. In the diffusion dominated material Ge, and to a lesser extent ZnSe, decaying reflectivity does not correlate with reduction of total carrier number. This has implications for the transmission properties of the switch, as transmission loss scales with $\sigma_{fca}NL$. Therefore the transmission recovers on a timescale much longer than the reflectivity lifetime. Contrary to this, if the plasma dynamics in GaAs are indeed dominated by carrier trapping, then the total number of nonequilibrium carriers will follow the reflectivity lifetime. Taking the 21 ps lifetime we measure here, this suggests an extremely fast maximum switching speed of nearly 50 GHz for a photonic device of this type.

To conclude, we have measured reflection efficiency and time dynamics of mid-infrared semiconductor switching in n-Ge, ZnSe, and GaAs, which show decreasing efficiency and lifetime in that order. For the purposes of an intracavity switch, GaAs and ZnSe are most attractive due to their low nonlinear absorption and relatively high efficiency. GaAs is ideal for applications where speed is critical, e.g. dumping an optical cavity with round trip time on the order of a few nanoseconds, due to its short reflectivity lifetime. In addition, GaAs is predicted to have more favorable reflectivity scaling at fluences higher than what we use in experiments. While semiconductor switching has been used for decades for specific applications, these results are important in material selection for future photonic devices as they are incorporated in high power, ultrafast mid-infrared laser systems.

Chapter 7
Conclusion

In this dissertation, different aspects of the nonlinear optical response of semiconductors such as GaAs, n-Ge, ZnSe, and Te, transparent in the mid-infrared spectral region have been experimentally studied. Two unique laser systems allowed systematic studies of high intensity light-semiconductor interactions ($I \sim$ 1–10 GW/cm^2) in two markedly distinct pulse length regimes, while remaining below laser induced damage thresholds. The bulk nonresonant nonlinear response at such high intensities around 10 μm wavelength has not been reported in the literature prior to these studies. Fundamentally, this is also an exciting parameter space where free carrier effects and nonperturbative intensity effects may play a role due to high laser ponderomotive energy.

First, we used a high-pressure 200 picosecond 0.2 GW CO_2 laser system to measure nonresonant nonlinear absorption and effective nonlinear refractive indices in GaAs, n-Ge, and ZnSe at 10.6 μm. Nonlinear absorption observed at intensities up to 5 GW/cm^2 was much stronger than expected for such nonresonant interactions, and could not be explained using a multiphoton ionization model. Instead, we postulated an accumulated, pulse length dependent absorption model which described the experimental data well. Four-wave mixing was used to characterize $n_{2,eff}$ in the same materials at 1000x higher intensity than had been previously employed. Importantly, we demonstrated an ability to control the effective nonlinearity of GaAs via free carrier enhancement – with relatively low optical loss – by modifying the driver laser beat-wave frequency.

Secondly, an ultrafast, 220 fs DFG source was applied to study the nonresonant nonlinear response of the same materials in a similar intensity regime, however with almost 1000x shorter pulses. $n_{2,eff}$ is not found to vary much for femtosecond pulses, establishing these materials as useful MIR photonics elements for diverse laser intensities, pulse lengths, and bandwidths. On the other hand, nonlinear absorption was found to have an entirely different character with femtosecond pulses. We invoke the Keldysh model to attribute the observed nonlinear absorption to nonperturbative scaling of photoionization rates at intensities between 5–20 GW/cm^2. We also perform the same set of measurements in narrow-band Tellurium, for which the $\chi^{(3)}$ nonlinearity was not known. It is

found that the bulk Te crystal has a giant $n_{2,eff} \geq 3 \times 10^{-12}$ cm^2/W – one of the largest known bulk nonlinearities. Because of this, Te shows immense promise as a material for compact or thin-film MIR photonic devices. Simulations of nonlinear propagation in tellurium are performed, revealing the importance and interplay of nonlinear, plasma, and multidimensional effects for long wavelength light-semiconductor interactions.

Finally, we demonstrated mid-infrared photonics applications using nonlinear crystals. Second harmonic generation is studied for the first time with short, intense CO_2 laser pulses, proving that the materials with the highest $\chi^{(2)}$ and figure of merit (Te and CGA) are poor frequency converters due to the onset of strong self-focusing. All-optical semiconductor switching is also investigated in the femtosecond regime, where the merits of n-Ge, GaAs, and ZnSe are revealed for switching high-power MIR pulses with wavelengths between 10-14 μm.

The results described throughout the dissertation and summarized above provide several avenues for future research. For example, source development: the beat-wave nonlinearity enhancement in GaAs (or other semiconductors) can be exploited to generate an ultrabroadband MIR source, and with further optimization of picosecond SHG, two-color MIR laser pulses can be tightly focused in air to generate THz radiation with high efficiency [174]. Discovery of the giant Kerr nonlinearity in Te, along with its peculiar crystal structure, also makes it an extremely intriguing material for MIR high-harmonic generation. Further experimental and simulation work is required to fully disentangle the microscopic dynamics.

In all, our measurements are important contributions in the field of mid-infrared nonlinear optics and light-semiconductor interaction, especially as mid-infrared lasers have recently emerged as the forefront of laser science. These sources' rapid and continued development into the future will only unveil further possibilities and extensions of our research.

Appendix A
Implementation of the Two Dimensional Generalized Nonlinear Schrödinger Equation

Solving nonlinear pulse propagation equations has been a topic of great interest for decades, and is still an active area of research. Many of the different techniques and strategies for their numerical implementation can be found within Ref. [38] and the references therein. For the purposes of this dissertation, we solve the generalized nonlinear Schrödinger equation (gNLSE) in a cylindrical geometry – r, z as spatial coordinates with azimuthal symmetry assumed. The full form, with all potential terms we use, is

$$\begin{aligned}\frac{\partial A}{\partial z} = \frac{i}{2k_0}\nabla_\perp^2 A + \left[i\left(k(\omega) - k(\omega_0) - \frac{\omega-\omega_0}{v_g(\omega_0)}\right) - \frac{\alpha_1}{2}\right]A \\ + \left[ik_0 n_2\left(1 + \frac{i}{\omega_0}\frac{\partial}{\partial T}\right)|A|^2 - \frac{\alpha_M}{2}|A|^{2M-2}\right]A \\ - \left[\frac{\sigma_{FCA}}{2}\int_{-\infty}^{T}\frac{\alpha_M|A(T')|^{2M}}{M\hbar\omega_0}dT' + ik_0 n_0\left(\sqrt{1 - \frac{\int_{-\infty}^{T}\frac{\alpha_M|A(T')|^{2M}}{M\hbar\omega_0}dT'}{N_{crit}}} - 1\right)\right]A\end{aligned} \tag{A.1}$$

In order, the first line comprises diffraction, dispersion, and linear loss whereas the second line includes nonlinear contributions – Kerr nonlinearity and multiphoton absorption. The third line gives the free-carrier or plasma effects, where the integral term is equivalent to the local accumulated plasma density that builds up over the duration of the pulse, $N(T)$. $T = t - z/v_g(\omega_0)$ transforms the solution into a frame moving with the group velocity of the central frequency of the pulse, $v_g(\omega_0)$. Care must be taken on the sign/direction of T depending on the direction of numerical propagation.

Certain elements of the nonlinear envelope equation (NEE) [43] are included, namely self-steepening (time derivative of the Kerr nonlinearity) and inclusion of the full dispersion $k(\omega)$. In most implementations of the NLSE, a perturbative expansion of the propagation constant is used, $k(\omega) \approx k_0 + (\omega-\omega_0)k_1 + \frac{1}{2}(\omega-\omega_0)^2 k_2 + \frac{1}{6}(\omega-\omega_0)^3 k_3 + \cdots$. Terms up to the second (k_2, GVD) or third order (k_3) dispersion are typically included. However, since we are considering relatively broadband pulses with additional spectral broadening during propagation, using the full dispersion

$k(\omega)$ is more accurate provided good Sellmeier equations exist [50]. Some frequency dependencies are not included, however, such as the frequency dependence of α_1, N_{crit}, or diffraction. Note that the frequency dependence of the diffraction operator is often referred to as space-time focusing [38]. Since we mainly simulate low-linear-loss materials with $N \ll N_{crit}$ and without strongly converging or diverging beams ($z_R \gg L$), and self-focusing is arrested via various mechanisms, these frequency dependencies are not expected to play a significant role.

Several assumptions are included in arriving at Eq. A.1, most importantly the slowly-varying envelope approximation and paraxial approximation [38]. These approximations break down for few cycle pulses or very tightly focusing or self-focusing beams. Throughout the work, because we are interested in propagation without extreme self-compression or self-focusing, these approximations are satisfied.

The gNLSE is solved numerically using the split-step method as described in many sources [23, 38]. This involves splitting the partial differential equation into a linear operator $\mathcal{L}$ and nonlinear operator $\mathcal{N}$ such that the equation can be rewritten as $\frac{\partial A}{\partial z} = (\mathcal{N} + \mathcal{L})A$. In general $\mathcal{L}$ does not depend on A, whereas by definition $\mathcal{N}$ does depend on A. With propagation step-sizes that are very short relative to all of the relevant length scales throughout propagation – that is L_{NL} L_D, z_R, and $1/(\sum_M \alpha_M I^{M-1})$ – $\mathcal{L}$ and $\mathcal{N}$ can be applied separately like

$$A(z + dz, T) \approx \exp(\mathcal{L}dz) \exp(\mathcal{N}dz) A(z, T). \tag{A.2}$$

The linear operator is applied in the frequency domain (ω or k_r) whereas the nonlinear operator is applied in time. The steps are symmetrized to improve accuracy as described in [23], where the order in which operators are applied is actually $\mathcal{L}\, dz/2 \rightarrow \mathcal{N}\, dz \rightarrow \mathcal{L}\, dz/2$. To transform the envelope into spatial frequency domain, the inverse Hankel transform is used as described in [205], and adapted from the code provided at [206].

The MATLAB code used to solve Eq. A.1 is reproduced at the end of this section. Note that the numerical structure of the complex electric field envelope $A(T)$, which here has units of $\left[\sqrt{I}\right] = \mathrm{W}^{1/2}/\mathrm{cm}$, is $A(r, t)$. As in any numerical simulation, care should be taken to balance the resolution of conjugate variables (in this case $t \leftrightarrow \omega$ and $r \leftrightarrow k_r$).

Much of the simulation work presented is modeling 220 fs pulses in Te. Strictly comparing τ and $1/\nu_0$, these approximately 9 cycle (in the electric field envelope) pulses are nearing the regime where few-cycle considerations are important. The slowly varying envelope approximation can be written as [43]

$$\frac{\partial A}{\partial z} \ll k_0 A, \quad \frac{\partial A}{\partial t} \ll \omega_0 A. \tag{A.3}$$

For the 220 fs, 10.3 μm pulses the right hand side is approximately 40x larger than the left hand side, satisfying the inequalities. Additionally, these ultrashort pulses quickly broaden in the presence of the positive dispersion in Te, making the SVEA an even better approximation. With few cycle pulses, the carrier-envelope phase (CEP) becomes important in describing light-matter interactions. The SVEA, by extension, also ignores CEP. This is further justified in modeling experiments as the ultrashort pulses are not CEP stabilized, and all measurements are averaged over many shots.

Since the gNLSE is an envelope code, the phase of the electric field at which free carriers are born is not known. This becomes important for few-cycle pulses, and requires a frequency resolved code such as the unidirectional pulse propagation equation (UPPE) [38]. In the context of light-semiconductor interactions, to properly include the effect of the phase at which the carriers are born, the fields and carriers must be coupled to the electronic band structure. As mentioned in Section 2.2.1, this is an active area of research and beyond the scope of this dissertation. Fortunately for pulses where the SVEA is satisfied, these effects will be averaged out - especially over many laser shots.

An important step before using any numerical model to fit experimental data is to run simple cases, ensuring that the basic underlying physics is accurately replicated. This is especially important for modeling highly nonlinear interactions like we do in this dissertation, as several different effects are all active at once and can be highly coupled with each other. Here, we show a brief walkthrough of this process to confirm that the Kerr nonlinearity - the most important physical process we study - is modeled correctly.

As discussed in Chapter 2, the underlying physical process behind the optical Kerr effect is a laser beam accumulating nonlinear phase as it propagates through a medium. Equation 2.9 defined the nonlinear length $L_{NL} = \lambda_0/2\pi n_2 I_0$ as the propagation length at which a laser pulse has

accumulated 1 radian of nonlinear phase.

We can ensure that the strength of our numerical nonlinearity is tuned correctly by propagating an intense pulse through a hypothetical dispersionless ($n_0 = 1$ for all λ) and lossless medium. If we also initialize a large beam such that $L_{NL} \ll z_R$ and $L_{NL} \ll z_{SF}$, diffraction and self-focusing are negligible. This leaves only the Kerr nonlinearity (and its associated self-steepening) as playing a significant role in solving Eq. A.1. The peak B-integral ($t = 0, r = 0$) during propagation over $L = L_{NL}$ is plotted in Fig. A.1, and results in 1 radian of nonlinear phase for this idealized scenario. This confirms that the Kerr nonlinearity (and thus self-phase modulation) is working as expected.

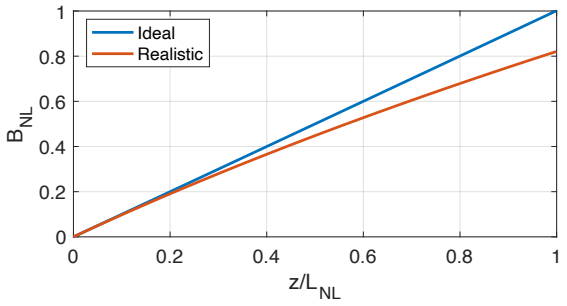

Figure A.1: Peak nonlinear phase accumulation over one nonlinear length in an ideal scenario, with no loss or dispersion, and a more realistic scenario with (nonlinear) loss and dispersion.

Also plotted is peak nonlinear phase accumulation of a more realistic case encountered in the lab. This is B_{NL} for a 1.5 GW/cm^2 peak intensity 10.3 μm beam with a 500 μm spot size propagating through tellurium (E $\perp$ c). In this case ($L_{NL} = 360$ μm), effects like dispersion and multiphoton absorption quickly modify the pulse peak power, resulting in less than the nominal nonlinear phase change. Note that in situations where self-focusing or self-compression is occurring, the realistic B_{NL} can be higher than the idealized case. The dispersion length discussed in Section 2.2.1, where the initial pulse length increases by a factor of $\sqrt{2}$ at $z = L_D$, is also tested and confirmed numerically.

It is worthwhile to investigate how the gNLSE code used in this dissertation handles self-focusing, which is a highly nonlinear process coupling together diffraction and the Kerr nonlinearity. In fact, including self-focusing is one of a few major reason why a 2-dimensional geometry was chosen to model the experiments in this dissertation (the other being the ability to numerically average nonlinear effects over a spatial beam profile). This is an instructive and interesting task; as self-focusing

is a runaway/positive feedback process, any small imbalance between the strength of diffraction and optical nonlinearity (such as a factor of $\sqrt{2}$ or less in one of the terms in Eq. A.1) can lead to wildly incorrect numerical propagation.

To investigate self-focusing, we use a representative MIR pulse centered at 10 μm with Gaussian temporal profile (τ = 1 ps) and radial profile (w_0 = 1 mm) without any initial divergence. We propagate these pulses through a material similar to air - that is with extremely weak dispersion that, for demonstration purposes, we take to be dispersionless ($n_0 = 1$ for all λ) and lossless. First, we confirm that the beam diffraction follows textbook Gaussian beam propagation if the nonlinearity is set to be zero (not shown).

To see self-focusing the nonlinearity is chosen to be 5×10^{-19} cm^2/W as measured in air [26]. By changing the initial peak power over the range 0.5-1.2 P_{crit}, we can study the very delicate balance between nonlinearity and diffraction. In Fig. A.2, the peak on-axis intensity is tracked for each of these initial powers as the pulse propagates over two Rayleigh ranges (z_R = 31.4 cm for these parameters). When $P = 0.5P_{crit}$, the intensity stays close to constant over the first $0.5z_R$, but then diffraction takes over and the far-field intensity is only slightly modified. The same is true for $P = 0.8P_{crit}$, though the peak intensity actually increases slightly first before diffraction wins out.

When $P = P_{crit}$, where diffraction and nonlinearity should cancel each other out and cause self-channeling, the character of our numerical propagation does indeed change. The intensity initially increases about 2x, but then stays steady over $2z_R$. This shows that the nonlinear focusing has nearly perfectly compensated for diffraction, at least over this length, and it occurs at just the peak power that is expected. This gives confidence in our numerical model.

Increasing the propagation length to $5z_R$ shows that the self-channeling remains nearly steady over $4z_R$, and then the central part of the pulse collapses above $z = 4.5z_R$. Looking closer at these interesting dynamics, it appears that this behavior is largely caused by the pulse shortening effects of self-focusing [207] combined with self-steepening. Initially, the central part of the pulse reshapes itself into a Townes profile, preferred for self-focusing [208]. Then self-steepening gradually forms a steep falling edge in time, which further changes the spatio-temporal structure. The steepening eventually forms an optical shock, causing the local intensity to enter a positive feedback loop and collapse. In reality, material dispersion mitigates these effects such that the pulse would not ever

evolve into a complete optical shock.

Increasing $P > P_{crit}$, even just by 5%, causes a rapid runaway of intensity as self-focusing gets trapped in a positive feedback loop. The obvious regime change between P below or above P_{crit} further confirms the validity of our model. The overall behavior of these curves follows that presented in Fig. 16 of Ref. [209], calculated in the quasi-static limit.

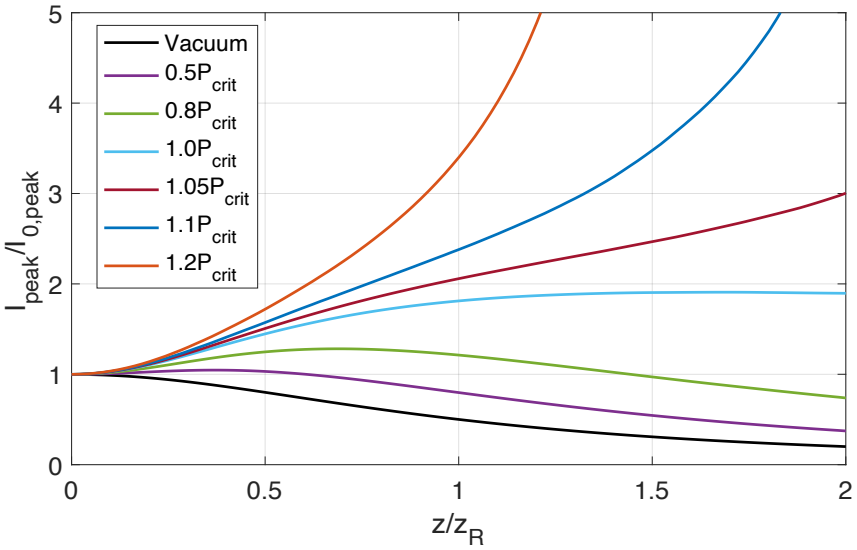

Figure A.2: On-axis peak intensity versus distance for different initial peak powers showing the delicate balance between diffraction and self-focusing when P is near P_{crit}.

Another aspect of self-focusing that is of great experimental and numerical interest is the length at which a self-focusing beam collapses to a singularity. Of course, this only occurs when there is no mechanism exists to arrest self-focusing - typically photoionization inhibits self-focusing before this point, as we demonstrated in Fig. 5.16. The self-focusing length z_{SF} defined in Eq. 2.13 is found numerically for a cw laser beam [210]. Regardless, z_{SF} can still give a good guide for the distance at which a pulse collapses, which we will call the collapse length, $z_{collapse}$.

Using the same initial pulses as in the previous analysis, we increase the peak power and propagate the self-focusing beams until they collapse. Simulations with extremely high radial resolution to resolve a beam in its final stages of collapse become unnecessarily expensive and time-consuming. Indeed, as the beam is nearing complete catastrophic collapse many runaway effects occur, including pulse shortening, which tend to violate approximations that the gNLSE depends on, like the SVEA.

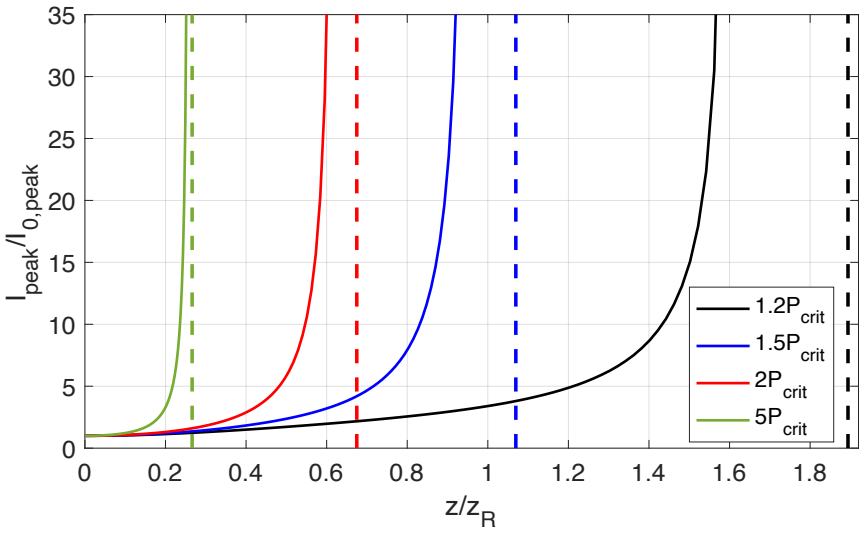

Figure A.3: On-axis peak intensity versus distance for different initial peak powers, showing the distances at which the beam collapses. Dashed lines are theoretical self-focusing distance in the quasi-static limit from Eq. 2.13.

Space-time focusing would also be required to accurately model the collapse. Therefore, we arbitrarily define $z_{collapse}$ as the propagation length at which the peak on-axis intensity has increased by 30x.

The simulation results are shown in Fig. A.3. For the whole range of peak powers tested, the $z_{collapse}$ is close to the theoretical self-focusing length (dashed lines). In all cases, the beam collapses before z_{SF} is reached; this is likely caused by the same effects as described above for short pulse self-focusing.

Overall, the extremely delicate process of self-focusing is very well described by our numerical modeling. This gives confidence in applying the model to highly nonlinear light-matter interactions, as we do throughout the dissertation.

MATLAB code

```
clear all
tic
%% Constants
c = 299792458;
h = 6.626e-34;
hbar = h/(2*pi);
e = 1.602e-19;
eps0 = 8.854e-12;
m0 = 9.11e-31;

%% Material Parameters %%
material = 'Te_o_Caldwell';
L = 5e-3; % Sample Length [m]
n2 = 3e-12; % [cm^2/W]

MPAorder = 3; % ceil(Eg/hv) - MPA order M
MPAcoeff = 6; % use correct units for MPA order [cm^(2M-3)/GW^(M-1)]

mPlas = 0.845; % reduced e-h mass [m0]
sigmaFCA = 5e-17; % FCA cross section [cm^2]
alphaExpt = 0; % linear absoprtion coefficient [cm^-1]
refl = 0;

%% Laser Parameters %%
lam0 = 10e-6; % central wavelength [m]
pulseEnergy = refl*10e-6; % pulse energy inside the crystal [J]
spotSize = 500e-6; % w0 (1/e^2 radius) [m]
tauFWHM = 220e-15; % pulse FWHM [s]
I0peak = 2*pulseEnergy/(tauFWHM*pi*spotSize^2); % Peak intensity [W/m^2]

%% Simulation Parameters %%
Nt = 2^13; % number of points in time and frequency
t_window = 20e-12; % full time window [s]

steps = 2000; % total propagation steps
nPlot = 10; %number of steps between expensive diagnostics (make divisor of steps)

dz = L/steps; % spatial step [m]
z = 0:dz:L; % space vector [m]

rGridPoints = 2^7; % number of points in r
rMax = 2.5*spotSize; % maximum radius [m]
```

```
43
44  %% Simulation/Diagnostic Options
45  parameterTest = false;
46  includeCarrierDynamics = true;
47
48  % Various diagnostics can be included to plot resulting spectrum, temporal
49  % profile, beam, make movie of propagation, excited carrier density, etc.
50  diagnostic1 = true;
51  diagnostic2 = false;
52
53  %% Convert to SI Units/Derived Quantities
54  n2 = n2*1e-4;
55  MPAcoeff = 10^(-13*MPAorder+15)*MPAcoeff; % factor in front is 10^(-13M+15)
56  sigmaFCA = sigmaFCA*1e-4;
57  alpha = alphaExpt*1e2;
58
59  nu0 = c/lam0; % central frequency [Hz]
60  w0 = 2*pi*nu0; % central angular frequency [rad/s]
61  E0 = sqrt(I0peak); % peak electrc field [sqrt(W)/cm]
62
63  %% Set up Hankel matrices
64  % adapted from 'Integer order Hankel transform' by Manuel Guizar on MATLAB
65  % Central File Exchange (Reference 206) and the work it is based on Ref. 205.
66  tmp = load('/Users/daniel/Documents/MATLAB/hankelZeros.mat');
67  ord = 0;
68  N = rGridPoints;
69
70  hankelZeros = tmp.c;
71  hankelZeros = hankelZeros(ord+1,1:N+1);
72
73  kMax = hankelZeros(N+1)/(2*pi*rMax);
74  r = hankelZeros(1:N)'*rMax/(hankelZeros(N+1));
75  kr = hankelZeros(1:N)'/(2*pi*rMax); % radial k spectrum [1/m]
76
77  [Jn,Jm] = meshgrid(hankelZeros(1:N),hankelZeros(1:N));
78
79  % htMatrix, htPrep, ihtPrep are matrices used in Hankel transform r->k
80  htMatrix = (2/hankelZeros(N+1))*besselj(ord,Jn.*Jm/hankelZeros(N+1))./(abs(besselj(ord
        +1,Jn)).*abs(besselj(ord+1,Jm)));
81  m1 = (abs(besselj(ord+1,hankelZeros(1:N)))/rMax)';   %% m1 prepares input vector for
        transformation
82  htPrep = diag(1./m1);
83  ihtPrep = diag(m1);
84  m2 = m1*rMax/kMax;
85
86  clear Jn Jm tmp
```

```
87
88  %% Time and frequency vector creation
89  Ntf = (-Nt/2):1:(Nt/2-1); % indices for time and frequency
90
91  dt = t_window/Nt; % time step [s]
92  t = dt*Ntf; % Time vector [s]
93
94  % Frequency centered at 0, corresponding to the real central frequency nu0
95  dnu = 1/t_window; % frequency step [Hz]
96  nu = fftshift(dnu*Ntf); % Frequency vector [Hz]
97  w = 2*pi*nu;
98  lam = c./(nu+nu0); % shift wavelength for plotting
99
100 %% Get dispersion parameters
101 NLSE2D_GetDispersionParameters
102 % Function using Sellmeier equations to calculate refractive index and the
103 % higher order dispersion parameters. index and beta0 = (w/c)*index are
104 % function handles, whereas beta0Vec and beta1 are vectors.
105
106 n0 = index(lam0*1e6); % linear refractive index at central wavelength
107 k0 = 2*pi*n0/lam0; % include first order wavenumber only
108
109 %% Create dispersion vector
110 dispVector = 1i*(beta0Vec - w*beta1 - beta0(w0));
111
112 %% Create transmission mask
113 % fully absorbs light outside the transmission range in the case of extreme
114 % spectral broadening
115 shortWavelengthBoundf = c/(1e-6*shortWavelengthBound);
116 longWavelengthBoundf = c/(1e-6*longWavelengthBound);
117 mask = ((nu+nu0)<shortWavelengthBoundf).*((nu+nu0)>longWavelengthBoundf);
118
119 %% Length scales for comparison
120 dispersionLength = tauFWHM^2/(4*log(2)*abs(beta2));
121 nonlinearLength = c/(I0peak*n2*w0);
122 solitonOrder = sqrt(dispersionLength/nonlinearLength);
123 Pcrit = 3.77*lam0^2/(8*pi*n0*n2);
124 peakPower = pulseEnergy/tauFWHM;
125 PonPcrit = peakPower/Pcrit;
126 zSF = 2*n0*spotSize^2/(lam0*sqrt(PonPcrit));
127 peakNLALength = 1./(MPAcoeff*(I0peak).^(MPAorder-1));
128
129 %% Initialize pulse
130 temporalStructure = exp(-2*log(2)*(t/tauFWHM).^2);
131
132 Einit = E0*exp(-r.^2/spotSize^2); % impose radial structure
```

```
Er = Einit;
Ekinit = htMatrix*(Einit./m1);

At = Er*temporalStructure; % create envelope At(r,t)
At0 = At; % initial time envelope
Af = fft(At,Nt,2); % create frequency envelope Af(nu,t)
Af0 = Af; % initial frequency envelope

I0 = abs(At).^2; % initial pulse intensity
It0 = abs(At(1,:)).^2; % initial pulse intensity at beam center
If0 = abs(Af(1,:)).^2; % initial pulse spectrum at beam center

IfFullBeam0 = trapz(r,r.*abs(Af).^2); % initial spec. integrated over beam

%% Create full-step diffraction operator (matrix)
diffOp = diag(exp(-1i*(dz/(2*k0))*(2*pi*kr).^2));

%% Create full-step dispersion and loss operator (matrix)
dispOp = diag(exp(dz*(dispVector.*mask - alpha/2)));

%% Critical Plasma Density
Ncrit = w0^2*m0*mPlas*n0^2*eps0/e^2; % critical plasma density [m^-3]

%% Propagation Loop
if parameterTest
    NLSE2D_ParameterTest
    return
end
disp('Propagation in Progress:');
fprintf('Progress:             ');

% Initial dispersion half step
zStep = dz/2;
Af = fft(At,Nt,2);
Af = Af*diag(exp((dz/2)*(dispVector.*mask - alpha/2))).*mask;
At = ifft(Af,Nt,2);

% Initial diffraction half step
Ak = htMatrix*(htPrep*At);
Ak = diag(exp(-1i*((dz/2)/(2*k0))*(2*pi*kr).^2))*Ak;
At = ihtPrep*htMatrix*Ak;

for step = 1:steps
    %%% Nonlinear operator on full step %%%
    SPM = 1i*(w0/c)*n2*abs(At).^2; % SPM

```

```
    SS_SPM = (w0*n2/(w0*c))*(conj(At).*deriv12D(At,dt,2)...
        + deriv12D(abs(At).^2,dt,2)); % self-steepening from SPM

    MPA = (MPAcoeff/2)*abs(At).^(2*(MPAorder-1)); % Multiphoton absorption
    wMPA = MPAcoeff*abs(At).^(2*MPAorder)/(MPAorder*hbar*w0);
    % local ionization rate to calculate local carrier density

    if includeCarrierDynamics
        % flip used to correct direction of time / sign of carrier density
        cumint = (MPAcoeff/(MPAorder*hbar*w0))...
            *cumtrapz(flip(t,2),flip(abs(At).^(2*MPAorder),2),2);
        FCA = flip((sigmaFCA/2)*cumint,2);
        carrierDensForDispersion = -flip(cumint,2);
        carrierDispersion = -1i*(w0/c)*n0...
            *(sqrt(1-carrierDensForDispersion/Ncrit) - 1);
    else
        FCA = 0;
        carrierDispersion = 0;
    end
    % nonlinear operator applied in time
    NLOp = exp(dz*(SPM + SS_SPM - MPA - carrierDispersion + FCA));
    At = At.*NLOp;

    % Linear operator on full or half step (half for final step)
    if step == steps
        % Apply dispersion operator
        Af = fft(At,Nt,2);
        Af = Af*diag(exp((dz/2)*(dispVector.*mask - alpha/2))).*mask;
        At = ifft(Af,Nt,2);

        % Apply diffraction operator
        Ak = htMatrix*(htPrep*At);
        Ak = diag(exp(-1i*((dz/2)/(2*k0))*(2*pi*kr).^2))*Ak;
        At = ihtPrep*htMatrix*Ak;

        zStep = zStep + dz/2;
    else
        % Apply full step dispersion operator
        Af = fft(At,Nt,2);
        Af = Af*dispOp.*mask;
        At = ifft(Af,Nt,2);

        % Apply full step diffraction operator
        Ak = htMatrix*(htPrep*At);
        Ak = diffOp*Ak;
        At = ihtPrep*htMatrix*Ak;
```

```
225
226         zStep = zStep + dz;
227     end
228
229     Af = fft(At,Nt,2);
230
231     % save different diagnostics every nPlot steps
232     if mod(step,nPlot) == 0
233         carrierDensityTracker(:,step/nPlot) = trapz(t,wMPA,2);
234         energyTracker(step/nPlot) = trapz(t,trapz(r,r.*abs(At).^2,1),2);
235         beamTracker(:,step/nPlot) = At(:,Nt/2); % tracks beam at peak of pulse.
236         fullPulseTracker(:,:,step/nPlot) = abs(At).^2;
237         fullSpectrumTracker(step/nPlot,:) = trapz(r,r.*abs(Af).^2);
238         zTracker(step/nPlot) = zStep;
239         fprintf('\b\b\b\b\b\b%5.2f%%', step/steps * 100);
240     end
241 end % end of propagation loop
242
243 fprintf('\n')
244 zTracker = [0 zTracker];
245 beamTracker = [Einit beamTracker];
246 carrierDensityTracker=[zeros(size(carrierDensityTracker(:,1))) carrierDensityTracker];
247 fullPulseTracker = cat(3,I0,fullPulseTracker);
248 fullSpectrumTracker = cat(1,IfFullBeam0,fullSpectrumTracker);
249 energyTracker = [trapz(t,trapz(r,r.*abs(At0).^2,1),2) energyTracker];
250 toc;
251
252 %% Beam at different positions in time
253 % intensity at time midpoint
254 IrMidTime = abs(At(:,Nt/2)).^2;
255 % intensity at beam center
256 ItMidBeam = abs(At(1,:)).^2;
257 % integrated spectrum
258 IfFullBeam = trapz(r,r.*abs(Af).^2);
259 % Intensity(r,t)
260 It = abs(At).^2;
261 % Intensity(r,nu)
262 If = abs(Af).^2;
263
264 %% Diagnostics (include as many as needed)
265 if diagnostic1
266     diagnostic1script
267 end
268 if diagnostic2
269     diagnostic2script
270 end
```

Appendix B
Semiconductor Band Structure Parameters

Semiconductor band structure parameters – effective masses and energy gaps – used throughout this dissertation are presented in Table B.1. Except where otherwise specified, values are taken from Ref. [107]. All values are given for minimum direct gap points in reciprocal space; the Γ point in GaAs, n-Ge, and ZnSe and the H point in Te. n-Ge has an indirect band gap of 0.66 eV, which has much lower absorption – indirect transitions are not considered here.

Reduced mass for calculation of e.g. electron-hole plasma frequency or Keldysh parameter is $m_{red} = (1/m_h + 1/m_{CB})^{-1}$. In calculating Keldysh ionization rates, transitions from the light-hole band are typically more likely and dominate the overall MIR ionization rate in the intensity range of most interest in this dissertation (1-10 GW/cm^2). Above 10 GW/cm^2, e.g. in calculating the Keldysh photoionization rate in the open-aperture z-scan measurements (Fig. 5.10), ionization rates from multiple channels (LH - CB and HH - CB) must be considered in concert. Similarly, Keldysh photoionization in tellurium is calculated using only the upper valence band (VB1). In E $\perp$ c the VB1 - CB energy gap is 0.33 eV and VB2 - CB energy gap is 0.44 eV, leading to approximately an order of magnitude lower ionization rate from VB2 between 1-10 GW/cm^2.

	E_g [eV]	Δ_{SO} [eV]	m_{CB}	m_{HH}	m_{LH}	m_{SO}
GaAs	1.42	0.341	0.067	0.55	0.083	0.165
n-Ge	0.795	0.295	0.038	0.345	0.0427	0.095
ZnSe	2.71	0.424	0.137	0.82	0.154	0.24
Te (E $\perp$ c)	0.33 [211]	–	0.104 [121]	0.45 [108]	–	–
Te (E // c)	0.342 [124]	–	0.07 [121]	0.45 [108]	–	–

Table B.1: Band structure parameters used in calculations throughout the dissertation.

Appendix C
Thermal Effects in Z-Scan Measurements at 1 kHz Repetition Rate

The refractive index of any material changes with temperature, which is often described in a linear approximation by

$$\Delta n \approx n_0 + T\frac{dn}{dT} \tag{C.1}$$

where $\frac{dn}{dT}$ (units 1/K) is the thermo-optic coefficient. When a laser beam experiences absorption passing through a material, most of the absorbed light energy eventually dissipates non-radiatively into heat, raising the local material temperature. In an ideal case where a Gaussian beam undergoes linear absorption, the deposited heat (and thus temperature) profile will be a Gaussian with $1/e^2$ radius $w_Q = w$ of the laser. In an M photon absorption process, the radial temperature distribution with theoretically have a radius $w_Q = w/\sqrt{M}$. Regardless of the absorption mechanism, a radial refractive index gradient will be set up in the material.

This is the familiar process of thermal lensing, which is a topic of extreme importance in laser systems design. However, these thermal effects can also manifest like an effective Kerr nonlinearity in experimental techniques measuring nonlinear phase shift. Of course, the closed aperture z-scan falls in this category – a hypothetical material with thermal lensing but identically zero n_2 would produce a z-scan trace similar to the classic z-scan trace observed countless times in the literature (and in this dissertation). Therefore, in order to claim that the z-scan traces we measure are dominated by instantaneous Kerr nonlinearities, we must prove that the focal length of the thermal lens is long relative to the nonlinear focal length. Equivalently, the thermal phase shift must be small relative to the nonlinear phase shift.

In this discussion, we focus on the z-scan measurements in tellurium performed with 220 fs MIR pulses at peak intensity up to 0.6 GW/cm^2 (Fig. 5.5), intensities at which we have shown non-negligible 3 photon absorption is present (Fig. 5.8). The energy deposited via 3PA diffuses radially on a characteristic time of $t_c = w_Q^2/4D$ [212], where $D = k/C$ is the thermal diffusivity (cm^2/s),

	Te (E $\perp$ c)	Te (E // c)	GaAs
C [J/K·cm^3]	1.23	1.23	1.76
κ [W/cm·K]	0.020	0.034	0.55 [213]
D [cm^2/s]	0.016	0.028	0.31
dn/dT [1/K]	–	–	2×10^{-4}

Table C.1: Thermal properties of Te. GaAs is shown for comparison.

κ is the thermal conductivity (W/cm·K), and C is the volumetric heat capacity (J/K·cm^3) (Table C.1). If t_c is shorter than the time between pulses in a high repetition rate laser ($1/f_{rep}$), there will be no accumulation of heat over many shots. However, if the characteristic thermal time is longer than the time between pulses, the heat will not fully diffuse away causing heat accumulation.

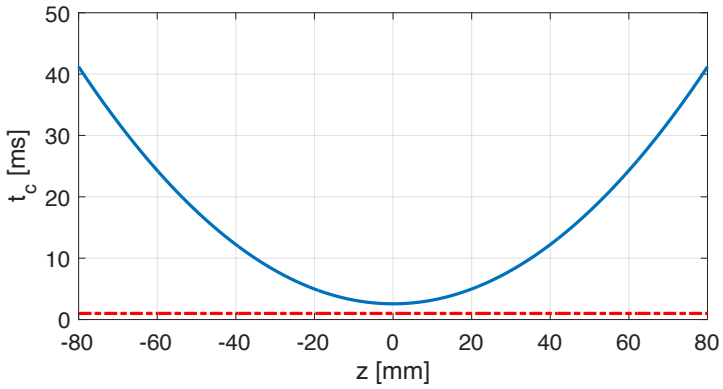

Figure C.1: Theoretical characteristic time for thermal diffusion calculated for tellurium in the closed aperture z-scan experimental setup in Section 5.3. D is averaged over both orientations.

As is seen in Fig. C.1, t_c in tellurium (assuming 3PA) is larger than $1/f_{rep} = 1$ ms for all z in the z-scan measurements discussed in Section 5.3, with the shortest characteristic time in the focus ($w_0 = 260$ μm) with $t_c = 3.71$ ms. This is largely due to the poor thermal properties in Te. It should be noted that GaAs, n-Ge, and ZnSe all have higher thermal diffusivity by approximately order of magnitude or more, which correspondingly reduces t_c to more acceptable levels. With this in mind, we must determine how important, if at all, thermal effects are in our z-scan measurements of n_2 in Te.

First, let's look qualitatively. The z-scan trace in Te (E $\perp$ c, Fig. 5.5(a)) is the consequence of a positive phase shift. The sign and magnitude of the thermo-optic coefficient is not known in bulk Te, but we can make some inferences. Since the nonresonant electronic nonlinearity is positive [17],

a dominant negative thermal nonlinearity ($dn/dT < 0$) is ruled out. Many semiconductors have $dn/dT > 0$ [214], which supports this claim.

If we momentarily assume that absorbed energy is instantaneously converted into heat, as the pulse propagates through the sample and accumulates thermal phase, the time derivative of the phase change is always positive. According to our definition of the instantaneous frequency (Section 2.1.3), this corresponds to a red-shift as the only spectral modulation. However, we observe nearly symmetric spectral broadening in SPM measurements performed at 1.5 GW/cm^2 (Fig. 5.6(a)). In addition, the absorbed energy is primarily electron-hole pair excitations, which do not transfer their energy to heat immediately, but instead on recombination timescales longer than the pulse duration. Tellurium has also been predicted to have an extremely high radiative recombination efficiency, $> 90\%$ [215], which will cause a non-negligible amount of absorbed energy to be lost to photoluminescence. Note that this is especially true for higher intensities, where high electron-hole densities are generated near the front surface of the crystal. These arguments together form good qualitative evidence that thermal nonlinearities do not play a significant role in z-scan measurements.

By making some approximations, we can be more quantitative with a heat accumulation model. We model the experiment with the gNLSE, where intensity loss on each propagation step of length Δz is

$$\frac{\Delta I(r,z,t)}{\Delta z} = -\alpha_1 I(r,z,t) - \alpha_3 I(r,z,t)^3, \tag{C.2}$$

with units W/cm^3. $I(z,r,t)$ is the intensity in a moving frame following the pulse. Free carrier absorption is small for the intensities of interest, as peak carrier densities reach only $\sim 10^{15}$ cm^{-3}. For our purposes we take $\alpha_3 = 6$ cm^3/GW^2, $n_2 = 3 \times 10^{-12}$ cm^2/W, and a higher end estimate of $\alpha_1 = 0.1$ cm^{-1}. Integrating $\Delta I/\Delta z$ over time results in the volumetric energy density deposited per pulse. Since $t_c > 1/f_{rep}$, we approximate this as a continuous heat source, as opposed to being discrete every millisecond. Multiplying by f_{rep} then gives the average power density deposited under high repetition rate irradiation. In the "weak" absorption limit, absorbed power density is relatively even longitudinally; we average the absorbed power density over length and ignore longitudinal thermal diffusion. Finally, assuming 100% of the absorbed power is converted to heat, the absorbed power density is identical to the continuous heat source density Q (W/cm^3). The

operations described above are represented mathematically as

$$Q(r,z) = Q(r) = \frac{f_{rep}}{L} \int_0^L \int_{-\infty}^{+\infty} \frac{\Delta I(r,z,t)}{\Delta z}\, dt\, dz. \tag{C.3}$$

This is the radial heat source profile throughout the sample, since we averaged over length.

Again with "weak" absorption, Q will be close to Gaussian. For this to be accurate, propagation effects like dispersion, self-focusing, or other spatio-temporal modifications (e.g. beam becoming flat-top) cannot be very strong. Simulating the laser propagation through Te at the beam focus, with $w_0 = 260$ μm and $\mathrm{I}_{0,peak} = 0.6$ GW/cm^2 gives just over 10% total energy loss. This corresponds to only ~ 20 nJ absorbed per pulse, or 20 μW average absorbed power, both small numbers.

Initial and final spatio-temporal profiles are shown in Fig. C.2(a-b). While there is clear pulse distortion, mostly due to dispersion, the resulting $Q(r)$ is still fit by a Gaussian with extremely high fidelity. In this case, $w_Q = 181$ μm, larger than the theoretical $w_Q = w/\sqrt{3} = 150$ μm.

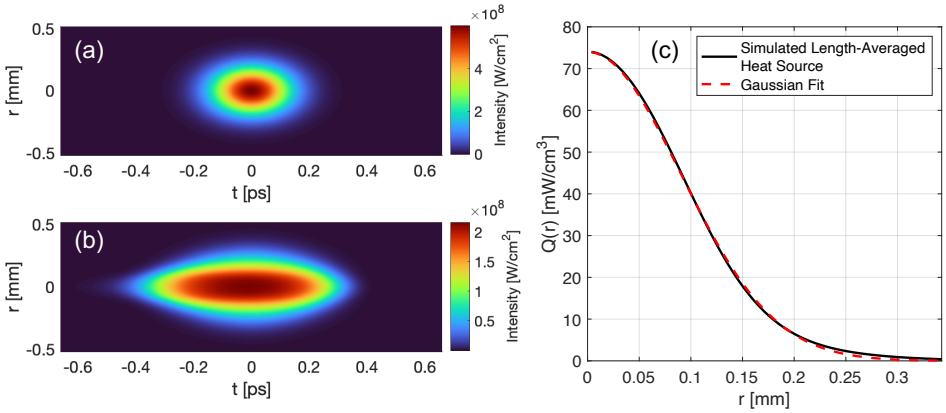

Figure C.2: (a) Initial simulated laser pulse in the focus of the z-scan setup, $I_0 = 0.6$ GW/cm^2, $w_0 = 260$ μm. (b) Simulated laser pulse after 5 mm of propagation through Te (E $\perp$ c). Note the change in color bar scale. Propagation is from left to right. (c) Heat source generated by linear and nonlinear absorption in Te, averaged over length and repetition rate.

After this, we have a heat source that is mathematically described as

$$Q(r) \approx Q_0 \exp\left(\frac{-2r^2}{w_Q^2}\right). \tag{C.4}$$

In this form, we adapt a theory developed by Gordon et al. in Ref. [212] to calculate the time

dependent temperature change $\Delta T(r,t)$ generated by this heat source. Following Refs. [212, 216], the temperature change is

$$\Delta T(r,t) = \int_0^t \int_0^\infty 2\pi r' Q(r') G(r,r',t') dt' dr' \tag{C.5}$$

where

$$G(r,r',t') = \frac{1}{4\pi\kappa t'} \exp\left(\frac{-r^2 - r'^2}{4Dt'}\right) \mathcal{I}_0\left(\frac{rr'}{2Dt'}\right) \tag{C.6}$$

is the Green's function for a line heat source in an unbounded cylindrical medium [217]. Here $\mathcal{I}_0$ is the modified Bessel function of the 1st kind. Integrating ΔT over r' gives an expression modeling the temperature profile as heat accumulates,

$$\Delta T(r,t) = \frac{Q_0}{C} \int_0^t \frac{\exp\left(-2\frac{r^2}{w_Q^2}\frac{1}{1+2t'/t_c}\right)}{1+2t'/t_c} dt'. \tag{C.7}$$

Simulated $\Delta T(r,t)$ is plotted in Fig. C.3 at $z = 0$ using the $Q(r)$ shown in Fig. C.2(c), with the accumulation time normalized to $t_c = 3.71$ ms. The magnitude of the temperature gain is quite small, with only 1 mK peak temperature rise calculated for $t = 5600 t_c = 20.8$ s. Clearly, the temperature rise slowly spreads radially out from the interaction region $w_0 = 260$ μm, and the peak temperature rises logarithmically with time. $t = 1 \times 10^5\, t_c$ is more than 6 minutes of real time, which is on the order of the time a z-scan measurement took in the lab. For practical purposes, this is a steady-state.

An issue in the model arises in this plot, that is for this particular beam size when $t > 1000\, t_c$ the temperature change is non-negligible at $r = 5$ mm. This is the position of the closest crystal facet (assuming the MIR beam is perfectly in the middle of the crystal). While some of the heat will conduct into the aluminum crystal mount or convect off the surfaces exposed to air, it will also lead to further accumulation of heat in the central region. For time-scales we consider, this should not increase the actual peak temperature gain by more than a few times.

To convert the temperature change to refractive index change, we must select a thermo-optic coefficient for tellurium. One option is to take the value for a common direct gap semiconductor

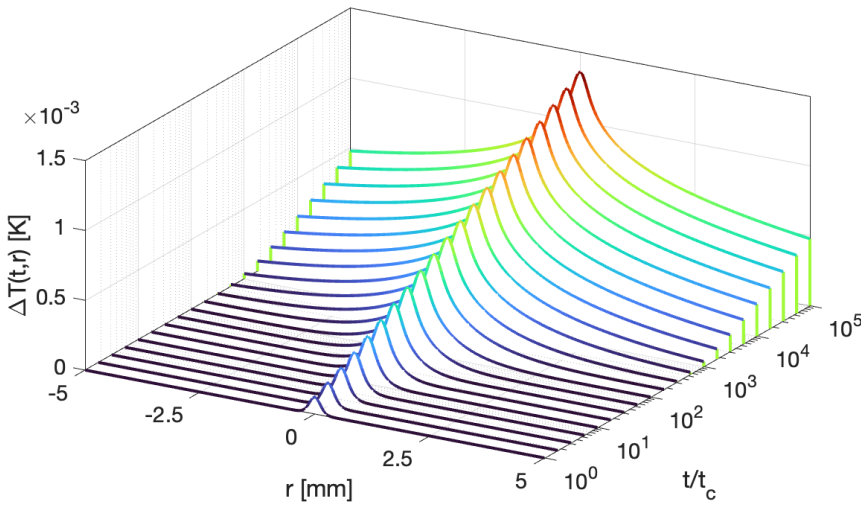

Figure C.3: Calculated temperature change accumulated over time in Te z-scan measurements. t_c = 3.71 ms.

such as GaAs. However, a thermo-optic coefficient has been estimated in thin-film Te [218]. It was found to be quite large, dn/dT = -3.5×10^{-3} K^{-1}. While this value in a thin-film should not be expected to be the same as in a bulk material (e.g. due to increased strain [219]), we will take this large magnitude of $dn/dT = 3.5 \times 10^{-3}$ to attempt to overestimate rather than underestimate the thermal effects.

Finally, we compare the phase shift that accumulates via thermal effects versus nonlinear effects. A thermal B integral is defined as

$$B_{therm}(r,t) = \frac{2\pi}{\lambda_0}\int_0^L \Delta T(r,z,t)\frac{dn}{dT}dz = \frac{2\pi L}{\lambda_0}\Delta T(r,t)\frac{dn}{dT}. \tag{C.8}$$

Peak B_{therm} accumulation calculated with the tellurium z-scan experimental parameters is plotted in Fig. C.4 for multiple z locations. The radial heat sources in all cases are close to Gaussian, so the peak thermal phase is at the beam center, $r = 0$. Based on the I^3 absorption scaling, it makes sense that the most heat is deposited at $z = 0$ where the beam is most intense, regardless of the faster t_c. According to these calculations, 1000 seconds after irradiation begins, the MIR laser accumulates only 15 mRad of thermal phase at the beam center. This should be compared to the nonlinear phase shift, which for these experimental conditions accumulates $B_{NL} = 3.1$ rad of phase.

Since $B_{NL}/B_{therm} > 200$, we conclude that thermal effects are insignificant in our closed aperture z-scan measurements in tellurium. This supports the qualitative reasoning above.

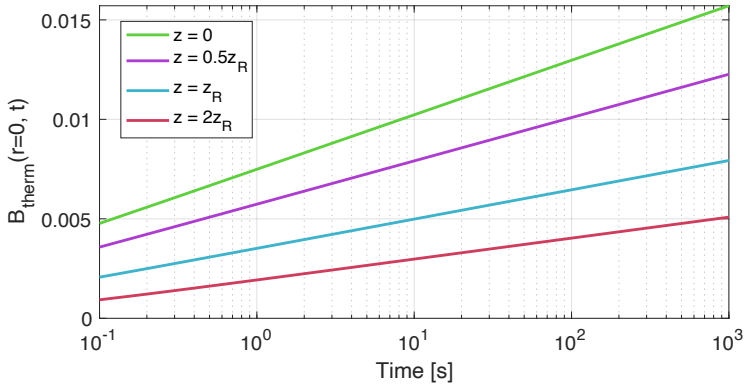

Figure C.4: Thermal phase accumulation at different z positions of the Te sample.

The focal length of the thermal lens can be estimated easily by the formula [216]

$$f = -\left(L\frac{\partial^2 n}{\partial r^2}\Big|_{r=0}\right)^{-1}, \tag{C.9}$$

where $\frac{\partial^2 n}{\partial r^2}\Big|_{r=0}$ is the curvature of the refractive index profile at the beam center. This parabolic approximation of the central temperature gradient works well on-axis, as shown in Fig. C.5. Ref. [212] shows that the thermal lens focal length stabilizes after only a few t_c, which our modeling shows as well. For the experimental conditions, f_{therm} is 4.8 m – recall that the detector in the closed aperture z-scan measurements is ∼40 cm from the focus.

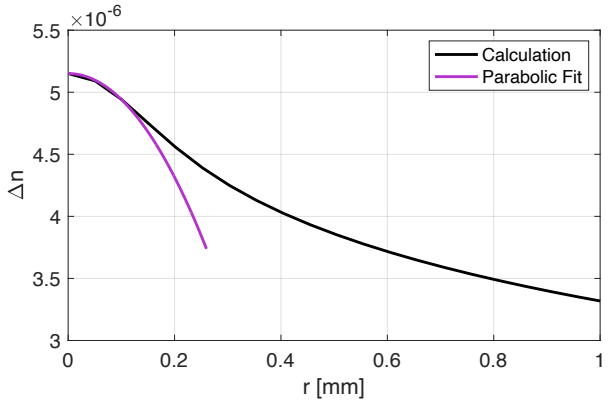

Figure C.5: Parabolic approximation to find thermal lens focal length.

While thermal effects are not important for the closed-aperture z-scan measurements, where far-field beam focusing is the critical observable, it may not be negligible in other measurements. Before this brief discussion it is crucial to mention that thermal effects *would not* change the results and conclusions drawn from other measurements performed in this dissertation. In the open-aperture z-scan, the full beam is collected after the sample and in SPM, accumulated thermal effects do not have any effect on spectrum.

SPM measurements in Te are performed with $I_0 = 1.5$ GW/cm^2 and beam size $w = 980$ μm. To get these higher intensities with much a much larger beam, most of the attenuation used in the closed-aperture z-scan measurements are removed. Therefore, much more energy is deposited per pulse. Following the same analysis as above, we find in this parameter space $t_c = 60$ ms and an on-axis heat source of 340 mW/cm^3, much higher than before. This results in temperature change up to 0.1 K and peak $B_{therm} = 0.93$ rad, compared with peak $B_{NL} \approx 4.5$ rad. However, due to the larger beam size, the thermal focal length is still 0.92 m. Again, since the thermal phase shift is *not* instantaneous, it will not cause any spectral modulation and does not influence the conclusions of SPM-based n_2 measurements in any way.

Applying this model to the highest intensities of the open aperture z-scan measurement is difficult, as there are is strong spatio-temporal perturbations and gNLSE simulations do not accurately represent experimental data (Section 5.6). Instead, we use the smallest beam size/highest intensity where our gNLSE simulations match well with experiment: $w = 410$ μm, $I_0 = 2.1$ GW/cm^2 (Fig. 5.14). We find $t_c = 12$ ms, and an even higher 540 mW/cm^3 heat source. The smaller t_c does result in only $\Delta T = 0.03$ K over 1000 s and 0.36 rad thermal phase compared to 4.7 rad nonlinear phase. The thermal lens focal length is 58 cm, much longer than the self-focusing length.

For completeness, GaAs, n-Ge, and ZnSe have weak linear absorption in the closed aperture z-scan measurements. While they are irradiated at higher power than Te, they have much better thermal properties and the total thermal effects are negligible.

To conclude, we find that thermal effects do not impact the closed-aperture z-scan measurements performed in this dissertation. Despite the high repetition rate laser and accumulation of heat, we showed above that thermal focusing effects are negligible compared to instantaneous nonlinear optical effects.

Appendix D
Supercontinuum Generation in Tellurium

Supercontinuum (SC) generation is a remarkable process where a short laser pulse undergoes extreme spectral broadening during propagation through a nonlinear medium. Several individual linear and third-order nonlinear optical effects may contribute, including self-phase modulation, dispersion, stimulated Raman scattering, and solitonic propagation [220, 221]. A majority of previous work on SC generation has been done using ultrafast NIR laser pulses to pump fibers. Fibers as the nonlinear medium compensate for relatively low Kerr nonlinearity with some huge advantages, namely scalable interaction length, guided propagation to maintain high intensity over long distances, and the ability to engineer material dispersion profiles (e.g. photonic crystal fibers [220]). High power MIR laser sources have driven interest in expanding the extent of SC generation to long wavelengths, where many applications in spectroscopy and imaging exist [222–225]. Chalcogenide fibers have been the material most studied, which have allowed for SC reaching as far as 16 μm [226, 227].

Alternatively, bulk crystals can be used as the nonlinear medium for SC generation. While scaling crystal length is typically not practical, optical nonlinearities can be orders of magnitude larger than those in fibers. Historically a predecessor of broadband radiation generation in fibers, bulk SC experiments have been successfully performed in crystals such as GaAs [52, 228, 229], YAG [230], and ZnSe [70], which provide naturally wide transparency ranges. So far, bulk SC generation has produced spectral broadening to wavelengths as long as 20 μm in GaAs [228]. Few materials have natural transparency throughout the MIR and into the far-infrared (FIR, 20+ μm). Our findings in tellurium (Chapters 5, 6), along with the measured transparency reaching to 30+ μm (Fig. 5.1) and demand of a pump pulse with wavelength longer than 8 μm to avoid two-photon absorption, have left the SC generation potential of this material untapped.

Here, we present preliminary experimental results of supercontinuum generation in Te pumped with 3.5 ps CO_2 laser pulses. Initial spectral measurements show generated light as far as 30 μm, but some experimental and modeling questions must be answered to verify the validity of the

measurements. At the time of writing, this is an ongoing project.

The crystal sample used is the 5 mm long Sample 1 from Fig. 5.1. The orientation allows for phase matched type I (eeo) SHG of 10.6 μm light. We pumped the crystal in two different orientations, first with the laser electric field polarized in the nominal phase matching direction. We also rotated the crystal by 90 degrees to detune from the SHG phase matching orientation.

The experimental setup is similar to that used to measure SHG (Chapter 6) with some slight modifications. First, the plasma shutter is optimized to screen the incoming pulse train more quickly. The transmitted pulse train used to pump the crystal contains up to 4 mJ in 3-4 short pulses. The faster ionization rise-time results in approximately 50% of the total energy contained in the most energetic pulse. The beam is focused to $w_0 = 450$ μm radius on the surface of Te. Careful measurement of the beam profile in this new experimental setup reveals that only 30% of the total energy is contained within the beam core. The calculated peak intensity inside the crystal reaches up to 20 GW/cm^2.

The light emerging from the crystal is collected as close to the back surface as possible in an attempt to collect quickly diverging red-shifted radiation. The same scanning monochromator (Horiba, iHR-550) used in the main text was used for spectral measurements. Three different gratings (100 grooves/mm blazed at 9 μm, 50 grooves/mm blazed at 12 μm, 50 grooves/mm blazed at 24 μm) with known relative spectral efficiencies were used to cover the entire Te transparency range. A calibrated cryogenically cooled HgCdTe detector (KRS-5 window) was used for signal detection. Known spectral sensitivity peaked at 20 μm.

Water absorption in air ($\sim$ 3.5 Torr), which has strong absorption beyond 20 μm [231], limited our measurements to a few spectral regions. These transmission windows are shown in Fig. D.1.

The measured SC spectrum is depicted in Fig. D.2 for the phase matched orientation. Only peak pulse intensities between 8-20 GW/cm^2 are binned and averaged. We observe signal between 7.5-32 μm continuously, which discretely extends to 5.3 μm via SHG. Total estimated energy contained in the long wavelength plateau (15-32 μ) is ≥ 0.5 μJ, or $> 10^{-4}$ of the initial pump energy.

Notably, there are clear peaks in the vicinity of 9.3 μm, 12.5 μm, and 14.5 μm. These correspond closely to predicted SRS sidebands in Te: anti-Stokes (AS1) and two separate Stokes (S1, S2) sidebands. The Raman spectrum of Te has multiple features, but the strongest is the symmetric

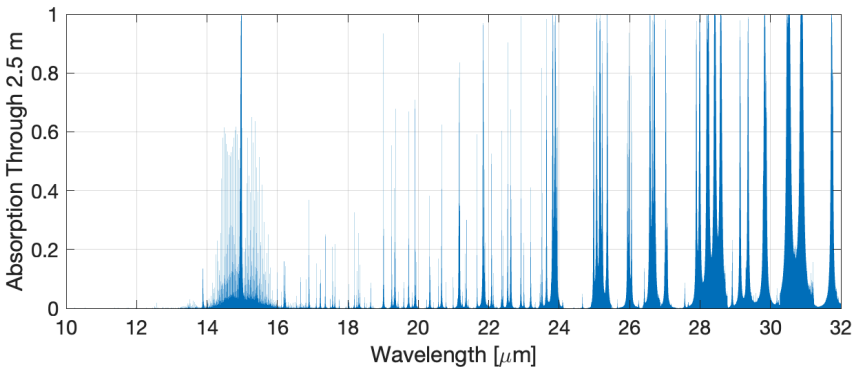

Figure D.1: Fraction of light absorbed in 2.5 m of air, the distance between crystal and detection. The HITRAN mean latitude winter model is used to describe the absorption spectrum of atmospheric water vapors. Beyond 20 μm, measurements are made only in spectral windows where absorption is negligible.

breathing mode of the helical Te chain with frequency 120 cm^{-1} [118, 138, 232]. The first two Stokes sidebands would theoretically appear at 12.2 and 14.2 μm with this frequency shift, and the first anti-Stokes at 9.4 μm.

When crystal orientation is changed to detune SHG phase matching, SHG is still present (albeit weaker). There are changes to the SRS sidebands between the two orientations. Most significantly, in the non-phase matched orientation, the signal at the 2nd Stokes SRS sideband is surprisingly higher than at the 1st Stokes sideband (Fig. D.3). These SRS dynamics are not fully understood at this time.

Although we detected light in the range of 10–30+ μm, the signal to noise ratio of these measurements is an unresolved question. There are parasitic ghosts of the pump central wavelength from the diffraction gratings at 16.5 and 24 μm (hence the gaps in the spectrum), but it is not clear how much of the observed signal in the long wavelength plateau is true long wavelength light versus residual/stray pump light. Further experimental confirmations of the noise spectrum and SC spectrum are required.

Preliminary modeling of the SC generation was performed with a 1 dimensional version of the gNLSE which includes a delayed SRS response and spectral noise to seed the SRS gain. Using a realistic n_2, the numerical supercontinuum spectrum is found to extend from 7.5–30 μm, but only when the delayed Raman response is turned on. Furthermore, nonlinear absorption is not

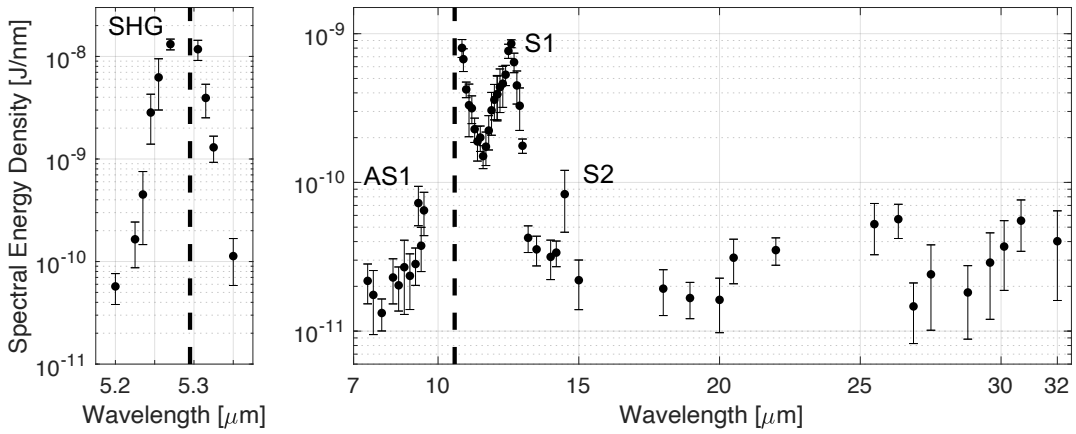

Figure D.2: Full SC spectrum measured in experiment. Pump wavelength and its second harmonic are both marked. Note the different vertical scale for the panels.

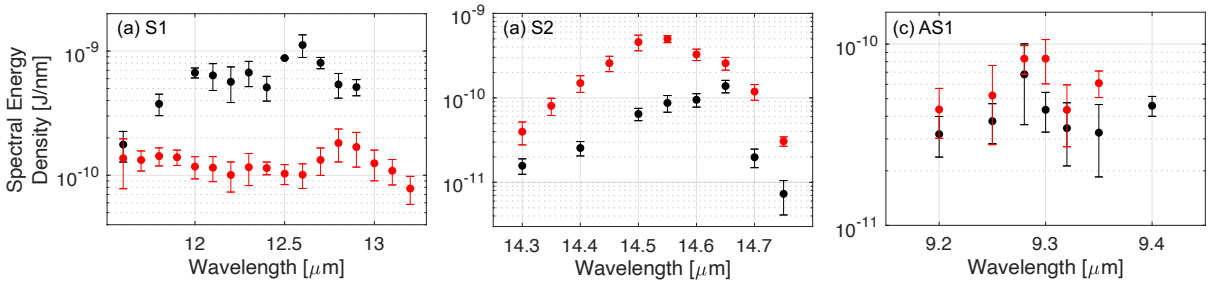

Figure D.3: Detailed measurements of the (a) 1st Stokes, (b) 2nd Stokes, and (c) 1st anti-Stokes SRS sidebands. Black data is measured in the phase matched orientation, while red data is from the non-phase matched orientation.

included in the model. In light of our measurements of NLA in Te presented in Chapter 5, NLA and free-carrier effects must be included in the 2D gNLSE to accurately model the SC generation process.

The zero GVD point of Te is at 16.6 μm for E $\perp$ c and 19.7 μm for E // c [108], which means that both orientations we study are in the positive (normal) GVD regime. Soliton fission and modulational instability, which often dominate SC spectra generated in the NIR, cannot occur – even when considering higher order dispersion [233]. We conclude that the observed spectral broadening is likely caused by SRS in combination with SPM, supported by the relatively strong sideband efficiency.

To summarize, tellurium is a promising candidate as a supercontinuum source to fill the far-

infrared spectral range with radiation. Further experimental work must be done to improve the signal to noise ratio in measurements as well as understand the complicated nonlinear dynamics of propagating CO_2 laser pulses in an extremely nonlinear medium. Pumping Te near its zero GVD point at 16.6 μm could present an interesting regime of SC generation; a 16.7 μm optically pumped CO_2 amplifier operating in the 021–011 band [234] might open an opportunity to test this scheme.

References

[1] D. M. Mittleman, Opt. Express **26**, 9417 (2018).

[2] H. A. Hafez, X. Chai, A. Ibrahim, S. Mondal, D. Férachou, X. Ropagnol, and T. Ozaki, Journal of Optics **18**, 093004 (2016).

[3] P. B. Corkum and F. Krausz, Nature Physics **3**, 381 (2007).

[4] Y. Fu, K. Nishimura, R. Shao, A. Suda, K. Midorikawa, P. Lan, and E. J. Takahashi, Communications Physics **3**, 92 (2020).

[5] B. Dromey, M. Zepf, A. Gopal, K. Lancaster, M. S. Wei, K. Krushelnick, M. Tatarakis, N. Vakakis, S. Moustaizis, R. Kodama, M. Tampo, C. Stoeckl, R. Clarke, H. Habara, D. Neely, S. Karsch, and P. Norreys, Nature Physics **2**, 456 (2006).

[6] S. M. Hendrickson, A. C. Foster, R. M. Camacho, and B. D. Clader, J. Opt. Soc. Am. B **31**, 3193 (2014).

[7] J. Wang, F. Sciarrino, A. Laing, and M. G. Thompson, Nature Photonics **14**, 273 (2020).

[8] T. H. Maiman, Nature **187**, 493 (1960).

[9] P. B. Corkum, Phys. Rev. Lett. **71**, 1994 (1993).

[10] T. Popmintchev, M.-C. Chen, D. Popmintchev, P. Arpin, S. Brown, S. Ališauskas, G. Andriukaitis, T. Balčiunas, O. D. Mücke, A. Pugzlys, A. Baltuška, B. Shim, S. E. Schrauth, A. Gaeta, C. Hernández-García, L. Plaja, A. Becker, A. Jaron-Becker, M. M. Murnane, and H. C. Kapteyn, Science **336**, 1287 (2012).

[11] A. D. Koulouklidis, C. Gollner, V. Shumakova, V. Y. Fedorov, A. Pugžlys, A. Baltuška, and S. Tzortzakis, Nature Communications **11**, 292 (2020).

[12] I. V. Pogorelsky, M. N. Polyanskiy, and W. D. Kimura, Phys. Rev. Accel. Beams **19**, 091001 (2016).

[13] D. Haberberger, S. Tochitsky, and C. Joshi, Opt. Express **18**, 17865 (2010).

[14] M. N. Polyanskiy, M. Babzien, and I. V. Pogorelsky, Optica **2**, 675 (2015).

[15] G. Andriukaitis, T. Balčiūnas, S. Ališauskas, A. Pugžlys, A. Baltuška, T. Popmintchev, M.-C. Chen, M. M. Murnane, and H. C. Kapteyn, Opt. Lett. **36**, 2755 (2011).

[16] U. Elu, T. Steinle, D. Sánchez, L. Maidment, K. Zawilski, P. Schunemann, U. D. Zeitner, C. Simon-Boisson, and J. Biegert, Opt. Lett. **44**, 3194 (2019).

[17] M. Sheik-Bahae, D. Hutchings, D. Hagan, and E. Van Stryland, IEEE Journal of Quantum Electronics **27**, 1296 (1991).

[18] Y. R. Shen, *The Principles of Nonlinear Optics*, 1st ed. (Wiley-Interscience, 2002).

[19] R. W. Boyd, *Nonlinear Optics*, 3rd ed., R. W. Boyd (Academic Press, 2008).

[20] R. DeSalvo, D. J. Hagan, M. Sheik-Bahae, G. Stegeman, E. W. V. Stryland, and H. Vanherzeele, Opt. Lett. **17**, 28 (1992).

[21] V. G. Dmitriev, G. G. Gurzadyan, and D. N. Nikogosyan, *Handbook of Nonlinear Optical Crystals* (Springer-Verlag, Berlin, 1999).

[22] P. N. Butcher and D. Cotter, *The Elements of Nonlinear Optics* (Cambridge University Press, 1990).

[23] G. P. Agrawal, *Nonlinear fiber optics*, 4th ed. (Academic Press, 2007).

[24] A. Houard, P. Walch, T. Produit, V. Moreno, B. Mahieu, A. Sunjerga, C. Herkommer, A. Mostajabi, U. Andral, Y.-B. André, M. Lozano, L. Bizet, M. C. Schroeder, G. Schimmel, M. Moret, M. Stanley, W. A. Rison, O. Maurice, B. Esmiller, K. Michel, W. Haas, T. Metzger, M. Rubinstein, F. Rachidi, V. Cooray, A. Mysyrowicz, J. Kasparian, and J.-P. Wolf, Nature Photonics **17**, 231 (2023).

[25] T. Nagy, P. Simon, and L. Veisz, Adv. Phys.: X **6**, 1845795 (2021).

[26] J. J. Pigeon, S. Y. Tochitsky, E. C. Welch, and C. Joshi, Opt. Lett. **41**, 3924 (2016).

[27] J. Marburger, Progress in Quantum Electronics **4**, 35 (1975).

[28] W. Liu and S. Chin, Opt. Express **13**, 5750 (2005).

[29] R. W. Boyd, S. G. Lukishova, and Y. R. Shen, *Self-Focusing: Past and Present* (Springer, 2009).

[30] B. S. Wherrett, J. Opt. Soc. Am. B **1**, 67 (1984).

[31] L. V. Keldysh, Sov. Phys. J. Exp. Theor. Phys. **20**, 1307 (1965).

[32] S. Y. Kruchinin, F. Krausz, and V. S. Yakovlev, Rev. Mod. Phys. **90**, 021002 (2018).

[33] C. K. N. Patel, R. E. Slusher, and P. A. Fleury, Phys. Rev. Lett. **17**, 1011 (1966).

[34] P. A. Wolff and G. A. Pearson, Phys. Rev. Lett. **17**, 1015 (1966).

[35] Y. Rosenwaks, M. C. Hanna, D. H. Levi, D. M. Szmyd, R. K. Ahrenkiel, and A. J. Nozik, Phys. Rev. B **48**, 14675 (1993).

[36] H. Y. Fan, Reports on Progress in Physics **19**, 107 (1956).

[37] M. Kira and S. W. Koch, *Semiconductor Quantum Optics* (Cambridge University Press, 2012).

[38] A. Couairon, E. Brambilla, T. Corti, D. Majus, O. de J. Ramírez-Góngora, and M. Kolesik, Eur. Phys. J-Spec. Top. **199**, 5 (2011).

[39] C. Husko, P. Colman, S. Combrié, A. D. Rossi, and C. W. Wong, Opt. Lett. **36**, 2239 (2011).

[40] E. Yablonovitch, Phys. Rev. Lett. **60**, 795 (1988).

[41] A. E. Siegman, *Lasers*, 1st ed. (University Science Books, 1986).

[42] A. Sommer, E. M. Bothschafter, S. A. Sato, C. Jakubeit, T. Latka, O. Razskazovskaya, H. Fattahi, M. Jobst, W. Schweinberger, V. Shirvanyan, V. S. Yakovlev, R. Kienberger, K. Yabana, N. Karpowicz, M. Schultze, and F. Krausz, Nature **534**, 86 (2016).

[43] T. Brabec and F. Krausz, Phys. Rev. Lett. **78**, 3282 (1997).

[44] U. Huttner, M. Kira, and S. W. Koch, Laser Photonics Rev. **11**, 1700049 (2017).

[45] G. Vampa, C. R. McDonald, G. Orlando, D. D. Klug, P. B. Corkum, and T. Brabec, Phys. Rev. Lett. **113**, 073901 (2014).

[46] I. Kilen, M. Kolesik, J. Hader, J. V. Moloney, U. Huttner, M. K. Hagen, and S. W. Koch, Phys. Rev. Lett. **125**, 083901 (2020).

[47] R. C. Miller, Appl. Phys. Lett. **5**, 17 (1964).

[48] W. Ettoumi, Y. Petit, J. Kasparian, and J.-P. Wolf, Opt. Express **18**, 6613 (2010).

[49] T. R. Ensley and N. K. Bambha, Opt. Express **27**, 37940 (2019).

[50] M. N. Polyanskiy, I. V. Pogorelsky, M. Babzien, K. L. Vodopyanov, and M. A. Palmer, Opt. Mater. Express **14**, 696 (2024).

[51] C. K. N. Patel, Phys. Rev. **136**, A1187 (1964).

[52] P. Corkum, IEEE Journal of Quantum Electronics **21**, 216 (1985).

[53] E. Welch, D. Matteo, S. Tochitsky, and C. Joshi, in *2018 IEEE Advanced Accelerator Concepts Workshop (AAC)* (2018) pp. 1–4.

[54] W. J. Witteman, *The CO_2 Laser*, 1st ed. (Springer Berlin, 1987).

[55] T. Chang and O. Wood, Appl. Phys. Lett. **23**, 370 (1973).

[56] D. Tovey, J. J. Pigeon, S. Y. Tochitsky, G. Louwrens, I. Ben-Zvi, C. Joshi, D. Martyshkin, V. Fedorov, K. Karki, and S. Mirov, Journal of Applied Physics **128**, 103103 (2020).

[57] D. Tovey, J. Pigeon, S. Tochitsky, G. Louwrens, I. Ben-Zvi, D. Martyshkin, V. Fedorov, K. Karki, S. Mirov, and C. Joshi, Opt. Express **29**, 31455 (2021).

[58] S. B. Mirov, I. S. Moskalev, S. Vasilyev, V. Smolski, V. V. Fedorov, D. Martyshkin, J. Peppers, M. Mirov, A. Dergachev, and V. Gapontsev, IEEE Journal of Selected Topics in Quantum Electronics **24**, 1 (2018).

[59] D. Martyshkin, V. Fedorov, S. J. Hamlin, and S. Mirov, Opt. Express **31**, 18525 (2023).

[60] C. V. Filip, R. Narang, S. Y. Tochitsky, C. E. Clayton, and C. Joshi, Appl. Opt. **41**, 3743 (2002).

[61] S. Tochitsky, E. Welch, M. Polyanskiy, I. Pogorelsky, P. Panagiotopoulos, M. Kolesik, E. M. Wright, S. W. Koch, J. V. Moloney, J. Pigeon, and C. Joshi, Nature Photonics **13**, 41 (2019).

[62] D. Haberberger, S. Tochitsky, F. Fiuza, C. Gong, R. A. Fonseca, L. O. Silva, W. B. Mori, and C. Joshi, Nature Physics **8**, 95 (2012).

[63] K. L. Vodopyanov, *Laser-based mid-infrared sources and applications* (John Wiley & Sons, Hoboken, NJ, 2020).

[64] P. Fuertjes, M. Bock, L. von Grafenstein, D. Ueberschaer, U. Griebner, and T. Elsaesser, Optica **9**, 1303 (2022).

[65] T. Skauli, P. S. Kuo, K. L. Vodopyanov, T. J. Pinguet, O. Levi, L. A. Eyres, J. S. Harris, M. M. Fejer, B. Gerard, L. Becouarn, and E. Lallier, Journal of Applied Physics **94**, 6447 (2003).

[66] C. J. Hutchinson, C. Lewis, J. A. Savage, and A. Pitt, Appl. Opt. **21**, 1490 (1982).

[67] M. Baudrier-Raybaut, R. Haïdar, P. Kupecek, P. Lemasson, and E. Rosencher, Nature **432**, 374 (2004).

[68] T. Kawamori, Q. Ru, and K. L. Vodopyanov, Phys. Rev. Appl. **11**, 054015 (2019).

[69] J. Gu, A. Schweinsberg, L. Vanderhoef, M. Tripepi, A. Valenzuela, C. Wolfe, T. R. Ensley, E. Chowdhury, and M. Kolesik, Opt. Express **29**, 7479 (2021).

[70] K. Werner, M. G. Hastings, A. Schweinsberg, B. L. Wilmer, D. Austin, C. M. Wolfe, M. Kolesik, T. R. Ensley, L. Vanderhoef, A. Valenzuela, and E. Chowdhury, Opt. Express **27**, 2867 (2019).

[71] P. Xia, C. Kim, F. Lu, T. Kanai, H. Akiyama, J. Itatani, and N. Ishii, Opt. Express **26**, 29393 (2018).

[72] A. F. Gibson, C. A. Rosito, C. A. Raffo, and M. F. Kimmitt, Appl. Phys. Lett. **21**, 356 (1972).

[73] F. Keilmann, IEEE J. Quantum Electron. **QE-12**, 592 (1976).

[74] J. C. R. Phipps and S. J. Thomas, Optics Letters **1**, 93 (1977).

[75] M. Woerner, T. Elsaesser, and W. Kaiser, Physical Review B **45**, 8378 (1992).

[76] Y. K. Danileiko, T. P. Levedeva, A. A. Manenkov, and A. V. Sidorin, in *Laser Induced Damage in Optical Materials: 1981*, edited by H. Bennett, A. G. nad D. Milam, and B. Newnam (ASTM International, 1983).

[77] C. Rauscher and R. Laenen, J. Appl. Phys. **81**, 2818 (1997).

[78] S. Y. Yuen, R. L. Aggarwal, N. Lee, and B. Lax, Opt. Commun. **28**, 237 (1979).

[79] S. Y. Yuen, R. L. Aggarwal, and B. Lax, J. Appl. Phys. **51**, 1146 (1980).

[80] H. Furuse, N. Mori, H. Kubo, H. Momose, and M. Kondow, Phys. Rev. B **74**, 205206 (2006).

[81] H. Furuse, N. Mori, H. Kubo, H. Momose, and M. Kondow, J. Mater. Sci.: Mater. Electron. **18**, 81 (2007).

[82] D. Seo, J. M. Gregory, , L. C. Feldman, N. H. Tolk, and P. I. Cohen, Phys. Rev. B **83**, 195203 (2011).

[83] R. B. James and D. L. Smith, IEEE J. Quantum Electron. **QE-18**, 1841 (1982).

[84] R. B. James, J. Appl. Phys. **54**, 3220 (1983).

[85] J. J. Wynne, Phys. Rev. **178**, 1295 (1969).

[86] T. Kawamori, P. G. Schunemann, V. Gruzdev, and K. L. Vodopyanov, APL Photonics **7**, 086101 (2022).

[87] D. Bois, P. Leyral, and C. Schiller, Journal of Electronic Materials **5**, 275 (1976).

[88] W. B. Jackson, N. M. Johnson, and D. K. Biegelsen, Applied Physics Letters **43**, 195 (1983).

[89] H. H. Li, Journal of Physical and Chemical Reference Data **9**, 561 (1980).

[90] J. Connolly, B. diBenedetto, and R. Donadio, in *Contemporary Optical Systems and Components Specifications*, Vol. 0181, edited by R. E. Fischer, International Society for Optics and Photonics (SPIE, 1979) pp. 141 – 144.

[91] W. C. Hurlbut, Y.-S. Lee, K. L. Vodopyanov, P. S. Kuo, and M. M. Fejer, Optics Letters **32**, 668 (2007).

[92] A. A. Said, M. Sheik-Bahae, D. J. Hagan, T. H. Wei, J. Wang, J. Young, and E. W. Van Stryland, J. Opt. Soc. Am. B **9**, 405 (1992).

[93] T. D. Krauss and F. W. Wise, Applied Physics Letters **65**, 1739 (1994), https://pubs.aip.org/aip/apl/article-pdf/65/14/1739/18507092/1739_1_online.pdf .

[94] C. L. Smallwood and S. T. Cundiff, Laser & Photonics Reviews **12**, 1800171 (2018).

[95] S. E. Trubnick, *Development of Teflon Bonding Technology for Nonlinear Optical Gallium Arsenide Devices*, M.s. thesis, University of California Los Angeles (2007).

[96] C. M. Cirloganu, L. A. Padilha, D. A. Fishman, S. Webster, D. J. Hagan, and E. W. V. Stryland, Opt. Express **19**, 22951 (2011).

[97] P. Zhao, M. Reichert, D. J. Hagan, and E. W. V. Stryland, Opt. Express **24**, 24907 (2016).

[98] S. Y. Auyang and P. A. Wolff, J. Opt. Soc. Am. B **6**, 595 (1989).

[99] M. M. Fejer, S. J. B. Yoo, R. L. Byer, A. Hartwit, and J. S. Harris, Jr., Phys Rev. Lett. **62**, 1041 (1989).

[100] J. N. Heyman, K. Craig, B. Galdrikian, M. S. Sherwin, K. Campman, P. F. Hopkins, S. Fafard, and A. C. Gossard, Phys Rev. Lett. **72**, 2183 (1994).

[101] K. L. Vodopyanov, K. O'Neill, G. B. Serapiglia, C. C. Phillips, M. Hopkinson, I. Vurgaftman, and J. R. Meyer, Appl. Phys. Lett. **72**, 2654 (1998).

[102] S. Sauvage, P. Boucaud, F. Glotin, R. Prazeres, J.-M. Ortega, A. Lemaitre, J.-M. Gerard, and V. Thierry-Mieg, Phys Rev. B **59**, 9830 (1999).

[103] K. Akiyama, N. Tomita, Y. Nomura, and T. Isu, Appl. Phys. Lett. **75**, 475 (1999).

[104] V. O. Petukhov, S. Y. Tochitsky, and V. V. Churakov, Sov. J. Quantum Electron. **17**, 389 (1987).

[105] A. Schliesser, N. Picqué, and T. W. Hänsch, Nature Photonics **6**, 440 (2012).

[106] E. A. Johnson, A. MacKinnon, E. P. O'Reilly, and M. Silver, Phys. Rev. Lett. **65**, 752 (1990).

[107] S. Adachi, *Properties of Group-IV, III-V and II-VI semiconductors* (John Wiley & Sons, West Sussex, England, 2005).

[108] R. S. Caldwell and H. Y. Fan, Phys. Rev. **114**, 664 (1959).

[109] V. Asnin, A. Bakun, A. Danishevskii, E. Ivchenko, G. Pikus, and A. Rogachev, Solid State Communications **30**, 565 (1979).

[110] T. Furukawa, Y. Shimokawa, K. Kobayashi, and T. Itou, Nature Communications **8**, 954 (2017).

[111] L. E. Vorob'ev, E. L. Ivchenko, G. E. Pikus, I. I. Farbshtein, V. A. Shalygin, and A. V. Shturbin, JETP Lett. **29**, 441 (1979).

[112] M. Sakano, M. Hirayama, T. Takahashi, S. Akebi, M. Nakayama, K. Kuroda, K. Taguchi, T. Yoshikawa, K. Miyamoto, T. Okuda, K. Ono, H. Kumigashira, T. Ideue, Y. Iwasa, N. Mitsuishi, K. Ishizaka, S. Shin, T. Miyake, S. Murakami, T. Sasagawa, and T. Kondo, Phys. Rev. Lett. **124**, 136404 (2020).

[113] G. Jnawali, Y. Xiang, S. M. Linser, I. A. Shojaei, R. Wang, G. Qiu, C. Lian, B. M. Wong, W. Wu, P. D. Ye, Y. Leng, H. E. Jackson, and L. M. Smith, Nature Communications **11**, 3991 (2020).

[114] T. Ideue, M. Hirayama, H. Taiko, T. Takahashi, M. Murase, T. Miyake, S. Murakami, T. Sasagawa, and Y. Iwasa, Proceedings of the National Academy of Sciences **116**, 25530 (2019).

[115] J. Chen, T. Zhang, J. Wang, L. Xu, Z. Lin, J. Liu, C. Wang, N. Zhang, S. P. Lau, W. Zhang, M. Chhowalla, and Y. Chai, Science Advances **8**, eabn3837 (2022).

[116] C. Zhao, C. Tan, D.-H. Lien, X. Song, M. Amani, M. Hettick, H. Y. Y. Nyein, Z. Yuan, L. Li, M. C. Scott, and A. Javey, Nature Nanotechnology **15**, 53 (2020).

[117] L. A. Agapito, N. Kioussis, W. A. Goddard, and N. P. Ong, Phys. Rev. Lett. **110**, 176401 (2013).

[118] J.-K. Qin, P.-Y. Liao, M. Si, S. Gao, G. Qiu, J. Jian, Q. Wang, S.-Q. Zhang, S. Huang, A. Charnas, Y. Wang, M. J. Kim, W. Wu, X. Xu, H.-Y. Wang, L. Yang, Y. Khin Yap, and P. D. Ye, Nature Electronics **3**, 141 (2020).

[119] A. Kramer, M. L. Van de Put, C. L. Hinkle, and W. G. Vandenberghe, npj 2D Materials and Applications **4**, 10 (2020).

[120] T. Doi, K. Nakao, and H. Kamimura, Journal of the Physical Society of Japan **28**, 36 (1970).

[121] H. Shinno, R. Yoshizaki, S. Tanaka, T. Doi, and H. Kamimura, Journal of the Physical Society of Japan **35**, 525 (1973).

[122] K. Nakayama, M. Kuno, K. Yamauchi, S. Souma, K. Sugawara, T. Oguchi, T. Sato, and T. Takahashi, Phys. Rev. B **95**, 125204 (2017).

[123] S. C. Liebscher, M. K. Hagen, J. Hader, J. V. Moloney, and S. W. Koch, Phys. Rev. B **104**, 165201 (2021).

[124] S. Tutihasi, G. G. Roberts, R. C. Keezer, and R. E. Drews, Phys. Rev. **177**, 1143 (1969).

[125] D. Hardy and C. Rigaux, physica status solidi (b) **38**, 799 (1970).

[126] D. Fischer, E. Bangert, and P. Grosse, physica status solidi (b) **55**, 527 (1973).

[127] N. Miura, R. Yoshizaki, and S. Tanaka, Solid State Communications **7**, 1195 (1969).

[128] M. Sheik-Bahae, A. Said, T.-H. Wei, D. Hagan, and E. Van Stryland, IEEE Journal of Quantum Electronics **26**, 760 (1990).

[129] J. A. Hermann and R. G. McDuff, J. Opt. Soc. Am. B **10**, 2056 (1993).

[130] S. C. Pinault and M. J. Potasek, J. Opt. Soc. Am. B **2**, 1318 (1985).

[131] H. Hirori, K. Shinokita, M. Shirai, S. Tani, Y. Kadoya, and K. Tanaka, Nature Communications **2**, 594 (2011).

[132] T. Brabec and F. Krausz, Rev. Mod. Phys. **72**, 545 (2000).

[133] D. S. Corrêa, L. De Boni, L. Misoguti, I. Cohanoschi, F. E. Hernandez, and C. R. Mendonça, Optics Communications **277**, 440 (2007).

[134] S. Pearl, N. Rotenberg, and H. M. van Driel, Applied Physics Letters **93**, 131102 (2008).

[135] M. P. Hasselbeck, A. A. Said, E. W. van Stryland, and M. Sheik-Bahae, Optical and Quantum Electronics **30**, 193 (1998).

[136] M. Sheik-bahae, P. Mukherjee, and H. S. Kwok, J. Opt. Soc. Am. B **3**, 379 (1986).

[137] P. D. Olszak, C. M. Cirloganu, S. Webster, L. A. Padilha, S. Guha, L. P. Gonzalez, S. Krishnamurthy, D. J. Hagan, and E. W. Van Stryland, Phys. Rev. B **82**, 235207 (2010).

[138] A. S. Pine and G. Dresselhaus, Phys. Rev. B **4**, 356 (1971).

[139] G. C. Bhar, Appl. Opt. **15**, 305 (1976).

[140] M. Hohenleutner, F. Langer, O. Schubert, M. Knorr, U. Huttner, S. W. Koch, M. Kira, and R. Huber, Nature **523**, 572 (2015).

[141] J.-L. Oudar, C. Schwartz, and E. Batifol, IEEE Journal of Quantum Electronics **11**, 623 (1975).

[142] S. Akturk, X. Gu, P. Bowlan, and R. Trebino, Journal of Optics **12**, 093001 (2010).

[143] F. Capasso, C. Sirtori, and A. Cho, IEEE Journal of Quantum Electronics **30**, 1313 (1994).

[144] L. Jia, J. Wu, T. Yang, B. Jia, and D. J. Moss, ACS Applied Nano Materials **3**, 6876 (2020).

[145] T. Yang, I. Abdelwahab, H. Lin, Y. Bao, S. J. Rong Tan, S. Fraser, K. P. Loh, and B. Jia, ACS Photonics **5**, 4969 (2018).

[146] I. V. Shadrivov, M. Lapine, and Y. S. Kivshar, *Nonlinear, tunable and active metamaterials*, 1st ed. (Springer, 2015).

[147] D. S. Chemla, D. A. B. Miller, and P. W. Smith, Optical Engineering **24**, 244556 (1985).

[148] L. Caspani, R. P. M. Kaipurath, M. Clerici, M. Ferrera, T. Roger, J. Kim, N. Kinsey, M. Pietrzyk, A. Di Falco, V. M. Shalaev, A. Boltasseva, and D. Faccio, Phys. Rev. Lett. **116**, 233901 (2016).

[149] O. Reshef, E. Giese, M. Z. Alam, I. D. Leon, J. Upham, and R. W. Boyd, Opt. Lett. **42**, 3225 (2017).

[150] P. Béjot, J. Kasparian, S. Henin, V. Loriot, T. Vieillard, E. Hertz, O. Faucher, B. Lavorel, and J.-P. Wolf, Phys. Rev. Lett. **104**, 103903 (2010).

[151] M. Sheik-Bahae and H.-S. Kwok, IEEE Journal of Quantum Electronics **23**, 1974 (1987).

[152] M. Sheik-Bahae, D. J. Hagan, and E. W. V. Stryland, Phys. Rev. Lett. **65**, 96 (1990).

[153] L. von Grafenstein, M. Bock, D. Ueberschaer, K. Zawilski, P. Schunemann, U. Griebner, and T. Elsaesser, Opt. Lett. **42**, 3796 (2017).

[154] J. Weisshaupt, V. Juve, . Holtz, S. Ku, M. Woerner, T. Elsaesser, S. Alisauskas, A. Pugzlys, and A. Baltuska, Nat. Photon. **8**, 927 (2014).

[155] A. V. Mtrofanov, A. A. Voronin, D. A. Sidorov-Biryukov, A. Pugzlys, E. A. Stepanov, G. Andriukaitis, T. Flory, S. Alisauskas, A. B. Fedotov, A. Baltuska, and A. M. Zheltikov, Sci. Rep. **5**, 8368 (2015).

[156] V. Shumakova, S. Ališauskas, P. Malevich, C. Gollner, A. Baltuška, D. Kartashov, A. M. Zheltikov, A. V. Mitrofanov, A. A. Voronin, D. A. Sidorov-Biryukov, and A. Pugžlys, Opt. Lett. **43**, 2185 (2018).

[157] W. B. Gandrud and R. L. Abrams, Appl. Phys. Lett. **17**, 302 (1970).

[158] G. W. Iseler, H. Kildal, and N. Menyuk, J. Electron. Mater. **7**, 737 (1978).

[159] R. C. Eckardt, Y. X. Fan, R. L. Byer, R. K. Route, R. S. Feigelson, and J. van der Laan, Appl. Phys. Lett. **47**, 786 (1985).

[160] Y. M. Andreev, V. Y. Baranov, V. G. Voevodin, P. P. Geiko, A. . Gribenyukov, S. V. Izyumov, S. M. Kozochkin, V. D. Pis'mennyi, Y. A. Satov, and A. P. Strel'tsov, Sov. J. Quantum Electron. **17**, 1435 (1988).

[161] G. B. Abdullaev, K. R. Allakhverdiev, M. E. Karasev, V. I. Konov, L. A. Kulevskii, N. B. Mustafaev, P. P. Pashinin, A. M. Prokhorov, Y. M. Starodumov, and N. I. Chapliev, Sov. J. Quantum Electron. **19**, 494 (1989).

[162] A. Zakel, J. L. Blackshire, P. G. Schunemann, S. D. Setzler, J. Goldstein, and S. Guha, Appl. Opt. **41**, 2299 (2002).

[163] M. N. Polyanskiy, I. V. Pogorelsky, M. Babzien, and M. A. Palmer, OSA Continuum **3**, 459 (2020).

[164] S. Y. Tochitsky, J. J. Pigeon, D. J. Haberberger, C. Gong, and C. Joshi, Opt. Express **20**, 13762 (2012).

[165] D. F. Gordon, V. Hasson, H. von Bergmann, Y. hsin Chen, A. Schmitt-Sody, and J. R. Penano, in *Ultrafast Bandgap Photonics*, Vol. 9835, edited by M. K. Rafailov and E. Mazur, International Society for Optics and Photonics (SPIE, 2016) pp. 108 – 112.

[166] E. Welch, D. Matteo, S. Tochitsky, G. Louwrens, and C. Joshi, Physics of Plasmas **29**, 053504 (2022).

[167] H. H. Li, International Journal of Thermophysics **1**, 97 (1980).

[168] S. Y. Tochitsky, V. O. Petukhov, V. A. Gorobets, V. V. Churakov, and V. N. Jakimovich, Appl. Opt. **36**, 1882 (1997).

[169] K. Vodopyanov, G. Knippels, A. van der Meer, J. Maffetone, and I. Zwieback, Optics Communications **202**, 205 (2002).

[170] A. Harasaki and K. Kato, Jpn. J. Appl. Phys. **36**, 700 (1997).

[171] V. V. Badikov, P. F. Gonzalez-Diaz, M. G. Santos, C. L. Siguenza, G. S. Shevyrdayeva, A. S. Solodukhin, and S. A. Trushin, in *Nonlinear Optical Interactions and Wave Dynamics*, Vol. 2800, edited by N. I. Koroteev, V. A. Makarov, and K. N. Drabovich, International Society for Optics and Photonics (SPIE, 1996) pp. 153 – 156.

[172] D. Chemla, R. Begley, and R. Byer, IEEE Journal of Quantum Electronics **10**, 71 (1974).

[173] J. J. Pigeon, D. A. Matteo, S. Y. Tochitsky, I. Ben-Zvi, and C. Joshi, J. Opt. Soc. Am. B **37**, 2076 (2020).

[174] A. Nguyen, P. G. de Alaiza Martinez, I. Thiele, S. Skupin, and L. Bergé, Phys. Rev. A **97**, 063839 (2018).

[175] D. Jang, R. M. Schwartz, D. Woodbury, J. Griff-McMahon, A. H. Younis, H. M. Milchberg, and K.-Y. Kim, Optica **6**, 1338 (2019).

[176] A. J. Alcock, P. B. Corkum, and D. J. James, Applied Physics Letters **27**, 680 (1975).

[177] J. Meyer, A. Y. Elezzabi, and M. K. Y. Hughes, IEEE J. Quantum Electron. **31**, 1292 (1995).

[178] A. J. Alcock, P. B. Corkum, D. J. James, K. E. Leopold, and J. C. Samson, Optics Communications **18**, 543 (1976).

[179] S. A. Jamison and A. V. Nurmikko, Applied Physics Letters **33**, 598 (1978).

[180] C. Rolland and P. B. Corkum, JOSA B **3**, 1625 (1986).

[181] A. Y. Elezzabi, J. Meyer, M. K. Y. Hughes, and S. R. Johnson, Optics Letters **19**, 898 (1994).

[182] S. Marchetti, M. Martinelli, R. Simili, M. Giorgi, and R. Fantoni, Applied Physics B **72**, 927 (2001).

[183] A. Leblanc, P. Lassonde, S. Petit, J.-C. Delagnes, E. Haddad, G. Ernotte, M. R. Bionta, V. Gruson, B. E. Schmidt, H. Ibrahim, E. Cormier, and F. Legare, Optics Express **27**, 28998 (2019).

[184] B. Mayer, C. Schmidt, J. Bühler, D. V. Seletskiy, D. Brida, A. Pashkin, and A. Leitenstorfer, New Journal of Physics **16**, 063033 (2014).

[185] S. Y. Tochitsky, R. Narang, C. Filip, C. E. Clayton, K. A. Marsh, and C. Joshi, Opt. Lett. **24**, 1717 (1999).

[186] R. Huber, F. Tauser, A. Brodschelm, M. Bichler, G. Abstreiter, and A. Leitenstorfer, Nature **414**, 286 (2001).

[187] M. Sheik-bahae and H. S. Kwok, Opt. Lett. **12**, 702 (1987).

[188] D. E. Aspnes, S. M. Kelso, R. A. Logan, and R. Bhat, J. Appl. Phys. **60**, 754 (1986).

[189] T. N. Nunley, N. S. fernando, N. Samarasingha, J. M. Moya, C. M. Nelson, A. A. Medina, and S. Zollner, J. Vac. Sci. Technol. B **34**, 061205 (2016).

[190] M. Aven, D. T. F. Marple, and B. Segall, J. Appl. Phys. **32**, 2261 (1961).

[191] J. Shah, *Ultrafast spectroscopy of semiconductors and semiconductor nanostructures* (Springer, Berlin, 1999).

[192] F. Kadlec, H. Němec, and P. Kužel, Phys. Rev. B **70**, 125205 (2004).

[193] G. Vaudel, T. Pezeril, A. Lomonosov, M. Lejman, P. Ruello, and V. Gusev, Phys. Rev. B **90**, 014302 (2014).

[194] H. Roskos, B. Rieck, A. Seilmeier, and W. Kaiser, Applied Physics Letters **53**, 2406 (1988).

[195] M. Mehendale, S. Sivananthan, and W. A. Schroeder, Appl. Phys. Lett. **71**, 1089 (1997).

[196] J. F. Young and H. M. van Driel, Phys. Rev. B **26**, 2147 (1982).

[197] R. Ziebold, T. Witte, M. Hübner, and R. G. Ulbrich, Phys. Rev. B **61**, 16610 (2000).

[198] E. J. Canto-Said, D. J. H. nd J. Young, and E. W. V. Stryland, IEEE Journal of Quantum Electronics **27**, 2274 (1991).

[199] U. Strauss, W. W. Ruhle, and K. Kohler, Applied Physics Letters **62**, 55 (1993).

[200] D. H. Auston, C. V. Shank, and P. LeFur, Phys. Rev. Lett. **35**, 1022 (1975).

[201] J. R. Milward, W. Ji, A. K. Kar, C. R. Pidgeon, and B. S. Wherrett, J. Appl. Phys. **69**, 2708 (1991).

[202] A. Y. Elezzabi, J. Meyer, and M. K. Y. Hughes, Appl. Phys. Lett. **66**, 402 (1995).

[203] E. C. Fox and H. M. van Driel, Phys. Rev. B **47**, 1663 (1993).

[204] T. Troha, F. Klimovič, T. c. v. Ostatnický, F. Kadlec, P. Kužel, and H. Němec, Phys. Rev. Lett. **130**, 226301 (2023).

[205] M. Guizar-Sicairos and J. C. Gutiérrez-Vega, J. Opt. Soc. Am. A **21**, 53 (2004).

[206] M. Guizar, "Integer order Hankel transform," (2016), (https://www.mathworks.com/matlabcentral/fileexchange/6570-integer-order-hankel-transform), MATLAB Central File Exchange. Retrieved August 9, 2022.

[207] J. Marburrger and W. Wagner, IEEE Journal of Quantum Electronics **3**, 415 (1967).

[208] K. D. Moll, A. L. Gaeta, and G. Fibich, Phys. Rev. Lett. **90**, 203902 (2003).

[209] J. Marburger, Progress in Quantum Electronics **4**, 35 (1975).

[210] E. L. Dawes and J. H. Marburger, Phys. Rev. **179**, 862 (1969).

[211] V. B. Anzin, M. I. Eremets, Y. V. Kosichkin, A. I. Nadezhdinskii, and A. M. Shirokov, Phys. Stat. Sol. (a) **42**, 385 (1977).

[212] J. P. Gordon, R. C. C. Leite, R. S. Moore, S. P. S. Porto, and J. R. Whinnery, Journal of Applied Physics **36**, 3 (1965).

[213] R. O. Carlson, G. A. Slack, and S. J. Silverman, Journal of Applied Physics **36**, 505 (1965).

[214] G. Ghosh, *Handbook of Therm-Optic Coefficients of Optical Materials with Applications*, 1st ed. (Academic Press, 1997).

[215] P. Bhaskar, A. W. Achtstein, M. J. W. Vermeulen, and L. D. A. Siebbeles, J. Phys. Chem. C **123**, 841 (2019).

[216] R. L. Swofford and J. A. Morrell, Journal of Applied Physics **49**, 3667 (1978).

[217] H. S. Carslaw and J. C. Jaeger, "Operational Methods in Applied Mathematics," (Dover, New York, 1963).

[218] K. Wang, X. Zhang, I. M. Kislyakov, N. Dong, S. Zhang, G. Wang, J. Fan, X. Zou, J. Du, Y. Leng, Q. Zhao, K. Wu, J. Chen, S. M. Baesman, K.-S. Liao, S. Maharjan, H. Zhang, L. Zhang, S. A. Curran, R. S. Oremland, W. J. Blau, and J. Wang, Nature Communications **10**, 3985 (2019).

[219] M. F. Hossain, H. P. Chan, and M. A. Uddin, Appl. Opt. **49**, 403 (2010).

[220] J. M. Dudley, G. Genty, and S. Coen, Rev. Mod. Phys. **78**, 1135 (2006).

[221] R. R. Alfano, *The Supercontinuum Laser Source*, 3rd ed. (Springer, 2018).

[222] M. Nisoli, S. D. Silvestri, O. Svelto, R. Szipöcs, K. Ferencz, C. Spielmann, S. Sartania, and F. Krausz, Opt. Lett. **22**, 522 (1997).

[223] K. Y. Kim, I. Alexeev, and H. M. Milchberg, Applied Physics Letters **81**, 4124 (2002).

[224] C. Poudel and C. F. Kaminski, J. Opt. Soc. Am. B **36**, A139 (2019).

[225] I. Zorin, P. Gattinger, A. Ebner, and M. Brandstetter, Opt. Express **30**, 5222 (2022).

[226] C. R. Petersen, U. Møller, I. Kubat, B. Zhou, S. Dupont, J. Ramsay, T. Benson, S. Sujecki, N. Abdel-Moneim, Z. Tang, D. Furniss, A. Seddon, and O. Bang, Nature Photonics **8**, 830 (2014).

[227] Z. Zhao, B. Wu, X. Wang, Z. Pan, Z. Liu, P. Zhang, X. Shen, Q. Nie, S. Dai, and R. Wang, Laser & Photonics Reviews **11**, 1700005 (2017).

[228] J. J. Pigeon, S. Y. Tochitsky, C. Gong, and C. Joshi, Opt. Lett. **39**, 3246 (2014).

[229] A. A. Lanin, A. A. Voronin, E. A. Stepanov, A. B. Fedotov, and A. M. Zheltikov, Opt. Lett. **40**, 974 (2015).

[230] F. Silva, D. R. Austin, A. Thai, M. Baudisch, M. Hemmer, D. Faccio, A. Couairon, and J. Biegert, Nature Communications **3**, 807 (2012).

[231] I. Gordon *et al.*, Journal of Quantitative Spectroscopy and Radiative Transfer **277**, 107949 (2022).

[232] H. O. H. Churchill, G. J. Salamo, S.-Q. Yu, T. Hironaka, X. Hu, J. Stacy, and I. Shih, Nanoscale Research Letters **12**, 488 (2017).

[233] A. Demircan and U. Bandelow, Applied Physics B **86**, 31 (2007).

[234] V. O. Petukhov and V. A. Gorobets, in *4th International Conference on Advanced Optoelectronics and Lasers* (2008) pp. 43–45.